



HAL
open science

Sublimation growth of Al_4SiC_4 and study of heterostructures of Al-Si-C system on SiC.

Hoang Long Le Tran

► **To cite this version:**

Hoang Long Le Tran. Sublimation growth of Al_4SiC_4 and study of heterostructures of Al-Si-C system on SiC.. Crystallography. Université Grenoble Alpes, 2018. English. NNT : 2018GREAI034 . tel-01859586

HAL Id: tel-01859586

<https://theses.hal.science/tel-01859586>

Submitted on 22 Aug 2018

HAL is a multi-disciplinary open access archive for the deposit and dissemination of scientific research documents, whether they are published or not. The documents may come from teaching and research institutions in France or abroad, or from public or private research centers.

L'archive ouverte pluridisciplinaire **HAL**, est destinée au dépôt et à la diffusion de documents scientifiques de niveau recherche, publiés ou non, émanant des établissements d'enseignement et de recherche français ou étrangers, des laboratoires publics ou privés.

THÈSE

Pour obtenir le grade de

DOCTEUR DE LA COMMUNAUTÉ UNIVERSITÉ GRENOBLE ALPES

Spécialité : Matériaux, Mécanique, Génie civil, Electrochimie

Arrêté ministériel : 25 mai 2016

Présentée par

Hoang-Long LE TRAN

Thèse dirigée par **Didier CHAUSSENDE** et
codirigée par **Eirini SARIGIANNIDOU**

préparée au sein du **Laboratoire des Matériaux et du Génie Physique**
dans **I'MEP-2**

Croissance en phase gazeuse d' Al_4SiC_4 et étude d'hétérostructures dans le système Al-Si-C sur SiC

Thèse soutenue publiquement le **15 Juin 2018**,
devant le jury composé de :

Dr. Elisabeth BLANQUET

Directeur de recherche CNRS, U. Grenoble Alpes, Examineur, Président

Dr. Sandrine JUILLAGUET

Maître de Conférences, U. Montpellier, Examineur

Dr. Gabriel FERRO

Directeur de recherche CNRS, UCB Lyon 1, Rapporteur

Dr. Joseph KIOSEOGLU

Professeur associé, Aristotle University of Thessaloniki, Rapporteur

Dr. Eirini SARIGIANNIDOU

Professeur associé, Grenoble INP, Co-directeur de thèse

Dr. Didier CHAUSSENDE

Directeur de recherche CNRS, U. Grenoble Alpes, Directeur de thèse



Acknowledgement

This PhD thesis came as result of the combined efforts and supports of people whom I had the pleasure to work with, and I would like to acknowledge.

First of all, I would like to express my deepest gratitude to my supervisor **Dr. Didier Chaussende** and co-supervisor **Dr. Eirini Sarigiannidou** for giving me opportunity to work in an interesting topic with them. From the very first day until the last moment of my thesis, they gave me many helpful suggestions which result in significantly improving my work and lead me to the way to become a scientist. With his experiences and perspectives as an expertise in crystal growth, Didier really guided me to the right way for understanding and advancing crystal growth field. For Eirini, with her kindness and thoroughness, she followed my work with countless advices and supports during the past three years. Again, I would like to thank them for being patient and supportive to correct and help me completing this dissertation.

Secondly, I would like to thank **Dr. Elisabeth Blanquet** for her kind help, her introduction to the thermodynamic calculation, and specially for presiding the Jury of my thesis. Special thanks go to **Dr. Joseph Kioseoglou** for his very kind help related to the GPA analysis and for being rapporteur of my thesis. I am very grateful to **Dr. Gabriel Ferro** for being rapporteur of my thesis and especially, his useful comments and for giving me an opportunity to improve the manuscript. I would like to thank **Dr. Juillaguet Sandrine** for being a member of the jury.

I would like also thank to all current and former members of the “Cristallogenèse group”. In particular, I am thankful to **Dr. Odette Chaix** for helping me in Raman spectroscopy, **Dr. Isabelle Gélard** for helping in conducting experiment, SEM and also for fruitful discussion, **Prof. Jean-Marc Dedulle** for helping me in COMSOL simulation, **Prof. Thierry Ouisse** for fruitful scientific discussion, **Joseph La Manna** for helping me in mechanical stuffs, **Dr. Dominique De Barros** for helping in building experimental apparatus. I would like also thank to **Dr. Nikolaos Tsavdaris**, **Dr. Kanaparin Ariyawong** and **Dimitrios Zevgitis** for sharing their results which are very helpful for me. Special thanks go to **Shiqi Zhang**, and **Dr. YunJi Shin** for their friendships, support, and joyful moments that we share inside and outside the laboratory.

I would like thank to all members of LMGP for their kindness and hospitality. Their warm greeting created a generous working environment. Exclusively thanks would go to **Hervé**

Roussel for helping me in XRD analysis, **Laetitia Rapenne** for helping me in TEM, and **Laurent Terrier** for introducing me to Uv-Vis spectrophotometer, **Beatrice Doisneau** for introducing me to SEM, and **Michele San Martin** for administrative work. I give my acknowledgements to the director of the lab **Prof. Franz Bruckert** and vice- director **Dr. Carmen Jimenez**.

I would like to thank to **Dr. Ioana Nuta** in SiMAP for sharing her office with me during my thermodynamic calculations.

Specials thank to all my friend in Grenoble: Trà, Thủy, Hương, Toại, Toàn, Chương, Maxime, Hongjun, Thomas, Morganne, Antalya, Evgenii, Damir, Simon, etc; their advices and encouragements are very important to me. It is my pleasure to be friend with them.

Especially, thank to my Pi for supporting, encouraging me, and making my life happy and complete. Thank you for everything, my love!

Finally, I would like to thank to my parents and to my brother, for all their supports, for encouraging and for loving me not only in PhD period but also in all of my life. This thesis is dedicated for them.

Table of contents

Introduction	1
Chapter I. State of art of Al₄SiC₄	5
1.1. History of Al ₄ SiC ₄	6
1.2. Structure and physical properties of Al ₄ SiC ₄	7
1.2.1. Crystalline structure	7
1.2.2. Vibrational properties	9
1.2.3. Ceramic and mechanical properties	13
1.2.4. Electronic properties	15
1.3. Al ₄ SiC ₄ as electronic materials	17
1.4. State of art of Al ₄ SiC ₄ synthesis	19
1.5. Purpose and contribution of the current thesis	24
Chapter II. Experimental apparatus	29
2.1. Experimental apparatus	30
2.1.1. Physical Vapor Transport reactor setup	30
2.1.2. Crucible	33
2.2. Characterization methods	35
2.2.1. X-Ray diffractometry (θ -2 θ , ω -scan and Rietveld refinement)	33
2.2.2. Raman spectroscopy	39
2.2.3. Transmission/absorption spectroscopy	41
2.2.4. Scanning electron microscopy	43
2.2.5. Transmission electron microscopy	45
Chapter III. Thermo-chemistry of the Al₄C₃-SiC system	51
3.1. Thermodynamic background	52
3.1.1. Al-Si binary system	52
3.1.2. Si-C binary system	53
3.1.3. Al-C binary system	54
3.1.4. Al-Si-C ternary system	56
3.2. Differential thermal analysis	57

3.2.1. Experimental apparatus	57
3.2.2. Experimental process	58
3.2.3. Experimental results and discussion	60
3.3. Thermodynamic calculation	64
3.3.1. Calculation methodology	64
3.3.2. Thermochemistry gas solid system	66
3.3.2.1. The vaporization of the powders	66
3.3.2.2. The condensation at seed	70
Conclusions of the chapter	77
Chapter IV. Al₄SiC₄ synthesis and sublimation growth	81
4.1. Simulation of temperature distribution	82
4.1.1. Effect of induction frequency	82
4.1.2. Temperature distribution	84
4.1.3. Effect of coil's position on sublimation growth	87
4.2. Al ₄ SiC ₄ synthesis	89
4.2.1. Remarks about oxygen in the system	89
4.2.2. Experimental process	90
4.2.3. Experimental results	91
4.2.4. Discussion	96
4.3. Al ₄ SiC ₄ sublimation growth	99
4.3.1. Experimental process	99
4.3.2. Experimental results	100
4.3.3. Discussion	109
4.4. Additional characterizations of the Al ₄ SiC ₄ deposits	112
4.4.1. Dependence of the growth mechanism on SiC substrate	112
4.4.2. Growth orientation and texture of Al ₄ SiC ₄ crystal layers	119
4.4.3. Optical properties	126
Conclusions of the chapter	129
Chapter V. Hetero-epitaxy of Al-Si-C based compounds on SiC	133
5.1. Introduction	134

5.2.	Al ₄ C ₃ single crystal	136
5.2.1.	Experiments	136
5.2.2.	Experimental results	139
5.2.3.	Characterizations of the Al ₄ C ₃ single crystals	139
5.3.	Al ₄ C ₃ /SiC hetero-epitaxy	142
5.3.1.	Experimental process	142
5.3.2.	Wetting behavior of Al/[0001] Si face 6H-SiC system	144
5.3.3.	Dissolution-precipitation mechanism of Al/[0001] Si face 6H-SiC system	151
5.3.4.	Strain field analysis	157
5.4.	Al ₄ SiC ₄ /SiC hetero-epitaxy	166
5.4.1.	Residual oxygen in the system	167
5.4.2.	Al ₄ SiC ₄ /SiC epitaxial relationship	169
5.4.3.	Strain field analysis of Al ₄ SiC ₄ /C face 4° off axis [0001] 4H-SiC	173
	Conclusions of the chapter	180
	General conclusions and perspectives	185

INTRODUCTION

Over the past decades, both optoelectronics and power electronics have drawn more attention and became a technological revolution during the last fifteen years. Indeed, these developments require a significant progress of the wide band gap (WBG) semiconductor materials such as silicon carbide (SiC) (*4H*-SiC with the band gap of 3.26eV^1), gallium nitride (GaN) ($\sim 3.45\text{eV}^2$), diamond ($\sim 5.5\text{eV}^3$). Among them, GaN-based alloys have actually brought the 2014 Nobel Prize in Physics jointly to Isamu Akasaki, Hiroshi Amano and Shuji Nakamura "for the invention of efficient blue light-emitting diodes LEDs which has enabled bright and energy-saving white light sources". The WBG materials have also application in the so-called "power electronics" which operate in almost everything from electric vehicles and industrial motors, to laptop power adaptors and inverters that connect solar panels and wind turbines to the electric grid.

Despite all these efforts, electronic and optoelectronic devices able to operate under harsh environmental conditions, e.g. high temperature, corrosive atmosphere, radiations, still need to be invented. It addresses a broad range of applications such as gas sensors, radiation sensors, high temperature logics, photo-electrodes for water splitting, etc. To adapt these exigent conditions, some requirements are needed such as:

- Band gap appropriate to the electronic application (able to work at high temperature and/or the UV-Visible energy range).

- High thermal conductivity to avoid the overheating and high temperature gradients in the devices.
- High semiconducting performances (high carrier mobility, high breakdown voltage...).
- High chemical and thermal inertia, resistance to corrosion, chemicals, oxidation, temperature...

Combining non-toxic and abundant elements, the Al-Si-C ternary system, which contains a variety of compounds of different chemical composition with the general formula $(Al_4C_3)_x(SiC)_y$, is viewed as a potential candidate. The prototype material will be Al_4SiC_4 , which has attracted a particular interest due to its interesting ceramic properties^{4, 5} and its semiconducting properties⁶. Indeed, as a refractory material, Al_4SiC_4 could be used as a high-temperature structural material and thermal coating for high temperature applications. With a predicted electronic band gap around $2.5eV$ ^{6, 7}, Al_4SiC_4 is ideal for photovoltaic and photo-electrochemical water splitting applications.

In this thesis, combining thermodynamic analysis with experimental approach, the synthesis of Al_4SiC_4 single crystals will be thoroughly investigated. Moreover, new hetero-epitaxy structures on hexagonal SiC will be proposed which could be of interest for many applications.

The structure of the present thesis consists of 5 chapters.

The first chapter is an introduction and a state of the art of Al_4SiC_4 followed by the presentation of its main structural characteristics and properties.

The second chapter is dedicated to the description of the experimental apparatus and characterization methods used in this thesis.

In the third chapter, the thermo-chemistry of the Al_4C_3 -SiC pseudo binary system will be investigated by thermodynamic calculation. Based on that, a vapor phase route for the growth of Al_4SiC_4 will be proposed and the experimental conditions such as raw composition, temperature, and temperature gradient are determined.

In the fourth chapter, experimental approaches will be presented in details. These approaches are developed based on the thermodynamic analysis of Al_4C_3 -SiC system presented in previous chapter. Moreover, results from structural and optical characterizations collected from the obtained Al_4SiC_4 crystals will be presented.

Finally, in the fifth chapter, different hetero-epitaxial structures of Al-Si-C system on hexagonal SiC substrate (i.e. Al₄C₃/SiC and Al₄SiC₄/SiC) will be studied using high resolution transmission electron spectroscopy. The interface of the structures will be carefully analyzed in order to investigate their epitaxial relationships and growth mechanism.

REFERENCE

1. C. Persson and U. Lindefelt, *Physical Review B* **54** (15), 10257-10260 (1996).
2. J. F. Muth, J. H. Lee, I. K. Shmagin, R. M. Kolbas, H. C. Casey, B. P. Keller, U. K. Mishra and S. P. DenBaars, *Applied Physics Letters* **71** (18), 2572-2574 (1997).
3. J. Camassel, S. Contreras and J.-L. Robert, *Comptes Rendus de l'Académie des Sciences - Series IV - Physics* **1** (1), 5-21 (2000).
4. X. X. Huang, G. W. Wen, X. M. Cheng and B. Y. Zhang, *Corrosion Science* **49** (5), 2059-2070 (2007).
5. X.-x. Huang and G.-w. Wen, *Ceramics International* **33** (3), 453-458 (2007).
6. D. Zevgitis, O. Chaix-Pluchery, B. Doisneau, M. Modreanu, J. La Manna, E. Sarigiannidou and D. Chaussende, presented at the Materials Science Forum, 2015, Vol. 821, pp. 974-977.
7. L. Pedesseau, J. Even, M. Modreanu, D. Chaussende, E. Sarigiannidou, O. Chaix-Pluchery and O. Durand, *APL Mater.* **3** (12), 121101 (2015).

CHAPTER I

STATE OF ART OF Al_4SiC_4

This chapter is an introduction to the “new” semiconductor Al_4SiC_4 and its synthesis techniques. In the first part, a brief overview of Al_4SiC_4 history is given with its physical properties such as, crystalline structure, vibrational properties, ceramic properties and electronic properties. The second part is dedicated to the synthesis of Al_4SiC_4 . The state of art of its growth techniques is given, which could be separated in three different approaches: solution growth, solid state sintering and sublimation growth. Finally, the purpose and the contribution of this thesis in the growth and characterization of Al_4SiC_4 will be presented.

1.1. History of Al₄SiC₄

Al₄SiC₄ was firstly mentioned by Barczak in a letter issued in 1961¹, where was first reported the X-ray diffraction data for this compound. According to the author, two different polymorphs of Al₄SiC₄ could be synthesized at high temperature: (i) α -Al₄SiC₄ phase with a hexagonal structure formed by melting the 4:1 molar mixture of aluminum and silicon with an excess of carbon in a sealed carbon container at 1620°C, and (ii) β -Al₄SiC₄ phase with an undescribed structure formed by annealing a 1:1 molar mixture of Al₄C₃:SiC at 1870°C.

Twenty years later, the X-ray crystallographic data of Al₄SiC₄ were refined by Schoennahl *et al.*² (1984). He found a different unit cell dimension as compared with that of Barczak and reported a full description of α -Al₄SiC₄ phase. However, β -Al₄SiC₄-the second polymorph proposed by Barczak was not observed. The process for the synthesis of Al₄SiC₄ powder was detailed in the report. The author also mentioned the possibility to synthesize small Al₄SiC₄ mono-crystals by firing at high temperature, either an Al₄SiC₄ sintered body or a mixture of Al₄C₃ and SiC raw materials. They also pointed out the extremely narrow temperature window, of about 30°C between 1950°C and 1980°C, conditions under which small yellowish transparent platelets were obtained.

In 1987, the phase equilibria in the ternary Al-Si-C system was experimentally investigated by Oden and McCune³ in order to help future research and development of a carbo-thermic reduction for aluminum. Ten years later, in 1996, the thermodynamic parameters of ternary system Al-Si-C were assessed by Grobner *et al.*⁴ thanks to the heat capacity given by Beyer *et al.*⁵ in 1984.

In the 1990s, the chemical interaction of Al/SiC interface was studied for the development of the SiC-reinforced aluminum composite materials⁶⁻¹³. Al₄SiC₄ was found as platelets formed by reacting SiC in excess of aluminum for 30 min at 1497°C. Moreover, due to the transiently formation of Al₄C₃ at the early stage of the reaction, the author also predicted the growth of Al₄SiC₄ by solid state diffusion¹³.

In 2002, an excellent oxidation resistance of Al₄SiC₄ at temperature lower than 850°C has been found¹⁴. Five years later, the mechanical and thermal properties of Al₄SiC₄ produced by solid state reaction were investigated^{15, 16}.

In 2008, the electronic structure of Al_4SiC_4 has been investigated theoretically through *ab initio* calculations by Hussain *et al.*¹⁷. An indirect band gap of 1.05eV was predicted, making Al_4SiC_4 as compound with semiconducting properties.

However, at the first glance, this bandgap value is not compatible with the transparency of the platelets reported by Schoennahl *et al.*, where Al_4SiC_4 crystal was recognized with a yellowish color². This discrepancy was the starting point of our investigation of Al_4SiC_4 . High quality single crystalline small platelets have been synthesized by our group in order to measure the UV-Vis absorption spectrum of Al_4SiC_4 . An optical band gap of about 2.5 eV¹⁸ was found to be in good agreement with the one computed more recently by Pedesseau *et al.*¹⁹. According to the calculated band gap structure, Al_4SiC_4 exhibits both indirect and direct band gap energies of 2.5eV and 3.2eV, respectively. Slightly higher than the band gap of 3C-SiC (cubic polytype of SiC), Al_4SiC_4 could be a potential material for applications such as high temperature electronics, photovoltaic or photo-electrochemical water splitting.

1.2. Structure and physical properties of Al_4SiC_4

1.2.1. Crystalline structure

From the crystallographic point of view, Al_4SiC_4 belongs to a family of aluminum-silicon ternary carbides with hexagonal layered structure which can be identified by the general formula $(\text{Al}_4\text{C}_3)_x(\text{SiC})_y$ ($x, y = 1$ or 2). According to the crystal structure illustrated in Figure 1.1, Al_4SiC_4 consists of two kinds of layers which are alternatively stacked along the $[0001]$ direction. One layer is the Al-C slab following the Al_4C_3 -type structure and the other layer consists of Si-C slab following the 2H-SiC structure. The crystal structure of Al_4SiC_4 was experimentally confirmed by Transmission Electron Microscopy (TEM) and X-ray Diffraction to belong to $P6_3mc$ space group with lattice parameters $a = 3.2812 (\pm 0.0045) \text{ \AA}$ and $c = 21.7042 (\pm 0.0554) \text{ \AA}$ ¹⁸ which are in good agreement with the reported crystallographic data².

Two other Al-Si-C ternary carbides such as $\text{Al}_4\text{Si}_2\text{C}_5$ and Al_8SiC_7 were discovered by Inoue²⁰ in 1980 and Kidwell²¹ in 1984, respectively. According to the stoichiometry, $\text{Al}_4\text{Si}_2\text{C}_5$ consists of one Al_4C_3 -type structural unit and two SiC-type structural units while Al_8SiC_7 consists of two Al_4C_3 -type structural unit and one SiC-type structural units.

The relative unit cells of different aluminum-silicon ternary carbides compounds are compared in Table 1.1.

Table 1.1: Crystallographic data of the different phases identified in the Al-Si-C system.

Formula	Space group	Lattice constant (Å)		c/a
		a	c	
SiC-4H ²²	P6 ₃ mc	3.08	10.06	3.27
SiC-6H ²²	P6 ₃ mc	3.08	15.09	4.90
Al ₄ C ₃ ²³	R-3m	3.33	24.98	7.50
Al ₄ SiC ₄ (Al ₄ C ₃ .SiC) ²	P6 ₃ mc	3.28	21.72	6.62
Al ₈ SiC ₇ (2Al ₄ C ₃ .SiC) ²¹	P3	3.31	19.24	5.81
Al ₄ Si ₂ C ₅ (Al ₄ C ₃ .2SiC) ²⁰	R-3m	3.25	40.10	12.34

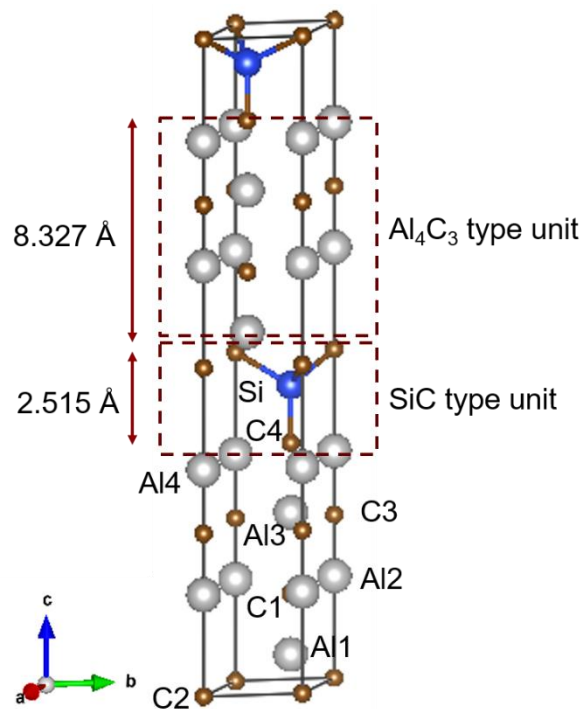


Figure 1.1: Crystal structure of Al₄SiC₄. The gray, blue, and brown balls represent Al, Si, and C atoms, respectively. The Al and C atoms in Al₄SiC₄ are indexed with numbers according to the Crystallographic Information File (CIF) given by Schoennahl et al.². The Al₄C₃ cell and SiC cell units in Al₄SiC₄ are also indicated with the height in normal direction of 8.327 and 2.515Å, respectively.

1.2.2. Vibrational properties

The vibrational properties of Al_4SiC_4 have been firstly reported by our group in 2014. The first Raman spectroscopy measurements were performed on Al_4SiC_4 single crystalline platelets which were successfully synthesized by the high temperature solution growth method¹⁸.

The typical unpolarized Al_4SiC_4 Raman spectrum shown in Figure 1.2 is characterized by 17 Raman lines in the 80-920 cm^{-1} range (7 A_1 modes, 5 E_2 modes and 5 E_1 modes). As compared with Al_4C_3 ²⁴, several common lines (at 255 cm^{-1} and 865 cm^{-1} for example) corresponding to similar Al-C vibrations were found. The symmetry assignment was also initially performed and reported in the unpolarized spectrum.

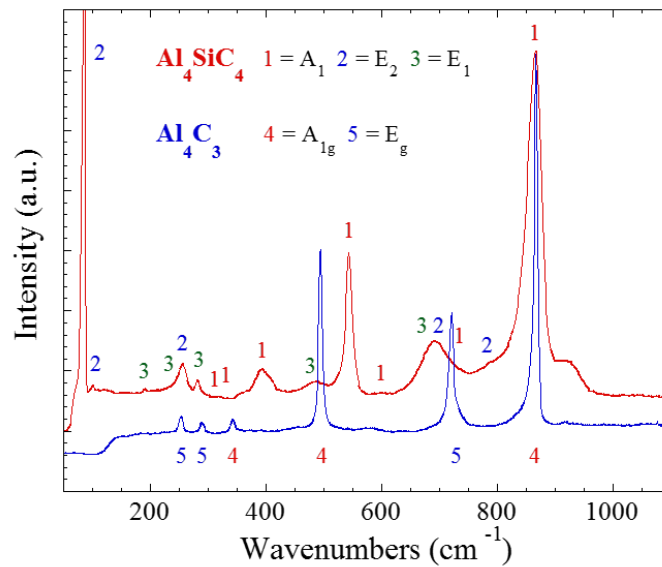


Figure 1.2: Unpolarized Raman spectra of Al_4SiC_4 and Al_4C_3 . Spectra were collected at room temperature in a backscattering geometry using a Jobin Yvon/Horiba LabRam spectrometer with different laser excitations ($\lambda = 488, 5.14.5$ and 632.8 nm). The laser spot size was $1 \mu\text{m}^2$ at the sample surface¹⁸.

The study of vibrational properties has been recently completed in 2017. In this work, both theoretical and experimental results have been reported²⁵. Experimentally, the Raman and Infrared (IR) spectroscopy analysis were performed on the Al_4SiC_4 single crystal in different polarized configurations (laser propagation // c axis, and laser propagation \perp c axis). In order to verify and complete the mode assignment, density functional theory (DFT) calculations have been used to describe the phonon spectra including the LO-TO splitting. A good agreement between the experimental and calculated Raman phonon modes allowed the symmetry

assignment of all the measured Raman modes. Based on the analyzed Raman data, most of the IR modes were assigned.

The Figure 1.3 (from reference 25) shows the polarized Raman spectra of Al_4SiC_4 single crystals collected in different configurations. With the laser propagation along the c-axis, two spectra are given for parallel polarization (Z(XX)Z) and cross polarization (Z(XY)Z). In case of laser propagation parallel to the crystal surface, spectra corresponding to the parallel polarization (X(ZZ)X or X(YY)X) and cross polarization (X(ZY)X) are given. Note that Z axis is parallel to the [0001] direction, X and Y are parallel with [10-10] and [12-30] direction, respectively. According to the crystalline structure, Al_4SiC_4 consists of 18 atoms with 54 zone center vibration modes. After subtraction of the three acoustic modes, the optical modes can be expressed as

$$\Gamma = 8A_1 + 9B_2 + 8E_1 + 9E_2$$

Where A_1 and E_1 are polar modes and are both Raman and IR active. E_2 modes are non-polar but are Raman active. B_2 modes are silent modes for both Raman and IR. Therefore, theoretically, 25 Raman lines and 16 IR lines are expected in the spectra.

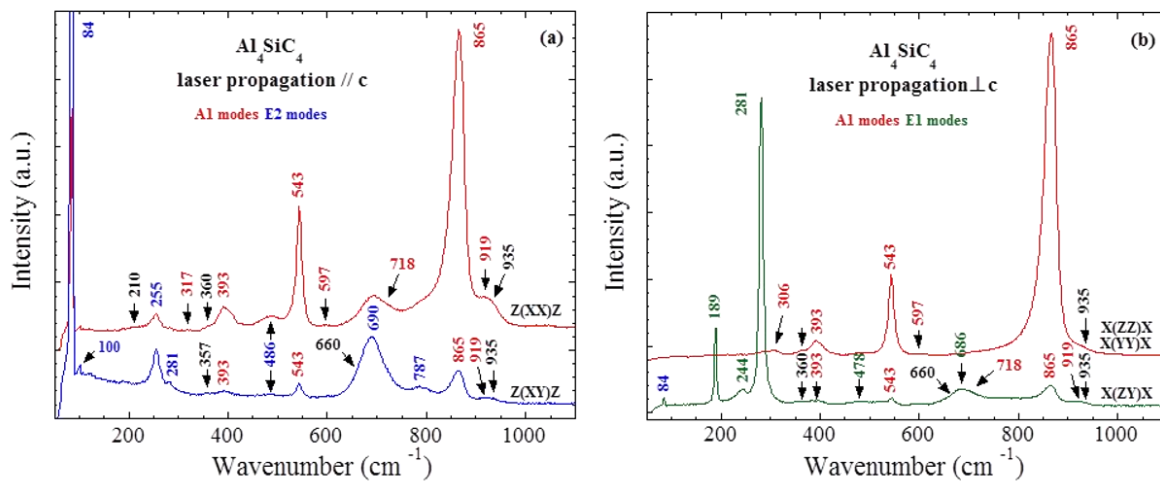


Figure 1.3: Polarized Raman spectra of Al_4SiC_4 single crystals collected in different configurations: (a) Spectra collected on the crystal surface (laser propagation along the c-axis) (b) Spectra collected on the crystal edge (laser propagation parallel to the crystal surface) ($\lambda = 514.5 \text{ nm}$)²⁵.

Indeed, for laser propagation parallel to c axis, from the Z(XX)Z polarization, A_1 and E_2 symmetry modes could be assigned. In another hand, the crossed Z(XY)Z polarization allows to mainly measure the modes of E_2 symmetry and additional weak A_1 mode. For the laser

perpendicular propagation to *c* axis, the X(ZY)X polarization allows to identify the E₁ symmetry modes while X(ZZ)Z polarization allows to identify the A₁ modes. As results, eight A₁ modes, seven E₂ modes, and five E₁ modes were experimental assigned. IR modes were also assigned in order to compare with Raman modes.

The experimental positions of Raman and IR modes are represented in Table 1.2 with the calculated positions reported in the literature²⁶. By comparing the calculated results in both studies, an overall agreement is observed for the symmetry assignment of Raman modes. However, the positions of Raman lines calculated by Pedesseau *et al.* is closer to the experimental values than the other. According to the author, this difference could be related to the improvement of the grid used for the computation. Concerning the LO-TO splitting values, a lower values was reported by Pedesseau *et al.*

It is worth noting that the Raman spectrum of Al₄SiC₄ is now correctly described, making Raman spectroscopy an easy tool for fast identification of the compound during this study.

Table 1.2: Calculated and experimental positions of Al_4SiC_4 Raman, Attenuated Total Reflection (ATR) and Fourier Transform Infrared (FTIR) modes and calculated values of the LO-TO splitting which were reported in literature²⁵. The positions in bold are non-assigned modes. The largest LO-TO splitting values are in italic.

Symmetry	Li <i>et al.</i> study ²⁶		Pedesseau <i>et al.</i> study ²⁵				
	ω_{calc}	$\Delta\omega_{\text{LO-TO}}$	ω_{calc}	$\Delta\omega_{\text{LO-TO}}$	ω_{exp} Raman	ω_{exp} ATR	ω_{exp} FTIR
E ₂	78.0		84		84		
E ₂	96.0		101		100		
E ₁	139.7	22.39	147	34		146	147
B ₂			171				
B ₂			177				
E ₁	188.6	9.18	192	8.5	189	181	198
E ₂	203.9		207		210	200	
E ₂	262.6		276		255		258
E ₁	268.1	9.96	280	2.5	244	220	233
E ₁	278.2	13.03	291	16	281		277
E ₂	280.5		293		281		
A ₁	290.1	73.02	293	95	306		305
A ₁	303.4	85.03	319	69.5	317	325	323
B ₂			365		357-360	355	354
A ₁	397.9	2.84	409	5	393	398	401
B ₂			433			454	457
E ₁	443.0	257.99	483	229.5	478	500	497
E ₂	443.6		483		486		
A ₁	517.8	120.06	535	122.5	543	541	521
B ₂			535				
A ₁	578.4	245.42	593	196	597	586	612
E ₁	596.4	230.89	624	189	686	630	612
E ₂	596.8		624		690		
B ₂			652		660	664	
A ₁	720.1	363.34	747	237	718	701	714
E ₁	755.5	70.13	784	86		750	764
E ₂	755.5		784		787		
E ₁	777.6	363.62	803	229.5		813	777
E ₂	777.7		803				
B ₂			835				
A ₁	807.7	234.44	844	247	865	841	800
B ₂			880			890	878
A ₁	862.0	116.80	898	166.5	919	920	
B ₂			913		935	954	

1.2.3. Ceramic and mechanical properties

Al_4SiC_4 was reported as an excellent oxidation resistance ceramic¹⁴. The oxidation tests in air were carried out on Al_4SiC_4 powder, which was synthesized by hot-pressed solid state reaction. For temperatures lower than 350°C, no mass gain by oxidation was observed. When the temperature varied from 350°C to 850°C, the mass slightly increased about 1 mass%, due to the formation of thin amorphous layer of SiO_2 on the surface. For temperatures higher than 850°C, the oxidation process of Al_4SiC_4 was separated into three stages: (i) from 850 to 1150°C, Al_2O_3 and SiO_2 were formed at the grain surface; (ii) at above 1150°C, the mass increased due to the oxidation; (iii) at 1600°C, the mullite ($3\text{Al}_2\text{O}_3 \cdot 2\text{SiO}_2$) was formed by the reaction between Al_2O_3 and SiO_2 .

The thermal conductivity of Al_4SiC_4 sintered bodies was also reported²⁷. A value of $80\text{W} \cdot \text{m}^{-1} \cdot \text{K}^{-1}$ was found in a temperature ranging from 25 to 1200°C.

The mechanical properties of Al_4SiC_4 bulk ceramic synthesized by hot-pressed reaction, were investigated in 2007^{16, 28}. The density, flexural strength, fracture toughness and Vickers hardness measured at room temperature are given in Table 1.3. The improvement of bending strength of Al_4SiC_4 with increasing test temperature has been observed. For instance, the bending strength at 1300°C was 450 MPa, which was 1.5 times higher than that at room temperature (297MPa). To explain this, the oxidation of the surface layer was suggested as the enhancement mechanism at high temperature (1000-1300°C). The properties of sintered α -SiC are also gathered in the Table 1.3 for comparison. Sintered Al_4SiC_4 has a lower density and a higher fracture toughness than α -SiC. However, sintered Al_4SiC_4 has a lower Vickers hardness and a lower flexural strength at room temperature than sintered α -SiC.

Table 1.3: Mechanical properties of Al_4SiC_4 sintered bodies²⁸ as compared with sintered α -SiC²⁹.

Al_4SiC_4	Al_4SiC_4	α -SiC
Density (g/cm ³)	2.97	3.16
Flexural strength (MPa) at		
25°C	297.1 ± 22.4	359
1000°C	385.4 ± 35.2	397
1200°C	388.3 ± 39.8	437
1300°C	449.7 ± 26.4	446
Fracture toughness (MPa m ^{1/2})	3.98 ± 0.05	3.1
Vickers hardness (GPa)	10.6 ± 1.8	32
Thermal expansion (x 10 ⁻⁶ °C ⁻¹) (200-1450°C)	6.2 ± 0.3	~5

Due to the absence of Al_4SiC_4 bulk crystal, only theoretical calculations have been performed in order to predict the mechanical properties of the single crystals.

The Figure 1.4 (from reference³⁰) shows the calculated stress-strain relation for Al_4SiC_4 and Al_4C_3 . As compared with Al_4C_3 , the calculated tensile stress-strain curves exhibit a similar trends along the c direction (0001). However, a significant difference was reported at a large shear strain between Al_4SiC_4 and Al_4C_3 ($[1-210](0001)$). By modeling the deformation process, the author demonstrated that the shear induced instability of Al_4SiC_4 is originated from the coupling bond between Al_4C_3 - and SiC-type structural units.

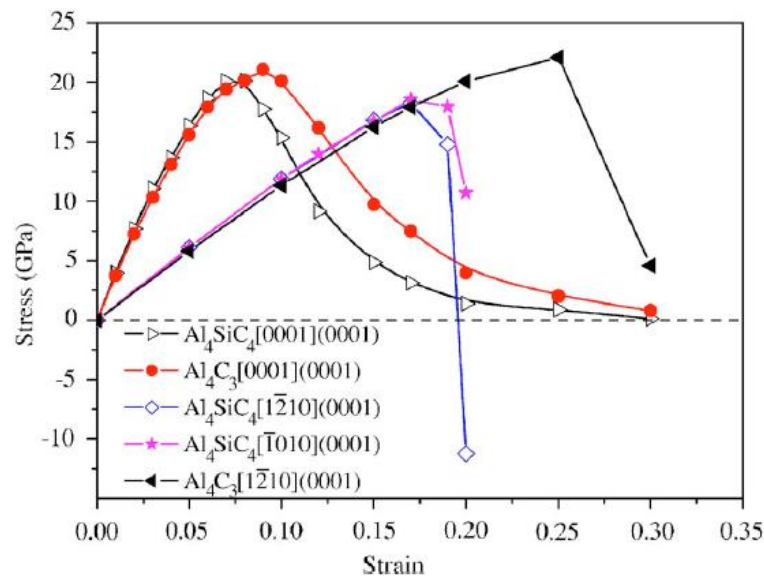


Figure 1.4: Calculated stress-strain relation for Al_4SiC_4 and Al_4C_3 . Empty triangles and solid circle represent tensile stress along c direction for Al_4SiC_4 and Al_4C_3 , respectively. Empty diamonds and solid pentagons represent the shear stresses of Al_4SiC_4 , for $[1-210](0001)$ and $[-1010](0001)$ direction, respectively. Solid triangle represents the shear stress in $[1-210](0001)$ direction.³⁰

Elastic properties of Al_4SiC_4 single crystal have been calculated^{19,26,30}. Six elastic constants, namely, C_{11} , C_{12} , C_{13} , C_{33} , C_{44} , C_{66} have been determined and are gathered in Table 1.4. Different models had been used and an overall agreement on the calculated results are observed.

Table 1.4: Calculated elastic constants, bulk modulus, shear modulus, piezoelectric constants, external piezoelectric contributions, and internal piezoelectric contributions of Al_4SiC_4 .

		Al_4SiC_4		
		Liao <i>et al.</i> ³⁰	Pedesseau <i>et al.</i> ¹⁹	Li <i>et al.</i> ²⁶
Elastic constants (GPa)	C_{11}	386	383.6	363
	C_{12}	118	121.9	52.1
	C_{13}	50	51.1	
	C_{33}	409	411	376.3
	C_{44}	122	118.4	111.6
	C_{66}	134	130.8	
Bulk modulus (GPa)	B	179	180.3	
Shear modulus (GPa)	G	140		
Piezoelectric constant (C/m^2)	e_{10}^0		-0.04	
	e_{33}^0		0.36	
	e_{31}^0		0.03	
External piezoelectric contributions (C/m^2)	e_{15}^0		0.13	
	e_{33}^0		-0.11	
	e_{31}^0		0.1	
Internal piezoelectric contributions (C/m^2)	e_{15}^{int}		-0.17	
	e_{33}^{int}		0.47	
	e_{31}^{int}		-0.07	

1.2.4. Electronic properties

Despite the early discovery from 1961, the bandgap structure and electronic properties of Al_4SiC_4 were only recently investigated from a theoretical point of view¹⁷. The authors performed calculations using the first-principles orthogonalized linear combination of atomic orbitals method (OLCAO) as implemented in the VASP code. OLCAO is a density-functional-theory-based method that uses the local density approximation (LDA) for the exchange-correlation potential. The bandgap structure of Al_4SiC_4 were predicted as an indirect bandgap of 1.05 eV and a direct bandgap of 1.91 eV. At first glance, such calculated values are not compatible with the yellowish color of the Al_4SiC_4 crystals which was observed from some previous experimental works².

Since no experimental results on the optical properties were available in the literature to confirm these prediction, some preliminary works on the synthesis of Al_4SiC_4 single crystal

were performed in 2014 by our group with the purpose to clarify this discrepancy and to investigate a few basic properties of this compound. The Figure 1.5 shows the transmittance spectrum collected in the 250-2500 nm wavelength range (0.5 to 5 eV) at room temperature which was performed on the Al_4SiC_4 single crystal platelets in the mm scale obtained by the solution growth method. An absorption edge of 2.5 eV was observed. Pedesseau *et al.*¹⁹ then reconsidered the calculation of the band structure using the plane-wave projector augmented wave (PAW) method as implemented in the VASP code. The local density approximation (LDA) was used for the exchange-correlation functional. The electronic band structure calculated including self-consistent many-body (scGW) contributions is represented in the Figure 1.6. An indirect and direct bandgap energies of about 2.5 eV and 3.2 eV, respectively, have been obtained. This result is in agreement with the experimental optical absorption. Two computation results using different methods are given in Table 1.5 for the comparison.

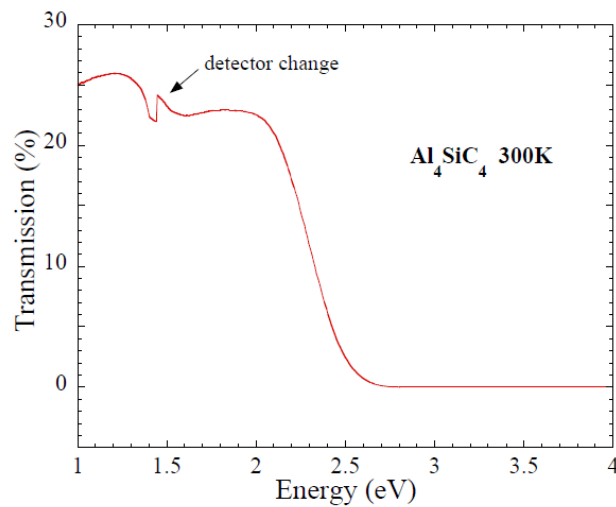


Figure 1.5: Al_4SiC_4 transmittance spectrum measured at 300K. An absorption edge is demonstrated around 2.5eV ¹⁸.

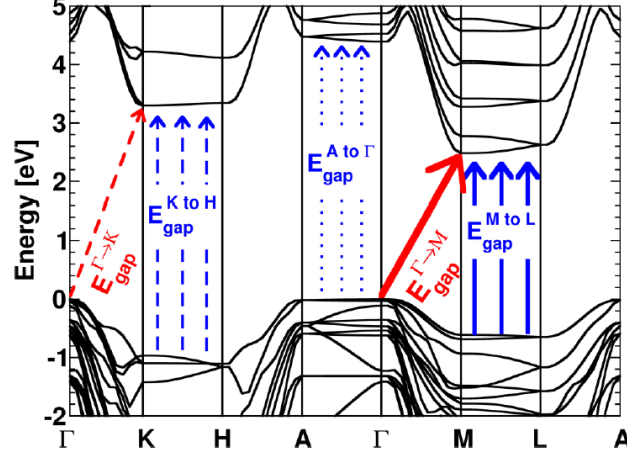


Figure 1.6: DFT electronic band structure of Al_4SiC_4 including many-body correction. Energy of the valence band maximum is set at zero. $E_g^{\Gamma \text{ to } M}$ and $E_g^{\Gamma \text{ to } K}$ are indirect band gaps, and $E_g^{M \text{ to } L}$, $E_g^{K \text{ to } H}$, $E_g^{\Gamma \text{ to } A}$ are direct bandgaps (red tilted arrows for indirect energy gaps; blue vertical arrows for direct energy gaps)¹⁹.

Table 1.5: The electronic bandgaps of Al_4SiC_4 crystal based on DFT calculations.

	Hussain <i>et al</i> ¹⁷ (2008)	Pedesseau <i>et al</i> ¹⁹ (2015)
$E_g^{\Gamma \text{ to } A}$ direct (eV) (5th)	$3.30 \leq E_g^{\Gamma \text{ to } A} \leq 3.36$	$4.40 \leq E_g^{\Gamma \text{ to } A} \leq 4.48$
$E_g^{K \text{ to } H}$ direct (eV) (4th)	$3.80 \leq E_g^{K \text{ to } H} \leq 3.91$	$4.26 \leq E_g^{K \text{ to } H} \leq 4.45$
$E_g^{\Gamma \text{ to } K}$ indirect (eV) (3rd)	2.02	3.30
$E_g^{M \text{ to } L}$ direct (eV) (2nd)	$1.91 \leq E_g^{M \text{ to } L} \leq 2.01$	$3.10 \leq E_g^{M \text{ to } L} \leq 3.25$
$E_g^{\Gamma \text{ to } M}$ indirect (eV) (1st)	1.05	2.48

1.3. Al_4SiC_4 as electronic materials

Most of the works reported so far on Al_4SiC_4 are related to high temperature structural material applications, with excellent ceramic properties and its resistance to oxidation and corrosion. Considering those properties, combined with its semiconducting properties, it is reasonable to envision, as compared to Si, many advantages for electronic devices able to operate at high temperature and more generally under harsh environment, such as gas sensors, radiation sensors, photo-electrodes for water splitting, etc. However since the synthesis process of Al_4SiC_4 single crystals has not been investigated yet, fine experimental characterizations on Al_4SiC_4 single crystal properties are still inaccessible. Hence, almost all the important

electronic properties of Al_4SiC_4 have not been explored yet in the literature such as the break down electric field, the carrier mobility (electron and hole), doping possibility etc. With an indirect bandgap around 2.5eV, Al_4SiC_4 will of course not compete with other wide bandgap semiconductors (i.e. GaN, AlN, α -SiC) in the field of high power electronics and/or short wavelength optoelectronics (UV-Vis LED and lasers). However, by analogy with 3C-SiC, it could offer some advantages for devices which are based on natural light absorption, such as photovoltaic and photo-electrochemical water splitting applications. Besides, one of the highest interest is its full compatibility with 4H- or 6H-SiC technology. It has a similar crystal lattice, and a complete chemical compatibility. With a smaller bandgap than SiC, we are thus speculating the possibility to develop original heterostructures and heterojunctions.

Some important properties of Al_4SiC_4 are compared to the well-known semiconductor materials (GaN, AlN, SiC) in Table 1.6. Note that the reported thermal conductivity of Al_4SiC_4 is relatively low, however, this value was measured for Al_4SiC_4 sintered bodies; a higher value is expected for Al_4SiC_4 single crystal.

Table 1.6: Properties of semiconductor materials^{26-28, 31, 32}.

Properties	Si	GaN	AlN	4H-SiC	3C-SiC	Al_4SiC_4	
Bandgap (eV)	1.12	3.39	6.2	3.2	2.36	2.5	
Density (g/cm ³)	2.329	6.15	3.23	3.21	3.21	2.97*	
Melting point at 1atm (°C)	1412	2500	3000	-	-	2080	
Thermal conductivity (W.cm ⁻¹ .C ⁻¹)	1.3	1.3	2.85	3.7	3.6	0.8*	
Thermal expansion (C ⁻¹)	a	2.60E-06	5.59E-06	4.15E-06	3.21E-06	2.77E-06	9.96E-06
	c		3.17E-06	5.27E-06	3.09E-06		

*Values reported for Al_4SiC_4 sintered bodies.

Simple consideration can be discussed concerning the potential dopant candidates for Al_4SiC_4 , as the structure consists of both SiC and Al_4C_3 -building blocks. Indeed, for the p-type doping, Al atoms ($Z=13$, with outer shell electron configuration: $3s^2 3p^1$) of the Al_4SiC_4 could be substituted by Mg atoms which has one electron less in the outer shell ($Z=12$, $3s^2$), it is also known as dopant source for p-type AlN³³. Si atoms ($Z=14$, $3s^2 3p^2$) in Al_4SiC_4 could be substituted by B atoms ($Z=5$, $2s^2 2p^1$). For the n-type doping, P ($Z=15$, $3s^2 3p^3$) and N ($Z=7$, $2s^2 2p^3$) could occupy the Si-site and C-site, respectively³⁴. Moreover, Al and Si could be substituted by each other to generate donor and acceptor level in the material because they occupy the consecutive positions in the periodic table. This self-doping behavior could lead to

a high carrier concentration of Al_4SiC_4 , however, it is more challenging for controlling the doping level of material.

1.4. State of art of Al_4SiC_4 synthesis

The ternary Al-Si-C phase diagram has been experimentally investigated in 1987 by Oden and McCune³. Sealed liquidus crucibles were used to determine isothermal sections for the ternary system at 2000 and 2150°C. The isopleth $\text{Al}_4\text{C}_3(\text{A})$ -SiC(S) in the range of 1900 to 2300°C was also established by a combination of thermal analysis and X-ray diffraction analysis of heat-treated and quenched samples.

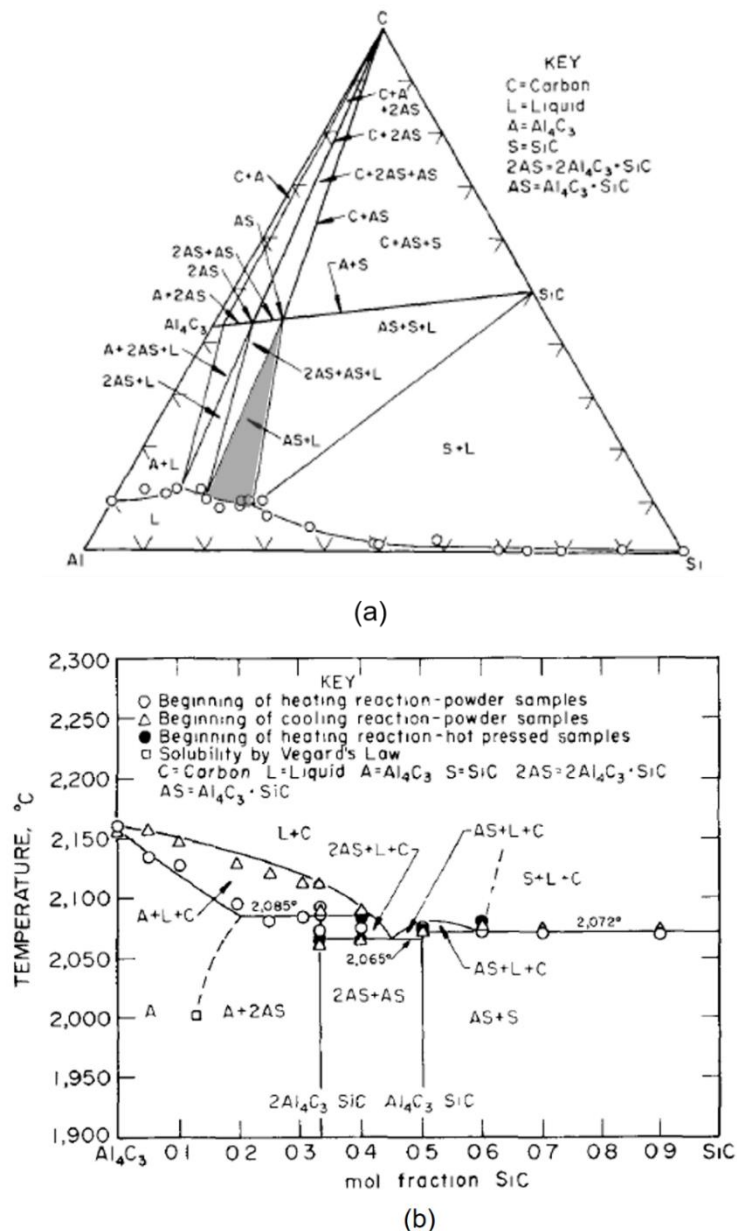


Figure 1.7: a) Ternary Al-Si-C isothermal section at 2000 °C, (b) Pseudo binary diagram Al_4C_3 -SiC³.

Solution growth. According to the ternary Al-Si-C isothermal section at 2000°C given in Figure 1.7(a), the liquid phase route to synthesize Al_4SiC_4 starting from the elements (Al, Si and C) is possible. The shaded part of the diagram represents the composition where Al_4SiC_4 and liquid are in equilibrium. However, even at high temperature (2000°C), this area is very small and narrow. And due to the high vaporization rate of Al, the initial composition could be easily shifted to the Si-rich region, and SiC could appear during the growth. Furthermore, the implementation of Al-rich Al-Si alloy at high temperature in graphite crucible is very difficult due to the strong reactivity of Al and graphite. For that reasons, the solution growth of Al_4SiC_4 is very challenging.

Nevertheless, a few attempts have been carried out by our group. The experiments have been performed in a high temperature furnace. High purity Al and Si pieces were melted in a graphite crucible which acted both as a container for the melt and as the carbon source. Al_4SiC_4 single crystals in the millimeter scale were grown by maintaining the melt at 1800°C before cooling down at a very low and controlled rate.

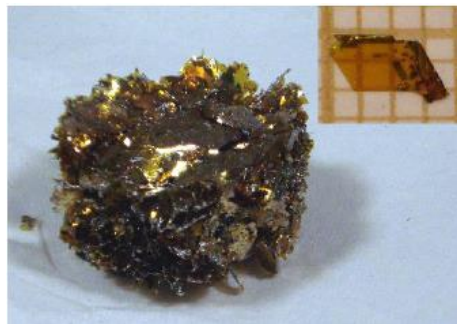


Figure 1.8: Picture of Al_4SiC_4 “aggregate” as extracted from the liquid¹⁸.

After cooling, most of Al_4SiC_4 crystals were embedded in the solidified melt. A selective chemical etchant able to extract the crystals was not found. Thus, to get the crystal, the liquid alloy has been partially sucked up before solidification. The single crystalline platelets of Al_4SiC_4 shown in Figure 1.8 were obtained after the experiment. However, the growth process was not well reproducible since the graphite crucible was easily damaged during the process due to the formation of Al_4C_3 from the direct contact with the Al-containing melt.

Sintering. Contrary to the limited investigation of the solution growth approach, the synthesis of Al_4SiC_4 bulk ceramic or powder by sintering attracted more attention from the ceramic community^{2, 5, 14, 15, 20, 27, 28, 35-37}. According to the pseudo-binary phase diagram given in Figure 1.7(b), Al_4SiC_4 can be synthesized by sintering the equimolar mixture of Al_4C_3 and

SiC at temperature under 2085°C which is the melting point of Al₄SiC₄³. This process was reported in detail by Schoennahl *et al.*². It requires several successive grinding and sintering steps due to the low yield of the solid state reaction. The equimolar mixture was used as the starting materials. The sintering reaction was completed after three successive annealing for 22 hours at 1800°C followed by grinding in order to avoid SiC residue. After the reaction, the obtained mixture of Al₄C₃ and Al₄SiC₄ was treated by hot concentrated HCl during 24 hours to remove the Al₄C₃ residue. After the treatment, Al₄SiC₄ powder was collected.

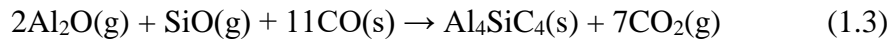
Hot pressed annealing was also reported by Beyer *et al.*⁵. An equimolar mixture of Al₄C₃ and SiC was ball-milled in argon atmosphere for 20 hours. After that, the powder mixture was placed in a graphite die and loaded into a vacuum induction furnace. Before the experiment, the furnace was evacuated and backfilled to the pressure of 50 kPa with argon. The sample was then hot pressed for 2 hours at 1857°C and 6.89 MPa to complete the reaction. Al₄SiC₄ single phase powder was obtained after the experiment.

Another sintering process using aluminum, graphite powder, and polycarbosilane (PCS) as starting materials had been reported by Huang *et al.*³⁷. The molar ratio of Al, graphite and SiC conversed from the PCS was 4:3:1 as required by the reaction:

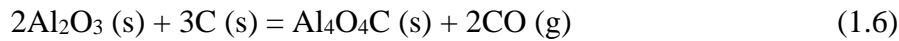
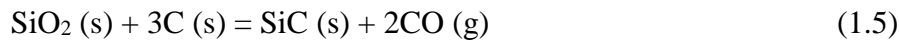
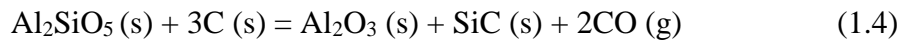


Al₄SiC₄ bulk ceramics were synthesized by two steps. In the first step, the mixture of powder was compacted under the pressure of 10-20 MPa and calcined at 700-1200°C for 60 min in the furnace with flowing argon. Al melted at 660°C and reacted with graphite to form Al₄C₃. At temperature range 700-1200°C, PCS pyrolyzed into SiC. At the second step, Al₄SiC₄ bulk ceramic was synthesized by hot-pressing reaction (25 MPa) at temperature 1700-2000°C in argon.

Another process using a mixture of Al(OH)₃, SiO₂, and phenolic resin as raw materials was reported by Lee *et al.*³⁸. The ceramic powders were introduced into a solution consisting of ethyl alcohol and phenolic resin (2:1 by weight). The mixtures were ball-milled with SiC media and compacted under a pressure of 1 MPa, then calcined at 1750°C in Ar flow. In this work, through the carbothermal reduction process, two steps of growth mechanism were assumed. The first one was gas-solid reaction and the second one is gas-gas reaction which correspond to the nucleation reaction and growth reaction, respectively. The crystallinity of Al₄SiC₄ was then strongly depended on the ratio of carbon particles acting as nuclei sites.



Moreover, another carbothermal reduction process was reported by Yu *et al.*³⁹ using the mixture of calcined bauxite (consists mostly of Al_2O_3 and sillimanite), silica and carbon black powder as starting materials. In this work, the mixture of powder (calcined bauxite: 57.77wt.%, carbon black: 36.23wt.%, silica: 6wt.%) was ball milled and heated up to 1800°C in argon flow. Three steps of carbothermal reactions were proposed which included the carbothermal reductions of sillimanite (Al_2SiO_5), SiO_2 and Al_2O_3 corresponding to the equation (4), (5) and (6), respectively.



Then, Al_4SiC_4 ceramic powder was formed at initial stage by the solid-solid reaction given below:



At the later stage, the growth reaction was continued by the gas-solid and gas-gas reaction given below:



The single phase and hexagonal plate-like Al_4SiC_4 powders were collected after the experiment of 3 hours.

A low temperature sintering process has also been proposed⁴⁰. Using the stoichiometric mixture of Al, Si and carbon black as starting materials, Al_4SiC_4 powders were synthesized at 1100°C for 5 minutes by the spark plasma sintering process. According to the author, the sub-micrometer scale powder was obtained because of the fast heating rate, low synthesis temperature and short heating time.

Sublimation growth. Beside the solution growth approach mentioned above, the crystallization from the vapor phase was expected as a potential way for high purity crystal growth. The formation of Al_4SiC_4 single crystal by sublimation had been mentioned in the first

study of Barzack in 1961¹. However, the experimental process was not explained in details. The sublimation process of Al_4SiC_4 was better explored by the detailed description of Schoennahl in 1984². In this work, the recrystallization on the surface of the sintered pellets with different compositions like pure Al_4SiC_4 , mixture of Al_4SiC_4 – Al_4C_3 or mixture of Al_4C_3 – SiC was investigated. The pellets with thickness of 5 mm were placed under a temperature gradient of 20°C/cm at a mean temperature of $1960 \pm 10^\circ\text{C}$ under argon. The experimental pressure was not mentioned in the report. During the process, single crystals gathered on the lower temperature surface while the dissociation happened on the other side. An extremely narrow temperature range between 1950°C and 1980°C for obtaining crystals was reported with the small yellowish transparent and orange platelets. The yellowish transparent and thin platelet was characterized as the Al_4SiC_4 phase confirmed by the Laue diffractogram while a composition of Al_4SiC_4 and Al_4C_3 was observed on the orange platelets. To explain that, a mechanism of growth in epitaxy between Al_4SiC_4 and Al_4C_3 was proposed by the authors. However, even though the yellowish platelet shows a good structure of Al_4SiC_4 single crystal, they have non uniform physical characteristics due to the lack of control over spontaneous nucleation. Additionally, some defects in the crystal structure and precipitation of graphite were observed in the crystals due to the not well controlled temperature variations.

In this thesis, we attempt to use the seeded sublimation growth technique also known as modified-Lely method to synthesize the Al_4SiC_4 single crystals. The mixture of Al_4C_3 and SiC has been used as source materials.

First proposed by Tairov and Tsvetkov⁴¹ in 1978, the modified-Lely method has been considered as a great step forward in the SiC bulk crystal growth history. The concept of this method is to vaporize the source powder at high temperature, then the gas species are transported and re-crystallized on a single crystal seed which is fixed onto the crucible lid. The vapor transport is created by a temperature gradient between the source and the seed material. The schematic representation of the growth method is shown in Figure 1.9.

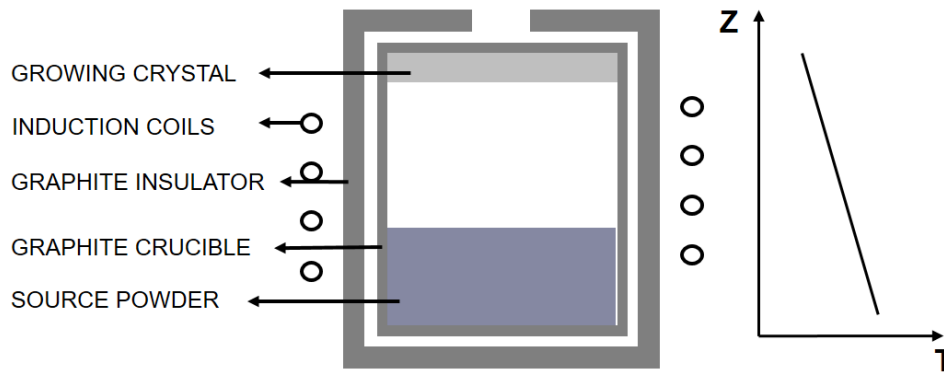


Figure 1.9: Schematic representation of the modified-Lely method and the temperature profile.

The reactor consists of a high density graphite crucible surrounded by insulating graphite foam. An induction heating system is used for operating the necessary temperature. Compared to the sublimation method used by Schoennahl², the widespread spontaneous nucleation occurring on surface of powder and the inner crucible wall can be suppressed and the growth process can then be controlled on the seed. Moreover, selecting this approach would benefit from the maturity of the sublimation process developed for SiC. Many studies of the process modeling and experiments have been done in order to control the distribution of temperature within the reactor and the gas species concentration fields⁴²⁻⁴⁵.

The development of the process will be discussed in detail in the chapter IV of this thesis.

1.5. Purpose and contribution of the current thesis

The present work is focused on the synthesis of single crystal or epitaxial layer of Al_4SiC_4 by the top seeded sublimation process. Three main topics will be discussed.

The first one is the thermodynamic studies of the Al_4C_3 -SiC pseudo-binary system. Thanks to the thermodynamic calculations, the vaporization and condensation phenomena will be discussed in order to propose a vapor phase route for the synthesis of Al_4SiC_4 .

The second one is the experimental demonstration of Al_4SiC_4 growth based on the conditions obtained from the thermodynamic calculations. From an extensive experimentally approach, a sublimation process to grow Al_4SiC_4 single crystals will thus be investigated. After that, texture characterization will be performed on the obtained single crystals in order to evaluate the dependence of growth orientation and quality of the deposit on different types of SiC substrates. Moreover, the UV absorption characterization will be conducted to investigate the optical properties of material.

As the third topic, the heterostructure of Al_4C_3 and Al_4SiC_4 on hexagonal SiC substrates will be investigated, as they could be of interest for many applications. By using transmission electron microscopy, the interface of the heterostructures will be characterized in order to study their crystallographic properties and give a feedback on the growth mechanism.

REFERENCE

1. V. J. Barczak, *Optical and X-Ray Powder Diffraction Data for Al_4SiC_4* , Journal of the American Ceramic Society **44** (6), 299-299 (1961).
2. J. Schoennahl, B. Willer and M. Daire, *Le carbure mixte Al_4SiC_4 : Préparation et données structurales*, Journal of Solid State Chemistry **52** (2), 163-173 (1984).
3. L. L. Oden and R. A. McCune, *Phase equilibria in the Al-Si-C system*, Metallurgical Transactions A **18** (12), 2005-2014 (1987).
4. J. Gröbner, H. L. Lukas and F. Aldinger, *Thermodynamic calculation of the ternary system Al-Si-C*, Calphad **20** (2), 247-254 (1996).
5. R. Beyer and E. Johnson, *Heat capacity of aluminum silicon carbide (Al_4SiC_4) from 5.26 to 1047 K*, The Journal of Chemical Thermodynamics **16** (11), 1025-1029 (1984).
6. J.-C. Viala, P. Fortier, B. Bonnetot and J. Bouix, *Interaction sous haute pression entre l'aluminium solide et le carbure de silicium*, Materials Research Bulletin **21** (4), 387-394 (1986).
7. V. Laurent, D. Chatain and N. Eustathopoulos, *Wettability of SiC by aluminium and Al-Si alloys*, Journal of Materials Science **22** (1), 244-250 (1987).
8. W. C. Moshier, J. S. Ahearn and D. C. Cooke, *Interaction of Al-Si, Al-Ge, and Zn-Al eutectic alloys with SiC/Al discontinuously reinforced metal matrix composites*, Journal of Materials Science **22** (1), 115-122 (1987).
9. D.-J. Lee, M. D. Vaudin, C. A. Handwerker and U. R. Kattner, *Phase Stability and Interface Reactions in the Al-SiC System*, MRS Online Proceedings Library Archive **120**, 357 (359 pages) (1988).
10. D. J. Lloyd and I. Jin, *A method of assessing the reactivity between SiC and molten Al*, Metallurgical Transactions A **19** (12), 3107-3109 (1988).

11. D. Lloyd, *The solidification microstructure of particulate reinforced aluminium/SiC composites*, Composites Science and Technology **35** (2), 159-179 (1989).
12. H. Liu, U. Madaleno, T. Shinoda, Y. Mishima and T. Suzuki, *Interfacial reaction and strength of SiC fibres coated with aluminium alloys*, Journal of Materials Science **25** (10), 4247-4254 (1990).
13. J. Viala, P. Fortier and J. Bouix, *Stable and metastable phase equilibria in the chemical interaction between aluminium and silicon carbide*, Journal of Materials Science **25** (3), 1842-1850 (1990).
14. O. Yamamoto, M. Ohtani and T. Sasamoto, *Preparation and oxidation of Al₄SiC₄*, Journal of materials research **17** (04), 774-778 (2002).
15. X. X. Huang, G. W. Wen, X. M. Cheng and B. Y. Zhang, *Oxidation behavior of Al₄SiC₄ ceramic up to 1700°C*, Corrosion Science **49** (5), 2059-2070 (2007).
16. X.-x. Huang and G.-w. Wen, *Mechanical properties of Al₄SiC₄ bulk ceramics produced by solid state reaction*, Ceramics International **33** (3), 453-458 (2007).
17. A. Hussain, S. Aryal, P. Rulis, M. Choudhry and W. Ching, *Density functional calculations of the electronic structure and optical properties of the ternary carbides Al₄SiC₄ and Al₄Si₂C₅*, Physical Review B **78** (19) (2008).
18. D. Zevgitis, O. Chaix-Pluchery, B. Doisneau, M. Modreanu, J. La Manna, E. Sarigiannidou and D. Chaussende, *Synthesis and Characterization of Al₄SiC₄: A “New” Wide Band Gap Semiconductor Material*, presented at the Materials Science Forum, 2015, Vol. 821, pp. 974-977.
19. L. Pedesseau, J. Even, M. Modreanu, D. Chaussende, E. Sarigiannidou, O. Chaix-Pluchery and O. Durand, *Al₄SiC₄ wurtzite crystal: Structural, optoelectronic, elastic, and piezoelectric properties*, APL Mater. **3** (12), 121101 (2015).
20. Z. Inoue, Y. Inomata, H. Tanaka and H. Kawabata, *X-ray crystallographic data on aluminum silicon carbide, α-Al₄SiC₄ and Al₄Si₂C₅*, Journal of Materials Science **15** (3), 575-580 (1980).
21. B. L. Kidwell, L. L. Oden and R. A. McCune, *2Al₄C₃SiC: a new intermediate phase in the Al-Si-C system*, Journal of Applied Crystallography **17** (6), 481-482 (1984).
22. J.-M. Bind, *Phase transformation during hot-pressing of cubic SiC*, Materials Research Bulletin **13** (2), 91-96 (1978).
23. M. von Stackelberg and E. Schnorrenberg, *The Structure of Aluminum Carbide, Al₄C₃*, Z. Phys. Client. B **27**, 37-49 (1934).

24. Y. Sun, H. Cui, L. Gong, J. Chen, J. She, Y. Ma, P. Shen and C. Wang, *Carbon-in-Al₄C₃ Nanowire Superstructures for Field Emitters*, ACS Nano **5** (2), 932-941 (2011).
25. L. Pedesseau, O. Chaix - Pluchery, M. Modreanu, D. Chaussende, E. Sarigiannidou, A. Rolland, J. Even and O. Durand, *Al₄SiC₄ vibrational properties: density functional theory calculations compared to Raman and infrared spectroscopy measurements*, Journal of Raman Spectroscopy (2017).
26. Y. Li, B. Xiao, L. Sun, Y. Gao and Y. Cheng, *Phonon optics, thermal expansion tensor, thermodynamic and chemical bonding properties of Al₄SiC₄ and Al₄Si₂C₅: a first-principles study*, RSC Advances **6** (49), 43191-43204 (2016).
27. I. K. M. S. Y. Akira, *Thermal conductivity and temperature dependence of linear thermal expansion coefficient of Al₄SiC₄ sintered bodies prepared by pulse electronic current sintering*, (2003).
28. G. Wen and X. Huang, *Increased high temperature strength and oxidation resistance of Al₄SiC₄ ceramics*, Journal of the European Ceramic Society **26** (7), 1281-1286 (2006).
29. R. Munro, *Material properties of a sintered α -SiC*, Journal of Physical and Chemical Reference Data **26** (5), 1195-1203 (1997).
30. T. Liao, J. Wang and Y. Zhou, *Atomistic deformation modes and intrinsic brittleness of Al₄SiC₄: A first-principles investigation*, Physical Review B **74** (17) (2006).
31. M. E. Levinshtein, S. L. Rumyantsev and M. S. Shur, *Properties of Advanced Semiconductor Materials: GaN, AlN, InN, BN, SiC, SiGe*. (John Wiley & Sons, 2001).
32. G. L. Harris, *Properties of silicon carbide*. (Iet, 1995).
33. K. B. Nam, M. L. Nakarmi, J. Li, J. Y. Lin and H. X. Jiang, *Mg acceptor level in AlN probed by deep ultraviolet photoluminescence*, Applied Physics Letters **83** (5), 878-880 (2003).
34. D. Larkin, *SiC Dopant Incorporation Control Using Site - Competition CVD*, physica status solidi (b) **202** (1), 305-320 (1997).
35. K. Inoue and A. Yamaguchi, *Synthesis of Al₄SiC₄*, Journal of the American Ceramic Society **86** (6), 1028-1030 (2003).
36. M. Hasegawa, K. Itatani, M. Aizawa, F. S. Howell and A. Kishioka, *Low-Temperature Synthesis of Aluminum Silicon Carbide Using Ultrafine Aluminum Carbide and Silicon Carbide Powders*, Journal of the American Ceramic Society **79** (1), 275-278 (1996).
37. X. Huang and G. Wen, *Reaction synthesis of aluminum silicon carbide ceramics*, Materials chemistry and physics **97** (1), 193-199 (2006).

38. J.-S. Lee, S.-H. Lee, T. Nishimura and H. Tanaka, *Hexagonal Plate-like Ternary Carbide Particulates Synthesized by a Carbothermal Reduction Process: Processing Parameters and Synthesis Mechanism*, *Journal of the American Ceramic Society* **92** (5), 1030-1035 (2009).
39. C. Yu, W. Yuan, C. Deng, H. Zhu and J. Li, *Synthesis of hexagonal plate-like Al₄SiC₄ from calcined bauxite, silica and carbon black*, *Powder Technology* **247**, 76-80 (2013).
40. S. H. Lee, H. C. Oh, B. H. An and H. D. Kim, *Ultra-low temperature synthesis of Al₄SiC₄ powder using spark plasma sintering*, *Scripta Materialia* **69** (2), 135-138 (2013).
41. Y. M. Tairov and V. F. Tsvetkov, *General principles of growing large-size single crystals of various silicon carbide polytypes*, *Journal of Crystal Growth* **52**, 146-150 (1981).
42. D. Hofmann, M. Bickermann, R. Eckstein, M. Kölbl, M. St G, E. Schmitt, A. Weber and A. Winnacker, *Sublimation growth of silicon carbide bulk crystals: experimental and theoretical studies on defect formation and growth rate augmentation*, *Journal of crystal growth* **198**, 1005-1010 (1999).
43. P. Wellmann, R. Müller, D. Queren, S. Sakwe and M. Pons, *Vapor growth of SiC bulk crystals and its challenge of doping*, *Surface and Coatings Technology* **201** (7), 4026-4031 (2006).
44. J. M. Dedulle, M. Anikin, M. Pons, E. Blanquet, A. Pisch, R. Madar and C. Bernard, *Free growth of 4H-SiC by sublimation method*, presented at the Materials Science Forum, 2004, Vol. 457, pp. 71-74.
45. N. Tsavdaris, K. Ariyawong, J.-M. Dedulle, E. Sarigiannidou and D. Chaussende, *Macroscopic Approach to the Nucleation and Propagation of Foreign Polytype Inclusions during Seeded Sublimation Growth of Silicon Carbide*, *Crystal Growth & Design* **15** (1), 156-163 (2014).

CHAPTER II

EXPERIMENTAL APPARATUS

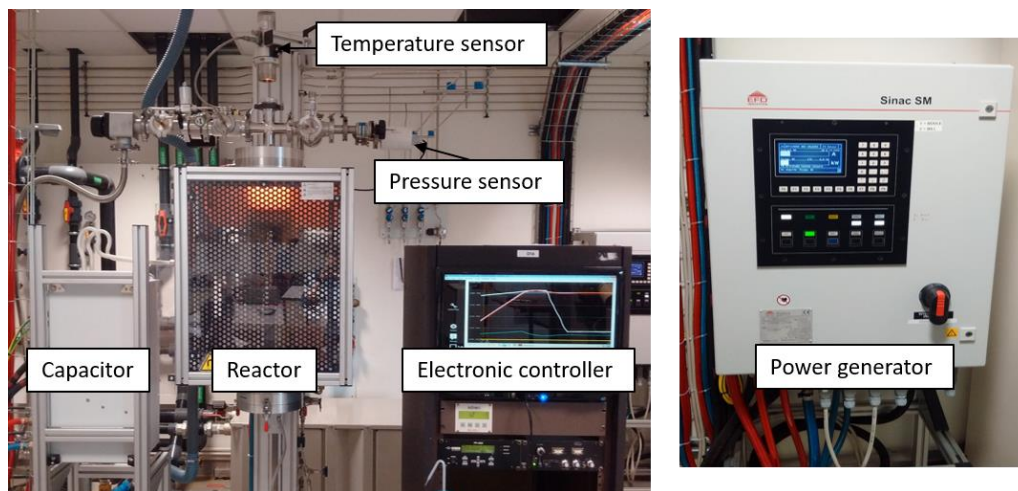
This chapter is a description of the experimental apparatus and characterization methods used in this thesis. In the first part, the setup of induction heating reactor used for the growth of the Al_4SiC_4 will be presented. The second part is dedicated to the characterization methods used in this work and their configurations.

2.1. Experimental apparatus

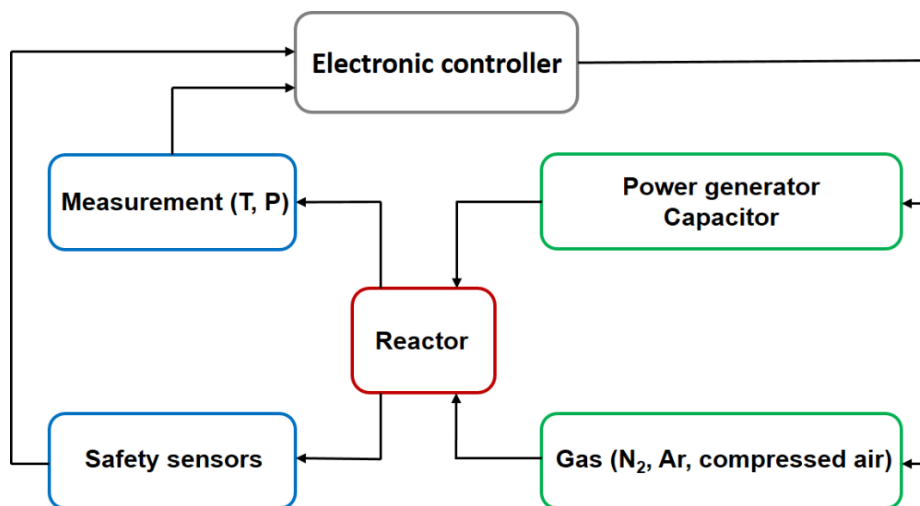
With working temperature above 1800°C, a specific induction heating reactor have been developed for the Physical vapor transport (PVT) process. In this section, different units of the PVT reactor and crucible used for experiments are described.

2.1.1. Physical Vapor Transport reactor setup

The experimental apparatus used for the growth of Al_4SiC_4 consists of the following units: the power generator, the capacitor box, the electronic controller, the measurement device (pressure and temperature), the reactor chamber and the power generator as shown in Figure 2.1.



(a)



(b)

Figure 2.1: (a) Photo of the experimental apparatus used for the PVT growth. (b) Schematic of the PVT reactor setup¹.

An AC circuit was designed for an induction heating reactor consisting of: a generator, a capacitor and an inductor. The equivalent RLC parallel circuit with resistance in series with inductor is drawn in Figure 2.2. Two types of power losses are considered in the RLC circuit: active losses due to the resistive components and reactive losses due to the inductance. The complex power S (Volt-Ampere) defined as the real power needed by our system is the vector summation of active P (Watts) and reactive Q (Volt-Amperes Reactive) powers and it is a product of root-mean-square of circuit voltage and current given by expression below:

$$S = V_{rms} I_{rms} = \sqrt{P^2 + Q^2} \quad (2.1)$$

Among them, the active power is the “real” power consumed by a resistor which will not cause a phase shift between voltage and current, whereas the reactive power counteracts the effects of “real” power caused by the phase shift of 90° between voltage and current. Thus, in order to reduce the generated reactive power of system, the capacitance is integrated in order to generate enough reactive power consumed by the inductor by causing the “opposite” phase shift (-90°) between voltage and current.

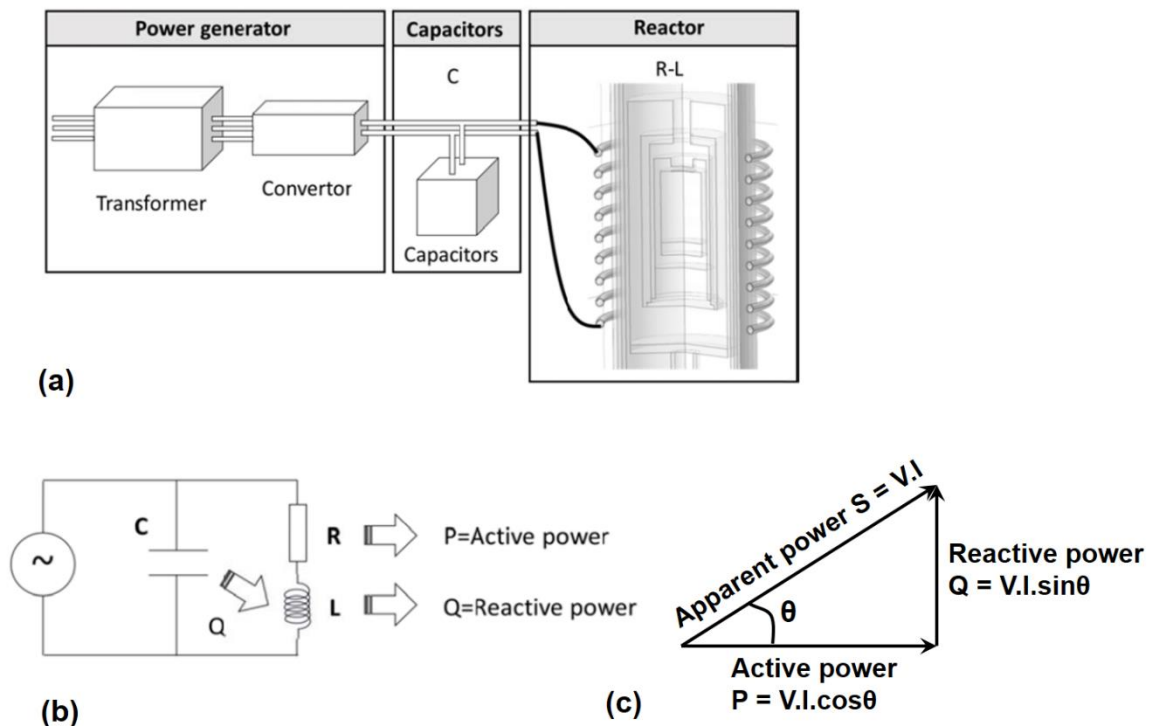


Figure 2.2: (a) Schematic representation of topological connection of power generator, capacitors, reactor; (b) the equivalent RLC parallel circuit²; (c) power triangle of RLC circuit representing the relation between apparent power, reactive power and active power.

The design of the coil was also optimized by modifying the geometric parameters such as: the number of turns, the diameter and the height of coil in order to reach the resonance condition by mean of an adaptation of the impedance, in which the impedance of the equivalent RLC circuit is near to the impedance of the power generator. Moreover, since the circuit topology of our system is a parallel circuit, the parallel resonance is considered for optimal design which has advantage that the current is magnified through the work coil, the power generator thus only needs to carry part of the load current that actually does the real work².

The electrical controller consists of a homemade electronic unit (automation) which controls all the peripheral electronic systems such as: a gas system (pressure controllers, mass flow controllers and pneumatic valves), and a heating system (temperature controllers).

The reactor chamber is composed of water cooled quartz jacket, which was mounted on specially designed aluminum flanges at the top and the bottom. The crucible is fixed on the vertical axis inside the quartz tube. Outside the tube, an induction coil is placed which is made by copper and cooled by water. The coil can move in the vertical direction in order to adjust the relative position between the crucible and the coil. The temperature inside the reactor is measured from the top by a dichromatic pyrometer, through a quartz window located in the top aluminum cover as illustrated in the Figure 2.3. The reactor chamber is perfectly sealed and no leakage can be detected using a secondary vacuum He tester. Two pressure sensors have been used to measure the pressure which are equipped on the top of the reactor as in the Figure 2.3. The first one is used for low pressure (< 1 mbar) and the second one is used for high pressure (> 1 mbar).

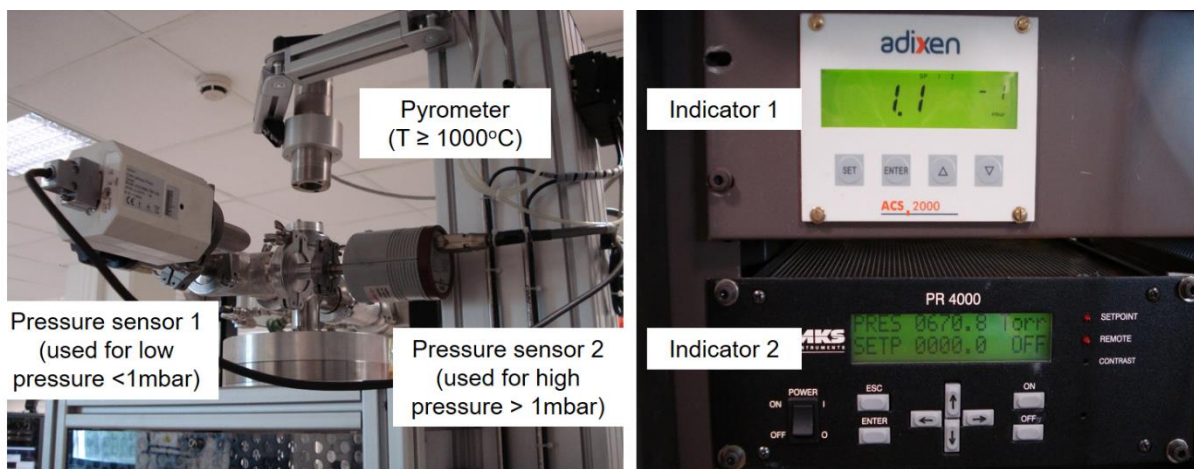


Figure 2.3: Photo of the dichromatic pyrometer and pressure sensors on the top of the reactor.

The reactor is connected to a gas panel as presented in the Figure 2.4, which was customized for experiments and consisted of argon and nitrogen. For these gases, a set of mass flow controllers, pneumatic valves and micro-valves ensures a large flexibility of gas injections under controlled total pressure. The input of gases is at the bottom part of the reactor. In this study, only argon has been used. At the top, a pressure safety valve and a butterfly valve are equipped. A rotary pump able to create a vacuum of 10^{-3} mbar is used for pressure control.

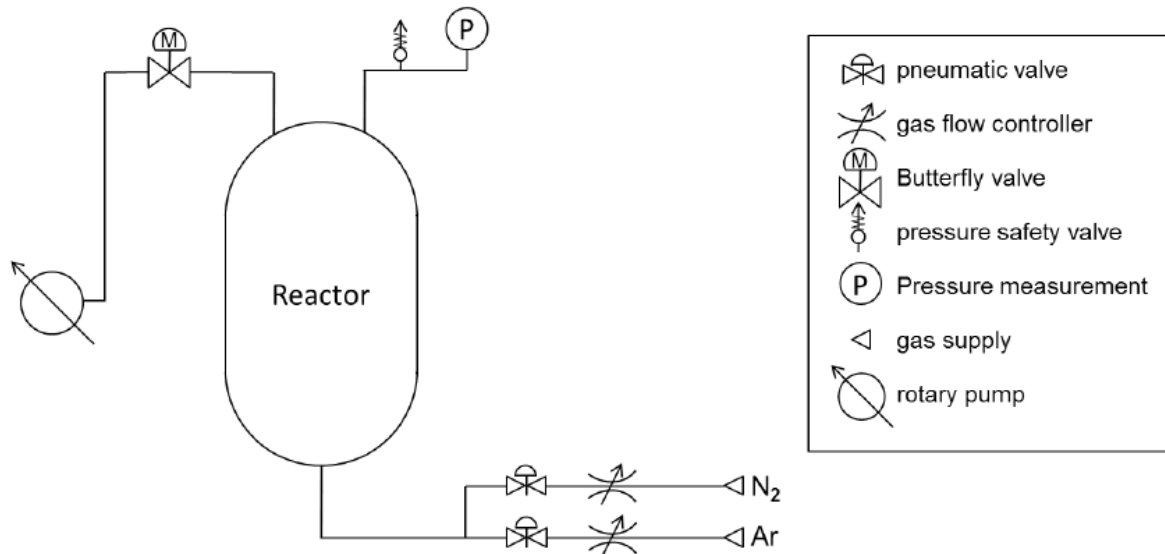


Figure 2.4: Gas panel of the PVT reactor.

2.1.2. Crucible

Known as a refractory material commonly using in carbide synthesis, graphite can withstand the high temperature processing (1700-2100°C) and has chemically stability with the Al_4C_3 -SiC system. Therefore, graphite has been used for the fabrication of the crucible in our experiments. The Figure 2.5 presents the schematic of the external part geometry. Depending on the requirement of the experimental processes, the inner part (called reaction chamber) will be modified to adapt the experimental conditions. Details of the each experimental geometry, i.e. the reaction chamber, will be described together with the corresponding experimental process in next chapters. In general, two different types of graphite materials are combined, the high density part is used to make crucible, and the porous graphite felt with “fiber-like” structure is used as an insulator. All the parts of the external graphite crucible used for experiments are presented in Figure 2.6.

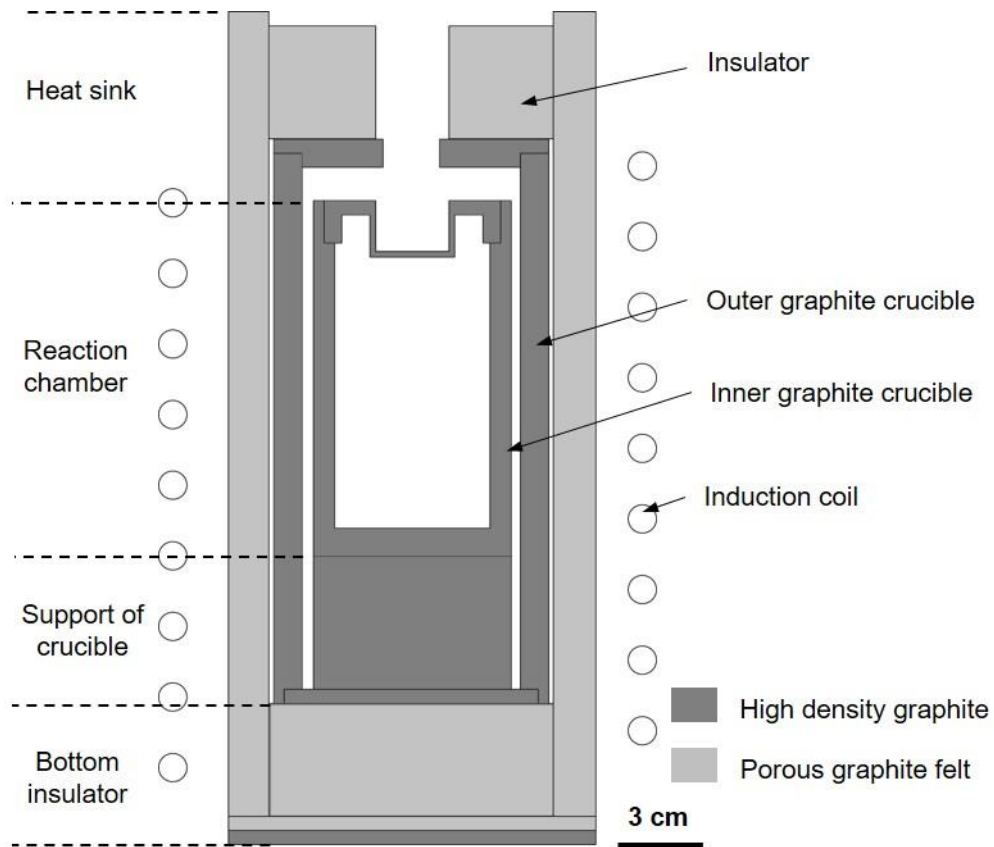


Figure 2.5: Schematic of the external part geometry.



Figure 2.6: Main parts of the external graphite crucible used for experiments.

2.2. Characterization methods

In order to characterize the properties of obtained crystals such as their morphology, chemical composition, crystallographic structure, optical properties..., many different methods have been used such as X-ray diffractometry, Raman spectroscopy, scanning electron microscopy, transmission electron microscopy and transmission/absorption spectroscopy. In this section, the general principle of the methods and their configurations used in this thesis will be described.

2.2.1. X-ray diffractometry (θ - 2θ , ω -scan and Rietveld refinement)

X-ray diffraction methods are the most effective methods for determining the crystal structure of materials³. The spectroscopic technique used in this work, namely X-ray diffractometry (XRD), is the most widely used diffraction method.

XRD principle. X-rays are electromagnetic waves with wavelength ranging from 0.01 to 10 nm and XRD method are based on the phenomenon of wave interferences. Two light waves with the same wavelength and traveling in the same direction can either reinforce or cancel each other, depending on their phase difference. When the phase difference has value of $n\lambda$ (with n is an integer), the constructive interference occurs.

$$n\lambda = 2d \sin\theta \quad (2.2)$$

The constructive interference condition as shown in the equation (2.2) is the basic law of diffraction called Bragg's Law. The path difference between two beams ($n\lambda$) depends on the incident angle (θ) and the spacing between the parallel crystal planes (d). Knowing the spacing of crystallographic planes by diffraction methods, we can determine the crystal structure of materials.

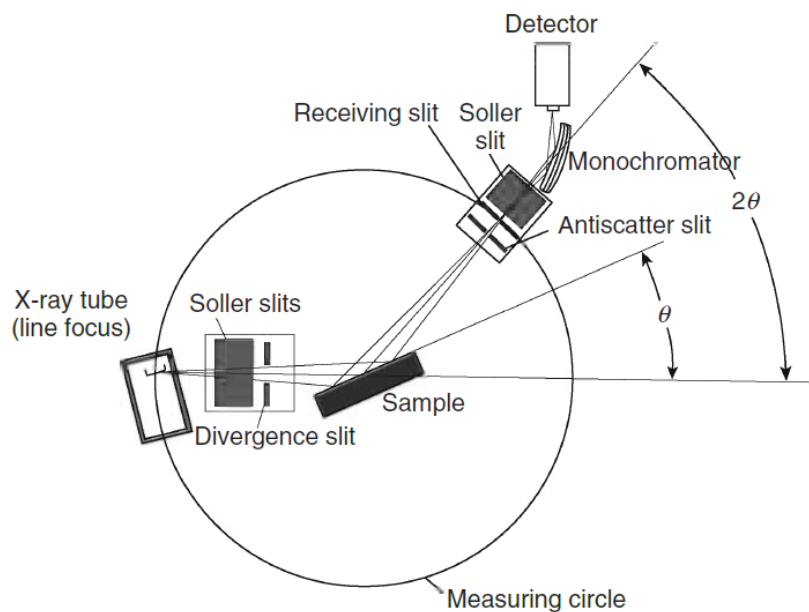


Figure 2.7: Bragg-Brentano geometry of X-ray diffractometer³.

θ - 2θ scan. In this work, the phase analysis has been conducted by XRD using a Bruker D8 Advance diffractometer with the Bragg-Brentano configuration which is shown in Figure 2.7. In this arrangement, the X-ray incident beam is fixed, but a sample stage rotates around the axis perpendicular to the figure plane in order to change the incident angle. The detector also rotates around the axis perpendicular to the plane of the figure but its angular speed is twice that of sample stage in order to maintain the angular correlation of θ - 2θ between the sample and detector rotation. With this configuration, the Bragg-Brentano patterns probe the information of (hkl) planes parallel to the sample surface.

The radiation of Cu K-alpha1 with wavelength of 0.15406 nm had been used with a 1-D linear detector enabling a resolution of 0.05°. Other parameters were 2.5° for soller slits, 0.3° for divergent slit, and 6.8 mm for anti-scatter slit. The scans had been conducted in the range of 10 to 90° in 2θ scale, with step of 0.008°, the duration of acquisition for each step was 2 sec.

ω -scan (rocking curve) and pole figure. In addition, in order to evaluate the structural quality of the crystals, a rocking curve analysis has been conducted. In principle, rocking curve analysis is a plot of X-ray diffraction intensity versus ω . In this configuration, the sample can be tilted along three independent axes: ω (Omega), ϕ (Phi), and χ (Chi). The ω - and χ - axis are parallel to the sample surface while the ϕ - axis is normal to the sample surface as presented in Figure 2.8. Among them, the ω represents the incident angle θ . The grain orientation can be probed by rotating the sample along the three axis. During the measurement, the X-ray source

and the detector are fixed at a specific Bragg angle while the sample is tilted along the ω -axis. In fact, for a textured sample, the grains can be tilted with respect to each other. Therefore, the width of a rocking curve is related to the distribution of grains along the ω -axis. A perfect crystal has an intrinsic width (FWHM) for that material.

The rocking curve analysis presented in this study were performed using the Siemens D5000 diffractometer (Schulz reflection geometry). A Ni foil was used to filter the $\text{CuK}\beta$ radiation resulting in $\text{Cu K}\alpha_1$ radiation with wavelength of 1.54186 \AA . The divergent beam with diameter of 1 mm has been used. The detector was a scintillation counter. Other parameters are 2.5° for Soller slits, 0.2 mm for anti-scatter slit, and 1 mm for detector slit. The pole figures were measured in the same diffractometer with similar parameters. During the measurements, the samples were radially tilted along χ - axis from 0° to 90° , for each χ angle, the samples were rotated 360° along the φ - axis.

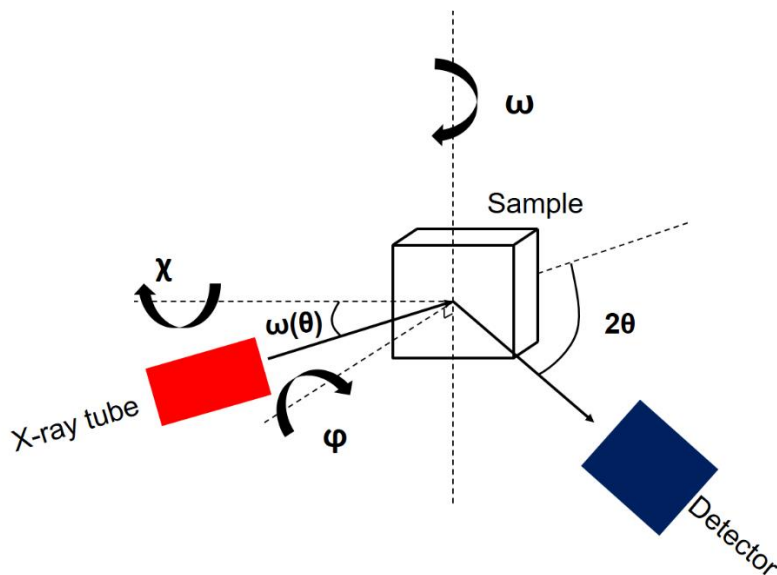


Figure 2.8: The ω -, φ - and χ - axis along which the sample can be tilted during the rocking curve measurement.

Rietveld refinement. To quantify the composition of the powder samples, a refinement using the Rietveld treatment has been also carried out on the measured θ - 2θ diffraction patterns. In principle, the Rietveld method refines the selected parameters to minimize the difference between an experimental pattern and a model based on the hypothesized crystal structure and instrumental parameters (calculated pattern)⁴. The Rietveld refinement is full profile fitting

method, which uses crystallographic constraints such as: (i) lattice parameters and space group to constrain peak positions, (ii) crystal structure to constrain peak intensity.

The purpose of the refinement is to minimize the residual function:

$$\sum_i \left[w_i (y_i^o - y_i^c) \right]^2 \quad (2.3)$$

Where $w_i = 1/\sqrt{y_i^o}$, y_i^o is the observed intensity and y_i^c is the calculated intensity at i^{th} step.

The calculated intensity at point (step) i of the diagram is determined by equation:

$$y_i^c = y_i^b + \sum_{\Phi} S_{\Phi} \sum_k G_{\Phi} (2\theta_i - 2\theta_k) I_k \quad (2.4)$$

Where G is the normalized profile shape function. I_k is the intensity of the k^{th} reflection. S is the scale factor of phase Φ . The summation is performed over all phases Φ and over all reflection k contributing to the respective point. y_i^b is the background of the refinement.

- The intensity of the Bragg reflections are calculated by equation:

$$I_k = m_k L_k |F_k|^2 P_k A_k \quad (2.5)$$

Where m_k is the multiplicity of k . L_k is the Lorentz-Polarization factor which depends on the instrument such as: geometry, monochromatic (angle α), detector, beam size/sample volume, and sample positioning. For a Bragg-Brentano instrument, $L_k = \frac{1 + \cos^2(2\alpha) \cos^2(2\theta)}{2(1 + \cos^2(2\alpha)) \sin^2 \theta \cos \theta}$.

$|F_k|^2$ is the structure factor. P_k is preferred orientation factor. A_k is absorption factor. The structure factor F_k depends on the position atomic by function:

$$|F_k|^2 = \left| \sum_{n=1}^N f_n e^{-B_n \frac{\sin^2 \theta}{\lambda^2}} \left(e^{2\pi i (hx_n + ky_n + lz_n)} \right) \right|^2 \quad (2.6)$$

Where N is number of atoms. x_n, y_n, z_n are coordinate of the n^{th} atom. f_n is the atomic scattering factor. B_n is the temperature factor.

- The scale factor is determined as:

$$S_{\Phi} = S_F \frac{f_{\Phi}}{V_{\Phi}^2} \quad (2.7)$$

Where S_F is the beam intensity. F_j is the volume fraction. V_j is the cell volume.

- The background in Rietveld refinement is a polynomial function in 2θ :

$$y_i^b = \sum_{n=0}^{N_b} a_n (2\theta_i)^n \quad (2.8)$$

Where N_b is the polynomial degree. a_n is the polynomial coefficients.

The quality of the refinement is evaluated by the weighted profile R-factor (R_{wp}) which is defined as:

$$R_{wp} = \sqrt{\frac{\sum_{i=1}^N [w_i (y_i^o - y_i^c)]^2}{\sum_{i=1}^N [w_i y_i^o]^2}} \quad (2.9)$$

In this thesis, the Rietveld refinement has been performed using the TOPAS software (version 4.2). Lorentz-Polarization factor was determined at 27.3 (for Ge monochromator). The polynomial degree of the background is 5. Other parameters such as: lattice constant, atomic positions, absorption coefficient, atomic scattering factor, temperature factor... were collected from the crystallographic information file (CIF) of materials.

2.2.2. Raman spectroscopy

Raman spectroscopy has been carried out in this work for a local phase identification, such as, for instance, for a single grain. In principle, Raman spectroscopy is a light scattering technique used to study vibrational (or rotational) modes in a chemical system. It is based on the Raman effect, or Raman scattering, which is an inelastic scattering process due to the interaction of a monochromatic light used for excitation with phonon of a lattice⁵.

When a material is excited by a monochromatic light, different scattering processes occur:

- The elastic scattering, called the Rayleigh scattering, where the incident and scattered photons have the same energy/frequency. It is the dominant scattering process.
- The inelastic scattering, the scattered photon has a different frequency of that of the incident photon. Raman scattering, which is an important inelastic scattering process,

involves transitions between the vibrational/rotational levels due to the absorption of an incident photon. It leads to a transition to a higher energy level, which is represented as an intermediate virtual state, followed by a spontaneous emission of a scattered photon as presented in the Figure 2.9. If the scattered photon has less energy than the incident one, the process is called Stokes Raman process. It corresponds to the excitation of the molecule from the vibrational ground state ($v=0$) to the first excited state ($v=1$) of a vibrational mode with energy $E_{\text{incident}} - E_{\text{scattered}}$. If the scattered photon has more energy than the incident photon, it is the anti-Stokes Raman process, and the molecule has relaxed from an excited vibrational state ($v=1$) to its ground state ($v=0$). The energy of the vibration is then equal to $E_{\text{scattered}} - E_{\text{incident}}$. Thus, the Stokes and anti-Stokes parts of a Raman spectrum can be symmetrically observed on both sides of the Rayleigh line, the more intense one being the Stokes one which is commonly measured in Raman spectroscopy. On the other hand, compared to the very intense Rayleigh line, the Raman lines have very weak intensities (at least $\times 10^{-6}$).

The energy lost (Stokes) or gained (anti-Stokes) by the photons in the scattering process is called the Raman shift (= Raman position) which is commonly expressed in wavenumbers (cm^{-1}) such as $\nu = 1/\lambda$. The Raman spectrum corresponds to the wavenumber dependence of the Raman scattered intensity. It can be used as a fingerprint to identify materials or molecules with a given crystallographic structure.

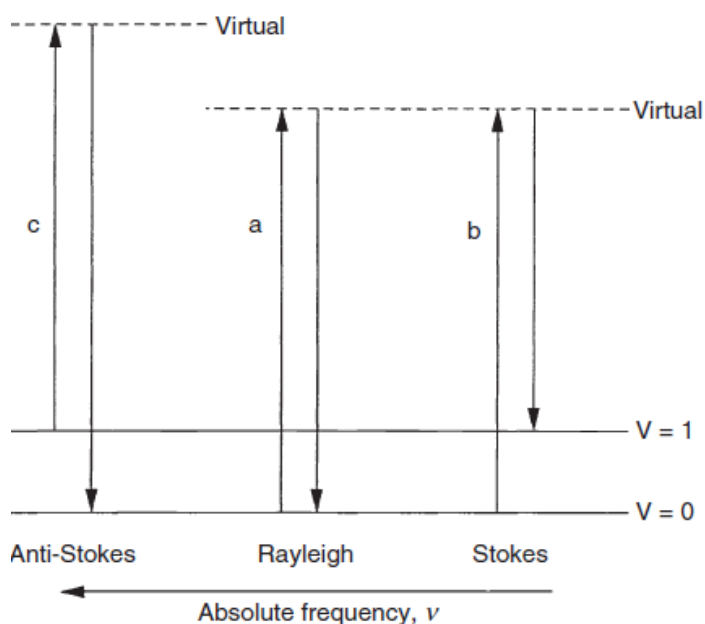


Figure 2.9: Elastic and inelastic scattering of incident light by molecules: Rayleigh, Stokes and anti-Stokes scattering⁶.

For that reason, the micro-Raman spectroscopy is commonly used for the structural characterization of materials and gives complementary information to other techniques such as XRD, TEM, etc. This technique is a local probe allowing the analysis in different points of a sample, the laser beam is focused on the sample surface down to the microscope. Moreover, no sample preparation is needed. The monochromatic light required by Raman spectroscopy can be provided only by a laser source. Lasers available at LMGP are listed in the Table 2.1.

Table 2.1: Available lasers for Raman micro-spectroscopy.

Laser type	Wavelength [nm]	Total power on the sample
He – Ne laser	632.8 (red)	11 mW
Ar – Ion laser	514.5 (green)	2.6 mW
Ar –Ion laser	488 (blue)	7.5 mW

In this work, the micro Raman spectroscopy analysis was performed at room temperature in a backscattering geometry using Jobin Yvon/Horiba LabRam spectrometer equipped with a liquid nitrogen cooled coupled charge device detector. The green laser excitation (wavelength=514.5 nm) was focused to a spot size smaller than $1 \mu\text{m}^2$ on the sample by using a 50 \times objective. In order to not heating up the samples, a filter $f_{1/4}$ has been used to reduce the laser power on the sample surface ($P_s=0.65 \text{ mW}$). Counting time was usually about 200sec. The measured Raman spectra were calibrated using the Raman line of a silicon substrate measured at room temperature (theoretical position is 520.7 cm^{-1}).

2.2.3. Transmission/absorption spectroscopy

Absorption/transmission spectroscopy is the analytical technique based on measuring the amount of light absorbed by a sample at a given wavelength.

In this work, to study the optical absorption of Al_4SiC_4 crystals, a Perkin Elmer Lambda 950 spectrophotometer has been used, which allows the measurement of transmittance and reflectance. Equipped with two light sources: a deuterium arc lamp for ultraviolet (UV) light and a tungsten-halogen lamp for visible and infrared (IR) light, the measurement has been performed in a total wavelength range of 250-2500 nm. Corresponding to the light sources, two different detectors were equipped, one photomultiplier (PM) for the UV and Visible wavelength, and an InGaAs sensor for the near infrared wavelength. The width slits of detectors were fixed at 4 and 2 nm, respectively. During the measurement, two detectors switched at 860.8 nm. The data interval was fixed at 2 nm, and the scan speed was 60 nm/min. Due to the limited size of the crystals, the holder samples with diameter of 3 and 5 mm have been used.

The spectrophotometer equipped with integrating sphere is shown in the Figure 2.10 with the geometry of measuring the total transmittance. An integrating sphere with diameter of 150mm, covered by spectralon has been used. With the incident light perpendicular to the surface of the sample, the optical absorption could be calculated from the total transmittance by equation⁷:

$$\alpha(\lambda) = \frac{1}{z} \ln \left(\frac{I_0}{I(\lambda)} \right) = \frac{1}{z} \ln \left(\frac{1}{T(\lambda)} \right) \quad (2.10)$$

Where z (μm) is the thickness of the sample, T (%) is the collected transmittance.

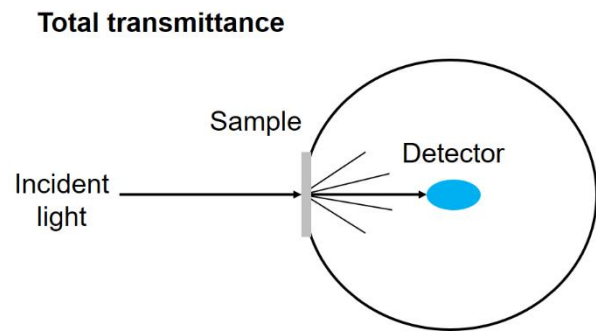
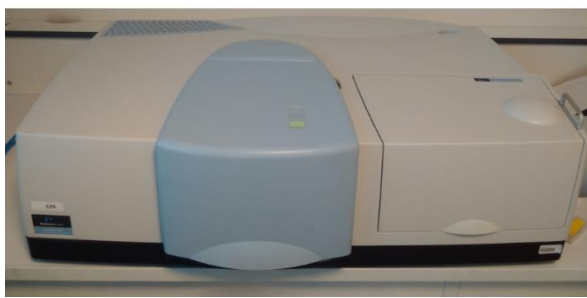


Figure 2.10: The Pelkin Elmer Lambda 950 spectrophotometer equipped with integrating sphere (left) and the geometry of the total transmittance measure (right).

Absorption coefficient. In making indirect transition, semiconductor can absorb or emit a phonon of energy. In other words, the optical absorption process involves both the absorption of a phonon and the emission of a phonon. Thus, as reported as an indirect band gap semiconductor by the theoretical calculation⁸, the absorption coefficient of Al_4SiC_4 could be determined by the function⁷:

$$\alpha_{abs}(\omega) = C_a \frac{(\hbar\omega - E_g + \hbar\omega_q)^2}{\exp(\hbar\omega_q / k_B T) - 1} \quad \text{in case a phonon is absorbed} \quad (2.11)$$

$$\alpha_{emis}(\omega) = C_e \frac{(\hbar\omega - E_g - \hbar\omega_q)^2}{1 - \exp(-\hbar\omega_q / k_B T)} \quad \text{in case a phonon is emitted} \quad (2.12)$$

Where C_a and C_e are constant, E_g is the band gap, $\hbar\omega_q$ is the energy of phonon absorbed (+sign) or emitted (-sign) involved in the indirect transition, $\frac{1}{\exp(\hbar\omega_q / k_B T) - 1}$ is the Bose-Einstein factor which is proportional to the probability for the absorption of a phonon.

Indeed, considering the absorption coefficient as function of incident photon energy, different thresholds can be observed for the absorption and emission processes. If we plot $\sqrt{\alpha(\omega)}$ as a function of $h\omega$, in the high photon energy range, $\sqrt{\alpha(\omega)}$ is proportional to $(\hbar\omega - E_g - \hbar\omega_q)$ in the high photon energy range, whereas in the low photon energy range, it is proportional to $(\hbar\omega - E_g + \hbar\omega_q)$.

2.2.4. Scanning electron microscopy

The scanning electron microscopy (SEM) is a type of electron microscope that makes use of the interaction between the focused beam of electrons and sample to provide the information about the sample surface topography and composition³.

As principle, the electron beam emitted from an electron gun is condensed to a fine probe for surface scanning. When the high-energy electrons interact with the specimen surface, they produce either elastic or inelastic scattering. The elastic scattering produces the backscattered electrons (BSEs) which are incident electrons scattered by atom in the specimen. The inelastic scattering produces the secondary electrons (SEs), which are electrons ejected from atoms in the specimen. The incident electrons interact with the sample within a tear-drop-shaped interaction volume as shown in the Figure 2.11. SEs are reflected at small angles and have much lower energy compared with incident electrons. They only escape from a volume near the surface with a depth of 5-50 nm. Otherwise, the BSEs are typically reflected at large angles and preserve 60-80% of the energy of incident electrons. With high energy, they can escape from a much deeper level in the interaction zone with a depth of 50-300 nm. For that reason, SEs are the primary signals for achieving the topographic contrast, while BSEs can provide information about the elemental composition contrast.

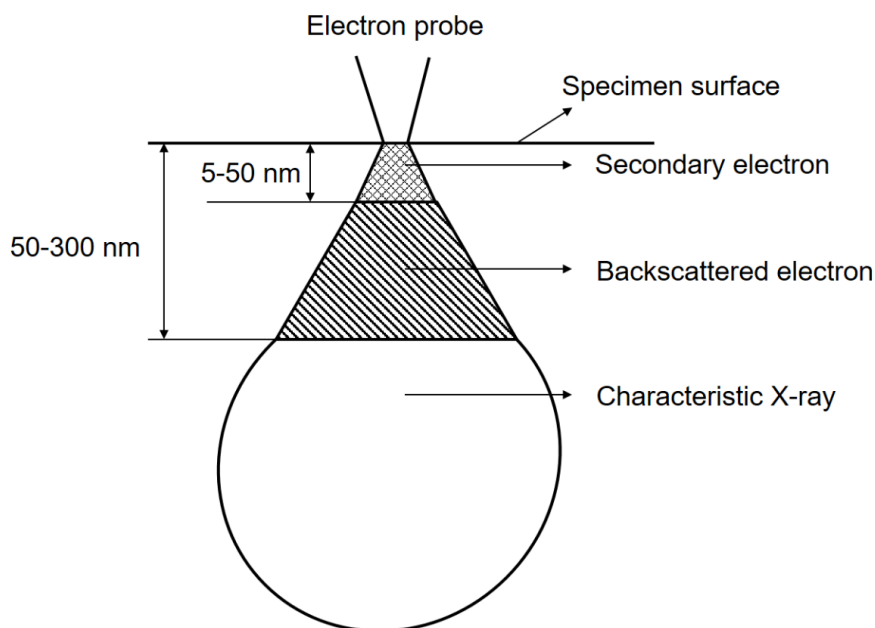


Figure 2.11: The interaction zone of electrons and specimen atoms below a specimen surface. Different signals are produced at different depth lengths (reproduced from reference³).

In this study, the microscope FEI QUANTA FEG 250 has been used to characterize the surface morphology, chemical composition and measure the thickness of deposited layer by cross section. Electron beams were formed in high vacuum (10^{-8} Pa) Schottky field emission gun (FEG).

For the topography analysis, an Everhart-Thornley detector (ETD) has been equipped for capturing the SEs signals. Working distance (WD) was fixed at 11 mm. The accelerating voltage was 15kV with the spot of 3. The diaphragm 6 had been used.

For the chemical composition analysis (also known as energy dispersive X-ray analysis - EDX), a silicon drift detector (SDD) has been equipped for capturing the BSEs signals. In order to characterize the surface of the samples, a lower energy beam of 10keV or 5keV can be used. For that reason, to increase the count rate for the analysis, the diaphragm 4 has been used with the spot of 5. The working distance was fixed at 11 mm. The quantitative analysis has been corrected by ZAF model, in which the matrix correction takes into account the (i) atomic number effects (Z), (ii) self-absorption effects (A) and (iii) secondary fluorescence effects (F). However, for the light elements (small Z) analysis, the mass absorption coefficients are still problematic due to the significant uncertainties even using the absorption-corrected models. Therefore, the EDX quantitative analysis cannot quantify exactly the carbon concentration.

2.2.5. Transmission electron microscopy

Same as SEM, transmission electron microscopy (TEM) also probes the sample structure by making use of the interaction with electrons. However, in this technique, the focused beam of electrons is transmitted through a specimen to form an image or diffraction pattern³.

In this work, a JEOL JEM 2010 microscope with a 0.19 nm point resolution has been used in order to characterize the crystallographic relationship of the heterostructures. The maximum accelerating voltage of the microscope is 200kV with a standard self-biasing LaB₆ filament as electron gun. The specimen stage can be tilted from -15 to 15° in both x- and y-direction.

Sample preparation. For the TEM experiments, the quality of the obtained data strongly depends on the quality of the prepared specimen. A TEM sample has to be electron transparent, thus the thickness range of a TEM specimen is in order of 50-500 nm to avoid the absorption of electron in material.

For that reason, the standard techniques of mechanical polishing and ion milling have been used for the preparation of our cross section samples as presented in Figure 2.12. At the beginning, the sample was cut in squares of ~ 2.5 mm with a diamond-wire saw. In order to observe different zone axes in the same sample, one of the squares is tilted by 90° with respect to the other, after that, they were glued together to create a sandwich. Then, the sandwich was cut in thin slices (~ 0.5 mm) which were used for the mechanical polishing. The slice was polished down to ~ 10 μm using the tripod polisher and a sequence of progressively finer grit diamond lapping films. After that, the specimen was bonded on the copper ring having a slot with a dimension of 2mm × 1mm. For the last step, the preparation was completed by the ion milling process. In this study, a Gatan's ion polishing system (PIPS) equipped with two high-powered Ar ion guns was used. The prepared conditions for all samples are: beam energy of 3 KeV, angles at +7°/-7° and a rotation of 3 rpm.

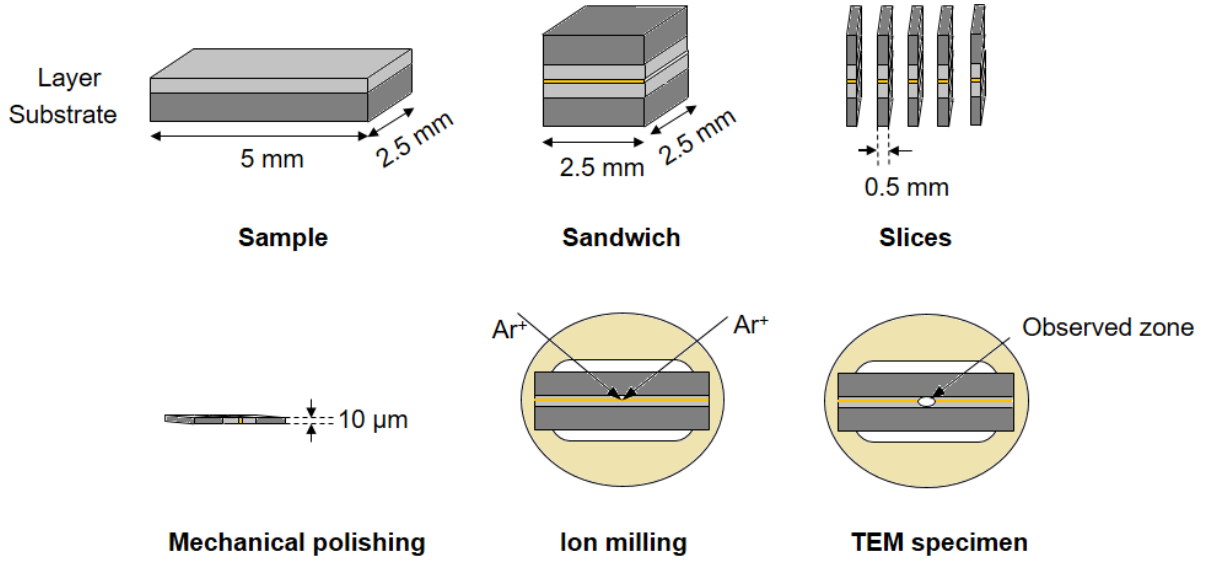


Figure 2.12: Schematic sequence for TEM cross section sample preparation using the standard techniques of mechanical polishing and ion milling.

Geometric phase analysis. Geometric phase analysis (GPA) is one of the most popular technique to extract the quantitative information from the high resolution TEM images. In this work, the GPA has been conducted to analyze the strain field at the interface of the heterostructures.

In fact, a TEM images of perfect crystalline material exhibits strong Bragg-reflections in its Fourier transform which indicates the periodicity and the orientation of the fringes in the image, while its phase decides the location of the fringes. The phase of any Bragg reflection \mathbf{g}_i is constant across the image. For a distorted lattice, the deformation can be seen as local shifts of the lattice fringes leading to a small change in the phase corresponding to \mathbf{g}_i which could be analyzed by GPA method. The principle steps of the GPA method could be summarized as below^{9, 10}:

- For the first step, the power spectra of the image intensity $I(r)$ is calculated in order to select reciprocal lattice vector \mathbf{g}_1 .
- For the second step, a mask (\mathbf{M}_1) characterized by its shape (Gaussian, Lorentzian, etc.) with a typical size has been chosen and applied to the Fourier transform $\tilde{I}(g)$ of the image. The mask is approximately centered on the selected peak \mathbf{g}_1 .
- Then, the inverse Fourier transform of the masked function is calculated which gives a complex image $I_{M_1}^{filt}(r)$ including amplitude $A_{M_1}(r)$ and phase image $P_{M_1}(r)$.

$$I_{M_1}^{filt}(r) = A_{g_1}(r) \exp\{iP_{g_1}(r)\} = A_{g_1}(r) \exp\{2\pi i \mathbf{g}_1 \cdot r + iP_{g_1}^r(r) - 2\pi ic\} \quad (2.13)$$

Where $P_{g_1}^r(r)$ is the reduced phase images, c is constant.

- In GPA method, only phase image is analyzed. Indeed, in order to optimize the calculated g_I value, we have to choose a reference region O of the image and minimize the following function with respect to g and the constant over all the pixel r of the region O .

$$S = \sum_{r \in O} \|P_{g_1}^r(r) - 2\pi(g \cdot r - c)\|^2 \quad (2.14)$$

The minimum is obtained for a vector $g_1(O)$ and constant $c(O)$. Then the new reduced phase image can be introduced as below

$$P_{g_1}^O(r) = P_{g_1}^r(r) - 2\pi g_1(O) \cdot r + 2\pi c(O) \quad (2.15)$$

- As supposing that the variation of the phase come from a local displacement field $u(r)$, r could be replaced by $r - u(r)$. Thus, we have:

$$P_{g_1}^O(r) = 2\pi g_1(O) \cdot (r - u(r)) - 2\pi c(O) \quad (2.16)$$

$$P_{g_1}^O(r) = -2\pi g_1(O) \cdot u(r) \quad (2.17)$$

In case of two dimensional strain analysis, these principal steps described before are repeated with a second g_2 vector which is non parallel to the first g_I vector. The set of the two obtained phase images $P_{g_1}(r)$ and $P_{g_2}(r)$ enable to calculate the local displacement, strain and rotation.

However, in this work, only the 1D-strain analysis has been used to analyze the 2D image in specific direction. Thus, supposing that the strain is zero in the reference area, the strain in considered area is calculated as

$$e_{GPA}(x) = \frac{d - d_o}{d_o} \quad (2.18)$$

Where $d = 1/g$ and $d_o = 1/g_o$ are the direct local lattice in the interested area and reference area respectively.

Mask function. As mentioned before, the mask M has been used to select the examined area around the reciprocal vector g_i in the Fourier transform of the direct image. We define the radius r_{dir} of the region R (over which GPA averages the information) and r_{rec} of the applied mask M .

In case of 1D image, the Gaussian mask centered at g_i has function as below:

$$\tilde{F}_M(g) = \exp\left(-\frac{(g - g_i)^2}{2\sigma^2}\right) \quad (2.19)$$

Where the radius of the Gaussian mask is $r_{rec} = 3\sigma$.

The multiplying in the reciprocal space by this Gaussian mask is equivalent to a convolution by the inverse Fourier transform of $\tilde{F}_{M_i}(g)$ in the direct space which is defined by the function:

$$F_M(x) = \sqrt{2\pi\sigma} \exp(-2\pi^2\sigma^2x^2) \exp(-2\pi g_i x) \quad (2.20)$$

Which has the standard deviation of $\frac{1}{2\pi\sigma}$. This function is not negligible over a region of

$$\text{radius } r_{dir} = \frac{3}{2\pi\sigma} = \frac{9}{2\pi r_{rec}}.$$

For instance, if we take $r_{rec} = 0.5g = 0.5/d$, then the radius of the region R in the direct space over which the GPA averages the information is $r_{dir} = 3d$. Note that, by increasing the region R or in another word, decreasing the mask size, the area in direct space become larger, and in which the results of the GPA are less accurate. However, with the large mask, the results could be perturbed by oscillations caused by the intense peak situated at the origin (Gibbs phenomenon)¹¹. In this study, different sizes of mask have been used like **0.25g** and **0.5g**.

In this thesis, the image processing involved in GPA has been realized on routine written on Digital Micrograph¹².

REFERENCE

1. N. Tsavdaris, Doctoral dissertation, Université Grenoble Alpes, 2015.
2. K. Ariyawong, Doctoral dissertation, Université Grenoble Alpes, 2015.
3. Y. Leng, *Materials characterization: introduction to microscopic and spectroscopic methods*. (John Wiley & Sons, 2009).
4. H. Rietveld, *A profile refinement method for nuclear and magnetic structures*, Journal of Applied Crystallography **2** (2), 65-71 (1969).
5. E. Le Ru and P. Etchegoin, *Principles of Surface-Enhanced Raman Spectroscopy: and related plasmonic effects*. (Elsevier, 2008).

6. P. Hendra, C. Jones and G. Warnes, *Fourier transform Raman spectroscopy: instrumentation and chemical applications*. (Ellis Horwood, 1991).
7. M. Dresselhaus, *Solid State Physics Part II Optical Properties of Solids*. (2001).
8. L. Pedesseau, J. Even, M. Modreanu, D. Chaussende, E. Sarigiannidou, O. Chaix-Pluchery and O. Durand, *Al₄SiC₄ wurtzite crystal: Structural, optoelectronic, elastic, and piezoelectric properties*, *APL Mater.* **3** (12), 121101 (2015).
9. M. J. Hÿtch, E. Snoeck and R. Kilaas, *Quantitative measurement of displacement and strain fields from HREM micrographs*, *Ultramicroscopy* **74** (3), 131-146 (1998).
10. J. L. Rouvière and E. Sarigiannidou, *Theoretical discussions on the geometrical phase analysis*, *Ultramicroscopy* **106** (1), 1-17 (2005).
11. A. Jerri, *The Gibbs Phenomenon in Fourier Analysis, Splines and Wavelet Approxima* (1998).
12. K. Kyou-Hyun, *DigitalMicrograph Script Source Listing for a Geometric Phase Analysis*, *Applied Microscopy* **45** (2), 101-105 (2015).

CHAPTER III

THERMO-CHEMISTRY OF THE Al_4C_3 -SiC SYSTEM

In order to propose a vapor phase route for the growth of Al_4SiC_4 , the thermodynamic study of the chemical system is essential. In this chapter, the thermo-chemistry of the Al_4C_3 -SiC pseudo-binary system will be investigated by thermodynamic calculation. In the first part, the thermodynamic background of the system will be reviewed such as: Al-Si binary system, Al-C binary system, Si-C binary system, and Al-Si-C ternary system. In the second part, some thermal analysis will be conducted using our homemade differential temperature analysis system in order to verify some specific points in the Al_4C_3 -SiC section. Finally, the classical thermodynamic calculation are carried out in order to study the vaporization and condensation phenomena in the Al_4C_3 -SiC system. The conditions to condense the different aluminum-silicon ternary carbides family are estimated. The results will be then used to develop an Al_4SiC_4 vapor growth process in the next chapter.

3.1. Thermodynamic background

3.1.1. Al-Si binary system

The Al-Si binary system shows a simple eutectic without any intermediate compound. The diagram is presented in Figure 3.1 which is reproduced from the one reported by Murray *et al.*¹. Beside the melting point of pure Al and pure Si at 660°C and 1414°C, respectively, the only invariant reaction is the eutectic transformation.



Which occurs at 577°C. The eutectic composition is 12.2 at.% of Si.

The eutectic is bordered by two solid solutions: α on the Al side and “pure” Si on the Si side. The maximum solubility of Si in Al is 1.5 at.% at the eutectic temperature and it decreases to 0.05 at.% at 300°C¹. On the other hand, the maximum solubility of Al in Si is only 0.016 at.% at 1190°C¹.

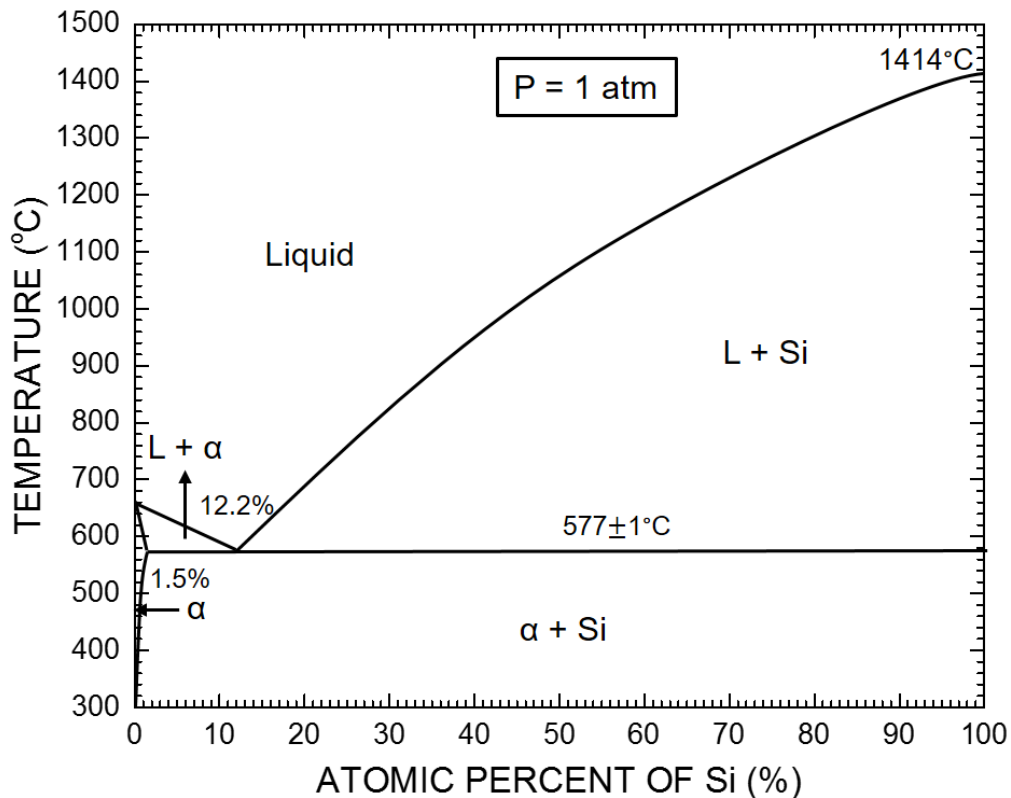


Figure 3.1: The Al-Si phase diagram, as reported in reference¹.

3.1.2. Si-C binary system

The equilibrium phase diagram of Si-C system at the pressure of 108 atm is presented in Figure 3.2, as reported by Scace *et al.*². The Si-C system consists of Si, graphite, and SiC which is the only intermediate compound. The system shows a peritectic transformation:



Which occurs at 2830°C, involving SiC and a liquid containing 19 at.% C. Moreover, very low solubility of C in the Si melt was reported. The solubility of carbon in the silicon melt was experimentally reported to vary between 0.01 and 19% in the temperature interval 1408-2830°C².

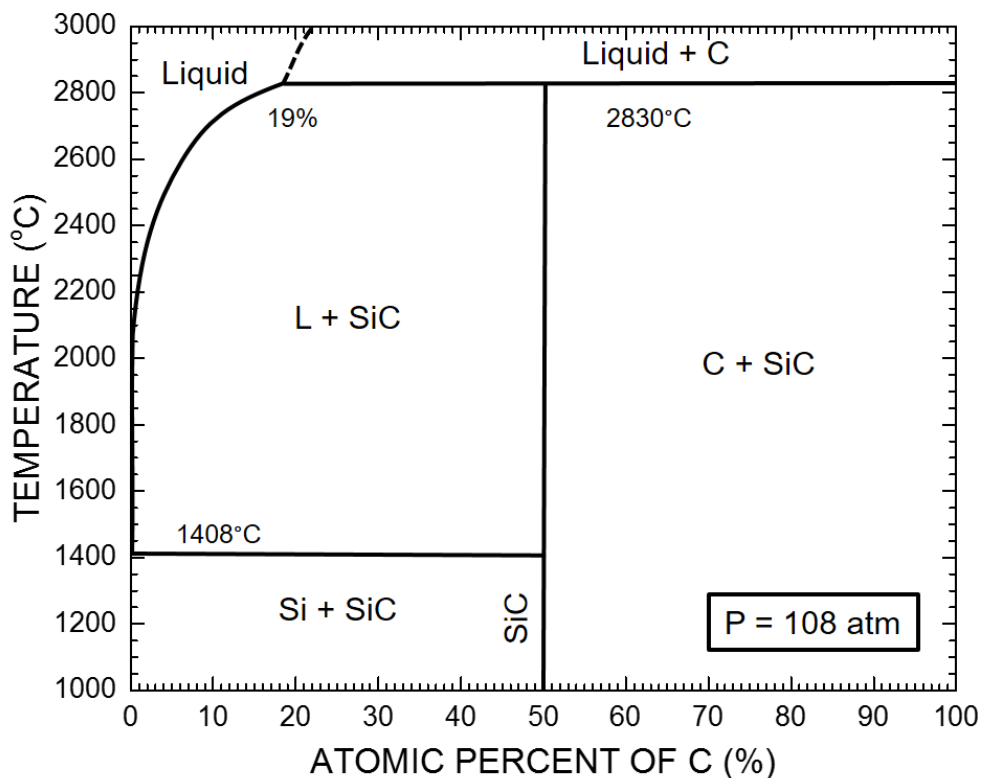


Figure 3.2: The Si-C phase diagram from reference².

At atmospheric pressure, SiC does not form any stoichiometric melt. According to theoretical calculations, the stoichiometric melting could be reached for pressures higher than 100000 atm and temperatures higher than 3200°C³.

For temperature lower than 2800°C, SiC decomposes incongruently leading to graphitization during vaporization. The SiC vaporization was analyzed by high temperature mass spectrometry fitted with Knudsen effusion cells⁴. The thermodynamic data were also

measured and critically assessed by Rocabois *et al.*⁵. Si(g), Si₂C(g), SiC₂(g) and Si₂(g) were identified as the main gaseous species vaporized from solid SiC at high temperature. In fact, in such a system, the measured partial pressures are lower than equilibrium ones due to kinetic barriers. The equilibrium partial pressures must be corrected by an evaporation coefficient to get accurate Hertz-Knudsen flows vaporized from the SiC surface⁴.

3.1.3. Al-C binary system

The Al-C diagram in the 1700-2400°C range is presented in Figure 3.3, as reported by Oden *et al.*⁶. The carbide Al₄C₃ is the only intermediate compound. Its melting point was experimentally reported at 2156°C and associated to the following peritectic reaction:



The solubility of the C in Al was also investigated. For the temperature below the peritectic point, the solubility of C is fitted by the following equation⁶:

$$\log(C) = 5.5307 - 10335.066 / (T + 273) \quad (3.4)$$

Where C is the atomic percent of carbon (%), T is the temperature (°C).

As compared with the solubility of carbon in silicon, the solubility of carbon in aluminum is much higher at high temperature. Indeed, as presented in the phase diagram, at the peritectic point of Al₄C₃, the solubility of carbon in aluminum is 18.9%.

The dissociation pressure of Al₄C₃ was experimentally investigated by Plante *et al.*⁷ in 1966 and Rinehart *et al.*⁸ in 1980 using Knudsen-effusion mass spectroscopy for temperature ranging from 1400 to 1727°C and from 1048 to 1334°C, respectively. The decomposition pressure of Al₄C₃ was also calculated by Qiu *et al.*⁹. Al(g), AlC(g), Al₂C₂(g), AlC₂(g) and Al₂C(g) had been identified as the main gaseous species vaporized from solid Al₄C₃. The calculated results of the Al vapor pressure as a function of temperature shown in Figure 3.4, are in good agreement with the early experimental data.

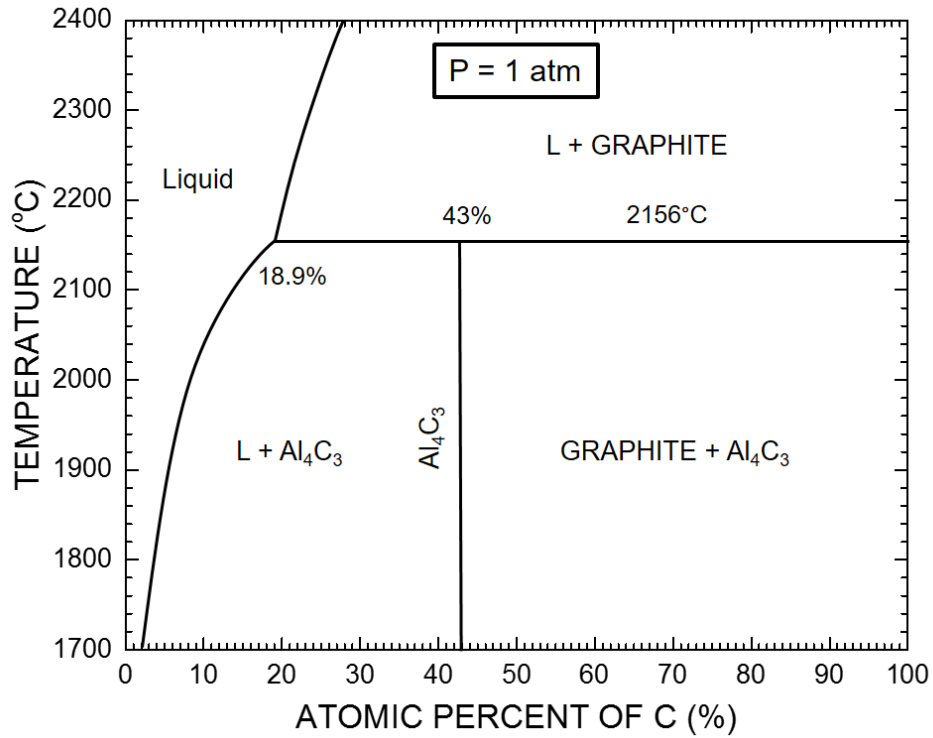


Figure 3.3: The Al-C phase diagram from reference⁶.

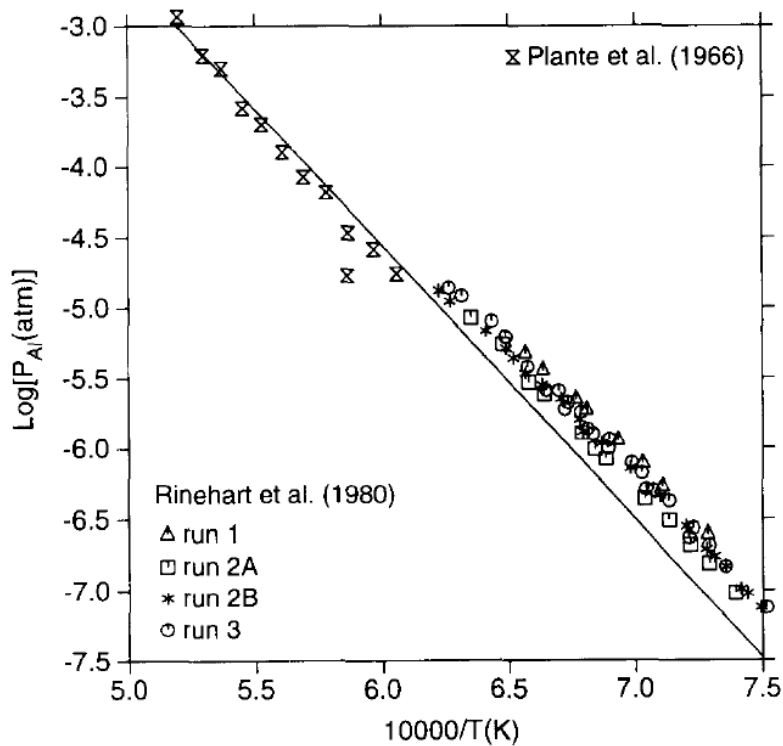


Figure 3.4: Calculated decomposition pressure of Al₄C₃ (solid line) as a function of temperature in comparison with the experimental results⁷⁻⁹. The calculation was done for the following equilibrium $\text{Al}_4\text{C}_3 = 4\text{Al}(\text{gas}) + 3\text{C}(\text{s})$. Figure is taken from the reference⁹.

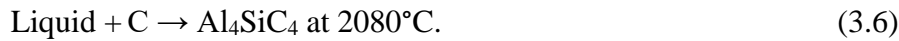
3.1.4. Al-Si-C ternary system

The Al-Si-C system was experimentally investigated by Oden *et al.*⁶. Three ternary compounds: Al_4SiC_4 , Al_8SiC_7 and $\text{Al}_4\text{Si}_2\text{C}_5$ were reported. They belong to the section between Al_4C_3 and SiC . Among them, Al_4SiC_4 and Al_8SiC_7 are believed to be stable and have been experimentally confirmed.^{6, 10, 11}. $\text{Al}_4\text{Si}_2\text{C}_5$ was reported by Inoue *et al.*¹² and never have been observed in later investigations.

The isopleth Al_4C_3 - SiC presented in Figure 3.5 was firstly investigated by Oden and McCune for the temperature ranging from 1900 to 2200°C by X-ray diffraction and thermal analysis. The ternary Al_8SiC_7 is formed according a peritectic reaction:



Beside of that, the equimolar phase Al_4SiC_4 was suggested to form according to a peritectic reaction:



These data were recently reassessed using the CALPHAD method by Gröbner *et al.*¹³. We have used these assessments for our calculations. The Al_4C_3 - SiC isopleth and the isothermal section at 2000°C of the Al-Si-C ternary system are shown in Figure 3.5 and Figure 3.6, respectively.

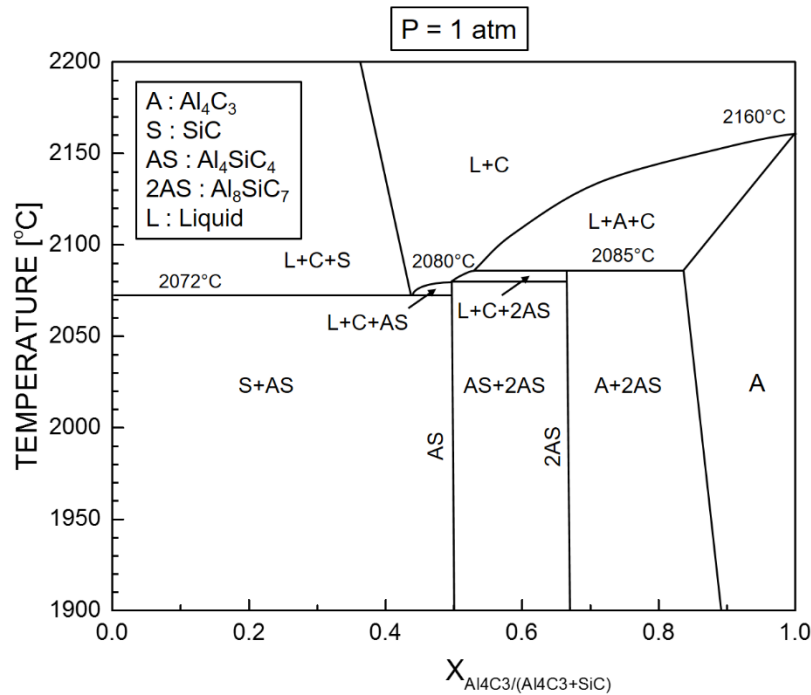


Figure 3.5: Quasi-binary phase diagram of Al_4C_3 - SiC calculated using the thermodynamic data assessed by Gröbner *et al.*¹³

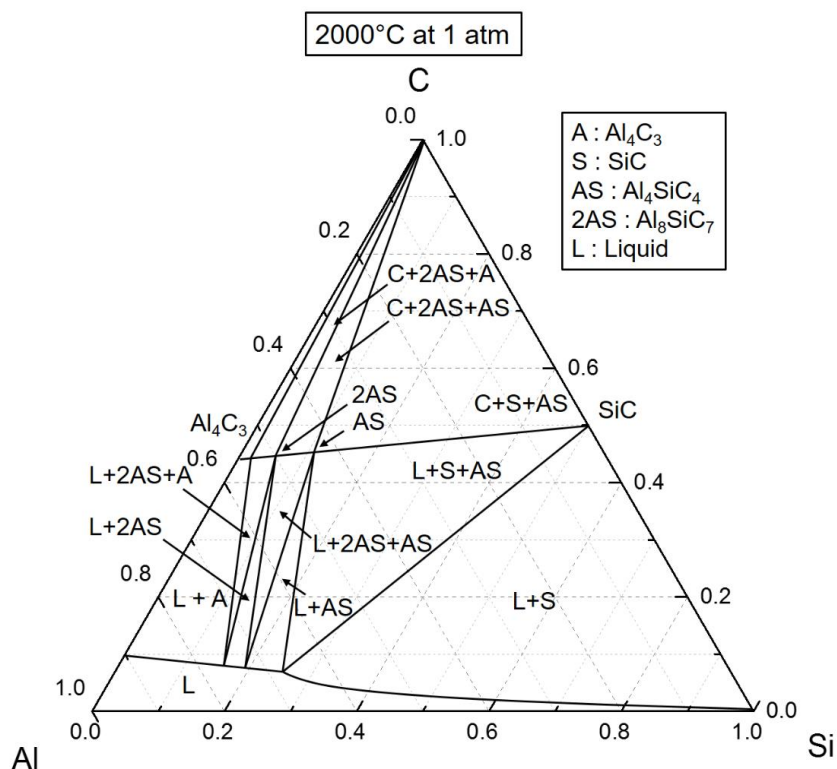


Figure 3.6: Al-Si-C isothermal section at 2000°C calculated using the thermodynamic data assessed by Gröbner et al.¹³.

3.2. Differential thermal analysis

In order to verify the temperature of invariant points in the phase diagram, a homemade differential thermal analysis (DTA) using the high temperature induction heated reactor has been implemented.

3.2.1. Experimental apparatus

The geometry of the set-up is illustrated in Figure 3.7. It includes two main parts: i) the graphite furnace which is made of high density graphite and surrounded by insulating graphite felt and ii) the reaction cell (small graphite closed crucible). Two di-chromatic pyrometers have been used to measure the temperature of the reaction cell at the top and at the bottom. The crucible geometry has been adapted in order to get the bottom temperature measurements as close as possible to the reaction cell. This bottom measurement (T_{PYRO_BOT}) is used to detect the deflection of temperature when a thermal event occurs. The top measurement (T_{PYRO_TOP}), which is used for the furnace temperature regulation, is not in direct contact with the reaction cell. It is thus somewhat decoupled to the reaction cell. Due to the small size of the reaction cell compared to the graphite furnace, the reaction cell can be considered as almost isothermal.

Moreover, the graphite crucible used to contain the powder is covered to prevent the sublimation of materials.

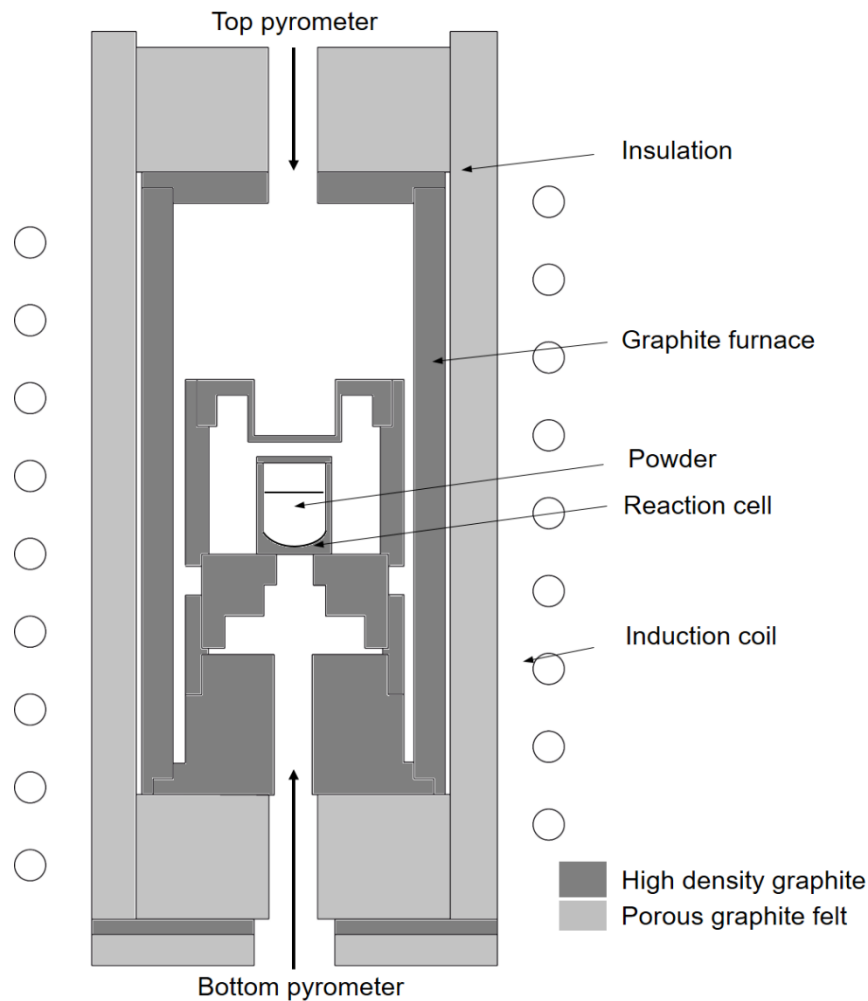


Figure 3.7: The geometry developed for the DTA analysis.

3.2.2. Experimental process

The raw materials were composed of the powder of Al_4C_3 (Alfa Aesar, 99+% purity, particles size $< 30\mu\text{m}$) and SiC (Sika tech E301, particle size $< 70\mu\text{m}$) with a molar ratio $X_{\text{Al}_4\text{C}_3}$ defined as $X_{\text{Al}_4\text{C}_3} = n\text{Al}_4\text{C}_3 / (n\text{Al}_4\text{C}_3 + n\text{SiC})$.

To prepare the experiment, the reactor was pumped out to achieve a vacuum $< 10^{-3}$ mbar. At the beginning, the reactor was manually heated up with a constant power to 1100°C , which is the lowest measurable value of the pyrometer. At that moment, the chamber is filled with 840 mbar of high purity argon to prevent the sublimation of the materials. Then each runs were composed of several temperature cycles, in order to check several times any temperature arrest. All the ramp of temperature (up and down) were done with the constant rate of $15^\circ\text{C}/\text{min}$.

Depending on the composition used, the temperature profiles were adapted. They are detailed in Figure 3.8, Figure 3.9 and Figure 3.10 for the $X_{Al_4C_3}=1$ (pure Al_4C_3), $X_{Al_4C_3}=0.5$ and $X_{Al_4C_3}=0.4$, respectively.

For the molar fraction $X_{Al_4C_3}=1$ (Al_4C_3 pure), the reactor was programmed to heat up to $2350^\circ C$ for the first curve with the constant rate of $15^\circ C/min$ which was the rate used for whole experiment. After 10 minutes at $2350^\circ C$, the reactor was cooled down to $1900^\circ C$ at $15^\circ C/min$. After 10 minutes at $1900^\circ C$, the temperature was increased again to $2350^\circ C$ for the second curve. After 10 minutes at $2350^\circ C$, the temperature was decreased to $1900^\circ C$. At the end, the reactor was cooled down by turning off the power. The experimental procedure is schematically represented in the Figure 3.8.

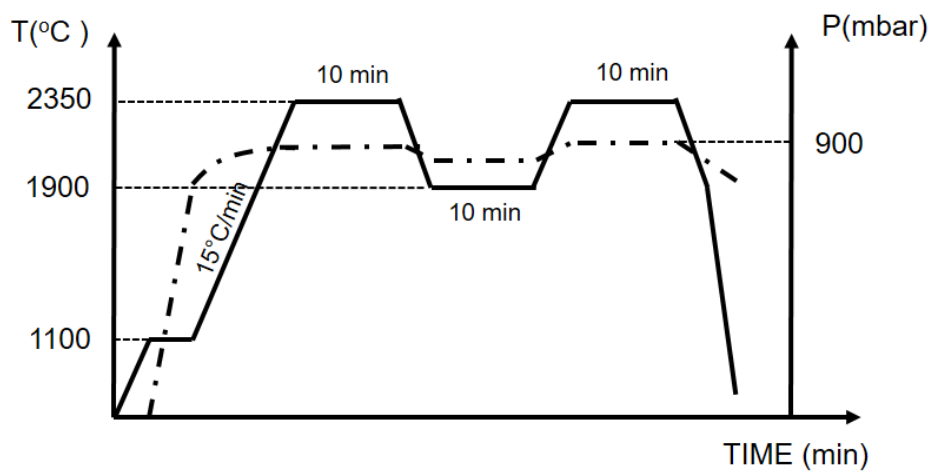


Figure 3.8: Experimental procedure used for the DTA measurement on pure Al_4C_3 . Black line corresponds to the temperature profile, dotted line corresponds to the pressure profile.

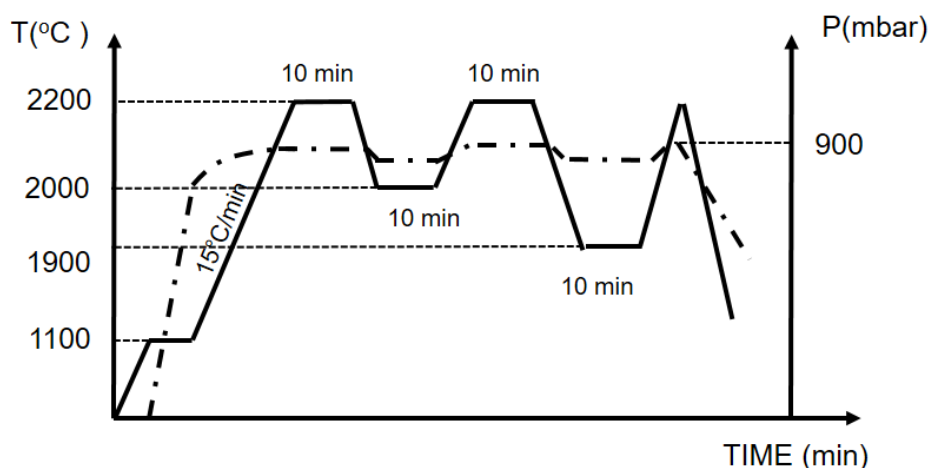


Figure 3.9: Experimental procedure used for the molar fraction $X_{Al_4C_3}=0.5$.

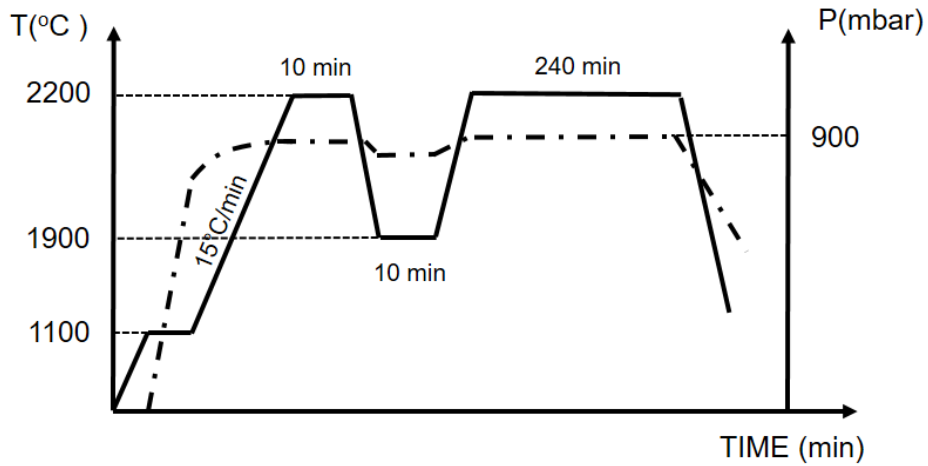


Figure 3.10: Experimental procedure used for the molar fraction $X_{Al_4C_3}=0.4$.

Due to the possible recalescence upon the cooling down, we mainly concentrated on heating steps. Moreover, a qualitative analysis by X-ray diffraction was also conducted for the composition after experiments in order to investigate the nature of the reaction.

3.2.3. Experimental results and discussion.

Mole fraction $X_{Al_4C_3}=1$. The Figure 3.11 presents the time-temperature thermal analysis curves obtained for the Al_4C_3 powder. During the first cycle, very small thermal events are detected with almost no link with the phase diagram. In fact, the raw Al_4C_3 powder is oxidized and partially consists of aluminum oxy carbides like Al_2OC and $Al_3O_{3.5}C_{0.5}$ which are revealed in the diffractogram presented in the Figure 3.12. This first curve was probably perturbed by the decomposition of the oxides (carbo-reduction) and only the second cycle will be considered.

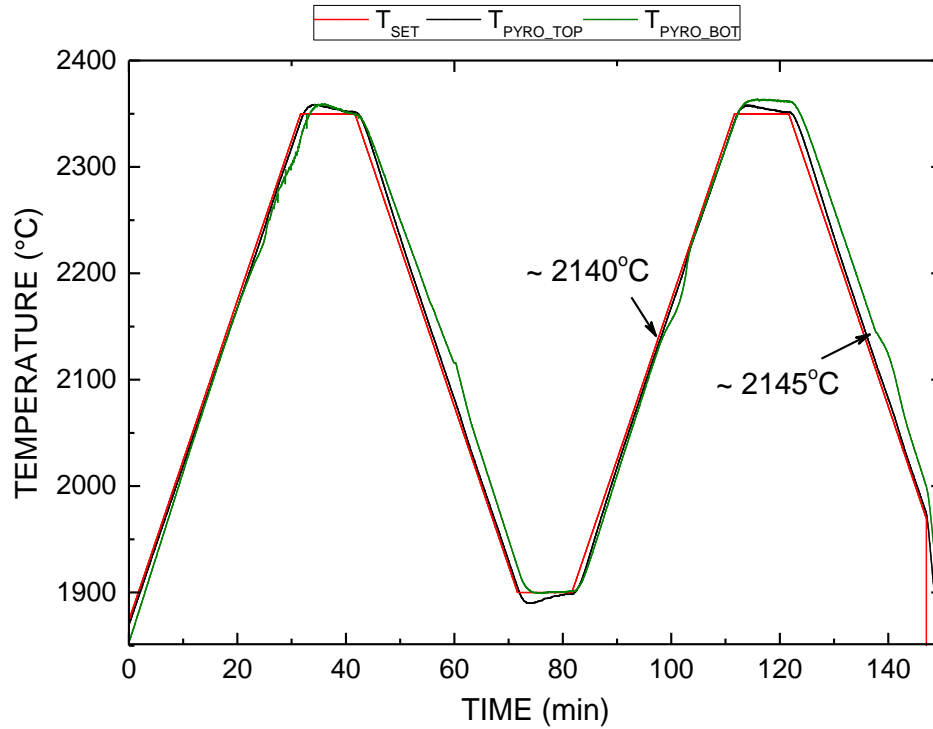


Figure 3.11: Time-temperature plot for the Al_4C_3 powder.

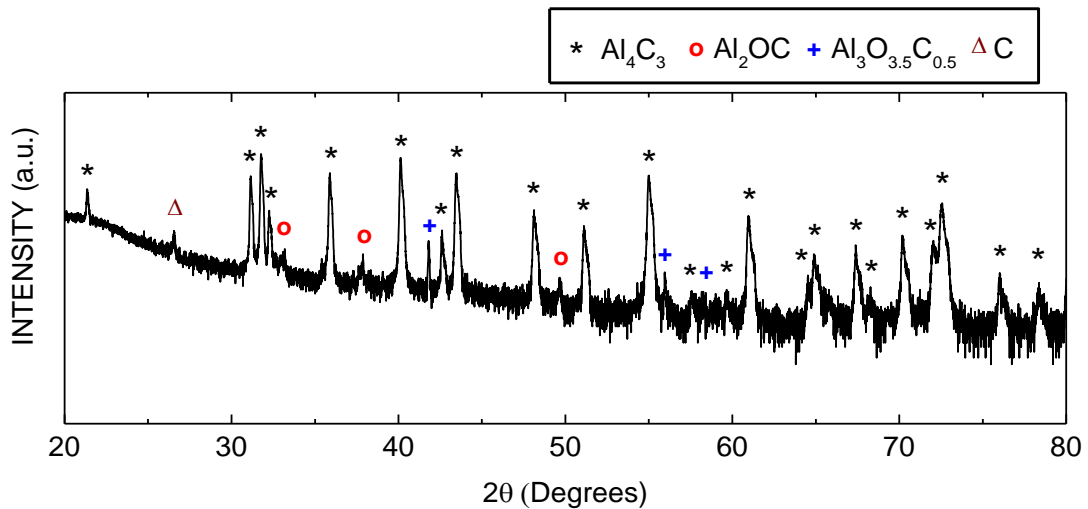


Figure 3.12: Diffractogram collected from the raw Al_4C_3 powder.

The thermal arrests detected during the second curve are magnified in the Figure 3.13. The baseline has been added as dotted line in order to better show the temperature deviation. The phase transition began at $2140^\circ C$ for the heating up, and $2145^\circ C$ for the cooling down corresponding to the endothermic and exothermic reactions, respectively. The endothermic reaction is the peritectic decomposition of Al_4C_3 to liquid and graphite (equation 3.3). Otherwise, the exothermic reaction is the transition from liquid + C to Al_4C_3 .

The observed thermal events are slightly amortized due to the fact that the measurement is not done directly on the sample but collected below (and outside) the reaction cell. A small conduction contribution is thus systematically included in the signal. That is also why the temperature is slightly lower than the previously reported one (around 2155°C). Note that our measurement is still within the absolute measurement error of the pyrometer, which is about 1% of the measured value.

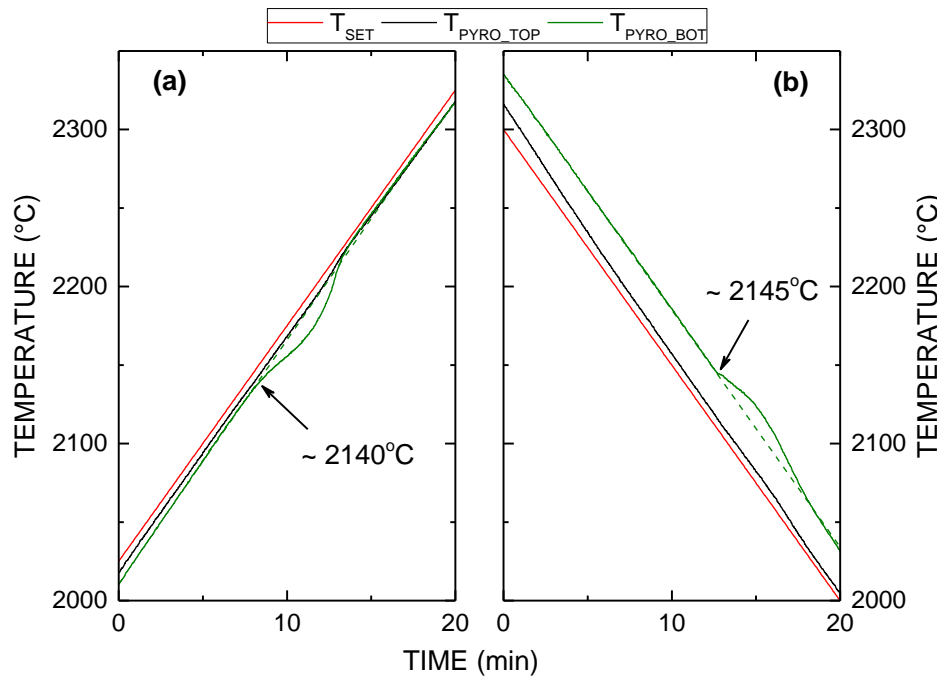


Figure 3.13: Time-temperature thermal analysis of Al_4C_3 powder: (a) heating-up process, (b) cooling-down process.

Mole fraction $X_{Al_4C_3}=0.5$ and 0.4 . For the mixture, the thermal events observed by the bottom pyrometer during the heating up process were compared. The Figure 3.14 represents the time-temperature thermal analysis curves for the molar fraction $X_{Al_4C_3}=0.5$ and $X_{Al_4C_3}=0.4$. For the $X_{Al_4C_3}=0.5$, a thermal arrest began at 2065°C corresponding to the peritectic decomposition of Al_4SiC_4 which was reported at 2080°C on the phase diagram. For the $X_{Al_4C_3}=0.4$, the thermal analysis curve indicates a reaction beginning at 2050°C which corresponds to the quasi-peritectic decomposition: $Al_4SiC_4 + SiC \rightarrow \text{liquid} + \text{graphite}$. After experiment, the powder sample was extracted and grinded by ball milling for the qualitative analyses using XRD measurements. As shown in the Figure 3.15, Al_4SiC_4 , SiC, Al_4C_3 , Al and Si phases are revealed in both of samples. The presence of Al-Si alloy in the composition is the vestige of the liquid phase produced by the peritectic decomposition. The observation of Al_4C_3

in the compositions after the analysis confirms the inherently sluggish nature of the peritectic reactions⁶ which leads to a typical shape of the observed thermal arrests.

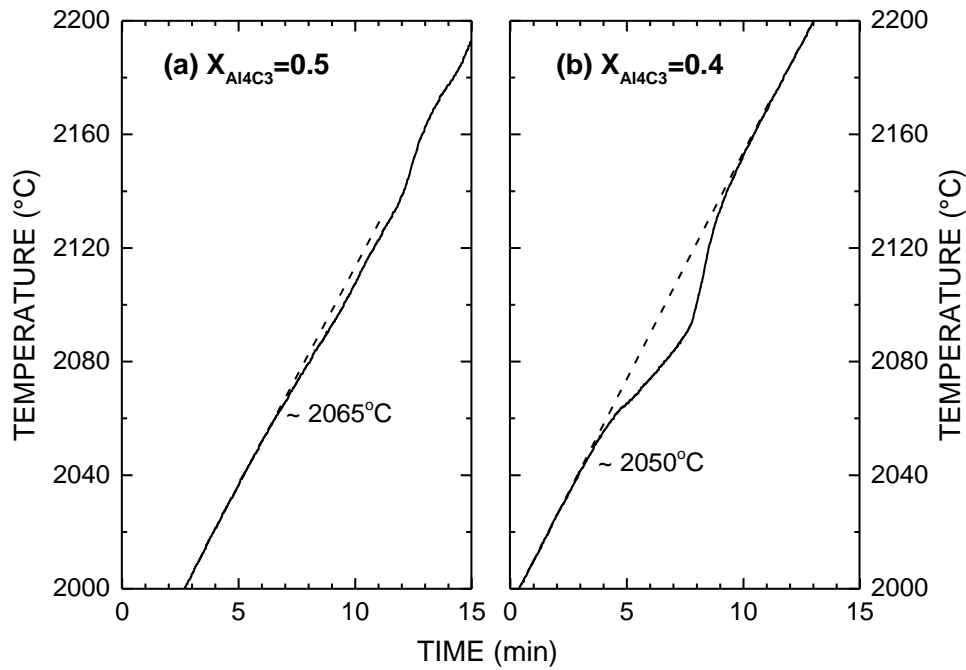


Figure 3.14: Time-temperature thermal analysis of the mixture Al_4C_3 -SiC with different composition: (a) $X_{Al_4C_3} = 0.5$; (b) $X_{Al_4C_3} = 0.4$. The heating up of the second curve are investigated.

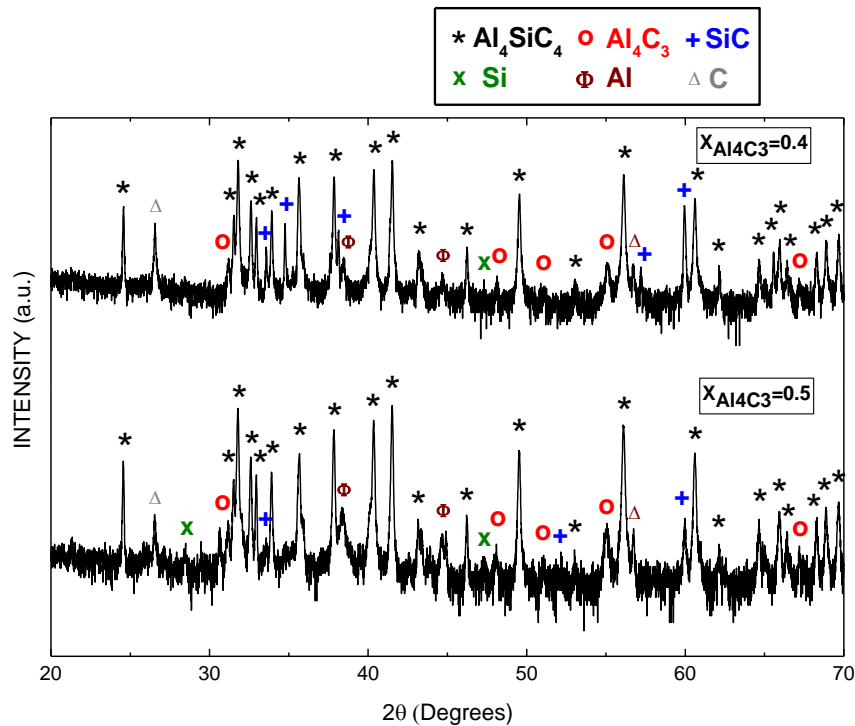


Figure 3.15: Diffractograms collected from the powder mixture after the DTA experiments.

In summary, the results obtained from our DTA analysis are in good agreement with the phase diagram reported in the literature. They also show that our temperature measurements are well calibrated and the global behavior of our high temperature furnace follows what is expected from the existing data of the literature.

3.3. Thermodynamic calculation

As mentioned in the chapter 1, Al_4SiC_4 could be synthesized from two different processes such as (i) solution growth and (ii) sintering. The solution growth could be performed by melting aluminum (Al) and silicon (Si) in carbon (C) environment with molar stoichiometry at 1800°C under atmospheric pressure¹⁴. However, this approach is difficult to reproduce. In fact, due to the reaction mechanism of liquid Al with graphite, the graphite crucible is quite often damaged (broken), leading to liquid loss. On the other hand, according to the phase diagram, Al_4SiC_4 phase could be synthesized by sintering an equimolar composition of Al_4C_3 and SiC at temperature below 2085°C . This approach was commonly used to synthesize the Al_4SiC_4 bulk ceramics or powders in the literature¹⁵. However, solid state reaction usually show a low yield leading to a phase mixture (unreacted residues) and are inherently not adapted for the growth of single crystals.

To overcome these drawbacks, and inspired by the development of the SiC bulk crystal growth process, we have investigated the vaporization and condensation phenomena in the Al_4C_3 -SiC binary system in order to propose a vapor phase route for the synthesis of Al_4SiC_4 single crystals.

3.3.1. Calculation methodology

Thermodynamic calculations of the ternary Al-Si-C were performed with the Factsage 7.1 package, using a set of coherent data from Scientific Group Thermodata Europe (SGTE), Scientific Group Thermodata Europe Pure Substances (SGPS), which is compiled from the refinement proposed by Gröbner *et al.*¹³ All the species considered in this work are gathered in Table 3.1.

Table 3.1: Details of the chemical species considered in the present work, with the corresponding databases.

	Chemical species	Database
Vapor phase	Al, Al ₂ , AlC, Al ₂ C, AlC ₂ , Al ₂ C ₂ , Si, Si ₂ , Si ₃ , SiC, Si ₂ C, SiC ₂ , Si ₂ C ₂ , Si ₃ C, Si ₃ C ₂ , Si ₄ C, C ₂ , C ₃ , C ₄ , C ₅ , Ar	SGPS
Liquid phase	Al, Si, C	SGTE
Solutions	Liquid alloys, Al-carbide with solubility for Si, Hexagonal closed packed phase with interstitial vacancy C	SGTE
Solid phase	Al ₄ SiC ₄ , Al ₈ SiC ₇ , SiC, Al ₄ C ₃ , C (graphite)	SGTE

Before discussing the gas phase composition, the validity of the compiled database has been assessed by computing an isothermal section at 2000°C and the pseudo-binary Al₄C₃-SiC section which are represented in Figure 3.6 and Figure 3.5, respectively. The calculations were found in perfect agreement with the experimental works of Oden *et al.*⁶.

The calculations were carried out by minimization of the total free energy of the system in the temperature range 1500 to 2100°C with the constant volume hypothesis. The vapor phase is assumed to behave as a perfect gas. As initial conditions, we set a mixture of SiC and Al₄C₃ with various compositions, an argon atmosphere and an excess of solid carbon. These conditions have been selected because they are close to the experimental ones which are presented in the next chapter. To simulate the sublimation growth process, i.e. a growth cavity submitted to a temperature gradient, we used the following procedure: firstly, the equilibrium vapor phase composition is calculated at a given temperature (T_{POWDER} which is the hot point) for a set of initial conditions. Then, all the gaseous species are selected and injected as input conditions in a second calculation, at a lower temperature (T_{SEED}). With such an approach, it is possible to describe on a pure thermodynamic footing, the nature and composition of the phases condensing at the seed side, which is the “cold point”. The scheme of calculation process is presented in Figure 3.16.

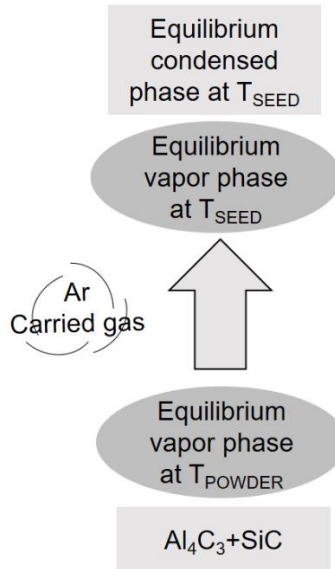


Figure 3.16: Scheme of thermodynamic calculation process.

3.3.2. Thermochemistry of the gas-solid system

In order to investigate the thermochemistry of the gas-solid system, two different phenomena have been separately considered such as the vaporization of the powders and the condensation at seed.

3.3.2.1. The vaporization of the powders

For the first step, the equilibrium vapor phase vaporized from the $\text{Al}_4\text{C}_3\text{-SiC}$ system was considered. Table 3.2 gives the computed equilibrium partial pressures of the different gaseous species at 2000°C for the initial composition of $X_{\text{Al}_4\text{C}_3} = 0.5$. We can see that the partial pressures spread over a large range of values, which are distributed on ten orders of magnitudes. For that reason, some species with small partial pressure can be neglected. The system can be described accurately by considering only 6 species include $\text{Al}(\text{g})$, $\text{Al}_2(\text{g})$, $\text{Al}_2\text{C}_2(\text{g})$, $\text{Si}(\text{g})$, $\text{SiC}_2(\text{g})$, $\text{Si}_2\text{C}(\text{g})$. The evolution of partial pressure of these species as function of temperature are plotted in Figure 3.17(a). Beside of that, the corresponding activities of Al, Si and C elements in the vapor phase composition are plotted in Figure 3.17(b).

Table 3.2: Equilibrium partial pressures of the different gaseous species computed from an initial mixture of $X_{\text{Al}_4\text{C}_3}=0.5$ at 2000°C .

Species	$\text{C}_2(\text{g})$	$\text{C}_3(\text{g})$	$\text{C}_4(\text{g})$	$\text{C}_5(\text{g})$	$\text{Al}(\text{g})$	$\text{Al}_2(\text{g})$	$\text{AlC}(\text{g})$
p_i [bar]	8.82E-10	1.01E-8	2.30E-12	1.01E-11	0.07	2.22E-4	1.35E-7

Species	AlC ₂ (g)	Al ₂ C ₂ (g)	Si(g)	Si ₂ (g)	Si ₃ (g)	CSi(g)	C ₂ Si(g)
p _i [bar]	2.88E-6	4.19E-4	1.08E-4	7.95E-7	3.90E-8	1.07E-8	1.36E-5

Species	CSi ₂ (g)	C ₂ Si ₂ (g)	CSi ₃ (g)	C ₂ Si ₃ (g)	CSi ₄ (g)
p _i [bar]	2.54E-5	4.36E-7	2.27E-7	1.22E-7	1.00E-10

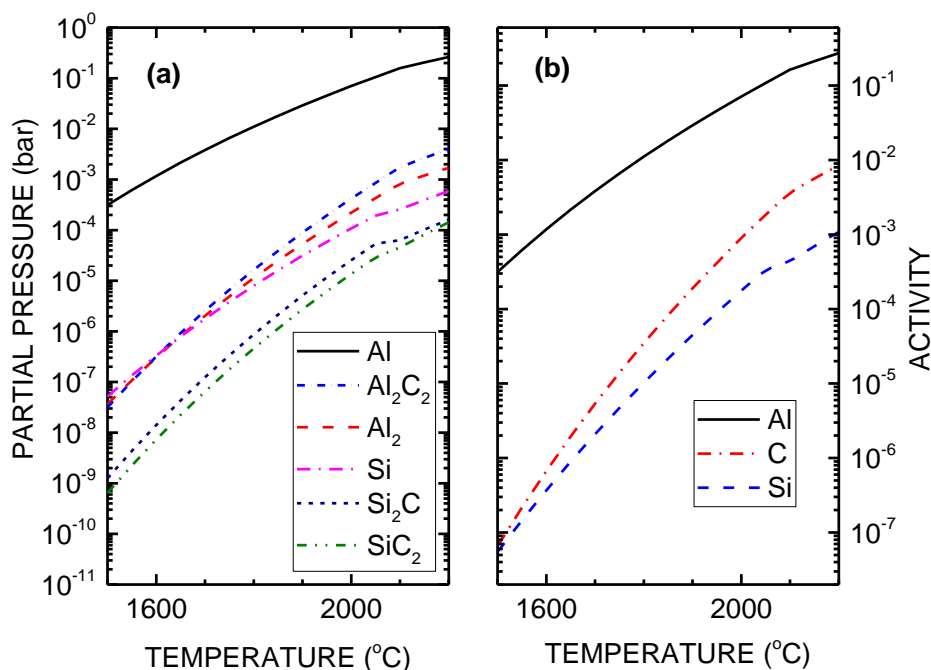


Figure 3.17: (a) Equilibrium partial pressures of the main vapor species as a function of temperature for an initial composition $X_{Al_4C_3}=0.5$ of the source materials. (b) Activities of Al, Si and C elements in the vapor phase as a function of temperature.

As expected, the vaporization of Al₄C₃-SiC mixture strongly increases with temperature. The vapor composition is characterized by the huge predominance of Al(g) which represents more than 95% of the total pressure. The most abundant carbon containing species is Al₂C₂(g) at any temperature. Similarly to aluminum, the dominant silicon containing species is atomic silicon Si(g). The partial pressure of Si₂C(g) and SiC₂(g) which are the common vaporization species of SiC, are about one order of magnitude lower than the main C- and Si-containing species. Concerning the activities of elements, as illustrated in the Figure 3.17(b), the activity of Al elements in the vapor phase is the highest with few order of magnitude higher than one of Si and C for the temperature range 1500-2200°C. The activity of C and the activity of Si are quite similar at temperature 1500°C, however, the difference increases with temperature. At

2200°C, the activity of C is about one order of magnitude higher than the activity of Si. Note that a small discontinuity around 2080°C corresponds to the peritectic decomposition: $\text{Al}_4\text{SiC}_4 \rightarrow \text{L} + \text{C}$.

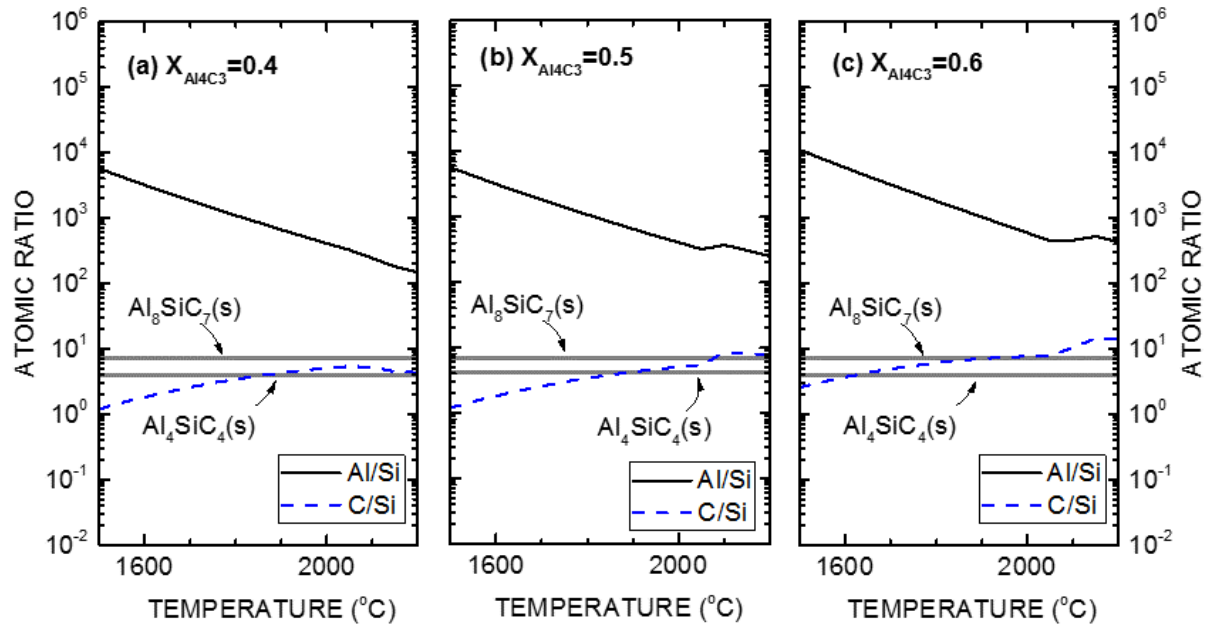


Figure 3.18: The atomic ratios C/Si and Al/Si in the vapor phase as a function of temperature for different starting composition (a) $X_{\text{Al}_4\text{C}_3}=0.4$; (b) $X_{\text{Al}_4\text{C}_3}=0.5$; (c) $X_{\text{Al}_4\text{C}_3}=0.6$. Gray lines represent the stoichiometry of the two solid compounds Al_4SiC_4 and Al_8SiC_7 .

In order to describe the gas phase stoichiometry, the atomic ratios C/Si and Al/Si in the vapor phase composition are plotted as function of temperature for different initial compositions. As illustrated in the Figure 3.18, two gray lines are added which marks the stoichiometry (C/Si) of the two solid compounds Al_4SiC_4 and Al_8SiC_7 . These two ternary carbides have atomic ratios of $\text{Al/Si}=\text{C/Si}=4$ for Al_4SiC_4 , and $\text{Al/Si}=8$, $\text{C/Si}=7$ for Al_8SiC_7 . With the strong evaporation of Al vapor species, a very strong deviation from the solid phase stoichiometry is figured out. Indeed, when the temperature increases, the Al/Si ratio decreases while the C/Si ratio increases. The Al/Si ratio is much higher than the stoichiometry of solid phase at any temperature. It is rather different for the C/Si ratio which matches the solid phase stoichiometry for specific temperatures. For instance, for the initial composition rich in SiC ($X_{\text{Al}_4\text{C}_3} = 0.4$), C/Si ratio is always smaller than the stoichiometry of Al_8SiC_7 . For the starting equimolar composition ($X_{\text{Al}_4\text{C}_3} = 0.5$), the vapor phase shows the same C/Si ratio as Al_4SiC_4 and Al_8SiC_7 at about 1880°C and 2080°C respectively. For the initial composition rich in Al_4C_3 ($X_{\text{Al}_4\text{C}_3} = 0.6$), beside of a higher Al/Si ratio, the vapor phase is characterized by a higher C/Si

ratio which matches with stoichiometry of Al_4SiC_4 and Al_8SiC_7 at about 1630°C and 1890°C , respectively. For that reason, even with a high predominance of Al in the vapor phase, the condensation of Al_4SiC_4 and Al_8SiC_7 are expected with some specific constraints.

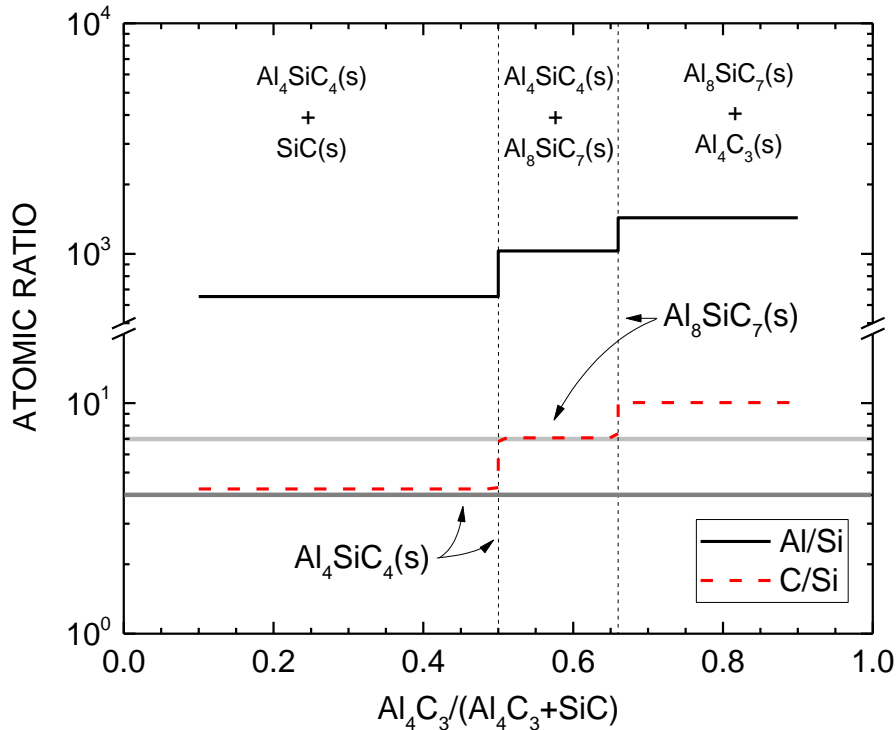


Figure 3.19: Al/Si and C/Si atomic ratios in the gas phase as a function of $X_{\text{Al}_4\text{C}_3}$ in the starting materials. Baking temperature was set at 1900°C . The equilibrium state of the mixture corresponding to the phase diagram are also indicated.

Based on that observation, the behavior of the vapor phase composition as a function of the initial composition of the source materials is also interesting. The description of the gas phase composition as a function of $X_{\text{Al}_4\text{C}_3}$ molar ratio is given in Figure 3.19, for a temperature fixed at 1900°C . Obviously, the apparent activity of Si in the gas phase decreases from the one in equilibrium with pure SiC(s) to zero, while shifting the composition from pure SiC(s) to pure $\text{Al}_4\text{C}_3\text{(s)}$ along the pseudo-binary section. Conversely, the apparent activity of Al increases from zero for pure SiC(s) to the equilibrium one for pure $\text{Al}_4\text{C}_3\text{(s)}$.

- For $X_{\text{Al}_4\text{C}_3} < 0.5$, the equilibrium state belongs to the $\text{Al}_4\text{SiC}_4\text{-SiC}$ two phase equilibrium. For a fixed total pressure, the variance of the system is $F = 4 - P = 1$. Then fixing the temperature totally determine the gas phase composition and is independent on the source composition.

- For the equimolar fraction $X_{\text{Al}_4\text{C}_3} = 0.5$, only Al_4SiC_4 phase is in equilibrium with the vapor. Since the system has one phase less, the variance increases by one ($F=2$). Thus, the stoichiometry of the gas phase is varying.

Indeed, the Al/Si and C/Si ratios increase with the molar fraction of Al_4C_3 . At any composition of the raw materials in the pseudo-binary section, the vapor phase is characterized by a strong excess of Al. However, the C/Si in the gas phase is almost matching the one of Al_4SiC_4 for an initial mole fraction < 0.5 and the one of Al_8SiC_7 for an initial mole fraction comprised between 0.5 and 0.66. For that reason, we speculate that these two initial compositions could be suited for the condensation of Al_4SiC_4 and Al_8SiC_7 , respectively.

The effect of total pressure on the vaporization of the mixture is also considered. The equilibrium calculation had been conducted with different starting amount of argon. As an inert gas, the argon does not contribute to the reaction thus the equilibrium pressure of the vapor species and the equilibrium calculation results are thermodynamically unchanged with the varying amount of argon. However, the total pressure has a significant impact on the mass transport from the powder source to the crystallization zone and can strongly affect the growth rate. This will be discussed in the experimental section.

3.3.2.2. The condensation at seed

Mole fraction $X_{\text{Al}_4\text{C}_3} < 0.5$. From those results, the initial mixture composition rich of SiC ($X_{\text{Al}_4\text{C}_3} < 0.5$) have been chosen for the Al_4SiC_4 synthesis because of the fit between vapor phase composition and the stoichiometry of material. In order to simulate the nature of the solid phase condensing at the crystallization area (cold point), the gaseous species vaporized from the powder have been injected as input condition for the equilibrium calculation. Obviously, as reaction kinetics and mass transport are not considered, the results presented here are only of a qualitative nature.

From the equilibrium gas phase composition calculated at 2000°C for the starting mole fraction $X_{\text{Al}_4\text{C}_3} = 0.4$, we computed the net amounts of solid compounds formed (Figure 3.20(a)) as a function of ΔT which is defined by $T_{\text{SOURCE}} - T_{\text{SEED}}$. The corresponding gas phase composition (Al/Si and C/Si) present in the crystallization zone is also plotted in Figure 3.20(b). Starting from the same temperature of the source, or differently said, the same flux of species vaporized from the source, we can identify different compounds condensing at the crystallization area, depending on the temperature difference. Indeed, Al_4SiC_4 condenses for small temperature differences (ΔT), typically smaller than 40°C . Between 40 and 80°C ,

Al_8SiC_7 dominates. Note that at $40 \pm 10^\circ\text{C}$, the crystallization conditions are characterized by the coexistence of the two ternary carbides. Then, for ΔT higher than 80°C , Al_4C_3 alone condenses.

Furthermore, the composition of the gas phase directly correlates with the different condensed solid compounds. The crystallization of Al_4SiC_4 requires a C/Si ratio close to the one in the solid and the minimum of Al/Si as well as Al/C; such conditions are found at low temperature gradient. Then by increasing the temperature gradient, Al/Si, and C/Si in the gas phase increase. It is thus not surprising that the ternary compound with higher Al_4C_3 content condenses. Finally, when the Al/Si and C/Si get too high, the silicon content of the gas phase becomes negligible and only Al_4C_3 is formed. However, due to the increase of Al/C ratio with the temperature difference, the amount of the Al_4C_3 decreases when the temperature difference increases. When the Al content of the gas phase gets too high, the equilibrium state belongs to the liquid phase instead of Al_4C_3 phase. The liquid phase is then mostly composed of Al (>90at.%) with small quantities of Si and C.

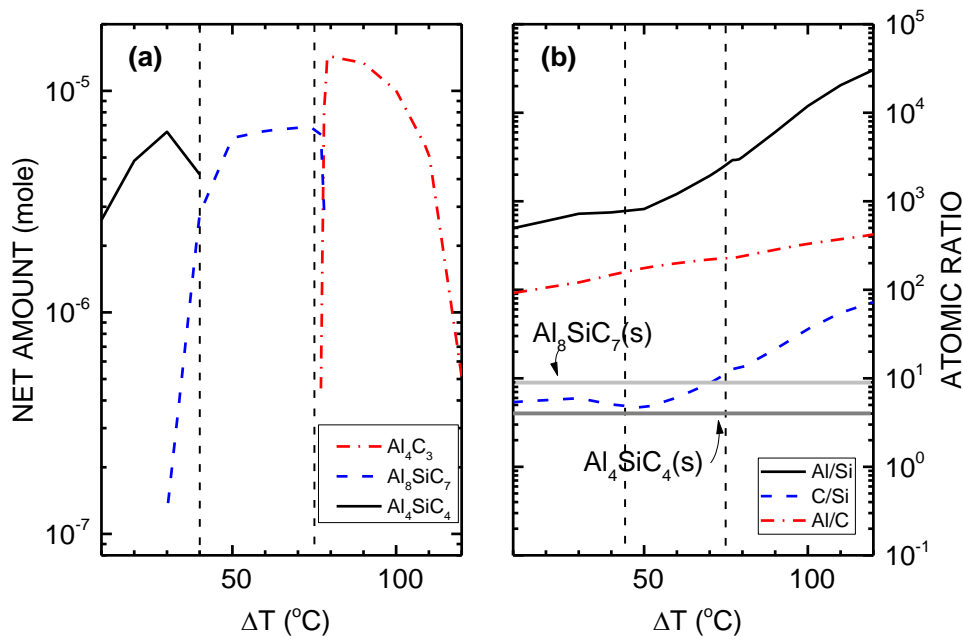


Figure 3.20: (a) The net amounts of solid compounds formed as a function of ΔT . (b) Corresponding gas phase composition in the crystallization zone (seed). The gas phase composition at the vaporization zone (source) has been calculated at 2000°C for an initial source composition $X_{\text{Al}_4\text{C}_3}=0.4$. ΔT is defined by $T_{\text{SOURCE}}-T_{\text{SEED}}$. Vertical dotted lines have been added as a guide for separating the different deposition conditions.

Using the same procedure as the one used in Figure 3.20(a), it is possible to predict the nature of the solid phase as a function of both T_{SOURCE} and T_{SEED} . A phase diagram can thus be drawn for the initial composition $X_{\text{Al}_4\text{C}_3} < 0.5$, as illustrated in Figure 3.21.

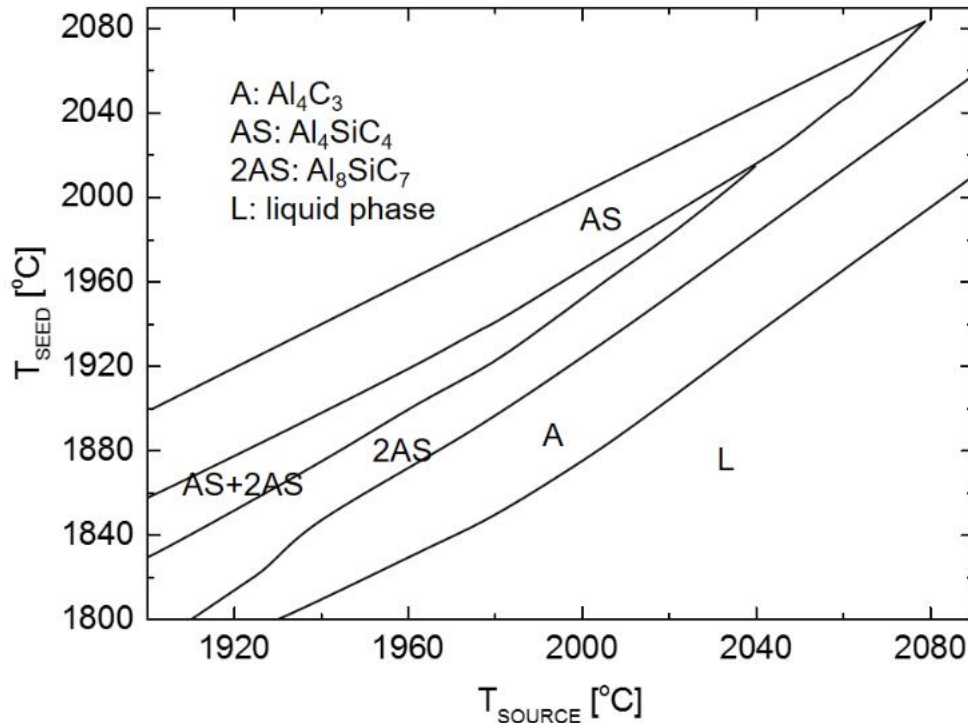


Figure 3.21: Diagram of the solid phases condensed from the vapor phase at equilibrium as a function of the temperatures of the seed and the source, for an initial composition $X_{\text{Al}_4\text{C}_3} < 0.5$. The diagram was calculated with a powder temperature higher than 1900°C .

A comparison between calculations performed in homogeneous phase (without any solid allowed to be formed) and in heterogeneous phase gives a good estimate of the main gaseous species which contribute to the deposit. The net contribution represented in Figure 3.22(a) is defined as the difference between the partial pressure of the different species calculated in homogeneous phase and the ones in heterogeneous phase. In order to weight the contribution of each gaseous components, we plotted in Figure 3.22(b) the relative contribution, defined as the ratio of the net contribution and the partial pressure from heterogeneous phase calculation. At low ΔT , condition under which the crystallization of Al_4SiC_4 occurs, $\text{Al}_2\text{C}_2(\text{g})$ makes the highest contribution to Al and C. On the other hand, atomic $\text{Si}(\text{g})$ is the most contributing specie to Si condensation. Obviously, the contribution of these species increases with the temperature gradient. A very simple reaction can thus be drawn for the condensation of Al_4SiC_4 from the vapor phase:



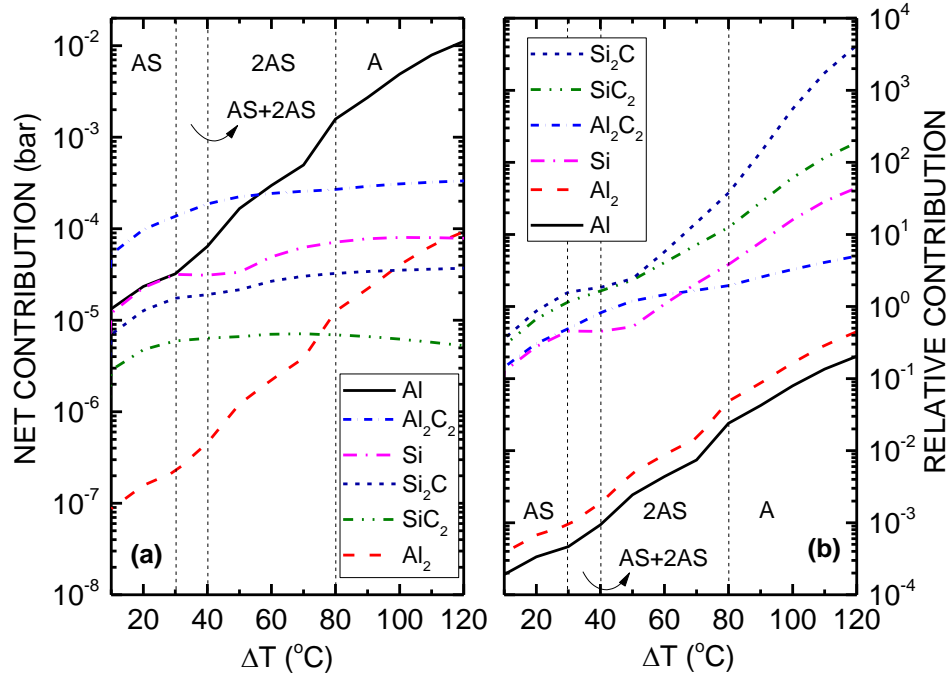


Figure 3.22: (a) Net contribution of the main vapor species (vaporized at 2000°C with pressure near 300 mbar) to the deposit as a function of the temperature gradient. (b) Relative contribution of the same species, defined by the ratio between the net contribution and the equilibrium partial pressure of the species, calculated in the heterogeneous case. Three condensed-phase zones are consecutively identified such as Al_4SiC_4 (AS), Al_8SiC_7 (2AS) and Al_4C_3 (A) by increasing the temperature gradient.

For a ΔT higher than 40°C, the net contribution of $Al_2C_2(g)$ and $Si(g)$ is quite stable. However, the contribution of monoatomic and polyatomic Aluminum molecules such as $Al(g)$ and $Al_2(g)$ increases strongly with temperature gradient, leading to an Al enrichment of the solid phase. Concerning the relative contribution, $Al_2C_2(g)$ and $Si(g)$ are by far the most contributing species, about a few orders of magnitude higher than $Al(g)$ and $Al_2(g)$. This also means that $Al_2C_2(g)$ and $Si(g)$ are the “thermodynamically limiting” species for the condensation over all the conditions studied.

Mole fraction: $0.5 < X_{Al_4C_3} < 0.63$. For $X_{Al_4C_3} = 0.6$, the equilibrium state of the source belongs to the Al_4SiC_4 - Al_8SiC_7 two phases domain which causes an increase of evaporation of Al and C vapor species. The net amount of the condensed solid phases are plotted as function of temperature gradient ΔT in Figure 3.23(a) for a source temperature of 2000°C. For a small temperature gradient, typically smaller than 65°C, Al_8SiC_7 is the only condensed phase. For ΔT higher than 65°C, Al_4C_3 dominates.

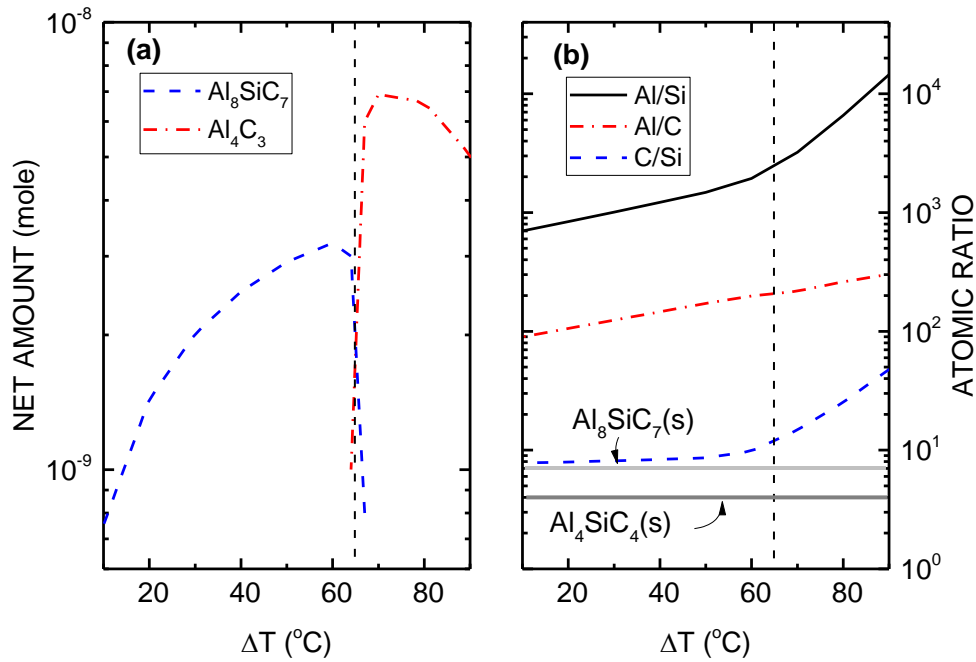


Figure 3.23: (a) The net amounts of solid compounds formed as a function of ΔT . (b) Corresponding gas phase composition in the crystallization zone (seed). The gas phase composition at the vaporization zone (source) has been calculated at 2000°C for an initial source composition $X_{\text{Al}_4\text{C}_3}=0.6$. Vertical dotted lines have been added as a guide for separating the different deposition conditions.

The corresponding gas phase composition (Al/Si, Al/C and C/Si) in the crystallization zone are also plotted in Figure 3.23(b). They all increase with the temperature gradient. As expected, the Al/Si and Al/C ratio are much higher than the stoichiometry of Al_8SiC_7 at any temperature difference. However, the C/Si is quite stable and close to the one of Al_8SiC_7 for the ΔT smaller than 65°C . For the ΔT higher than 65°C , due to the dramatically increase of Al/Si and C/Si, Al_4C_3 condenses.

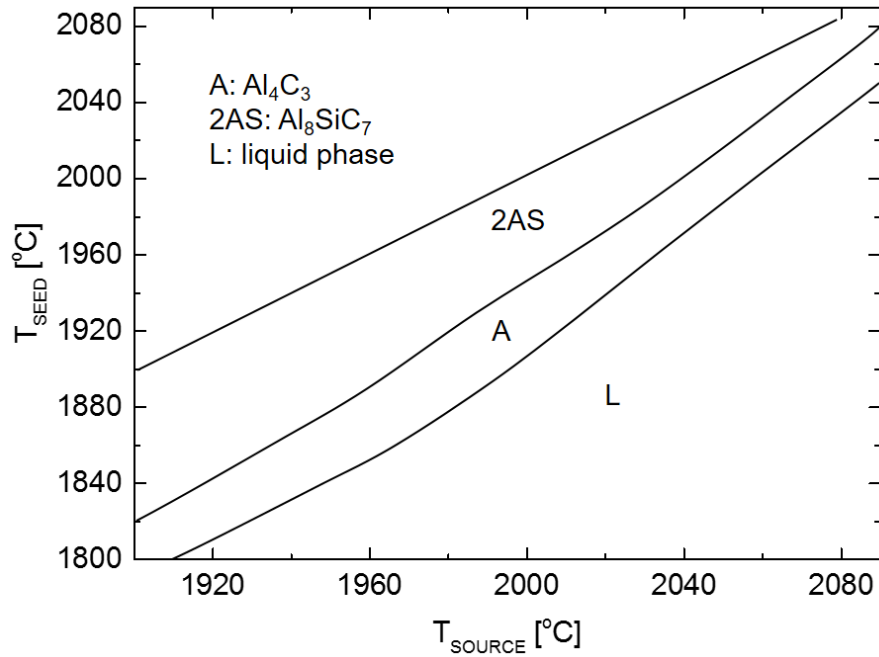


Figure 3.24: Diagram of the solid phases condensed from the vapor phase at equilibrium as a function of the temperatures of the seed and the source, for an initial composition $0.5 < X_{Al_4C_3} < 0.63$. The diagram was calculated with a powder temperature higher than 1900°C .

Similarly, a condensed phase diagram has been drawn as a function of both T_{SOURCE} and T_{SEED} in Figure 3.24 which specifies the suitable conditions for the condensation of Al_8SiC_7 and Al_4C_3 phases.

Mole fraction $X_{Al_4C_3} > 0.63$. For $X_{Al_4C_3} = 0.8$, the equilibrium state of the source belongs to the Al_4C_3 - Al_8SiC_7 two phases domain. The Al/Si and C/Si ratios in the vapor phase have their maximum value in the pseudo-binary section. It is not surprising that the deposit formed with a gas phase vaporized from a source placed at 2000°C contained Al-rich and C-rich compounds (Figure 3.25). For a ΔT smaller than 40°C , the deposit is dominated by Al_4C_3 . Al_8SiC_7 also forms in the crystallization zone, but with one order of magnitude lower amount than Al_4C_3 . For the ΔT higher than 40°C , due to the increase of the Al/Si and C/Si with temperature difference, only Al_4C_3 phase condenses. Similarly to the previous case, a phase diagram of the condensed phase is drawn as function of temperature difference (Figure 3.26). Only powder temperatures higher than 1900°C have been investigated.

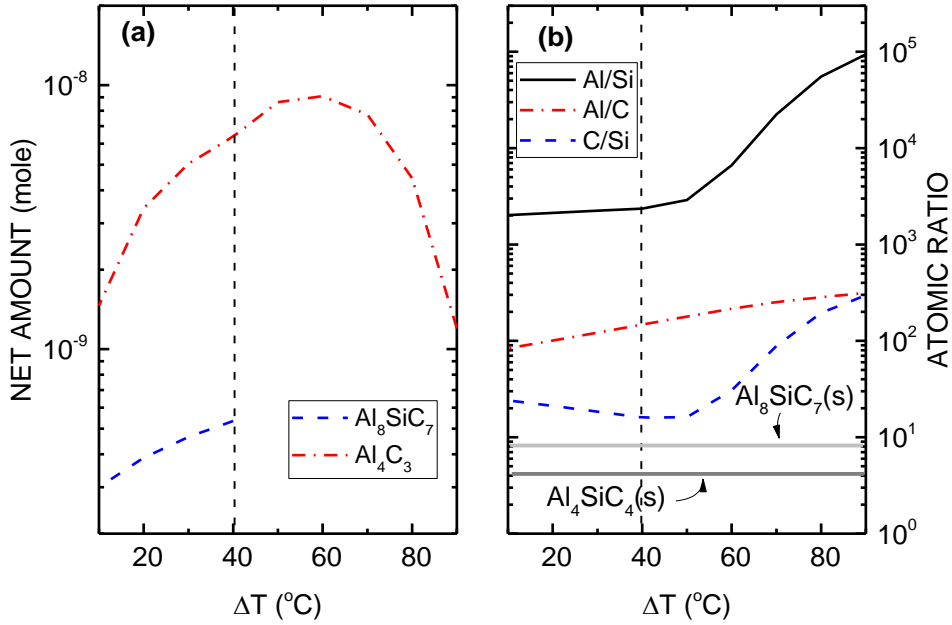


Figure 3.25: (a) The net amounts of solid compounds formed as a function of ΔT . (b) Corresponding gas phase composition in the crystallization zone (seed). The gas phase composition at the vaporization zone (source) has been calculated at 2000°C for an initial source composition $X_{\text{Al}_4\text{C}_3}=0.8$. Vertical dotted lines have been added as a guide for separating the different deposition conditions.

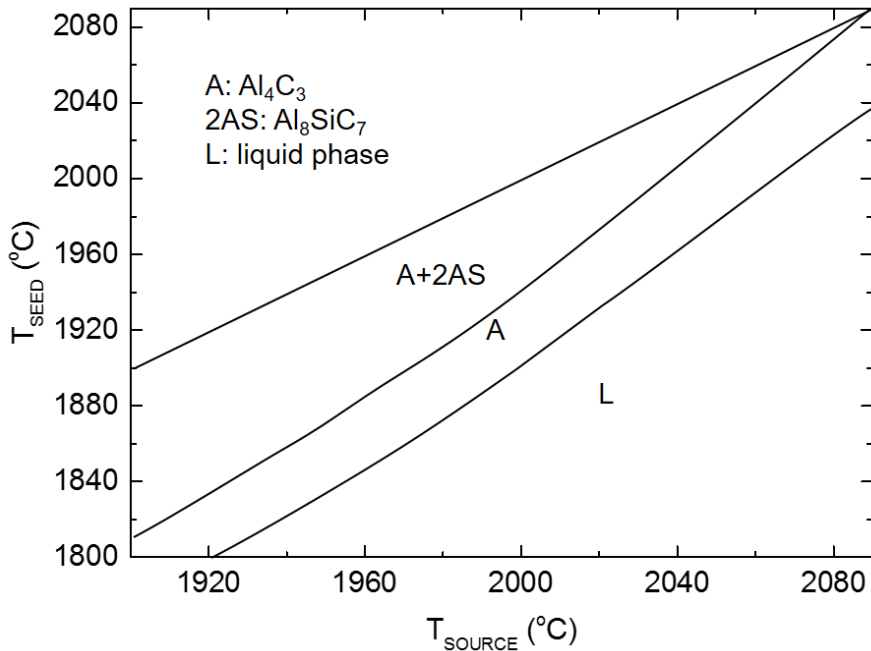
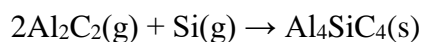


Figure 3.26: Diagram of the solid phases condensed from the vapor phase at equilibrium as a function of the temperatures of the seed and the source, for an initial composition $X_{\text{Al}_4\text{C}_3}>0.63$. The diagram was calculated with a powder temperature higher than 1900°C.

CONCLUSIONS OF THE CHAPTER

The thermal analysis results carried out by our homemade DTA system have a good agreement with current knowledge of the thermodynamic of the Al_4C_3 -SiC system. It shows first that the experiments conducted in our experimental setup match well with the published data. This is not so often the case for such high temperature studies as most of the measurements and reported data are strongly related to the way they have been measured. Differently said, they are “apparatus-dependent”. Taking this statement on the opposite way, we can also say that our high temperature set-up is well calibrated, the small deviation from the reported data being within the precision of the used optical pyrometer. This quick validation of both phase diagram description and our experimental set-up was very encouraging for the strategy followed in the present work.

After that, a classic thermodynamic analysis has been performed to describe the vaporization and condensation phenomena in the system. As expected, the vaporization of the system exhibits a strongly predominant of Al vapor. Furthermore, $\text{Al}(\text{g})$, $\text{Al}_2(\text{g})$, $\text{Al}_2\text{C}_2(\text{g})$, $\text{Si}(\text{g})$, $\text{SiC}_2(\text{g})$, $\text{Si}_2\text{C}(\text{g})$ are determined as the main vapor species to describe the vaporization of the system. The condensed phase diagrams at equilibrium are established for different initial composition of the source materials ($X_{\text{Al}_4\text{C}_3} < 0.5$ and > 0.5). They allowed to describe the suitable conditions for condensing the different aluminum-silicon ternary carbides. More specifically, Al_4SiC_4 alone could be thermodynamically synthesized following two main constraints: i) a SiC-rich initial composition ($X_{\text{Al}_4\text{C}_3} < 0.5$) and ii) a temperature difference smaller than 40°C . Moreover, the most contributing species to the formation of Al_4SiC_4 are identified as $\text{Al}_2\text{C}_2(\text{g})$ and $\text{Si}(\text{g})$, suggesting the following reaction as the “thermodynamically limiting” one:



Besides of that, the condensation of Al_8SiC_7 requires an Al_4C_3 rich source material. For instance, with $X_{\text{Al}_4\text{C}_3} = 0.6$, single phase Al_8SiC_7 could be thermodynamically synthesized with the temperature difference less than 65°C between the vaporization and condensation zones.

Based on this thermodynamic analysis, the experimental implementation of the synthesis of a single phase Al_4SiC_4 will be carried out and detailed in the next chapter.

REFERENCE

1. J. L. Murray and A. J. McAlister, *The Al-Si (Aluminum-Silicon) system*, Bulletin of Alloy Phase Diagrams **5** (1), 74 (1984).
2. R. Scace and G. Slack, *Solubility of carbon in silicon and germanium*, The journal of chemical physics **30** (6), 1551-1555 (1959).
3. R. Glass, D. Henshall, V. Tsvetkov and C. Carter, *SiC-seeded crystal growth*, MRS Bulletin **22** (03), 30-35 (1997).
4. A. Pisch, A. M. Ferrara, C. Chatillon, E. Blanquet, M. Pons, C. Bernard, M. Anikin and R. Madar, *Evaporation behavior of SiC powder for single crystal growth-An experimental study on thermodynamics and kinetics*, presented at the Materials Science Forum, 2000, Vol. 338, pp. 91-94.
5. P. Rocabois, C. Chatillon, C. Bernard and F. Genet, *Thermodynamics of the Si-C system II. Mass spectrometric determination of the enthalpies of formation of molecules in the gaseous phase*, High Temperatures. High Pressures **27** (1), 25-39 (1995).
6. L. L. Oden and R. A. McCune, *Phase equilibria in the Al-Si-C system*, Metallurgical Transactions A **18** (12), 2005-2014 (1987).
7. E. Plante and C. Schreyer, *DISSOCIATION PRESSURE OF ALUMINUM CARBIDE USING A ROTATING KNUNDSSEN CELL*, NBS J RES PHYS CHEM **70** (3), 253-257 (1966).
8. G. H. Rinehart and R. G. Behrens, *Vaporization thermodynamics of aluminum carbide*, The Journal of Chemical Thermodynamics **12** (3), 205-215 (1980).
9. C. Qiu and R. Metselaar, *Solubility of carbon in liquid Al and stability of Al₄C₃*, Journal of alloys and compounds **216** (1), 55-60 (1994).
10. B. L. Kidwell, L. L. Oden and R. A. McCune, *2Al₄C₃SiC: a new intermediate phase in the Al-Si-C system*, Journal of Applied Crystallography **17** (6), 481-482 (1984).
11. J. Viala, P. Fortier and J. Bouix, *Stable and metastable phase equilibria in the chemical interaction between aluminium and silicon carbide*, Journal of Materials Science **25** (3), 1842-1850 (1990).
12. Z. Inoue, Y. Inomata, H. Tanaka and H. Kawabata, *X-ray crystallographic data on aluminum silicon carbide, α -Al₄SiC₄ and Al₄Si₂C₅*, Journal of Materials Science **15** (3), 575-580 (1980).
13. J. Gröbner, H. L. Lukas and F. Aldinger, *Thermodynamic calculation of the ternary system Al-Si-C*, Calphad **20** (2), 247-254 (1996).

14. D. Zevgitis, O. Chaix-Pluchery, B. Doisneau, M. Modreanu, J. La Manna, E. Sarigiannidou and D. Chaussende, *Synthesis and Characterization of Al₄SiC₄: A “New” Wide Band Gap Semiconductor Material*, presented at the Materials Science Forum, 2015, Vol. 821, pp. 974-977.
15. J. Schoennahl, B. Willer and M. Daire, *Le carbure mixte Al₄SiC₄: Préparation et données structurales*, *Journal of Solid State Chemistry* **52** (2), 163-173 (1984).

CHAPTER IV

Al_4SiC_4 SYNTHESIS AND SUBLIMATION GROWTH

In chapter III, the thermodynamic study of the Al-Si-C system has been presented, with a special focus on the vapor phase description. More specifically, the possibility to obtain the ternary carbides, such as Al_4SiC_4 , through a vaporization/condensation process in the Al_4C_3 -SiC pseudo-binary system has been theoretically investigated. From an experiment point of view, two different approaches are presented in this chapter IV. First, a pressureless sintering process is proposed in order to investigate the reaction between Al_4C_3 and SiC in the powder. The aim is to track the powder behavior while annealed at high temperature. The second purpose is to answer the question: is it possible to get a pure Al_4SiC_4 , single phase from solid state reactions? Second, an actual sublimation growth process is attempted for obtaining Al_4SiC_4 crystals. For an accurate control of the experiments, the temperature distribution within the reactor has been assessed by numerical simulation, using the finite element method, and is presented in the first part of this chapter. The most important experimental results will be presented and discussed with respect to the thermochemistry of the system presented in chapter III. Finally, some characterizations have been conducted on the obtained heterostructures in order to investigate the dependence of morphology, growth mechanism and texture quality of Al_4SiC_4 deposit on different SiC substrates. Afterwards, the optical absorption properties of obtained Al_4SiC_4 crystalline layer will close this chapter.

4.1. Simulation of temperature distribution

In order to estimate the inner temperature distribution of the reactor, numerical simulations of induction heating coupled with heat transfers have been performed using the Finite Element Method (FEM) software - COMSOL Multiphysics based on the model developed for SiC sublimation growth¹. We will not detail the models as there is no specific development conducted for the current work. Only slight modifications of the inner geometry have been performed. So we suggest the reader to refer to K.Ariyawong's PhD thesis for a full description of the simulation tool, the implementation and coupling of the different models. Here we only focus on selected features which are important for the present study. All the simulations have been conducted in a 2D axisymmetric geometry.

4.1.1. Effect of induction frequency

The reason why the effect of induction frequency has been assessed is for a trivial technical reason. As a matter of fact, we had to change the induction generator during the PhD progress. The first induction furnace was set to a high operating frequency, about 100kHz. Such conditions have been applied to the sintering experiments. Then a second induction generator has been implemented for all the sublimation growth experiments. In this case, the operating frequency was much lower, around 15kHz. It was thus important to check the temperature distribution in the crucible, while the frequency was shifted from 100kHz to 15kHz.

In principle, the Foucault currents induced by the alternating current AC in the induction coil, directly dissipate as Joule effect at the external periphery of the susceptor (i.e. the furnace). Then, all the inner parts of the crucible are mainly heated by the radiation from the furnace. Thus, the proportion of the heat due to the inductive losses and the radiation is dependent on the geometry and the electromagnetic skin depth (δ) which can be calculated from the expression (4.1), applicable in case of good conductor material ($\sigma \gg \omega\epsilon$)²:

$$\delta = \sqrt{\frac{2}{\sigma\omega\mu}} \sqrt{\sqrt{1 + \left(\frac{\omega\epsilon}{\sigma}\right)^2} + \frac{\omega\epsilon}{\sigma}} \approx \sqrt{\frac{2}{\sigma\omega\mu}} \quad (4.1)$$

Where ω is the angular frequency of the electromagnetic wave (s^{-1}), σ is the conductivity of the material ($S.m^{-1}$), ϵ is the dielectric permittivity ($F.m^{-1}$) and μ is the magnetic permeability ($H.m^{-1}$).

It can be seen that the skin depth is inversely proportional to the operating frequency. For instance, in our PVT reactor, when the generator is operated at 100 kHz, the penetration depth is around 5 mm. This value is smaller than the thickness of the graphite furnace (10 mm). Hence, almost all the resistive power losses (i.e. Joule losses) induced by the electromagnetic field dissipate into the outer 5mm of the furnace thickness as shown in the Figure 4.1(b). The inner crucible is then mainly heated by radiation. Otherwise, when the operating frequency is reduced to 15kHz, the penetration depth increases to 13mm, as shown in the Figure 4.1(a). The resistive power losses dissipate through the whole thickness of the susceptor walls, and even further, directly in the inner crucible. In another words, the induction heating enters deeper into the heart of the crucible when the frequency decreases. The effect is twofold: first it ensures a higher heating yield, reducing the external losses in the graphite insulation felts. Second, it spreads the heating source which allows a significant reduction of the radial temperature gradients.

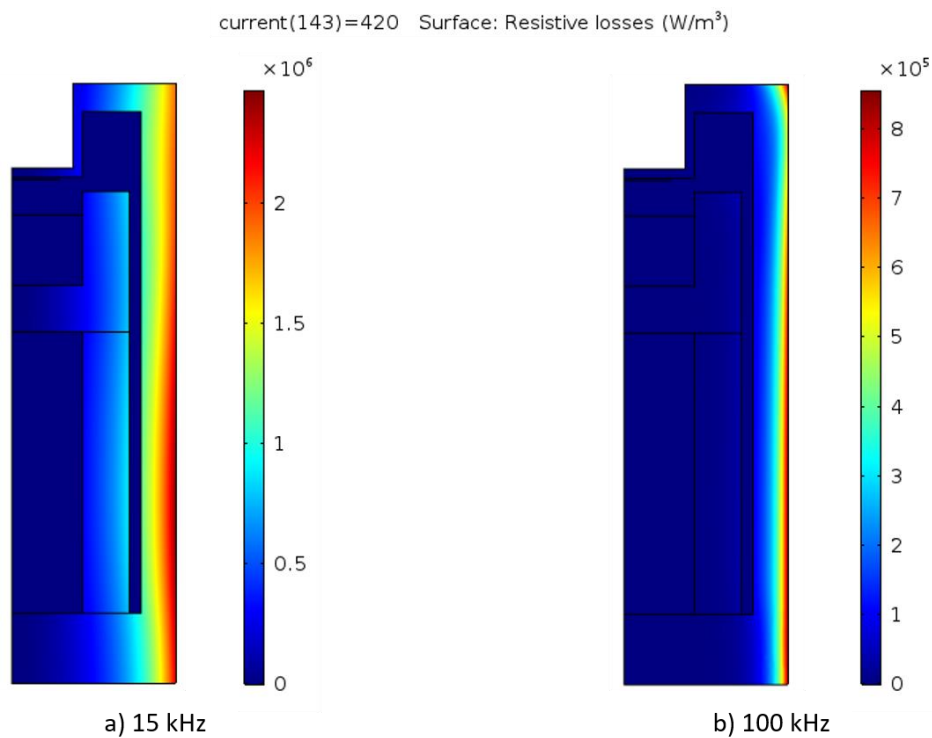


Figure 4.1: Resistive power losses dissipated in the crucible. Only half of the crucible is represented. Calculations have been performed with a two-dimensional axisymmetric geometry, with two different operation frequencies: a) 15 kHz; b) 100 kHz, and for electric current in the induction coil of 420 A.

4.1.2. Temperature distribution

The simulations are based on the assumption that the production and consumption of heat related to chemical reactions in the powder and in the gas mixture are neglected. The only heat source comes from the induction heating. It can be computed, per unit volume, as:

$$Q = \sigma \langle -\mathbf{E} \cdot \mathbf{J} \rangle = \frac{1}{2} \sigma \omega^2 (\mathbf{A} \cdot \mathbf{A}^*) \quad (4.2)$$

Where \mathbf{E} is the electric field, \mathbf{J} is the total current density, \mathbf{A} is the magnetic vector potential, σ is the electrical conductivity, and ω is the angular frequency of the magnetic field.

Heat transfer in the reactor is defined by the movement of energy according to the temperature difference. Three mechanisms of heat transfer take place in the PVT reactor: (i) conduction (mainly in the solid), (ii) convection between the solid and the ambient (here only gases) and (iii) radiation due to the emission of electromagnetic waves from hot solid surfaces.

We know from previous computations on similar systems that convection does not play a significant role on the global heat transfers. Then, at first approximation, the convective heat transfers are neglected in order to reduce the computational cost¹. Thus, we will only consider conduction and radiation. Among them, in the investigated high temperature range, radiation is by far the dominant contribution which controls the temperature distribution in the crucible.

Note that the external parts of the crucible (furnace, graphite insulation, etc.) are similar in any cases. Only the inner parts of the crucible are changed, geometrically adapted to the specific objective of the experiments. We have used two main inner geometries namely the “sublimation growth geometry” and the “sintering geometry”, which are detailed following.

Sublimation growth geometry. Figure 4.2 shows the schematic drawing of the crucible used for the Al_4SiC_4 sublimation growth process. The temperature at the back side of the seed is experimentally measured by an optical bi-chromatic pyrometer fixed on top of the reactor. The corresponding computed value is T_{PYRO} . These two values, measured and computed at the top of the crucible will be used to match computations on experimental conditions. The distance between the powder surface and seed is fixed at 5 mm in all experiments in order to get small temperature difference, as revealed by the thermodynamic calculations. In the figure, four different temperatures, taken along the symmetry axis will be used for the discussion. These temperatures, namely T_{PYRO} , T_{SEED} , $T_{\text{P_TOP}}$, $T_{\text{P_BOT}}$, have been obtained from the simulations. Note that with this geometry, a generator operating at 15kHz has been used.

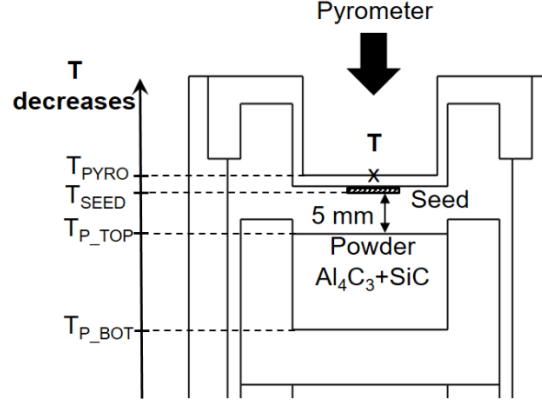


Figure 4.2: Schematic drawing of the crucible and cavity setup used for Al_4SiC_4 sublimation growth process. The distance between the powder surface and the seed is fixed at 5mm. Four different temperatures, T_{PYRO} , T_{SEED} , T_{P_TOP} , and T_{P_BOT} , taken along the symmetry axis from the simulations will be used for the discussions.

The calculations are performed in a two-dimensional axisymmetric geometry, with the physical model and boundary conditions implemented and optimized by K.Ariyawong¹. As an illustration, the distribution of temperature computed in the crucible for an electric current applied in the coil of 400A is depicted in Figure 4.3(a). The four specific temperature, as defined in Figure 4.2, are plotted as a function of the electric current through the induction coil (Figure 4.3(b)) for a reference position of the coil with respect to the crucible. We define two important temperature differences as follow:

$$\Delta T_1 = T_{P_TOP} - T_{SEED} \quad (4.3)$$

$$\Delta T_2 = T_{P_BOT} - T_{P_TOP} \quad (4.4)$$

Over the conditions investigated (T_{PYRO} varies from 1700 to 2100°C, pressure of 300 mbar), the difference between T_{PYRO} and T_{SEED} and the difference ΔT_1 are almost unchanged, about 5°C and 35°C, respectively. Otherwise, the difference ΔT_2 increases slightly as function of electric current. For $T_{PYRO} = 2000^\circ\text{C}$, ΔT_2 is typically of 65°C.

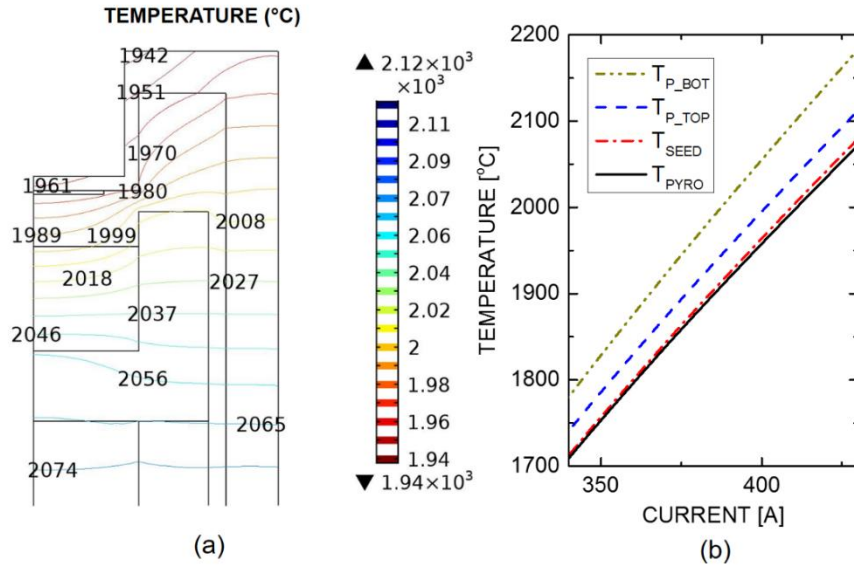


Figure 4.3: (a) Distribution of temperatures computed in the crucible (unit: °C) for an electric current applied in the coil of 400 A. (b) plot of the temperatures calculated at four different locations along the symmetry axis of the crucible, as defined in Figure 4.2, as a function of the applied current.

Sintering geometry. The schematic drawing of the crucible used for the Al_4SiC_4 sintering process is presented in Figure 4.4. Similarly, temperature gradients will be estimated by using a set of calculated temperatures as indicated in the figure: T_{PYRO} , T_{PE_TOP} , T_{PE_BOT} .

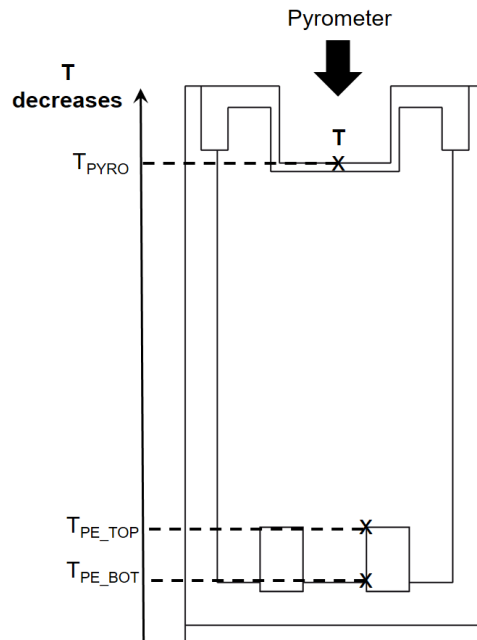


Figure 4.4: Schematic drawing of the crucible used for the sintering process. Three different points are used to estimate the temperature distribution and to track its evolution: T_{PYRO} , T_{P_TOP} , and T_{P_BOT} .

Note that for this geometry, a generator operating at 100 kHz has been used. The temperatures calculated at three main points are plotted as a function of the applied current in Figure 4.5(b). The two considered temperature differences are defined as follow:

$$\Delta T_{ME} = T_{PE_TOP} - T_{PYRO} \quad (4.5)$$

$$\Delta T_{PE} = T_{PE_BOT} - T_{PE_TOP} \quad (4.6)$$

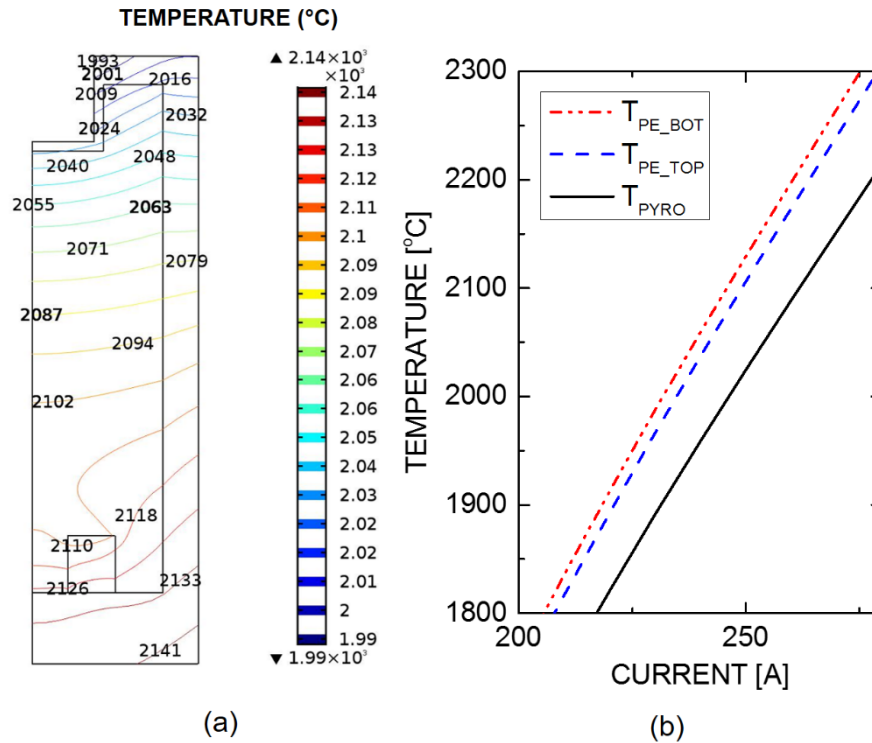


Figure 4.5: (a) Distribution of temperatures computed for an electric current of 250A, and represented in half of inner crucible (unit:°C). (b) Temperatures, calculated at three different locations defined in Figure 4.4, as a function of the applied current.

For T_{PYRO} varying from 1900 to 2100°C, the difference ΔT_{PE} is almost unchanged (about 20°C) while the difference ΔT_{ME} slightly varies from 77 to 84°C.

4.1.3. Effect of the coil position on sublimation growth

In fact, moving the coil vertically is the easiest way to change the axial temperature gradient. The effect of the induction coil position and the design of the heatsink on the temperature distribution had been thoroughly investigated in the literature³⁻⁵. Based on a similar approach, and fixing the crucible design, we controlled the axial temperature gradient ΔT_1 and ΔT_2 by simply moving up and down the induction coil. Figure 4.6 shows the effect of the coil position while keeping the same input power. As a general trend, the absolute temperature within the growth cell (i.e. powder space and seed substrate) increases while the induction coil is moved

up and decreases while the coil is moved down. It relates to the position of the “hot point” which is defined as the hottest point generated by the induction heating, and which is roughly at the center of the coil. At higher position of the coil, the hot point is moved closer to the reaction zone, leading to a higher absolute temperature.

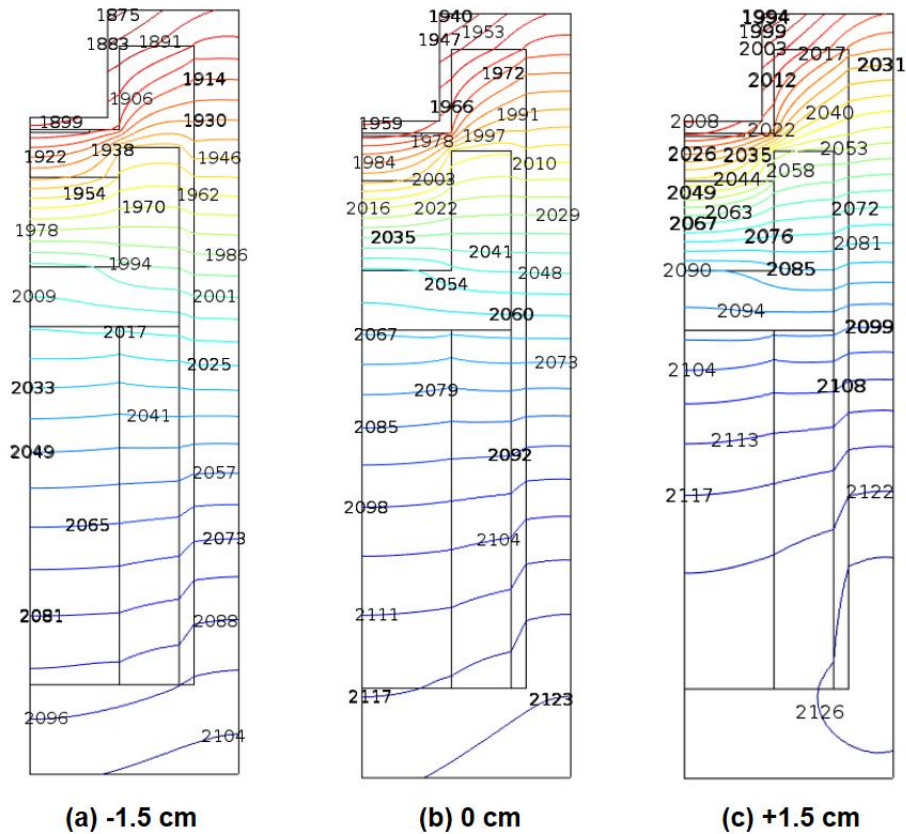


Figure 4.6: Isotherms distribution (color lines) in the crucible for the same input current of 400A and different coil positions (a) -1.5 cm; (b) 0 cm (reference position); (c) 1.5 cm.

However, if we fix the measured temperature (T_{PYRO}) at 2000°C, as presented in Figure 4.7, moving up the coil with respect to the reference position ($X=0$) leads to a decrease of the temperature gradients. Otherwise, by moving down the coil, the temperature gradients increase. The linear relation between the temperature gradient and the position of the induction coil is demonstrated.

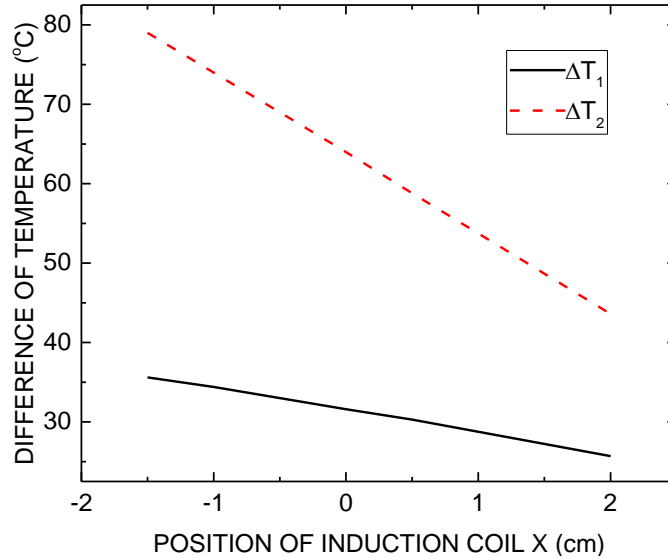


Figure 4.7: Computed axial temperature gradient as a function of the induction coil position with T_{PYRO} fixed at 2000°C . The coil was moved up and down with respect to the reference position ($X=0$).

4.2. Al_4SiC_4 synthesis

With the original goal of producing a pure, single phase Al_4SiC_4 source material, a pressureless sintering-like experiment process is implemented. The former idea came from the Al_4C_3 -SiC binary section of the phase diagram where Al_4SiC_4 should present a congruent melting. It was thus reasonable to think that if a pure Al_4SiC_4 source material could be obtained, a single crystal could be pulled from the stoichiometric melt. Differently said, “a simple” Czochralski process could be implemented. Thus, the solid state reaction between Al_4C_3 and SiC is investigated. Due to the higher vaporization rate of Al_4C_3 , this series of experiments have been conducted in the Al_4C_3 -rich condition ($X_{\text{Al}_4\text{C}_3} \geq 0.5$). Based on that, the mechanism and yield of the reaction will be discussed with respect to the thermochemistry of the Al_4C_3 -SiC system in such conditions.

4.2.1. Remarks about oxygen in system

Before the experiment, a XRD analysis of the raw materials has been carried out. As mentioned in the previous chapter, the raw Al_4C_3 powder is always oxidized, forming aluminum oxy carbides like Al_2OC and $\text{Al}_3\text{O}_{3.5}\text{C}_{0.5}$. According to the diffractogram presented in the Figure 4.8(b), the raw SiC powder does not contain any measurable amount of oxides. Either, the oxide is not crystalline, and thus does not shows diffraction peaks, or the oxide content is too small to be detected.

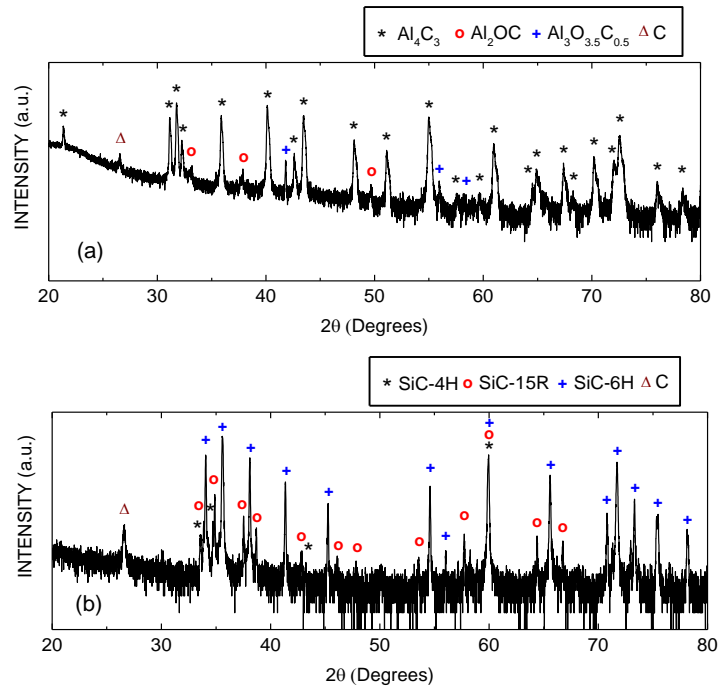


Figure 4.8: Diffractograms collected from the raw (a) Al_4C_3 powder and (b) SiC powder.

In fact, the problem of oxides in Al_4C_3 has been discussed for the DTA experiments in the previous chapter. Since the DTA was not perturbed from the second heating curve (section 3.2.3) and no oxides left after the sintering-like experiments, we can state that these oxides were totally decomposed upon heating up to the growth temperature. This is probably due to the strongly reducing environment of the experiments, all being contained in graphite pieces and graphite insulations.

The reduction process of the surface oxides obviously generate O-containing vapor species. A possible consequence of that could be the formation of parasitic phases during the early stages of the sublimation growth on a seed substrate. The occurrence of such an effect will be studied by high resolution transmission electron microscopy in the next chapter. Then, once the O-containing species have been evacuated, there is no longer any impact on the thermochemistry of the system during the growth.

4.2.2. Experimental process

In order to study the solid state reaction between Al_4C_3 and SiC, sintering experiments with pellets prepared from a mixture of powders, were conducted. The raw materials were composed of a mixture of high purity powders of Al_4C_3 (Alfa Aesar, 99+% purity, particles size $< 30\mu\text{m}$) and SiC (Sika tech E301, particle size $< 70\mu\text{m}$) with a molar ratio $X_{\text{Al}_4\text{C}_3}$ defined as $X_{\text{Al}_4\text{C}_3} = n\text{Al}_4\text{C}_3 / (n\text{Al}_4\text{C}_3 + n\text{SiC})$. Firstly, the powders were manually mixed with different

compositions. After that, the mixture was pressed under 4.8 bar to prepare cylindrical pellets with dimensions of 1cm × 1.2cm (diameter × height). Finally, they were placed in the graphite reactor, on cylindrical grooves (1cm × 0.2cm) which were used to fix the position of the pellets during the experiments. Four different pellets were used for each experiment, placed in symmetric positions. The four pellets of the same run were thus supposed to see exactly the same temperature profile and temperature distribution. The baking temperature varied from 1900 to 2100°C, with a gas pressure fixed at 800 mbar of argon. The baking time was set at 6 hours and the pellets were not pressed during the process. Note that before the experiments, Al₄C₃ was carefully stored in a desiccator to avoid any hydrolysis, well known for this carbide.

To prepare the experiments, the reactor was pumped out to achieve a vacuum of 10⁻³ mbar. At the beginning, the reactor was manually heated up with a constant power until a temperature higher than 1000°C, which is the lowest measurable value of the pyrometer, was reached. At that moment, 600 mbar of argon was introduced to limit the sublimation of the raw materials. After that, the heating rate was fixed at 12°C/min until the baking temperature. During baking, the pressure was adjusted at 800 mbar. At the end, the reactor was naturally cooled down by simply turning off the generator. The general process receipt is represented in Figure 4.9.

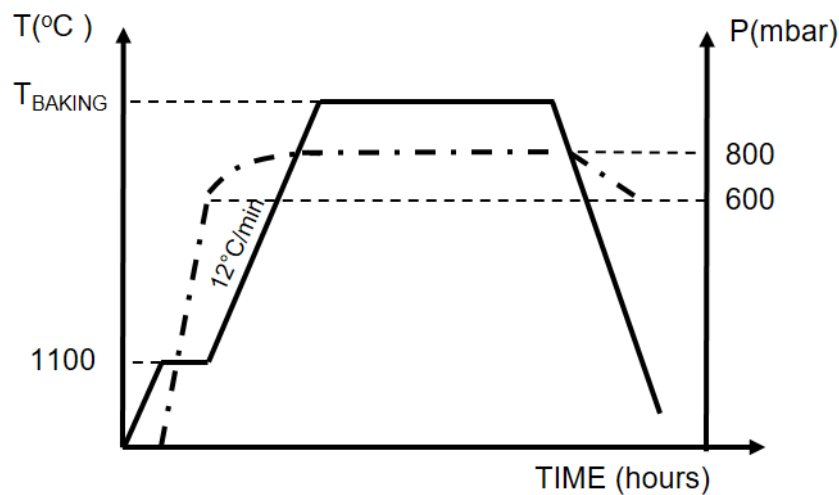


Figure 4.9: Process receipt implemented for the sintering experiments with pellets of powder. The variation of temperature (solid line) and pressure (dash line) along the different steps are represented.

4.2.3. Experimental results

Top views of the pellets after experiments at different baking temperatures are presented in Figure 4.10. Four pellets with different initial compositions have been used for each

experiment. The experimental conditions and the initial compositions of the pellets are listed in the Table 4.1. After experiments, first local identification of the phases on the surface of the pellets was conducted by Raman spectroscopy. After that, the pellets were grinded by ball milling and characterized by X-ray diffraction using the $\text{CuK}\alpha 1$ radiation in a Bragg-Brentano configuration. Refinements using the Rietveld treatment have been also carried out to analyze quantitatively the different phases. Qualitative and quantitative results are gathered in Table 4.1.

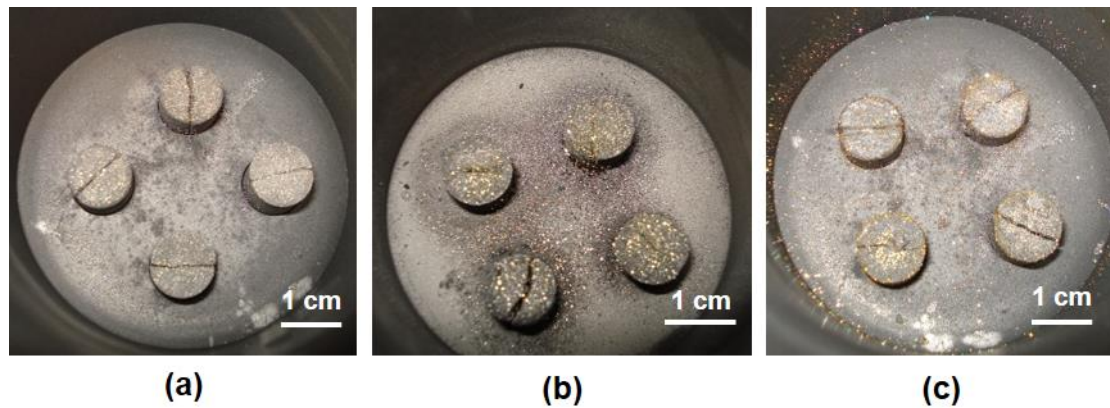


Figure 4.10: Top view of the pellets after experiments at different temperatures: (a) 1900°C; (b) 2000°C; (c) 2100°C.

For the first series, the pellets with the mole fraction $X_{\text{Al}_4\text{C}_3}$ varying from 0.5 to 0.8 were annealed at 1900°C during 6 hours. The diffractograms of the corresponding samples are presented in Figure 4.11. Al_4SiC_4 , Al_8SiC_7 , Al_4C_3 , SiC and C are observed in the samples. Some yellowish crystals formed on the top surface of the pellets. Raman spectra collected from a large number of those yellowish crystals revealed that two different compounds coexisted, as shown in Figure 4.12. The first spectrum corresponds to the Al_4SiC_4 crystals, whose spectrum was already identified by our group⁶. The second one was not identified in the literature yet. As mentioned in chapter III, the condensation of Al_8SiC_7 is thermodynamically possible for the mole fraction $X_{\text{Al}_4\text{C}_3} > 0.5$ applying a small temperature difference ($< 60^\circ\text{C}$). By correlation with the phases identified with XRD, and since the Raman spectra of other phases are already known, we speculate that spectrum 2 corresponds to Al_8SiC_7 . It also sounds reasonable since both spectra shows many similarities, which is not surprising considering the similarities of the crystalline structure of both carbides. Moreover, no other crystalline phases, such as oxides have been observed by XRD in the samples.

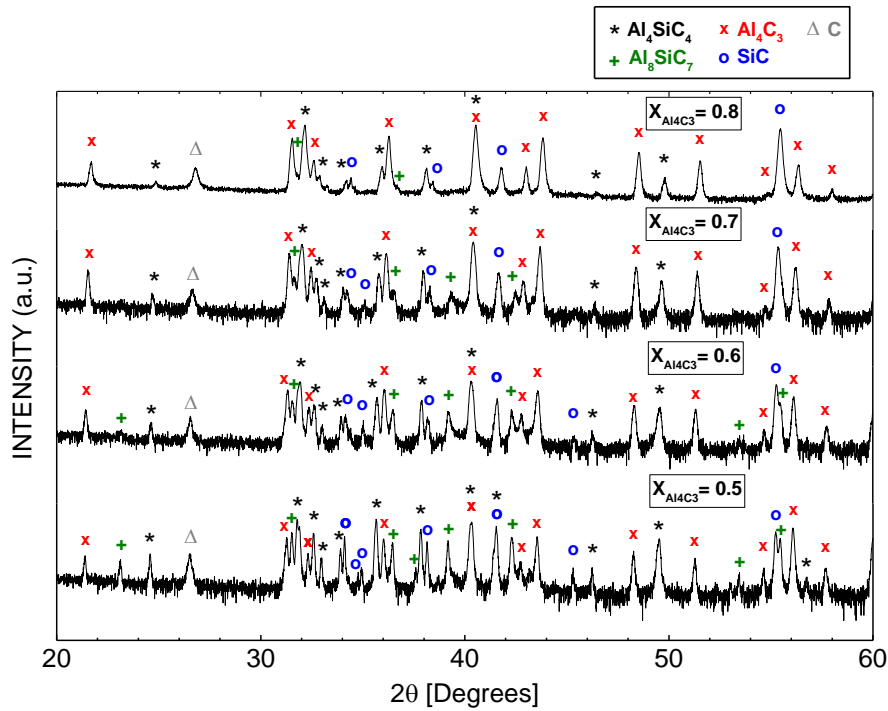


Figure 4.11: X-ray diffractograms collected from the pellets with different starting compositions after annealing 6 hours at 1900°C.

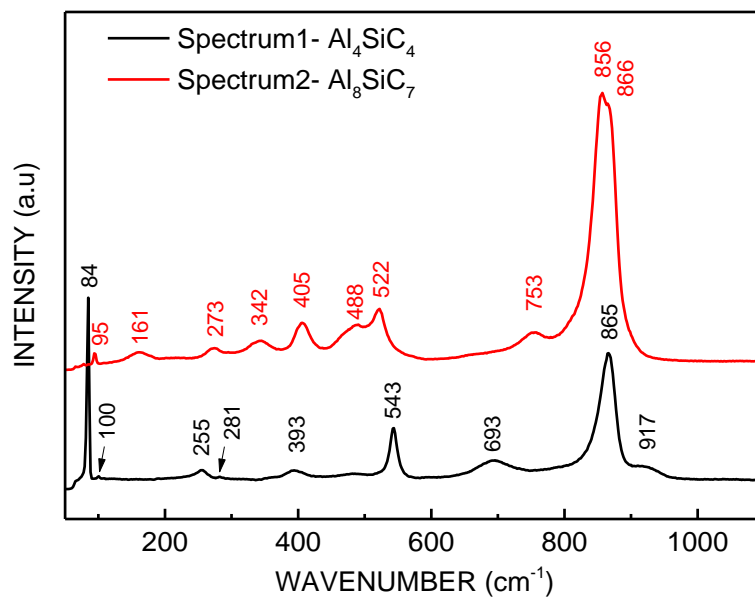


Figure 4.12: Raman spectra collected from the yellow crystals formed on the surface of the pellets after baking at 1900°C.

The second series of experiments were performed at 2000°C with the initial mole fraction $X_{\text{Al}_4\text{C}_3}$ varying from 0.5 to 0.7. At first glance, the pellets have a darker color and more Al_4SiC_4 crystals were observed on the top surface of the pellets after the baking. Concerning the phase

analysis, Al_4C_3 was not found in the samples. The X-Ray diffractograms presented in Figure 4.13 show the presence of Al_4SiC_4 , Al_8SiC_7 , SiC and C .

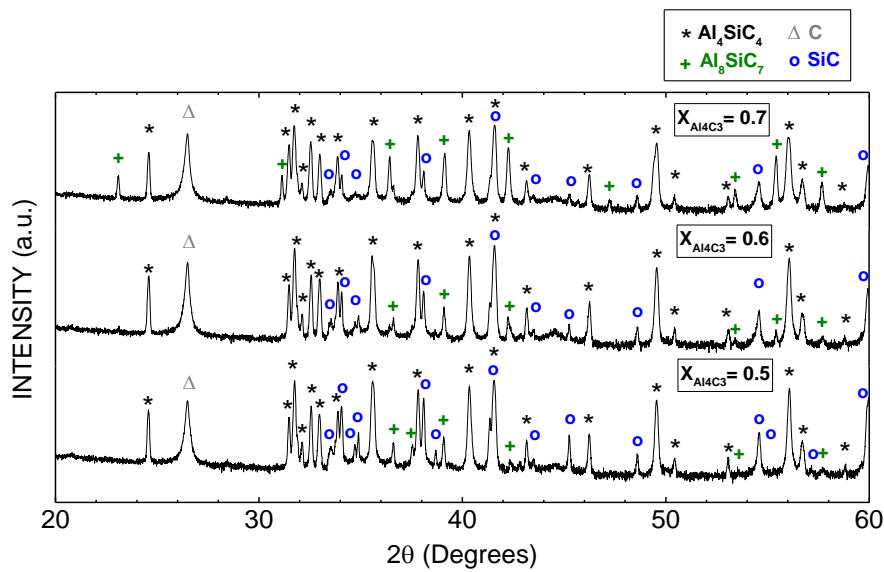


Figure 4.13: X-ray diffractograms collected from samples with different starting compositions, after annealing 6 hours at 2000°C .

For the final series of experiments, the heat treatment was conducted at 2100°C with initial compositions $X_{\text{Al}_4\text{C}_3}$ varying from 0.5 to 0.65. In this case, a large amount of Al_4SiC_4 formed on the surface of the pellets, and also deposited on the crucible walls. The compositions of Al_4SiC_4 , Al_8SiC_7 , SiC and C are extracted from the X-ray analyses, which are given in Figure 4.14.

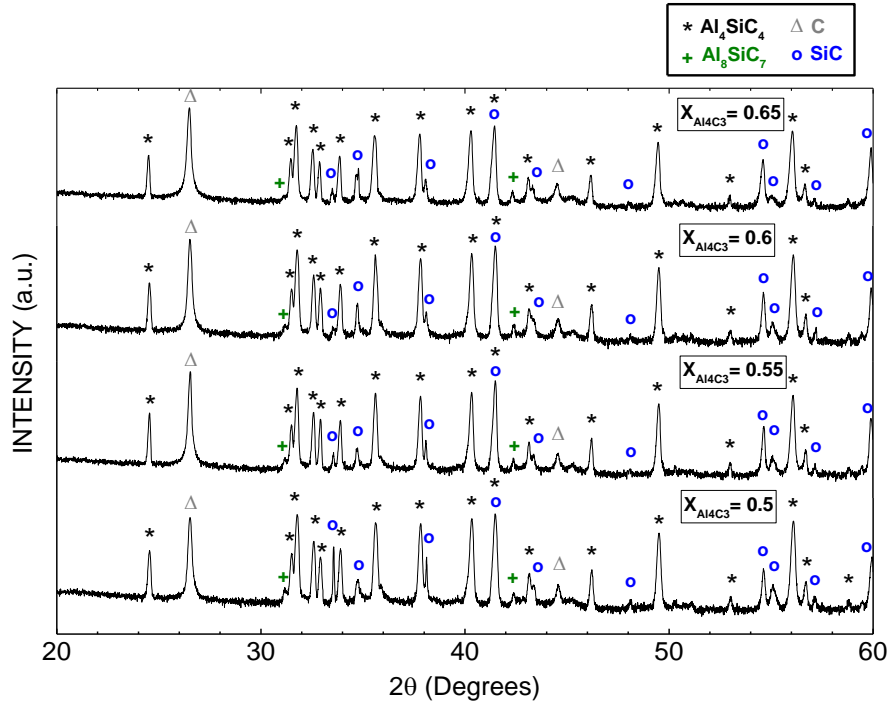


Figure 4.14: X-ray diffractograms collected from samples with different starting compositions, after annealing 6 hours at 2100°C.

Table 4.1: Mole fraction of each phases, obtained by XRD Rietveld analyses of the samples for different experimental conditions. The weighted profile R -factor (R_{wp}), which indicates the discrepancy between measured data and simulation results⁷, is also given.

Nb Exp	$X_{Al_4C_3}$	Temperature (°C)	Mole fraction					R_{wp} (%)
			Al_4SiC_4	Al_8SiC_7	Al_4C_3	SiC	C	
BILL07_01	0.5	1900	0.15	0.15	0.07	0.43	0.20	21.53
BILL07_02	0.6	1900	0.12	0.19	0.29	0.22	0.18	20.99
BILL07_03	0.7	1900	0.03	0.02	0.75	0.11	0.08	23.82
BILL07_04	0.8	1900	0.05	0.03	0.55	0.07	0.30	9.44
BILL09_02	0.5	2000	0.14	~ 0	0	0.58	0.28	20.88
BILL09_03	0.6	2000	0.16	~ 0	0	0.36	0.48	22.78
BILL09_04	0.7	2000	0.16	0.04	0	0.32	0.48	17.79
BILL08_01	0.5	2100	0.20	~ 0	0	0.21	0.59	13.60
BILL08_02	0.55	2100	0.12	~ 0	0	0.10	0.78	16.49
BILL08_03	0.6	2100	0.15	~ 0	0	0.15	0.70	13.95
BILL08_04	0.65	2100	0.10	~ 0	0	0.13	0.77	15.09

4.2.4. Discussion

In order to compare with the raw composition, the molar fraction of the three elements (Al, Si, C) have been extracted from the Rietveld analyses; they are presented in Table 4.2.

Table 4.2: Molar fraction of the three elements, extracted from the XRD Rietveld analyses of the samples for different experimental conditions.

Nb Exp	$X_{Al_4C_3}$	Temperature (°C)	Mole fraction initial			Mole fraction final		
			Al	Si	C	Al	Si	C
BILL07_01	0.5	1900	0.44	0.11	0.44	0.39	0.14	0.47
BILL07_02	0.6	1900	0.48	0.08	0.44	0.47	0.08	0.46
BILL07_03	0.7	1900	0.51	0.05	0.44	0.48	0.06	0.45
BILL07_04	0.8	1900	0.53	0.04	0.43	0.50	0.03	0.46
BILL09_02	0.5	2000	0.44	0.11	0.44	0.20	0.27	0.53
BILL09_03	0.6	2000	0.48	0.08	0.44	0.25	0.20	0.55
BILL09_04	0.7	2000	0.51	0.05	0.44	0.30	0.16	0.54
BILL08_01	0.5	2100	0.44	0.12	0.44	0.28	0.15	0.57
BILL08_02	0.55	2100	0.46	0.10	0.44	0.23	0.11	0.66
BILL08_03	0.6	2100	0.48	0.08	0.44	0.26	0.13	0.62
BILL08_04	0.65	2100	0.49	0.07	0.44	0.20	0.12	0.68

To get an easier visualization, we also plotted in Figure 4.15, the evolution of the global composition in the Gibbs triangle, as a function of both temperature and starting composition. The following features can be observed:

- Even if the initial compositions all lie in the Al_4C_3 -SiC pseudo-binary system, the final compositions are all shifted to the Al_4C_3 -SiC-C triangle.
- At 1900°C and 2000°C, the final elemental composition follows almost the same trend as the initial composition. For a given temperature, when $X_{Al_4C_3}$ increases, the global composition roughly exhibit an increase of the Al/Si ratio under the constant C content (moving parallel to the Al-Si side).
- At 2100°C, the final composition does not follow the initial one. There is also no monotonous evolution. Nevertheless, the composition moves in terms of C content at a constant Al/Si ratio.
- For a given initial composition, baking the pellets at 1900°C and 2000°C roughly shifts the composition towards an aluminum depletion. The depletion is rather limited (a few

mole%) at 1900°C after 6 hours, but rather strong at 2000°C, more than 20 mole% after the same baking time. The loss by vaporization mainly consists of Al.

- At 2100°C, the composition looks more erratic but the global composition shows a depletion of both Al and Si. The higher temperature also activates the vaporization (i.e. the loss) of Si. It is worth noting that in this case, the phase diagram states that during the baking time, the ternary carbides should not exist at the temperature higher than the melting and/or decomposition points. The phases observed should thus come from different reaction paths, but not fully understood at this time.

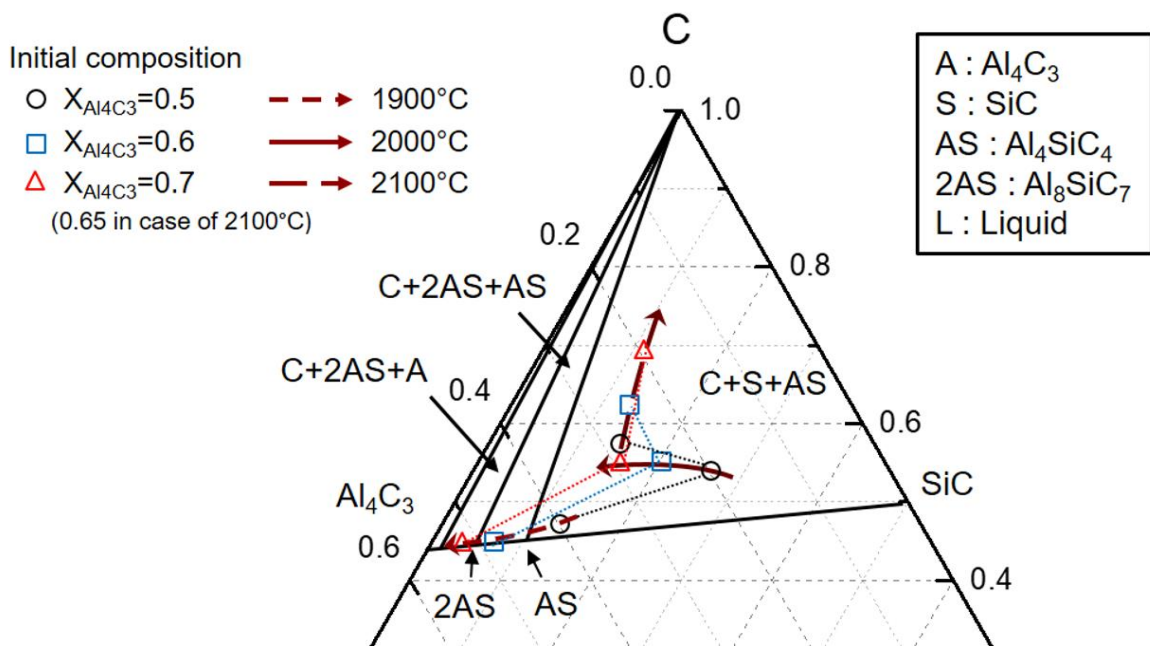


Figure 4.15: Evolution of the global composition in the Gibbs triangle as function of temperature and starting composition.

Now if we have a look at the phase analysis obtained by XRD, the following features can be obtained:

- At 2000°C and 2100°C, all the pellets consist of Al_4SiC_4 -SiC-C mixtures. The nature of the phases identified is consistent with the global elemental compositions, all lying within the Al_4SiC_4 -SiC-C three phases equilibrium domain in the Figure 4.15. For that reason, Al_4C_3 was not found in the samples. The very small quantities of Al_8SiC_7 , sometime encountered (less than a few mole%), are considered as parasitic effect and can be neglected. As compared between the series at 2000 and 2100°C, the vaporization of SiC increases causing the increase of graphite content in the samples.

- At 1900°C, the distribution of the different phases shows more variations and the nature of the phases vs global compositions exhibit some discrepancies. For instance, for an initial composition $X_{\text{Al}_4\text{C}_3} = 0.5$, all the compounds Al_4SiC_4 , Al_8SiC_7 , SiC , Al_4C_3 and C have been identified by XRD after baking, whereas the global composition clearly lies within the Al_4SiC_4 - SiC - C three phase equilibrium domain. The same behavior has been observed for $X_{\text{Al}_4\text{C}_3} = 0.6$, and $X_{\text{Al}_4\text{C}_3} = 0.7$, though the global composition correspond to the Al_8SiC_7 - Al_4SiC_4 - C . The presence of Al_4C_3 and SiC in such conditions are evidence of the incomplete solid state reaction between the powders. Several reasons could be mentioned. First, the sintering is performed without external pressure, which significantly reduce the intimate contact between the reactants. Second, the particles size could be not the optimal ones. For instance, SiC particles were 17 times bigger than Al_4C_3 particles (particles size of $3 \pm 0.9 \mu\text{m}$ and $52 \pm 12.8 \mu\text{m}$ for Al_4C_3 and SiC , respectively). Thus the surface area of the SiC is much smaller than the one of Al_4C_3 . Third, and assuming solid state reaction only, the reaction rate should be limited by the cross diffusion of Al and Si (mainly) through the product reaction that form at the intergrain, typically the ternary carbides. It is well known that diffusion in carbides is rather small and is usually claimed that it is almost negligible in SiC up to extremely high temperature, higher than the temperatures used in our experiments.

As a matter of fact, understanding the behavior of the source materials when heating an Al_4C_3 - SiC mixture at high temperature for long time requires to consider at least two phenomena: i) the reaction between the different components in the sample to reach the equilibrium state, and ii) the relative vaporization rates of the different elements which can lead to significant changes of the overall composition. According to such considerations, the evolution of the source materials after heat treatment was found in overall agreement with the known phase diagram and the thermodynamic calculations presented in chapter III. The main discrepancy occurs at the lowest temperatures (i.e. 1900°C) and can be essentially explained by incomplete solid state reactions. This first set of experiments have not permitted to synthesize the expected pure, single Al_4SiC_4 phase. A possibility would be to start from an aluminum rich mixture, in order to compensate the high vaporization rate of Al . However, the implementation of such mixture which would form Al -based liquid upon heating up, is more difficult because the liquid Al is extremely reactive with the graphite crucible. Nevertheless, these results provide relevant information for the further understanding for the evolution of the source materials during the PVT process.

4.3. Al₄SiC₄ sublimation growth

Inspired by the standard industrial crystal growth process of SiC, we investigate in this section, a sublimation growth process for Al₄SiC₄ using a mixture of Al₄C₃ and SiC as raw materials. In this case, due to the high relative vaporization rate of Al₄C₃, experiments have been conducted in the SiC-rich conditions ($X_{\text{Al}_4\text{C}_3} < 0.5$). As a general approach, the vaporization and condensation phenomena in Al₄C₃-SiC system will be investigated in order to determine the growth conditions of single Al₄SiC₄ phase.

4.3.1. Experimental process

Similarly to the sintering process, source materials were composed of a mixture of high purity powders of Al₄C₃ (Alfa Aesar, 99+% purity) and SiC (Sika tech E301) with a composition defined by the molar ratio of Al₄C₃ ($X_{\text{Al}_4\text{C}_3}$). However, the mixture, loaded in a graphite container, was not pressed before the experiment. The pressure and the temperature were controlled during the process. A bi-chromatic optical pyrometer have been used to measure the temperature from the back side of the crystallization area. The growth temperature varied from 1900 to 2000°C, and the growth pressure was fixed at 150 or 300 mbar using argon atmosphere. SiC substrates were chosen as seed and stuck at the top of the crystallization area using a graphite glue. Different types of SiC substrates such as [0001] oriented 6H-SiC on-axis and 4H-SiC 4° off-axis (towards [11-20]) with different polarities (Si face and C face) were used to evaluate the epitaxial relationships. The initial surface of the SiC substrates were polished by chemical mechanical polishing in all cases.

The experimental procedure is represented in Figure 4.16. At the beginning, the reactor was pumped out to achieve a vacuum of 10⁻³ mbar. Later, the reactor is manually heated up with a constant power until a temperature higher than 1000°C was reached. Afterwards, the heating rate was fixed at 30°C/min until the growth temperature. A pressure of ≈ 800 mbar is fixed during heating up in order to limit the sublimation of the raw materials. Once the growth temperature was reached, the pressure was decreased to the growth pressure. During the growth, all parameters were kept stable. At the end of the annealing process, the pressure was increased to 800 mbar to prevent any re-sublimation, and the reactor was cooled down by turning off the power.

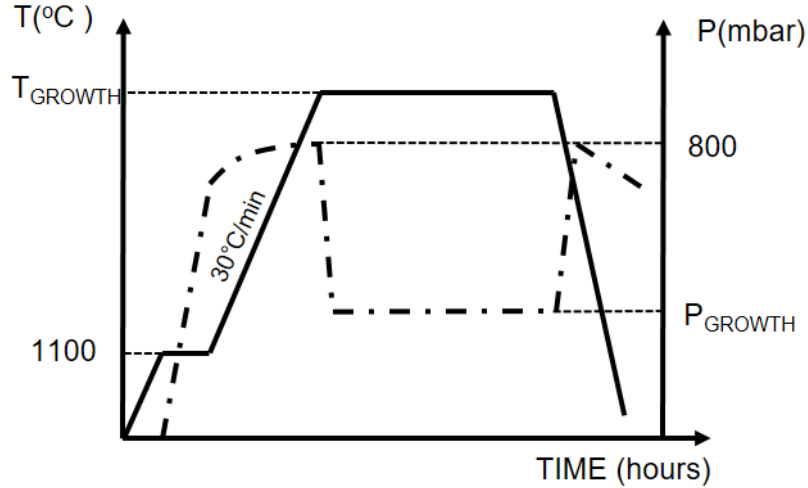


Figure 4.16: Representation of the process receipt used in all sublimation growth experiments. The variation of temperature (solid line) and pressure (dash line) at different steps are shown.

4.3.2. Experimental results

To draw an accurate picture of the vaporization-condensation phenomena in the Al_4C_3 -SiC system, it is necessary to combine the thermochemistry of the system together with the mass transport occurring in the crucible. For that, we have to differentiate what occurs within the powder, i.e. the formation of the different strata, to what happens in the open cavity above the powder. In the first part, the powder evolution as function of time will be investigated. In the second part, the deposit on the SiC substrate will be considered.

Powder evolution. A series of experiments were performed at a temperature of 2000°C and a pressure of 300 mbar with baking time varying from 20 minutes to 2 hours. The second set of experiments has been conducted at 1900°C , 150 mbar with the same initial composition but for longer time. According to the thermodynamic calculations results, an initial composition $X_{\text{Al}_4\text{C}_3} < 0.5$ has been chosen as the most convenient condition for the crystallization of Al_4SiC_4 . Figure 4.17(a) is a camera picture of the section of the source material after baking an Al_4C_3 -SiC mixture, having an initial molar composition $X_{\text{Al}_4\text{C}_3}=0.2$, during 2 hours at 2000°C . Three different layers can be clearly evidenced on the section, namely the bottom (3), medium (2) and top (1) layers. The initial level of the powder mixture is indicated by the black dashed line between layers (1) and (2). A backscattered electron (BSE) picture of each layer of the cross section has been added to Figure 4.17. For each stratum, a sample of powder has been extracted and grinded by ball milling for the qualitative (phase identification) and quantitative (atomic ratio of each phase) analyses using XRD measurements.

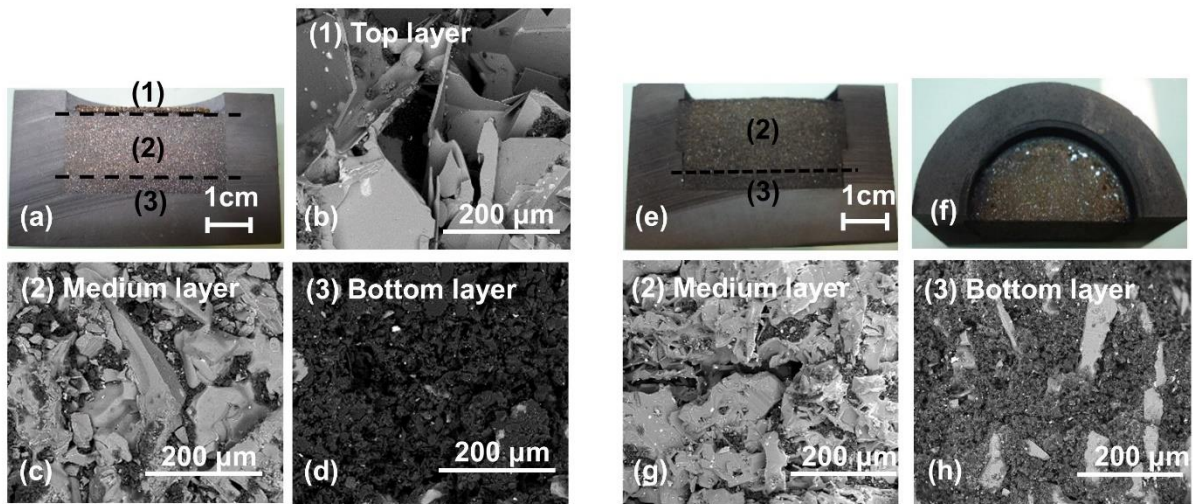


Figure 4.17: a) Cross section of the powder load after experiment; the composition of raw materials is $X_{Al4C3} = 0.2$ and the baking conditions are $T=2000^{\circ}\text{C}$, $P=300$ mbar and time=2 hours. Three different layers, denoted as (1) top, (2) medium and (3) bottom layers can be identified. Corresponding backscattered electron (BSE) pictures are presented on picture b, c, and d, respectively. Pictures e and f are cross-section and top view pictures of a powder load baked 4 hours at 1900°C and 150 mbar with the same initial composition. In this case, only two different layers can be identified which are denoted as medium and bottom layers. The corresponding BSE pictures are presented on pictures g and h.

X-ray diffractograms collected from each stratum after baking at 2000°C , 300mbar in 2 hours are given in Figure 4.18.

- (1) The top layer (layer 1) is mainly composed of an entanglement of very thin, light-orange platelets. This layer was formed above the initial level of the powder and was thus only due to the vaporization-condensation reaction in the open cavity. XRD analysis revealed a majority of Al_4SiC_4 and very small amounts of SiC, Al and Si. Small particles containing Al and Si are visible on the surface of the platelets in the SEM pictures which look like solidified droplets. These minority phases could form during cooling down or could be residues coming from a cross contamination during the separation of layers (1) and (2).
- (2) The medium layer (layer 2) exhibits a higher density of solid with at least two contrasts of grey levels, suggesting the coexistence of several phases. No real platelet could be

observed and the solid shows a granular texture. The phases identified by XRD are Al_4SiC_4 , SiC , C , Al and Si with the corresponding composition given in Table 4.3.

- (3) The bottom layer (layer 3), with a dominant black color, consists of a high density of small grains having a contrast close to that of the graphite crucible. Indeed, this stratum is mostly composed of SiC (80 mol%) and graphite (19 mol%) with a very small amount of Al_4SiC_4 (1 mol%). The graphitization front propagating from the edge of the grains to the center, it is not surprising to observe a black color (attributed to graphite with BSE) although XRD revealed a much higher SiC content, probably confined as core of the grains and not directly observable using BSE.

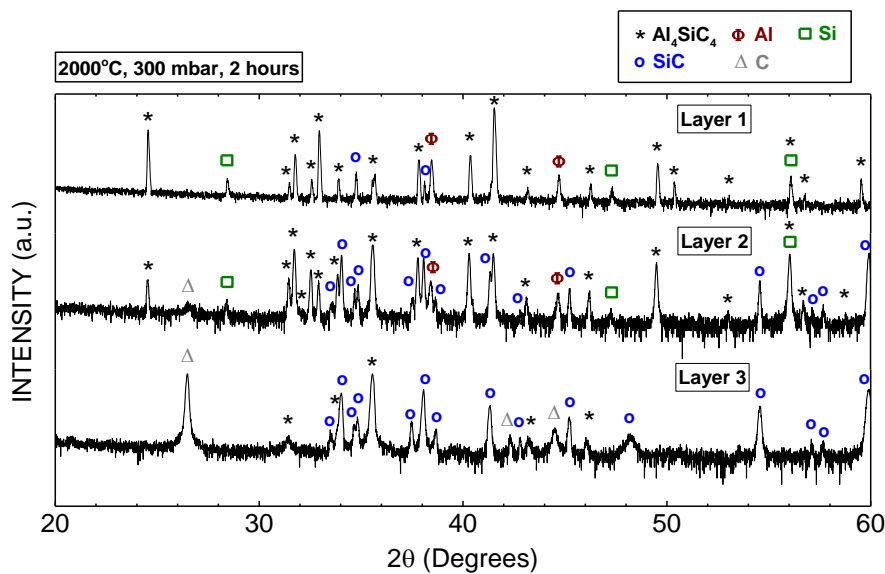


Figure 4.18: X-ray diffractograms collected from each stratum of powder load after experiment. The composition of raw materials $X_{\text{Al}_4\text{C}_3} = 0.2$ and the baking conditions are $T=2000^\circ\text{C}$, $P=300$ mbar and $\text{time}=2$ hours.

From 20 min to 2 hours, the X-ray diffractograms collected from the medium layer (layer 2) are given in Figure 4.19. The composition of Al_4SiC_4 , SiC , C , Al and Si was tracked and listed in Table 4.3.

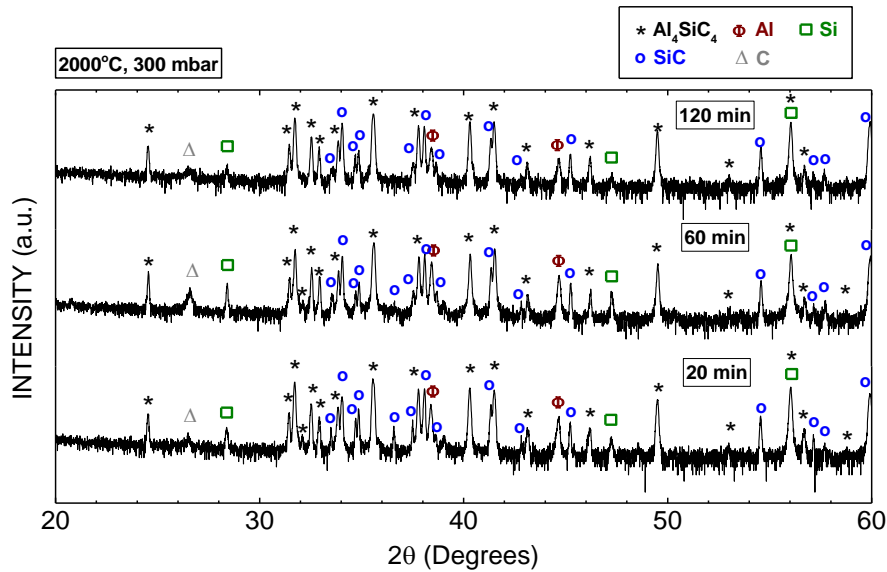


Figure 4.19: X-ray diffractograms collected from the medium layer of powder load after annealing during different time. The composition of raw materials $X_{Al4C3}=0.2$ and the baking conditions are $T=2000^{\circ}C$, $P=300$ mbar.

At $1900^{\circ}C$, there is no evidence of the formation of the top layer (1) and the cross section of the powder annealed during 4 hours shows only layers (2) and (3) (Figure 4.17(e)). In this case, only Al_4SiC_4 , SiC and C are observed in the X-ray diffractograms of the medium layer from 2 to 6 hours as shown in the Figure 4.20. The composition was also tracked and gathered in Table 4.3.

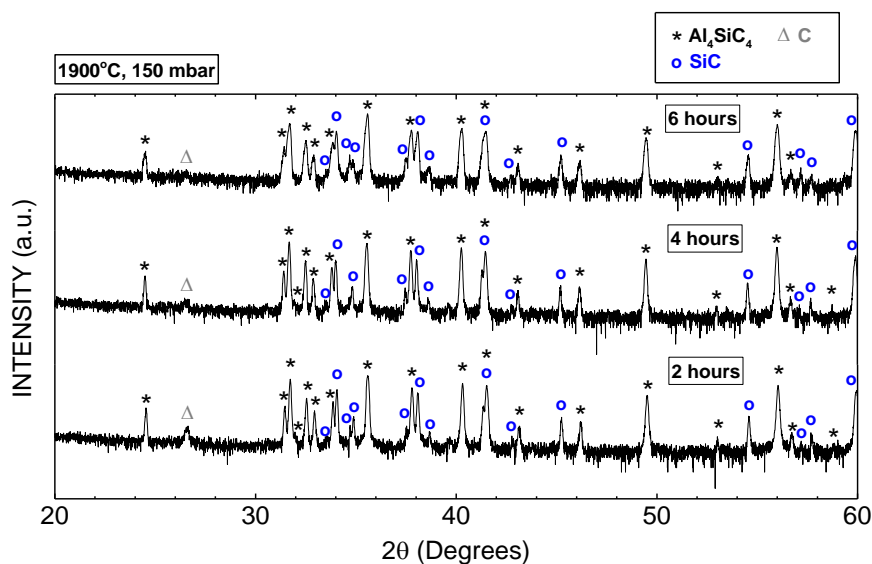


Figure 4.20: X-ray diffractograms collected from each stratum of powder load after annealing during different time. The composition of raw materials $X_{Al4C3} = 0.2$ and the baking conditions are $T=1900^{\circ}C$, $P=150$ mbar.

Table 4.3: Molar fraction of each components, obtained by XRD Rietveld analyses of powder samples extracted from the medium layer (located in the middle of the crucible and close to the powder surface) for different experimental conditions.

Experimental conditions	Mole fraction				
	Al ₄ SiC ₄	SiC	C	Si	Al
2000°C, 300 mbar, 20 min	0.13	0.43	0.06	0.04	0.34
2000°C, 300 mbar, 60 min	0.10	0.34	0.14	0.03	0.39
2000°C, 300 mbar, 120 min	0.13	0.53	0.11	0.02	0.21
1900°C, 150 mbar, 120min	0.20	0.59	0.21		
1900°C, 150 mbar, 240 min	0.29	0.60	0.11		
1900°C, 150 mbar, 360 min	0.19	0.74	0.07		

In order to get an estimation of the mass fluxes coming from two carbides, we firstly measured the weight loss (defined as initial weight-final weight, in percentage) as a function of time of pure SiC powder. Experiments have been performed at two different temperatures 1900°C and 2000°C under a pressure of 300 mbar with the geometry used for sublimation growth. The same volume of powder and annealing conditions have been applied in order to keep a constant source to seed distance and an equivalent temperature distribution. As plotted in the Figure 4.21, the weight loss of SiC powder are almost linear as a function of time for both temperatures. Due to the “high” pressure, vaporization rate of SiC is very slow. After reaching the baking temperature, the vaporization rate is about 10 and 7 mg/hour for 2000°C and 1900°C, respectively. It should be noticed that the initial weight of SiC is around 22g.

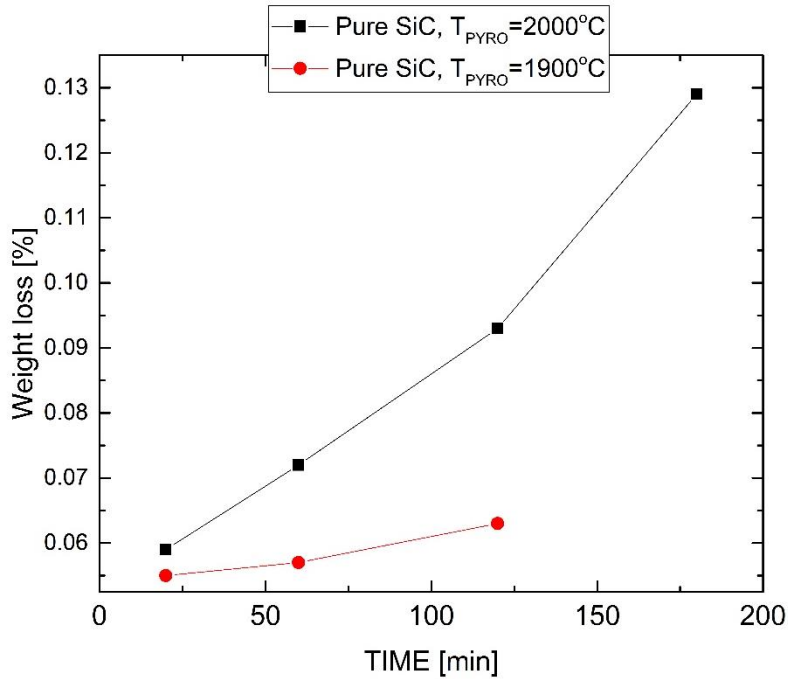


Figure 4.21: Evolution of the weight loss (%) of the pure SiC powder as a function of time for two different temperatures 1900°C and 2000°C. Experiments were performed under a pressure of 300mbar.

To compare the mass fluxes sublimated from the mixture ($X_{Al_4C_3}=0.2$) in both conditions, the weight loss of the mixture are plotted as function of time in Figure 4.22 beside the one of pure SiC. The vaporization rate of the mixture at 2000°C and 300 mbar is two order of magnitude higher than the one of pure SiC with the same conditions. A dramatic increase of the vaporization rate demonstrates the dominant role of Al_4C_3 in the sublimation flux of the mixture. Moreover, the vaporization rate is strongly dependent on temperature. Indeed, at lower temperature (1900°C and 150mbar), 6 hours of annealing are necessary to get almost the same weight loss than after 2 hours at 2000°C and 300 mbar.

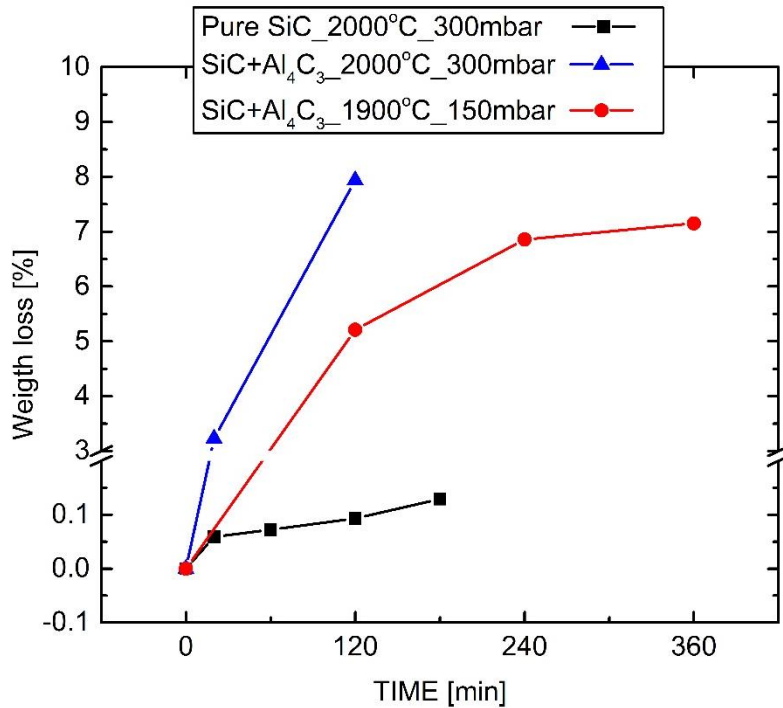


Figure 4.22: Evolution of the weight loss (%) of the powder as a function of time for two initial compositions: pure SiC (black curve) for annealing condition of $T=2000^{\circ}\text{C}$, $P=300\text{ mbar}$ and $\text{Al}_4\text{C}_3\text{-SiC}$ mixture with a composition of $X_{\text{Al}_4\text{C}_3}=0.2$. The mixture was annealed in two different annealing conditions: $T=2000^{\circ}\text{C}$, $P=300\text{ mbar}$ (blue curve); and $T=1900^{\circ}\text{C}$, $P=150\text{ mbar}$ (red curve).

Deposit on the 4° off-axis C-face 4H-SiC substrate. At the beginning, the effect of pressure and temperature have been considered. By fixing the temperature at 1900°C , the deposition rate is $30\ \mu\text{m/h}$ for a pressure of 300 mbar . When the pressure decreases to 150 mbar , the deposition rate just increases slightly to $37\ \mu\text{m/h}$. Otherwise, by increasing the growth temperature to 2000°C and keeping the pressure at 300 mbar , the deposition rate increases dramatically from 30 to $75\ \mu\text{m/h}$. This comparison demonstrates that in such conditions, the deposition rate is much more temperature dependent than pressure dependent. Thus, the effect of pressure will be neglected in the discussion.

Figure 4.23 shows the evolution of the deposit thickness as a function of time for two different sublimation conditions. Due to the smaller deposition rate, the experiments at 1900°C and 150 mbar were performed for longer time. The error bars added to the plots are standard deviation of the thickness values. They have been calculated from a statistically relevant number of measurements along the deposit diameter. It is thus kind of tracer of the evolution of the deposit roughness at a macroscopic scale. Obviously, such roughness increases first with the film thickness, but also with the deposition rate.

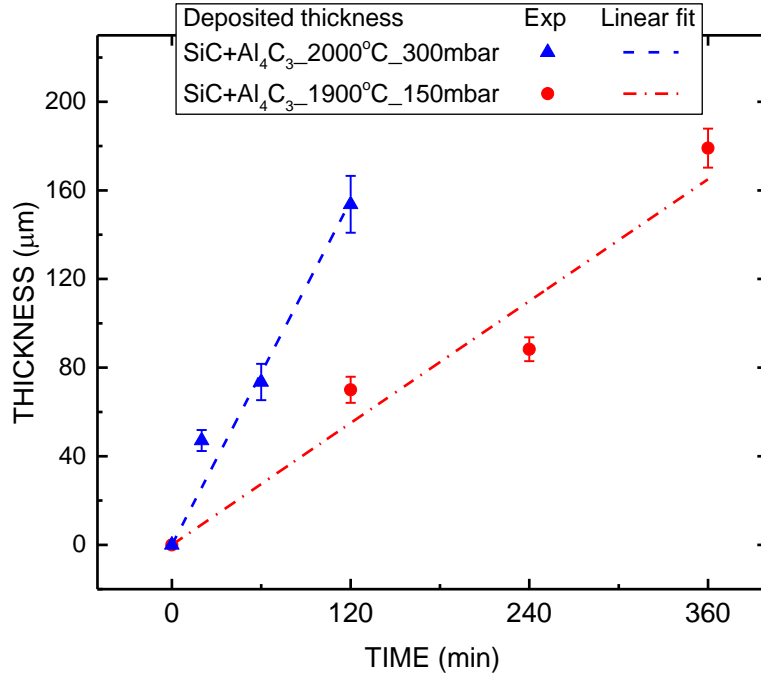


Figure 4.23: Thickness of deposited layer as function of annealing time for two different experimental conditions with Al_4C_3 -SiC mixture.

The nature of the deposited layers are identified by XRD analysis. The X-ray diffractograms collected from the deposited layers are shown in Figure 4.24, corresponding to the different points gathered in Figure 4.23. At 2000°C, 300mbar and after 20 minutes, the deposit consists of Al_4SiC_4 with a preferred [0001] orientation. After 1 hour, Al_4C_3 peaks start to appear in the deposit with the same orientation [0001]. After 2 hours, Al_4SiC_4 and Al_4C_3 both are present in the deposit and the diffractogram is similar to that of a poly-crystal, i.e. without any specific orientation. For the experiments at 20 minutes and 1 hour, some very small peaks, identified as belonging to Al and Si appear. By observing the surface of these deposits with SEM, it was found some microscopic solidified droplets and nano-fibers bundles developed from the droplets as shown in Figure 4.25. Energy Dispersive X-ray Spectroscopy (EDS) analysis were performed in order to identify their compositions which are gathered on Table 4.4. The first one located on the deposit layer shows the stoichiometric composition of Al_4SiC_4 . The second one was performed on the nano-fibers bundle and the third one was performed on the solidified droplets. The amount of oxygen present in EDS analysis probably came from oxidation during storage. Due to their location (only at the deposit surface) and their composition (very small amount of Si), these were supposed to be formed from the vapor phase during the cooling down, which will be discussed later.

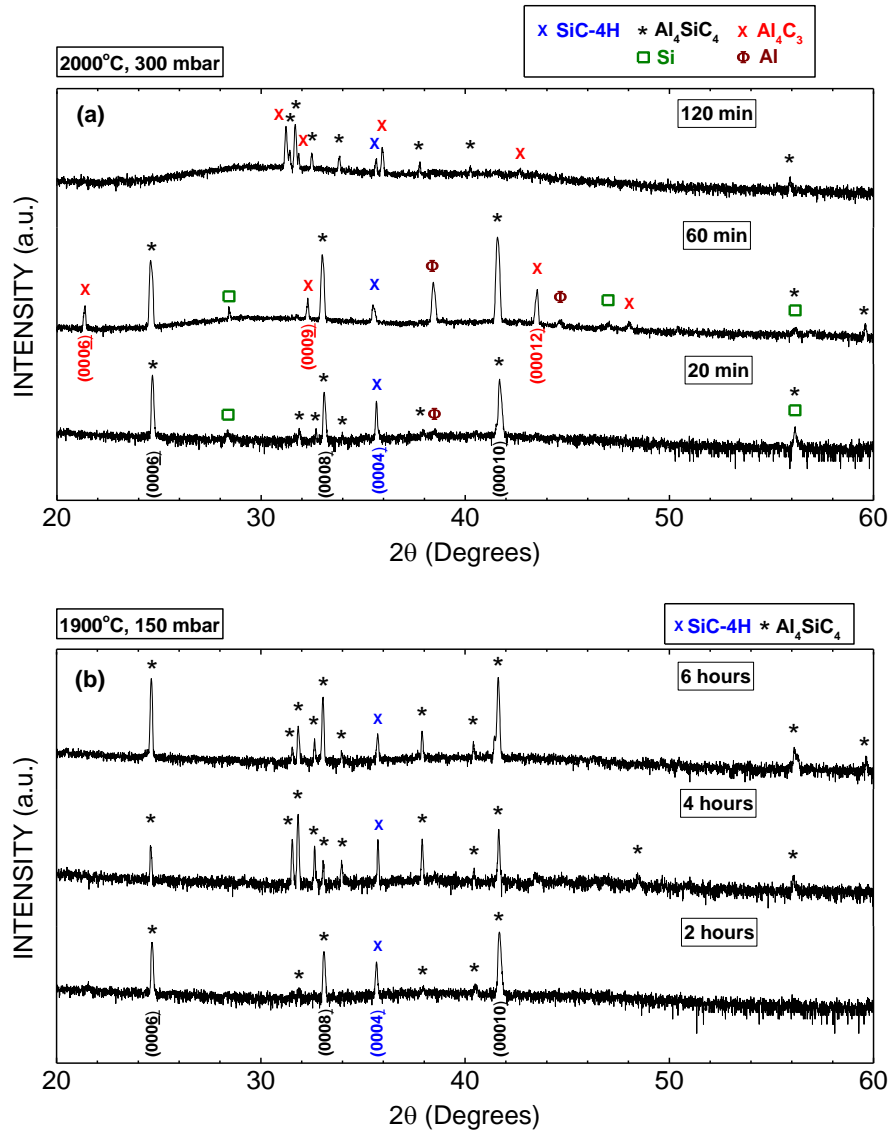


Figure 4.24: X-ray diffractograms collected from the deposited layers on 4° off axis 4H-SiC substrates (C face) after sublimation at (a) 2000°C, 300 mbar and (b) 1900°C, 150 mbar during different time. Al₄C₃-SiC mixture with a composition of $X_{Al_4C_3}=0.2$ has been used as the raw material. The preferred orientation found in the layers are also indicated.

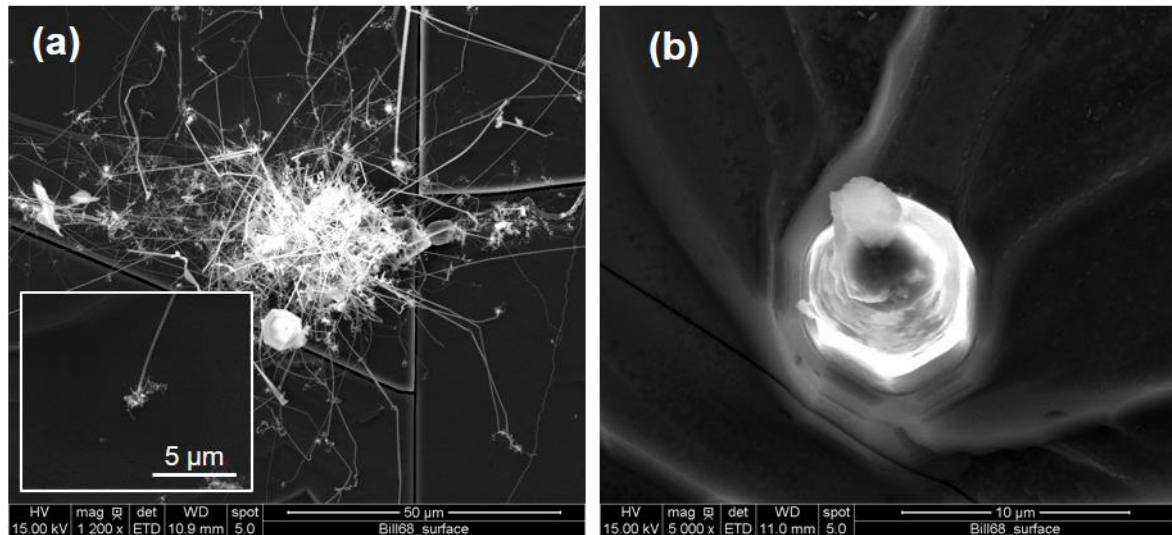


Figure 4.25: SEM image observing the surface of deposit after growth at 2000°C, 300 mbar in 20 minutes. (a) Droplet with nano-fibers, figure inset is the tip of fiber; (b) Solidified droplet.

Table 4.4: EDS analysis results on three different locations corresponding to the image given in figure Figure 4.25. The beam energy of 5kV has been used.

Elements	Energy Dispersive X-ray Spectroscopy analysis (atomic%)			
	Al	Si	C	O
Al ₄ SiC ₄ surface	48.7	13.6	37.3	0.4
Droplet (a)	55.1	1.4	17.6	25.9
Droplet (b)	26.7	3.4	61.4	8.5

At 1900°C, from 2 to 6 hours, the deposit only consists of Al₄SiC₄. After 2 hours, the Al₄SiC₄ layer clearly shows a preferred orientation [0001] which is the one of the SiC substrate. For longer time, even if the {0001} family peaks keep the strongest intensities, some other orientations develop causing the increase of the roughness of deposited layer.

4.3.3. Discussion

In order to compare with the raw composition, the molar fraction of the three elements (Al, Si, C) have been extracted from the Rietveld analyses of the powders, only for the medium layer. The results obtained for different time and the two annealing conditions investigated in this section are gathered in Table 4.5. At 1900°C, the elemental composition of the source was roughly constant even for long baking time, i.e. 6 hours, in agreement with the results of section

4.2. At 2000°C, the medium layer showed an enrichment in Al of about 10% during the first hour. Then for longer time, the composition progressively shifted back to the initial one.

Table 4.5: Molar fraction of the three elements, extracted from the XRD Rietveld analysis of the powder in the medium layer, for different experimental conditions.

Experimental conditions	Mole fraction		
	Al	Si	C
Initial composition, $X_{Al_4C_3}=0.2$	0.27	0.27	0.46
2000°C, 300 mbar, 20 min (1)	0.33	0.24	0.43
2000°C, 300 mbar, 60 min (2)	0.37	0.22	0.42
2000°C, 300 mbar, 120 min (3)	0.29	0.26	0.45
1900°C, 150 mbar, 120min (4)	0.25	0.25	0.5
1900°C, 150 mbar, 240 min (5)	0.29	0.23	0.48
1900°C, 150 mbar, 360 min (6)	0.24	0.28	0.48

As mentioned before, at a given temperature, the vaporization rate of the pure SiC is constant over the investigated time. Even if the mechanism is a non-congruent vaporization, it states that the flux of Si is constant. It is rather different for Al_4C_3 . The vaporization rate of the Al_4C_3 -SiC mixture is extremely strong at the beginning and progressively reaches a saturation (Figure 4.22). Indeed, there is no Al_4C_3 left after the annealing time investigated. Thus for short-time experiments (20 min to 60 min) at 2000°C, the vapor composition at the seed surface was dominated by Al-containing vapor species during the growth. While the pressure was increased in order to prevent the sublimation during the cooling down, the vaporization of Si-containing species was blocked which interrupted the formation of Al_4SiC_4 . Instead, solidified droplets were formed due to the supersaturated vapor phase with Al(g). Note that the equilibrium vapor pressure of Al at 2000°C is around 61 mbar⁸ which is lower than the partial pressure of Al(g) calculated in the experimental condition (95mbar). After that, nano-fibers of Al were developed from the droplets due to a vapor-liquid-solid mechanism⁹. The evidence of the droplet remained on the tip of the fiber as shown in the insert of Figure 4.25(a).

According to the phase diagram, with an initial mixture having a composition $X_{Al_4C_3}= 0.2$, the equilibrium state should belong to the Al_4SiC_4 -SiC two phase equilibrium. As the solid state reaction rate between Al_4C_3 and SiC is rather slow, we can speculate that a part of it has directly vaporized, producing this initial high vaporization rate. Furthermore, being a non-

congruent melting compound, Al_4C_3 produces some graphite upon vaporization. This is what we have experimentally observed. Once all Al_4C_3 is consumed, the vaporization rate decreases and then is governed by the Al_4SiC_4 -SiC equilibrium.

At 1900°C , even if the bottom of the powder starts to graphitize (Figure 4.17(h)), the Al, Si, C elemental composition of the medium layer (Figure 4.17(g)) is almost constant up to 6 hours of annealing. There is no Al_4SiC_4 layer forming at the top of the powder. Differently said, the source material facing the seed keeps the same atomic composition, which belongs to the initial pseudo-binary section. As a consequence, stable conditions for the condensation of Al_4SiC_4 on the SiC substrate are fulfilled, over all deposition time.

At 2000°C , the evolution is rather different. The huge flux of species coming from the bottom layer (layer 3) leads to a strong enrichment of the medium layer with Al. Progressively, a crust of Al_4SiC_4 platelets (layer 1) also develops on the powder surface. Before the formation of this crust, the vaporization is fixed by the Al_4SiC_4 -SiC two-phase equilibrium. Similarly to what has been observed at 1900°C , such case provides proper conditions for the condensation of Al_4SiC_4 on the SiC substrate. However, when the crust of Al_4SiC_4 is formed, the surface “emitting” the flux of species to the seed is a pure Al_4SiC_4 one. From a thermodynamic point of view, this is associated to an increase of the Al activity and a decrease of the Si activity in the gas phase. In other words, the gas phase composition experiences an increase of the Al/Si and C/Si ratios. The SiC substrate seeing high Al and C fluxes compared to the one of Si, it is not surprising to condense Al_4C_3 once this situation is reached. Indeed, as observed in the cross section of the deposited layer in Figure 4.26(a), which was grown in 2 hours, three different layers have been identified by EDS analysis. The atomic percentage profile of Al, Si and C given in Figure 4.26(b) corresponds to SiC, Al_4SiC_4 , and Al_4C_3 respectively. It demonstrates the late formation of Al_4C_3 .

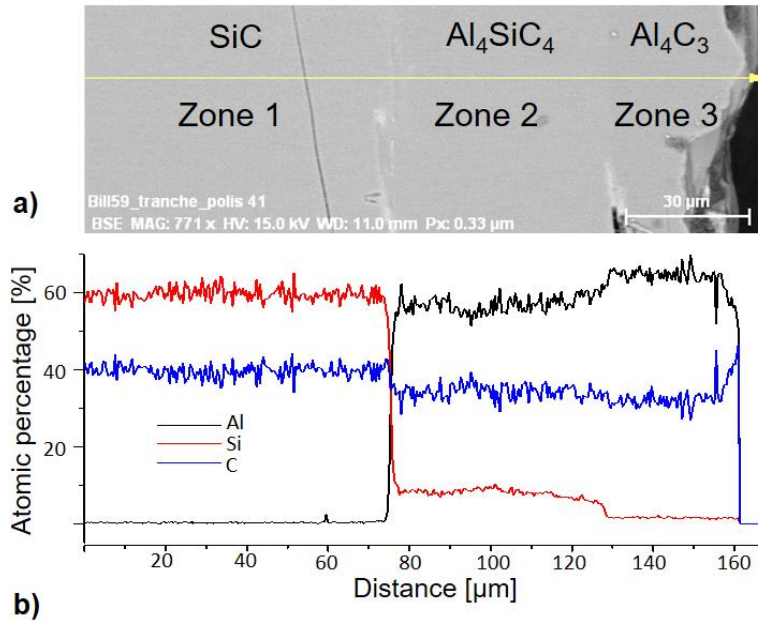


Figure 4.26: Cross section of the deposited layer after growth at 2000°C, 300mbar during 2 hours, with the corresponding EDS analysis.

As mentioned in the previous chapter, the condensation of single phase Al₄SiC₄ at the seed area requires a small temperature difference between the source and seed, typically lower than 40°C. Designed with the help of numerical simulation, the temperature distribution in our crucible perfectly fits with this condition for the temperature range from 1800 to 2000°C. Thus the conditions for the Al₄SiC₄ single phase condensation estimated by thermodynamic calculation was experimentally verified, at least at the initial stage for experiments at 2000°C.

4.4. Additional characterizations of the Al₄SiC₄ deposits

In this section, some characterizations have been conducted in order to describe the morphology of the growth surface, and to get some information about the growth mechanisms, the growth orientation and the structural quality of the Al₄SiC₄ layers on different types of SiC substrates. The absorption properties of free-standing Al₄SiC₄ crystalline layers (without substrate) have been also investigated.

4.4.1. Dependence of the growth mechanism on SiC substrate

For studying the dependence of growth mechanism on the different types of SiC substrates, an experiment has been carried out at short time. The conditions are: a source composition with a molar ratio of X_{Al₄C₃}=0.2, a growth temperature of 1900°C, a growth pressure of 300mbar and a growth time of only 10 min. Four different SiC substrates have been used: two 4° off-

axis 4H-SiC wafers, each with a specific polarity (C face and Si face), and two on-axis 6H-SiC again with both polarities (C face and Si face). The four seeds are stuck on the graphite holder and are processed in the same run. They are thus supposed to see exactly the same temperature distribution and supersaturation conditions.

According to the X-ray diffractograms gathered in the Figure 4.27, the deposit only consists of Al_4SiC_4 with the [0001] preferred orientation which is also the growth orientation of the substrates.

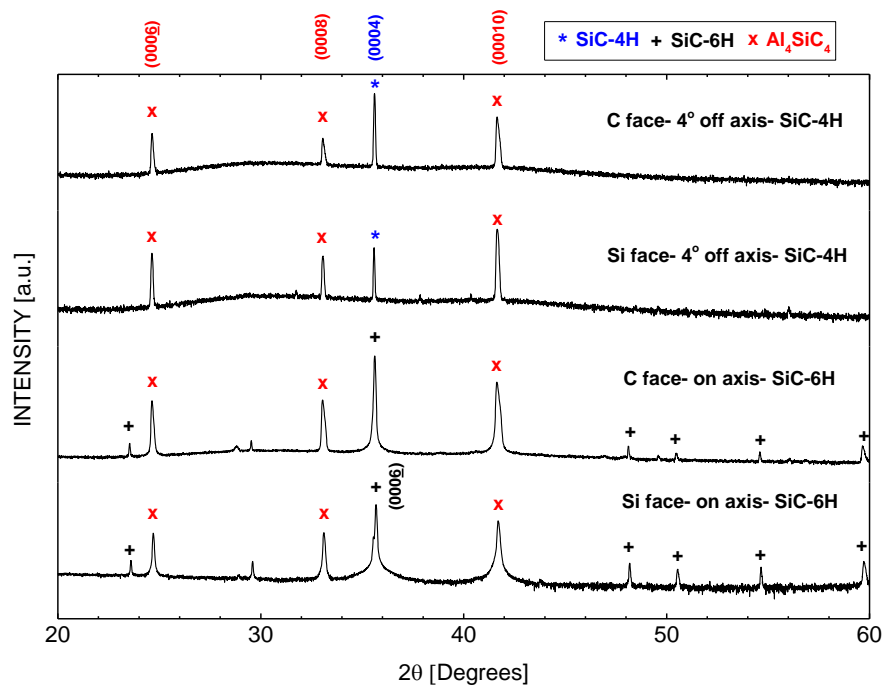


Figure 4.27: X-ray diffractograms collected from the deposited layers after 10 min of growth at 1900°C , 300mbar on different types of SiC substrate: 4° off-axis 4H-SiC substrate C face and Si face, on-axis 6H-SiC substrate C face and Si face. Initial composition of the source: $X_{\text{Al}_4\text{C}_3}=0.2$ (molar fraction).

Surface morphologies of the deposits have been observed using SEM (Figure 4.28). Different features can be observed.

- All the surfaces show hexagonally-based patterns, which are characteristics of the hexagonal crystal habits related to the structure. By analogy with hexagonal-SiC, we can speculate that the flat edges of the hexagon corresponds to the $\{1-100\}$ family planes and the tips corresponds to the $\{11-20\}$ family planes.
- Layers grown on on-axis 6H-SiC substrates (Si face and C face) exhibit hexagonal hillocks (complete hexagons), separated by typically few tens of microns. Between the

hillocks, the surfaces look flat but contain many small pits. Following the crystal orientations, many cracks are also visible at different scales. For instance, in the central part of the pictures (between hillocks), we can see an array of periodic lines, crossing each other with angles of 60° . These lines could be microcracks within the layers. At a larger scale, big cracks are clearly evident, with some parts of the layers which have been most probably peeled off. In terms of mechanism, hillocks are usually attributed to either spiral growth or two-dimensional (2D) nucleation. In both cases, the growth is associated to the lateral movement of steps on the surface in every directions.

- For the off-axis samples, and for both polarities (Si face and C face), there is a clear preferred orientation for the lateral expansion in the basal plane, creating a train of parallel steps. This preferred direction corresponds to a tip of the hexagon and is indicated by white arrows. As demonstrated for the case of SiC growth, the step edges can have different faceting depending on the step propagation direction, i.e. depending on the miscut direction. As shown in Figure 4.28, if the miscut of the substrate is inclined toward $[11-20]$, zigzag steps appear. If the miscut of the substrate is inclined toward $[1-100]$, then the steps are perfectly straight and parallel. As evidenced in Figure 4.28(a) and (b), the step edges have a zigzag configuration which corresponds to an off-orientation toward $[11-20]$, which is also the miscut orientation of the substrate (4° toward $[11-20]$).

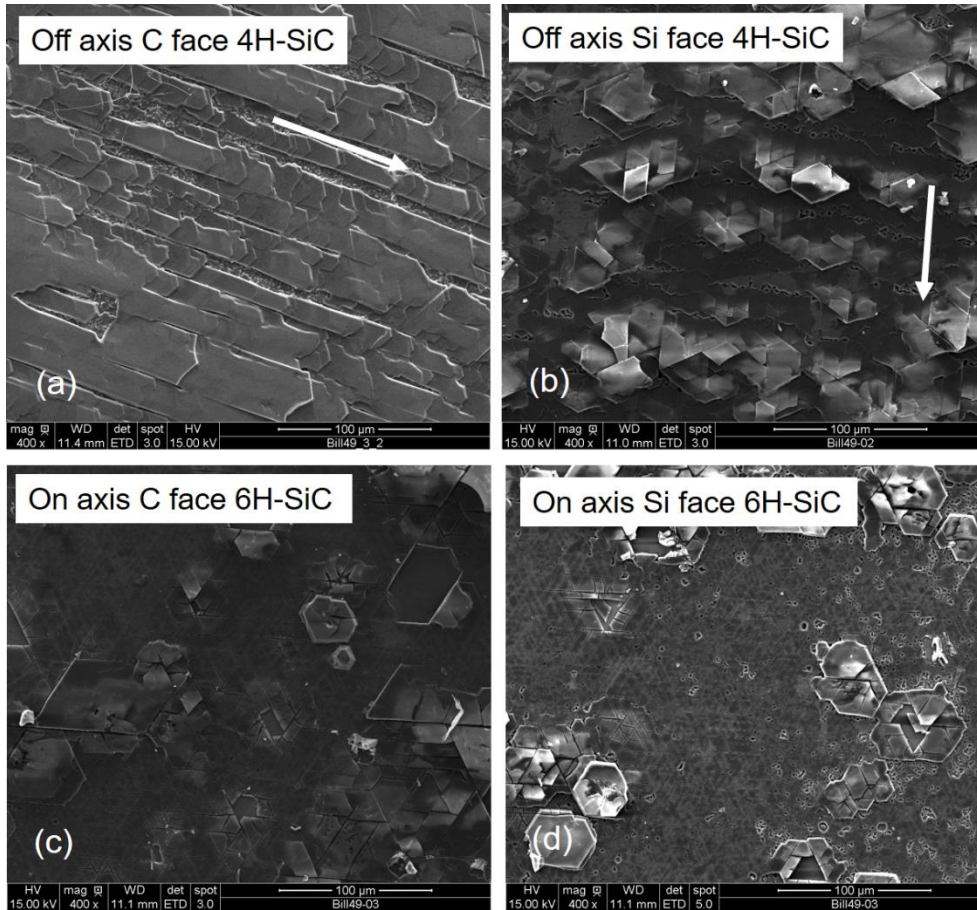


Figure 4.28: SEM images collected from the surface of Al_4SiC_4 layers grown at $1900^\circ C$, 300mbar, during 10 min and with an initial composition of the source of $X_{Al_4C_3}=0.2$. Different types of SiC substrate have been used: (a) 4° off axis C face 4H-SiC, (b) off axis Si face 4H-SiC, (c) on axis C face 6H-SiC, (d) on axis Si face 6H-SiC. The orientation of steps on off-oriented substrates have been indicated by arrows.



Figure 4.29: Configurations of steps on off-oriented (0001) faces toward $[11-20]$ and $[1-100]$ ¹⁰. This description has been proposed on α -SiC.

Dependence of the growth rate on the substrate orientation

The effect of substrate orientation on the growth rate has been studied for longer experiments. For that, two sets of sublimation growth experiments have been performed:

1. Temperature = 1900°C, pressure = 300mbar, duration = 2 hours, three different substrates: 4° off-axis 4H-SiC C face, on-axis 6H-SiC Si face and on-axis 4H-SiC Si face. Results are gathered in the Figure 4.30(a). For a given orientation (on-axis Si face), the growth rates on both polytypes 6H and 4H-SiC are almost similar, around 21 $\mu\text{m}/\text{h}$. There is no effect of polytype on the growth rate. Otherwise, if we compare on-axis Si face and off-axis C face, there is a significant difference in growth rates, the second one being much higher, around 32 $\mu\text{m}/\text{h}$. Note that the results are collected from the same run ensuring that the observed differences did not come from reproducibility issues between experiments. The raised question is: such a difference in growth rate comes from the polarity (Si vs. C face) or miscut angle (on-axis vs. off-axis)?
2. To help answering the question, a second set of samples has been done: temperature = 1900°C, pressure = 150 mbar, duration = 6 hours, two different substrates: 4° off-axis 4H-SiC, C face and Si face. A slight difference in the growth rates between both polarities of off-axis 4H-SiC substrates has been observed (Figure 4.30(b)). The growth rate on C-face is slightly higher than on Si-face.

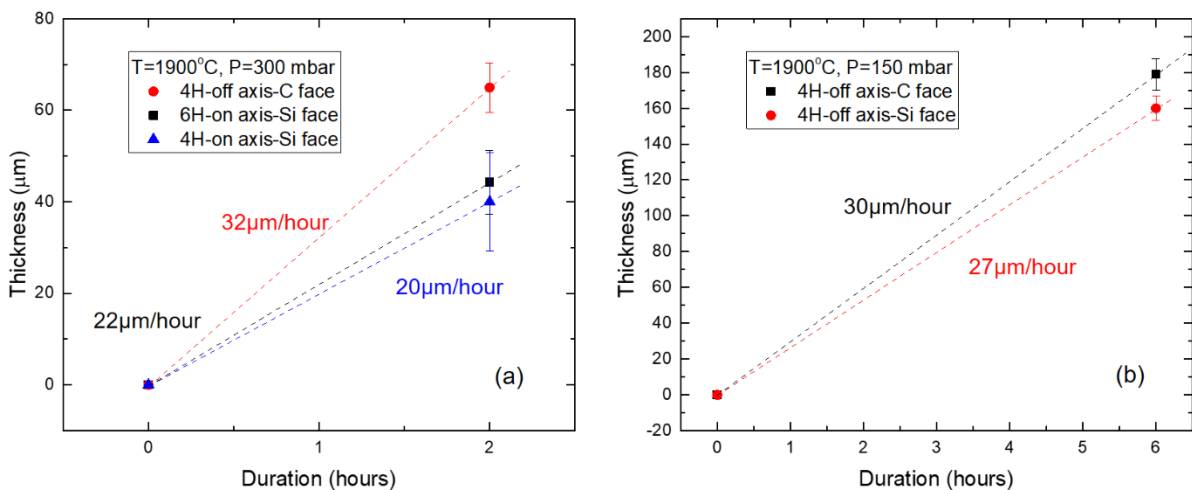


Figure 4.30: Dependence of the growth rate on different type of SiC substrates: (a) 4° off-axis 4H-SiC C face, on-axis 6H-SiC Si face and on-axis 4H SiC Si face. (b) 4° off-axis 4H-SiC, C face and Si face. The error bars of the measurements are added.

Simple qualitative considerations on the growth mechanisms can explain the different experimental trends which have been observed. Indeed, on well oriented [0001] substrates, the surface step-density is low, meaning that the terrace width is much larger than the diffusion length of adatoms on the surface. Thus, the growth is mainly driven by two dimensional nucleation on terraces, which is possible when the supersaturation is higher than a critical value. The growth rate is thus controlled by the nucleation frequency of new steps (2D nuclei). Once the 2D nucleus formed, it can laterally expand as a single step would. On off-axis substrates, the step density is high and the corresponding terrace width is narrow. In this case, there is no need to generate new steps, making the growth energetically more favorable. For that reason, the growth rate is mainly limited by mass transport. Such a difference in growth mechanism could explain the higher growth rate on off-axis substrate as compared to on-axis.

We also saw that there is no effect on the nature of polytypes during the growth on on-axis substrate for a given polarity. We can thus state that there is no effect of the polytype on the 2D nucleation frequency substrate. This can be intuitively understood as follows: for a given polarity, for example Si-face, the top surface of the SiC substrate is a hexagonal compact plane of Si-atoms. The adatoms interact essentially with the dangling bonds on this top surface, without “seeing”, at least at the first order, the structure below the surface. This is of course a rough approximation, but it explains why the 2D nucleation is similar whatever the polytype.

Considering the effect of polarity, i.e. Si-face vs. C-face, it is not surprising that on off-axis substrates, there is no significant effect of polarity. As the growth proceeds via the lateral movement of steps, i.e. that the incorporation of adatoms is performed at the step edges, which is not polarity dependent, the growth rate is thus not directly impacted by the polarity. Nevertheless, the surface termination of the terraces can slightly affect the diffusion length of adatoms and the adsorption/desorption coefficients. This can give rise to slight variations, as can be seen in Figure 4.30(b), but does not change dramatically the growth rate. In the case of on-axis SiC substrates, the situation is rather different. Indeed, the 2D nucleation frequency is directly related to the surface chemistry (termination). For SiC, it is well established that the C-face has higher chemical reactivity than Si face¹¹. We can speculate that under a 2D nucleation limited growth mechanism, the growth rate would be higher on the C-face than on the Si-face, due to a higher nucleation frequency on the C-face. Unfortunately, for technical reasons, we could not check this point.

Problem of cracks in the deposit layer

In both cases of on-axis, and off-axis substrates, many cracks have been observed in the deposited layer. In fact, these cracks are more visible with an increasing thickness of the deposit. Figure 4.31 presents an optical microscope picture of a $185 \pm 5 \mu\text{m}$ thick layer. Following the hexagonal crystalline structure, these cracks may be probably attributed to both the lattice mismatch and the difference in thermal expansion coefficient between Al_4SiC_4 and SiC. When the film and the substrate experience different rate of thermal expansion and contraction, the deposit can experience significant compressive or tensile stress during the temperature cycle, leading to crack formation. Indeed, Al_4SiC_4 has a thermal expansion coefficient (CTE) α in the basal plane of $9.96 \times 10^{-6} \text{ }^\circ\text{C}^{-1}$ ¹², much higher than the thermal expansion coefficient of 4H-SiC, which is approximately $3.2 \times 10^{-6} \text{ }^\circ\text{C}^{-1}$ ¹³.

From the lattice mismatch at room temperature ($\Delta a = 6.5\%$), and considering the CTE of both materials SiC and Al_4SiC_4 , we can roughly estimate the lattice mismatch at growth temperature. For the growth temperature $T=1900^\circ\text{C}$, the lattice mismatch can be calculated as:

$$\Delta a_T = \frac{a_{\text{AlSiC}}(T) - a_{\text{SiC}}(T)}{a_{\text{SiC}}(T)} \quad (4.7)$$

$$\text{Where } a_{\text{AlSiC}}(T) = (\alpha_{\text{AlSiC}} \Delta T + 1) a_{\text{AlSiC}}(25^\circ\text{C}) = 3.341 \text{ \AA} \quad (4.8)$$

$$a_{\text{SiC}}(T) = (\alpha_{\text{SiC}} \Delta T + 1) a_{\text{SiC}}(25^\circ\text{C}) = 3.099 \text{ \AA} \quad (4.9)$$

$$\Rightarrow \Delta a_T = 7.8\% \quad (4.10)$$

Thus, the lattice mismatch increases of 20% at growth temperature. With such a high mismatch, many extended defects such as misfit dislocations should be introduced to adapt both lattices. The critical thickness above which dislocations are generated to release the excess elastic energy due to the lattice mismatch will be evaluated in the next chapter. Besides, during the cooling down, the difference in CTE should be at the origin of strong thermos-elastic strain, whose energy is released by the formation of periodic cracks of the layer.

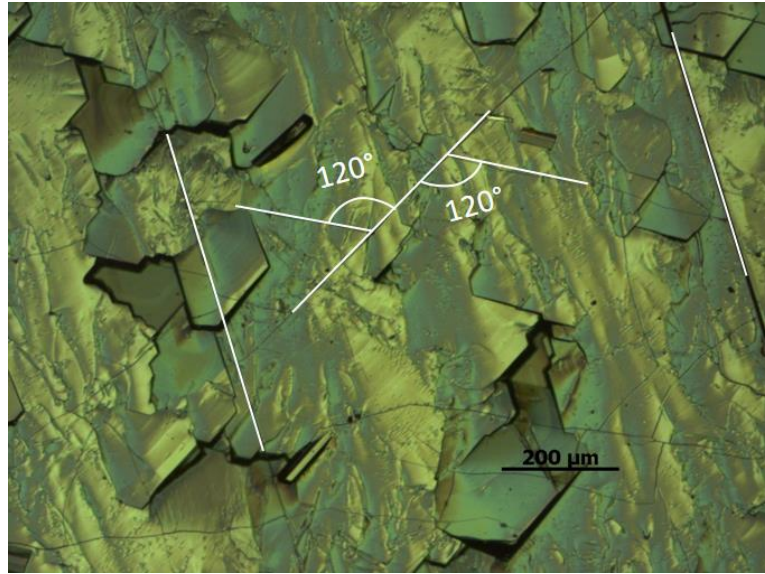


Figure 4.31: Optical microscopy picture of the surface of a crystalline Al_4SiC_4 layer deposited on a 4° off axis C-face SiC-4H substrate. Growth conditions are: $T=1900^\circ\text{C}$, $P=150\text{mbar}$, duration: 6 hours. Thickness of the deposit: $185 \pm 5 \mu\text{m}$. Example of cracks on the surface have been indicated by white lines.

4.4.2. Growth orientation and texture of Al_4SiC_4 crystal layers

The dependence of growth orientation and texture of Al_4SiC_4 on different types of SiC substrates has been investigated through short experiments which have been presented in section 4.4.1 ($X_{\text{Al}_4\text{C}_3}=0.2$, $T=1900^\circ\text{C}$, $P=300\text{mbar}$, duration=10min). A detailed rocking curve analysis has been carried out for Al_4SiC_4 layer deposited on different kind of substrates, namely 4H-SiC 4° off-axis C-face and Si-face, 6H-SiC on-axis C-face and Si-face. Results of the analyses, including the position (Omega), FWHM, Phi and Chi of the rocking curves are gathered in Table 4.6 for different reflections: (0004) of 4H-SiC, (00012) of 6H-SiC, (00010) and (10-16) of Al_4SiC_4 . The thickness of the Al_4SiC_4 layers is approximately $7 \pm 1 \mu\text{m}$.

Table 4.6: Rocking curve analysis of the Al_4SiC_4 layers deposited on different SiC substrates. Symmetrical plan (00010) and asymmetrical plan (10-16) are considered for the comparison.

Hetero-structure	Material	Plan	Omega ($^\circ$)	FWHM RC ($^\circ$)	Phi ($^\circ$)	Chi ($^\circ$)
$\text{Al}_4\text{SiC}_4/4\text{H-SiC } 4^\circ$ off-axis C face	4H-SiC	(0004)	17.836	0.253	4.1	4.2
	Al_4SiC_4	(00010)	20.761	1.780	4.2	4.4
		(10-16)	20.215	1.130	24.3	56.3
$\text{Al}_4\text{SiC}_4/4\text{H-SiC } 4^\circ$ off-axis Si face	4H-SiC	(0004)	13.701	0.363	90	0
	Al_4SiC_4	(00010)	16.578	1.213	90	0
		(10-16)	16.055	0.834	91	51.9

Al ₄ SiC ₄ /6H-SiC on-axis C face	6H-SiC	(00012)	36.697	0.295	88.8	-0.9
	Al ₄ SiC ₄	(00010)	19.798	1.405	89.3	-0.8
		(10-16)	20.174	1.174	87.5	51
Al ₄ SiC ₄ /6H-SiC on-axis Si face	6H-SiC	(00012)	37.498	0.304	90	-0.3
	Al ₄ SiC ₄	(00010)	20.664	0.832	90	-0.2
		(10-16)	20.182	0.655	87.4	51.6

The growth orientation of the Al₄SiC₄ deposits has been determined and systematically compared to the growth orientation of the corresponding SiC substrates. For the off-axis 4H-SiC substrates, the tilt angle of substrates could contribute to the offset in the Chi or Omega measurements (the samples have been tilted along the Chi and Omega axis, which are parallel to the sample surface).

Let consider first the layer grown on 4H-SiC off-axis C face substrate. The Theta values are equal to the theoretical values. The symmetrical (0004) reflection of 4H-SiC has Chi value of 4.2° which corresponds to the tilt angle of the substrate. The (00010) reflection of Al₄SiC₄ has a Chi value of 4.4°, which demonstrates a relative tilt angle of 0.2° between the basal planes of both the deposit and the substrate. The asymmetrical (10-16) reflection of Al₄SiC₄ has an offset of 4.4° in Chi which, if compared to the theoretical value (51.9°), also exhibits a relative tilt angle of 0.2°. These offsets in Chi are illustrated in the pole figures shown in Figure 4.32.

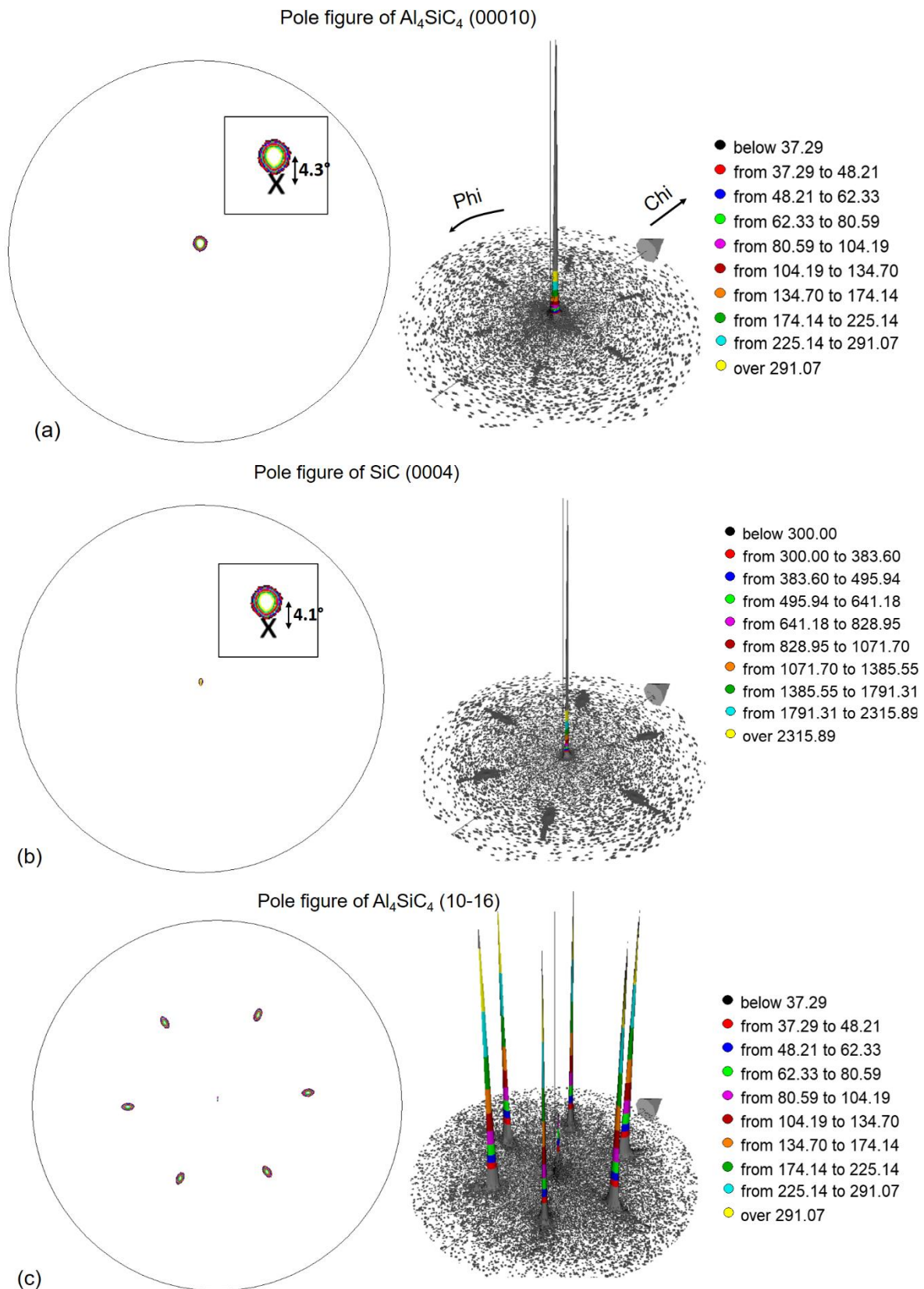


Figure 4.32: Pole figures (2D and 3D) of (a)(00010) reflection of Al_4SiC_4 , (b)(0004) reflection of SiC, (c)(10-16) reflection of Al_4SiC_4 . Inset pictures is the zoom at the center of the 2D pole figure.

In the case of the 4H-SiC off-axis Si face substrate, the tilt angles of both the substrate and the deposited layer contribute to the offset in Omega. Indeed, Omega of the (0004) SiC reflection (13.7°) has 4.1° offset as compared to the theoretical value (17.8°). Similarly, Omega of the (00010) and the (10-16) reflections of Al_4SiC_4 deposit has also 4.3° offset as compared to the theoretical value. Therefore, a similar relative tilt angle of 0.2° between the basal plane of the deposit and the substrate has been found.

Concerning the use of 6H-SiC on-axis Si face and C face substrates, theoretical values of Omega and Chi have been found, which indicates the perfect alignment of the Al_4SiC_4 lattice on the one of the SiC substrate.

An estimation of the Al_4SiC_4 crystal quality has been performed through rocking curve measurement. For that, the full width at half maximum (FWHM) of the (00010) and the (10-16) reflections of Al_4SiC_4 have been compared and gathered in Figure 4.33. The trends are clear: first, the FWHM increases with the relative tilt angle between Al_4SiC_4 and SiC substrate. It is thus higher on off-axis SiC substrate. Second, the FWHM is systematically lower on the Si-face than on the C-face, for a given initial miscut angle. The gain in quality while using Si-face SiC substrates is significant as the FWHM is typically reduced by a factor of two.

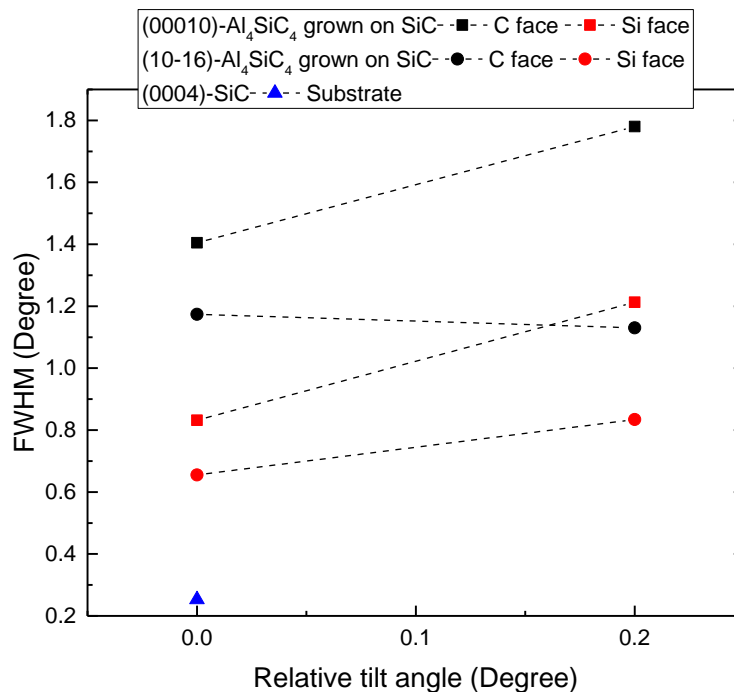


Figure 4.33: Dependence of the Al_4SiC_4 structural quality on the relative tilt angle (between the Al_4SiC_4 deposit and the SiC substrate) and the polarity of the SiC substrates (Si-face and C-face). FWHM of symmetrical (00010) and asymmetrical (10-16) reflections have been

considered. FWHM of (0004) reflection of 4H-SiC substrate is also indicated as reference value.

According to the XRD measurements, the Al_4SiC_4 layers grown on off-axis SiC substrates are slightly tilted by 0.2° with respect to the substrate. This type of tilting, usually called Nagai tilt, has been widely studied in the hetero-epitaxial growth of different materials on off-axis substrates^{14, 15}. In fact, due to presence of misfits and lattice deformation (strain) which accommodate the lattice mismatch in the normal direction (Δc), there may be a deviation of the growth direction of the epilayer relative to the one of the substrate. For that reason, a higher FWHM has been found in the epilayer grown on off-axis substrates as compared to on-axis substrate. Differently said, the layer needs to accommodate both in the basal plane and along the c direction when off-axis substrate is used. The relative tilt angle is illustrated by $\Delta\alpha$ in the model of the interface between Al_4SiC_4 and off-axis SiC substrate shown in Figure 4.34. This lattice deformation at the interface of the hetero-structure will be studied in more details by high resolution transmission electron microscopy in the next chapter.

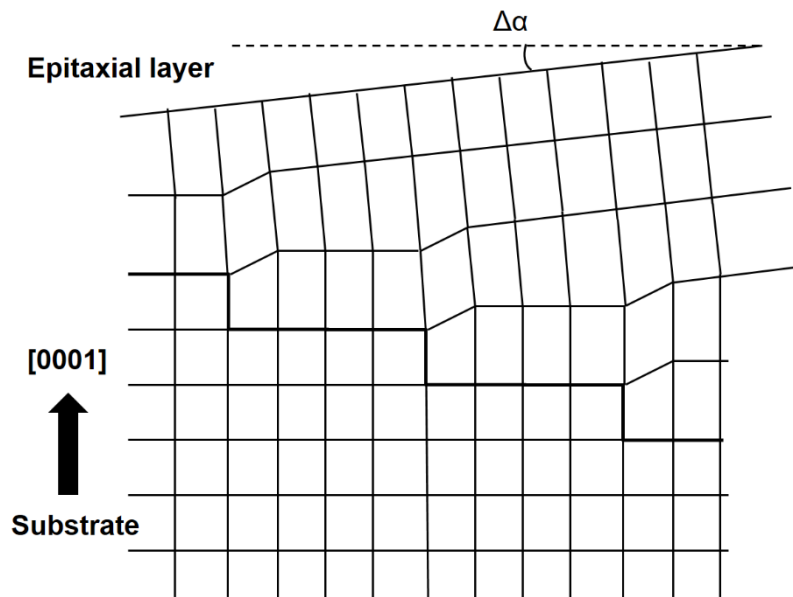


Figure 4.34: Model of the interface between Al_4SiC_4 and off-axis SiC substrate. To simplify the drawing, the lattice mismatch in the horizontal (basal) plane is neglected in the figure.

In theory, with a step height of $2c=20.12\text{\AA}$ and a 4° off angle of the [0001] 4H-SiC surface, the step width on the substrate could be simply calculated as:

$$L = \frac{h}{\tan \alpha} = \frac{2c}{\tan 4^\circ} = 287.7 \text{\AA}. \quad (4.11)$$

Supposing that this step width is preserved in the epilayer, the tilt angle of the Al_4SiC_4 deposit due to the mismatch lattice in the normal direction is:

$$\alpha' = \tan^{-1}\left(\frac{c'}{L}\right) = 4.3^\circ. \quad (4.12)$$

Where $c'=21.72\text{\AA}$ is the lattice constant of Al_4SiC_4

Thus, a relative tilt angle ($\Delta\alpha$) of 0.3° between the Al_4SiC_4 epilayer and the SiC substrate is estimated which is close to the experimental result (0.2°).

In case of on-axis substrates, the dependence of the Al_4SiC_4 structural quality on the polarity of SiC substrates is interesting. Indeed, the epitaxial layer grown on the Si-face has smaller FWHM, which corresponds to a better crystalline quality, than the one grown on the C-face substrate. The reason is still unclear, but we can propose the following element. As already discussed, the [0001] C-face of SiC shows a higher chemical reactivity than the [0001] Si-face. In terms of nucleation, the impact of such a reactivity difference has been demonstrated by the study of the nucleation of 3C-SiC (cubic) on 6H- or 4H-SiC (hexagonal). For such a case, the nucleation frequency on the C-face has been reported as much higher than on Si-face. Differently said, the density of nuclei per surface unit should be higher on the C-face than on Si-face. Assuming that the growth mechanism is composed of two dimensional nucleation on terraces followed by lateral expansion due to the movement of step edges, then the creation of the texture described in Figure 4.35 could be obtained. With a larger domain density on the C-face, i.e. a higher mosaicity in the deposited layer, a larger FWHM could be explained.

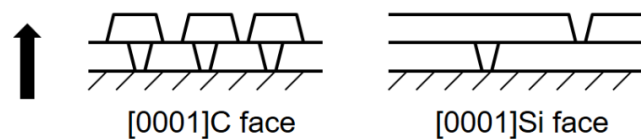


Figure 4.35: Schematic representation of the growth process on [0001] C face and [0001] Si face from on-axis SiC substrates.

Rocking curve of thick Al_4SiC_4 crystal

The texture analysis has also been performed on thick Al_4SiC_4 crystalline layers. The XRD rocking curve has been measured on a $185 \pm 5 \mu\text{m}$ thick Al_4SiC_4 layer which was grown on C-

face 4H-SiC substrate (4° off axis) at 1900°C, 150 mbar in 6 hours (Figure 4.36). The diffraction peak of (00010) plane at position 2Theta=41.7° has been chosen for the analysis.

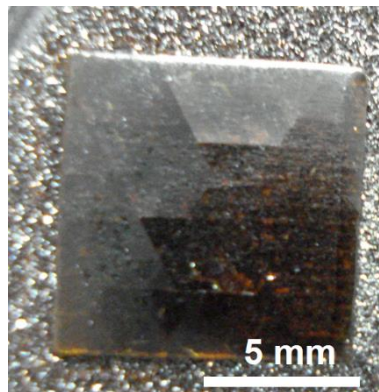


Figure 4.36: Al_4SiC_4 layer deposited on a 1cm x 1cm SiC-4H substrate at a temperature of 1900°C and a pressure of 150mbar in 6 hours.

The rocking curve of the (00010) reflection is shown in the Figure 4.37(a). A FWHM of 0.303° was obtained by fitting the curve with a Lorentzian function. As a reference, the (004) rocking curve of a perfect Si single crystal was also measured in Figure 4.37(b). The value of the FWHM of Si is 0.083°, giving an estimation of the diffractometer limit.

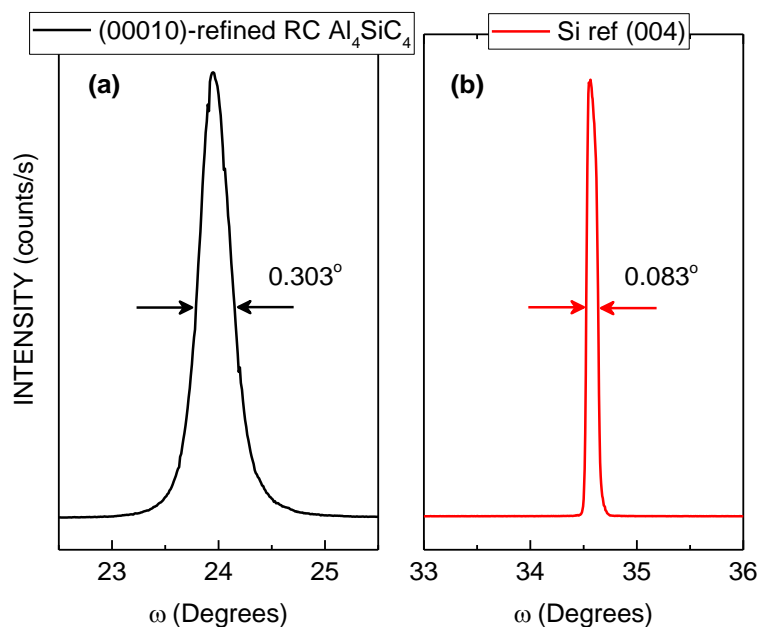


Figure 4.37: (a) Rocking curve of the (00010) reflection of 185 μm thick Al_4SiC_4 crystal obtained from the sublimation growth at 1900°C and 150 mbar; (b) Rocking curve of the (004) reflection of Si single crystal used as the reference.

First, it is interesting to compare the FWHM value of Al_4SiC_4 to other hetero-epitaxial systems on SiC substrates. For example, AlN grown on [0001] 6H-SiC substrate by PVT without using any buffer layer, shows a (0002) reflection FWHM of 0.14° ¹⁶. Hetero-epitaxy of 1 μm thick GaN on [0001] 6H-SiC by plasma-assisted molecular-beam epitaxy exhibits a FWHM of the rocking curve of the (0002) reflection about 0.2° ¹⁷. Note that the lattice mismatch of GaN/6H-SiC and AlN/6H-SiC are $\Delta a/a = 3.4\%$ and 1% , respectively, which are much smaller than the lattice mismatch between Al_4SiC_4 and SiC ($\Delta a/a = 6.5\%$). In addition, these hetero-epitaxial systems have a certain degree of maturity due to the huge amount of research works conducted so far, hence, we feel that the FWHM obtained for such a highly mismatched Al_4SiC_4 on SiC system, is really promising.

Second, the FWHM of the rocking curve passes from $1.2\text{-}1.7^\circ$ to 0.3° by thickening the Al_4SiC_4 layer from $7\ \mu\text{m}$ to $185\ \mu\text{m}$. A significant improvement of the crystalline quality thus takes place with the thickness.

4.4.3. Optical properties

The optical absorption of the Al_4SiC_4 crystal deposited on the SiC-4H substrate has been investigated by Uv-Vis-NIR spectroscopy. The total transmittance spectra in the 250-2500 nm range was collected on the Al_4SiC_4 crystal layer delaminated from the substrate with the incident light perpendicular to the basal plane. The absorption coefficient as function of wavelength is calculated from the transmittance spectra.

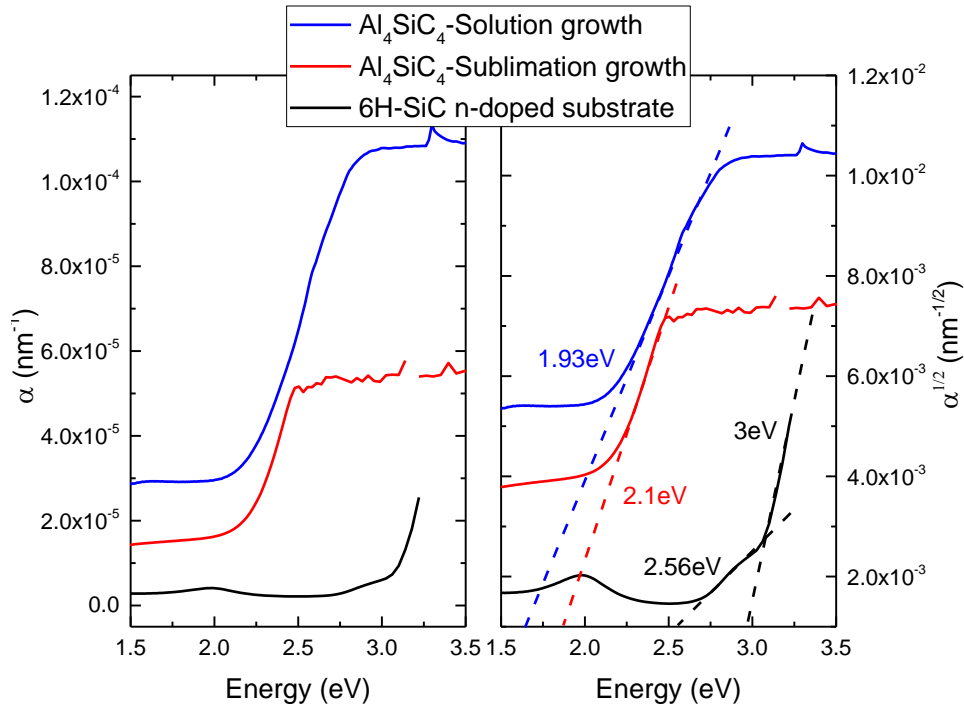


Figure 4.38: (a) Absorption coefficient plotted as a function of photon energy of Al_4SiC_4 crystal obtained from solution growth and sublimation growth with the thickness of 50 and 185 μm , respectively and SiC-6H (n-doped) substrate with the thickness of 350 μm (b) Square root of the absorption coefficient as a function of photon energy. The spectra have been collected at room temperature.

The Figure 4.38 shows the absorption coefficient of Al_4SiC_4 crystal obtained from different processes like solution growth⁶ and sublimation growth with the thickness of 50 and 185 μm , respectively. The solution growth process using Al, Si and graphite crucible as initial material has been described in chapter 1. Moreover, the absorption coefficient of the SiC-6H n-type doped substrate, used for the sublimation growth of Al_4SiC_4 has also been added as a reference. As mentioned in the literature¹⁸, a superposition of the phonon absorption (2.56 eV) and phonon emission (3.0 eV) processes is observed in SiC. It is rather different for Al_4SiC_4 . The indication of phonon emission and absorption processes are not clearly separated. Both samples of Al_4SiC_4 exhibit simply an absorption edge at 1.93 eV and 2.1 eV for solution grown crystal and sublimation grown crystal, respectively. The origin of this difference is unknown at this stage. A possibility could be a much high dopant concentration in the case of solution grown crystal, which could give rise to bandgap shrinkage. In the case of SiC, the incorporation of nitrogen in both solution and sublimation growth processes is an extensively studied topic. Nitrogen is reported as the most abundant dopant in SiC bulk growth, because it is extremely

difficult to purify the raw materials and also to remove it from the building materials of the growth crucible (graphite and graphite insulation). Moreover, the residual nitrogen level in solution grown crystals is usually higher than in sublimation grown crystals because of the difference in liquid/solid and gas/solid partition coefficients. Even by using high purity graphite materials, the background level of nitrogen is typically around 10^{17}cm^{-3} ¹⁹ and 10^{19}cm^{-3} ²⁰, for sublimation grown crystals and solution grown crystals, respectively. By analogy with SiC, and supposing that nitrogen is also a donor in Al_4SiC_4 , a higher doping level is expected for the solution grown crystals as compared to the sublimation grown crystals.

CONCLUSIONS OF THE CHAPTER

In this chapter, two high temperature approaches for the synthesis of Al_4SiC_4 have been investigated, both starting from a mixture of Al_4C_3 and SiC raw powders. Numerical simulation has been implemented on the real reactor geometry to visualize the temperature distribution within the reaction zones. All the results have been discussed with respect to the thermodynamic calculations reported in chapter III.

First, a solid state reaction process (pressureless sintering) has been investigated. Whatever the initial composition of Al_4C_3 and SiC , a single Al_4SiC_4 phase could not be achieved. We have shown that the behavior of the Al_4C_3 - SiC mixture baked at high temperature for long time could be described by considering two phenomena: i) the solid state reaction between two carbides, which shows a low reaction yield, and ii) the relative vaporization rates of different elements which can lead to significant changes of the overall composition. According to such considerations, the evolution of the source materials after heat treatment was found in overall agreement with the known phase diagram and the thermodynamic calculations presented in chapter III.

Second, a vapor phase process, based on vaporization and condensation phenomena has been implemented. In good agreement with the thermodynamic calculation results presented in chapter III, the experimental conditions to grow Al_4SiC_4 single crystals from the vapor phase was determined with the following constraints: i) a SiC -rich initial composition ($X_{\text{Al}_4\text{C}_3} < 0.5$) of the source materials, ii) a small temperature gradient between the source and the seed to avoid condensation of parasitic phases, iii) moderated mass transport to avoid strong evolutions of the system and again, the condensation of parasitic phases. The source material has shown a complex evolution, giving rise to the formation of strata. This could be explained by the interplay between thermodynamics and mass transport phenomena, i.e. the relative vaporization rate of the different species. We have successfully applied this sublimation growth process to the hetero-epitaxial growth of high quality, thick single phase Al_4SiC_4 layers, on hexagonal- SiC commercial wafers.

Preliminary results on the characterization of surface morphologies, crystalline quality and optical properties have been reported. For example, we have shown that the nature of the substrate (C-face vs. Si-face, off-axis vs. on-axis) has a significant effect on the mosaicity of the layer and also on the crystal lattice matching between the layer and the substrates. Indeed, a relative tilt angle (Nagai type tilt) of 0.2° between the basal planes of the Al_4SiC_4 epilayer

and the SiC substrate has been observed when the growth is performed on 4° off-axis substrates. For thin layers, the best quality has been obtained on Si-face on-axis SiC substrates. Also, the quality significantly improved with the thickness, a FWHM of 0.303° has been measured for the (00010) reflection of a 185 µm thick Al₄SiC₄ layer, which is a good value, considering the high lattice mismatch between the epilayer and the substrate.

REFERENCE

1. K. Ariyawong, *Process modeling for the growth of SiC using PVT and TSSG methods*, Doctoral dissertation, Université Grenoble Alpes, 2015.
2. E. Jordan and K. Balmain, *Electromagnetic Waves and Radiating Systems*, Prentice Hall, Englewood Cliffs, New Jersey (1968).
3. R.-H. Ma, H. Zhang, S. Ha and M. Skowronski, *Integrated process modeling and experimental validation of silicon carbide sublimation growth*, Journal of crystal growth **252** (4), 523-537 (2003).
4. R. Madar, M. Pons, J. M. Dedulle, E. Blanquet, A. Pisch, P. Grosse, C. Faure, M. Anikin and C. Bernard, *Numerical simulation of SiC boule growth by sublimation*, presented at the Materials Science Forum, 2000, Vol. 338, pp. 25-30.
5. C. Moulin, M. Pons, A. Pisch, P. Grosse, C. Faure, A. Basset, G. Basset, A. Passero, T. Billon and B. Pelissier, *SiC single crystal growth by sublimation: experimental and numerical results*, presented at the Materials Science Forum, 2001, Vol. 353, pp. 7-10.
6. D. Zevgitis, O. Chaix-Pluchery, B. Doisneau, M. Modreanu, J. La Manna, E. Sarigiannidou and D. Chaussende, *Synthesis and Characterization of Al₄SiC₄: A “New” Wide Band Gap Semiconductor Material*, presented at the Materials Science Forum, 2015, Vol. 821, pp. 974-977.
7. D. B. Wiles and R. A. Young, *A new computer program for Rietveld analysis of X-ray powder diffraction patterns*, Journal of Applied Crystallography **14** (2), 149-151 (1981).
8. C. B. Alcock, V. P. Itkin and M. K. Horrigan, *Vapour Pressure Equations for the Metallic Elements: 298–2500K*, Canadian Metallurgical Quarterly **23** (3), 309-313 (1984).

9. R. Wagner and W. Ellis, *Vapor-liquid-solid mechanism of single crystal growth*, Applied physics letters **4** (5), 89-90 (1964).
10. H. Matsunami, T. Ueda and H. Nishino, *Step-controlled epitaxial growth of SiC*, MRS Online Proceedings Library Archive **162** (1989).
11. S. Nishino, H. Matsunami and T. Tanaka, *Growth and morphology of 6H-SiC epitaxial layers by CVD*, Journal of Crystal Growth **45**, 144-149 (1978).
12. Y. Li, B. Xiao, L. Sun, Y. Gao and Y. Cheng, *Phonon optics, thermal expansion tensor, thermodynamic and chemical bonding properties of Al₄SiC₄ and Al₄Si₂C₅: a first-principles study*, RSC Advances **6** (49), 43191-43204 (2016).
13. M. E. Levinshtein, S. L. Rumyantsev and M. S. Shur, *Properties of Advanced Semiconductor Materials: GaN, AlN, InN, BN, SiC, SiGe*. (John Wiley & Sons, 2001).
14. A. Pesek, K. Hingerl, F. Riesz and K. Lischka, *Lattice misfit and relative tilt of lattice planes in semiconductor heterostructures*, Semiconductor science and technology **6** (7), 705 (1991).
15. H. Nagai, *Structure of vapor-deposited Ga_xIn_{1-x}As crystals*, Journal of Applied Physics **45** (9), 3789-3794 (1974).
16. Y. Shi, Z. Y. Xie, L. H. Liu, B. Liu, J. H. Edgar and M. Kuball, *Influence of buffer layer and 6H-SiC substrate polarity on the nucleation of AlN grown by the sublimation sandwich technique*, Journal of Crystal Growth **233** (1), 177-186 (2001).
17. Q. K. Yang, A. Z. Li, Y. G. Zhang, B. Yang, O. Brandt and K. Ploog, *Growth and mosaic model of GaN grown directly on 6H-SiC(0001) by direct current plasma assisted molecular beam epitaxy*, Journal of Crystal Growth **192** (1), 28-32 (1998).
18. W. J. Choyke and L. Patrick, *Absorption of Light in Alpha SiC near the Band Edge*, Physical Review **105** (6), 1721-1723 (1957).
19. N. Tsavdaris, *Incorporation d'azote et stabilité des polytypes de la croissance en phase gazeuse de monocristaux de SiC*, Doctoral dissertation, Université Grenoble Alpes, 2015.
20. Y. J. Shin, *Study of a high temperature solution growth process for the development of heavily doped 4H-SiC substrates*, Doctoral dissertation, Université Grenoble Alpes, 2016.

CHAPTER V

HETERO-EPITAXY OF

Al-Si-C BASED COMPOUNDS ON SiC

Different heterostructures of Al-Si-C based compounds on hexagonal SiC substrates will be studied in this chapter like $\text{Al}_4\text{C}_3/\text{SiC}$ and $\text{Al}_4\text{SiC}_4/\text{SiC}$. In the first part, Al_4C_3 single crystals have been successfully grown from the reaction between liquid Al and SiC at 1700°C . These crystals allowed the first optical absorption measurements in order to estimate the optical bandgap of Al_4C_3 . In the second part, the heterostructure of Al_4C_3 on [0001] oriented SiC substrates is investigated. A synthesis process from the chemical interaction between Al and the Si face of [0001] hexagonal SiC substrate at 800°C is proposed for the fabrication of the heterostructure. The characteristics of the heterostructure such as the wetting behavior of the system, growth mechanism of the epilayer and the crystallographic relationships between the layers and the substrate are investigated at a nanoscopic scale by using high resolution transmission electron microscopy (HRTEM). The third part is dedicated to the hetero-epitaxy of Al_4SiC_4 on SiC substrates which has been successfully grown by the sublimation process described in the previous chapter. By using HRTEM, the interface of heterostructure of Al_4SiC_4 grown on different kind of SiC substrates will be observed and analyzed.

5.1. Introduction

A major current challenge for the semiconductor devices is to develop materials for the next generation of high temperature electronics, optoelectronics and generally speaking, electronic power conversion applications. For that purpose, bandgap engineering is a powerful technique for the design of new semiconductor devices. By creating heterojunctions, band diagrams with nearly arbitrary and continuous bandgap variations could be made for a given application¹.

For instance, the III-V nitride material system, which includes AlN, GaN, InN and their alloys, have bandgaps varying from the infrared to the ultraviolet region². It opened the possibility of using these materials for applications in light emitting diodes (LEDs), laser diodes and photodetectors.

In carbides, the investigation of hetero-structures is almost an open field. The only well documented case in the viewpoint of bandgap engineering, is the research efforts that have been done in order to develop heterostructures using different SiC polytypes³. The reported bandgaps of different SiC polytypes are gathered in Table 5.1. Since the high quality hexagonal SiC (4H and 6H) wafers are commercially available, the heterostructure of 3C-SiC (cubic polytype of SiC) on oriented hexagonal SiC substrate is promising for the development of semiconductor devices thanks to the high electron mobility of 3C-SiC⁴ ($\sim 1000 \text{ cm}^2 \cdot \text{V}^{-1} \cdot \text{s}^{-1}$), which is independent of the crystallographic direction⁵. However, the growth of high quality 3C-SiC on c-oriented hexagonal SiC substrates is still challenging due to the high probability of forming double position boundaries during the nucleation of the epilayer⁶.

In this work, new heterostructures of Al-Si-C based compounds on hexagonal SiC are proposed, such as Al₄C₃/SiC and Al₄SiC₄/SiC, in order to provide new directions for the development of carbide heterostructures. Bandgap energy as a function of lattice constant (*a*) for different SiC polytypes (6H, 4H, 3C), nitrides, Al₄C₃ and Al₄SiC₄ is shown in the Figure 5.1. Our experimental measurements of the optical bandgap of Al₄C₃ and Al₄SiC₄ have been added in Table 5.1.

In fact, the proposed heterostructure of Al₄C₃ and Al₄SiC₄ on hexagonal SiC substrates have some advantages. First, they are composed of light and abundant elements, contrary to their nitrides counterparts (Ga- and In-based semiconductors). Second, Al₄C₃ and Al₄SiC₄ are fully chemically compatible with SiC substrates. Third, they have an hexagonal structure and the ability to be epitaxial grown on hexagonal SiC substrates⁷. Their epitaxial relations will be investigated further in this chapter. Last, they have the bandgap close to the one of 3C-SiC,

which can make them interesting for similar applications such as photo-electrochemical water splitting⁸ (applicable for Al_4SiC_4 , but not Al_4C_3) and impurity photovoltaic devices⁹. However, these heterostructures still have some drawbacks, such as the instability of Al_4C_3 in air and the large lattice mismatch ($\Delta a/a$) with α -SiC substrate (6.5% and 8% for Al_4SiC_4 and Al_4C_3 , respectively).

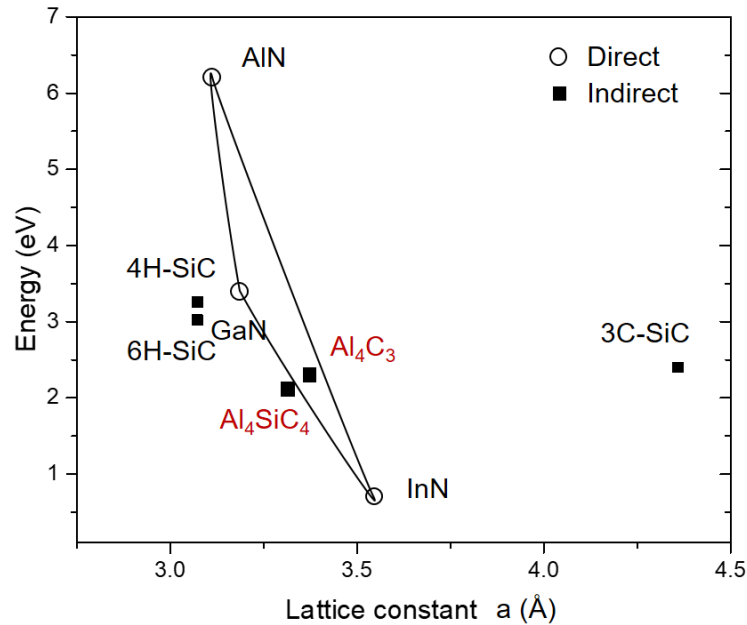


Figure 5.1: Bandgap energy versus lattice constant of III-V nitrides (such as: AlN , GaN and InN) and carbides (SiC , Al_4C_3 , and Al_4SiC_4) at room temperature.

Table 5.1: Bandgap energy and lattice constants of hexagonal SiC (4H and 6H), cubic SiC (3C), Al_4C_3 and Al_4SiC_4 ¹⁰.

		3C-SiC	4H-SiC	6H-SiC	Al_4C_3	Al_4SiC_4
Bandgap (eV) (exp)		2.39	3.26	3.02	2.3	2.1
Lattice constant (Å)	a	4.359	3.081	3.081	3.329	3.28
	c		10.061	15.092	24.98	21.72

In order to establishing the basic knowledge for the development of the carbide heterostructure $\text{Al}_4\text{C}_3/\text{SiC}$ and $\text{Al}_4\text{SiC}_4/\text{SiC}$, the synthesis processes are proposed. Afterwards, based on HRTEM images, their growth mechanisms, and their characteristics such as epitaxial relationship and strain state at the interface will be investigate.

5.2. Al₄C₃ single crystals

Known as the only intermediate compound in the Al-C system, Al₄C₃ could be synthesized by the chemical interaction between aluminum and SiC at temperature near the melting point of Al¹¹ (650°C) which is much lower than the growth temperature of α-SiC (>2000°C by sublimation growth) and Al₄SiC₄ (~1900°C by sublimation growth). However, Al₄C₃ easily hydrolyzes at room temperature to form aluminum hydroxide and methane¹². It is probably the reason why the electrical and optical properties of Al₄C₃ have so far not been experimentally investigated in the literature. With the purpose of investigating the experimental bandgap of Al₄C₃ for the first time, the synthesis of Al₄C₃ single crystals was conducted by our group.

5.2.1. Experiments

A first strategy to synthesis Al₄C₃ crystals was to use the reaction between SiC and Al pieces, as reported by Viala et al.¹¹. SiC wafer has been used after the treatment in HF (30 min in HF 50%) to remove the native oxide on the surface. In fact, the formation of Al₄C₃ could prevent the dissolution of SiC in liquid Al¹³. Therefore, for the completed dissolution of SiC in Al liquid, the initial composition should be located in the green area shown in Figure 5.2, where only aluminum rich ternary liquid phase is in equilibrium. Thus, the molar fraction of SiC: $X_{SiC} = n_{SiC} / (n_{SiC} + n_{Al})$ should be smaller than 1%.

For the experiments, the raw materials were composed of the Al pieces (99.5%) and 4H-SiC single crystals (Dow Corning) with a molar ratio 100:1. SiC crystals were placed on top of Al pieces. To avoid the interaction between Al and graphite, an alumina crucible has been used. The geometry used for the synthesis of Al₄C₃ is presented in Figure 5.3, which is the same as the one used for the differential thermal analysis presented in chapter III.

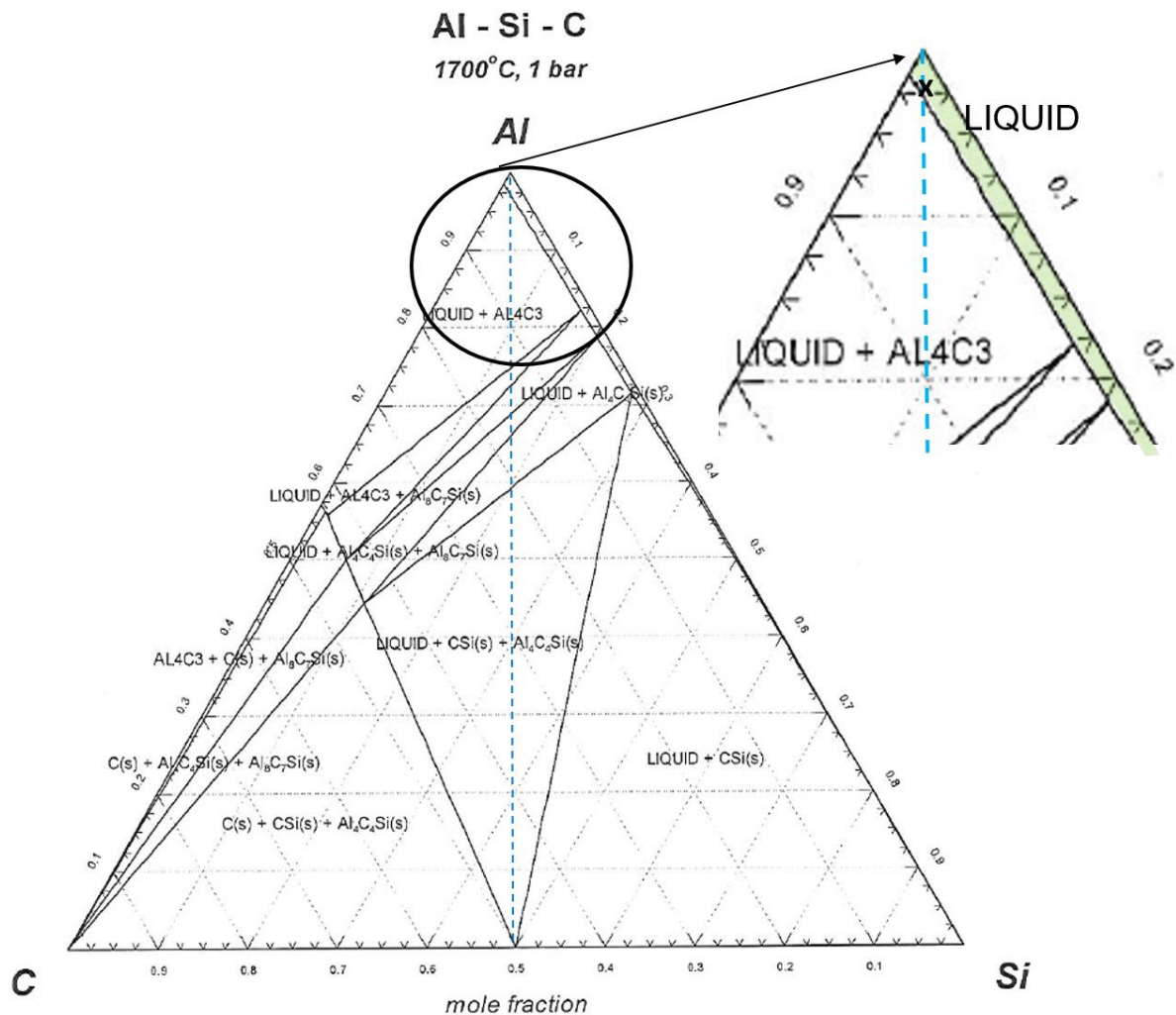


Figure 5.2: Al-Si-C isothermal section at 1700°C calculated by Factsage using the European database (SGTE). The raw composition is marked in the green area. .

Initially, the reactor was pumped out to achieve a vacuum lower than 10^{-3} mbar. At the beginning, the reactor was manually heated up to 1100°C with a constant power, this temperature being in the detecting range of the pyrometer. At that time, the chamber was filled with 800 mbar of high purity argon to prevent the sublimation of the materials. After that, the heating rate was fixed at 15°C/min until the growth temperature (1700°C) as controlled by the top pyrometer. The temperature was held at 1700°C for 6 hours. In the next step of the process, the reactor was cooled down to 1200°C with a cooling rate of 15°C/min. As a last step, the reactor was cooled down to room temperature by turning off the power. A scheme of the experiment receipt is represented in Figure 5.4.

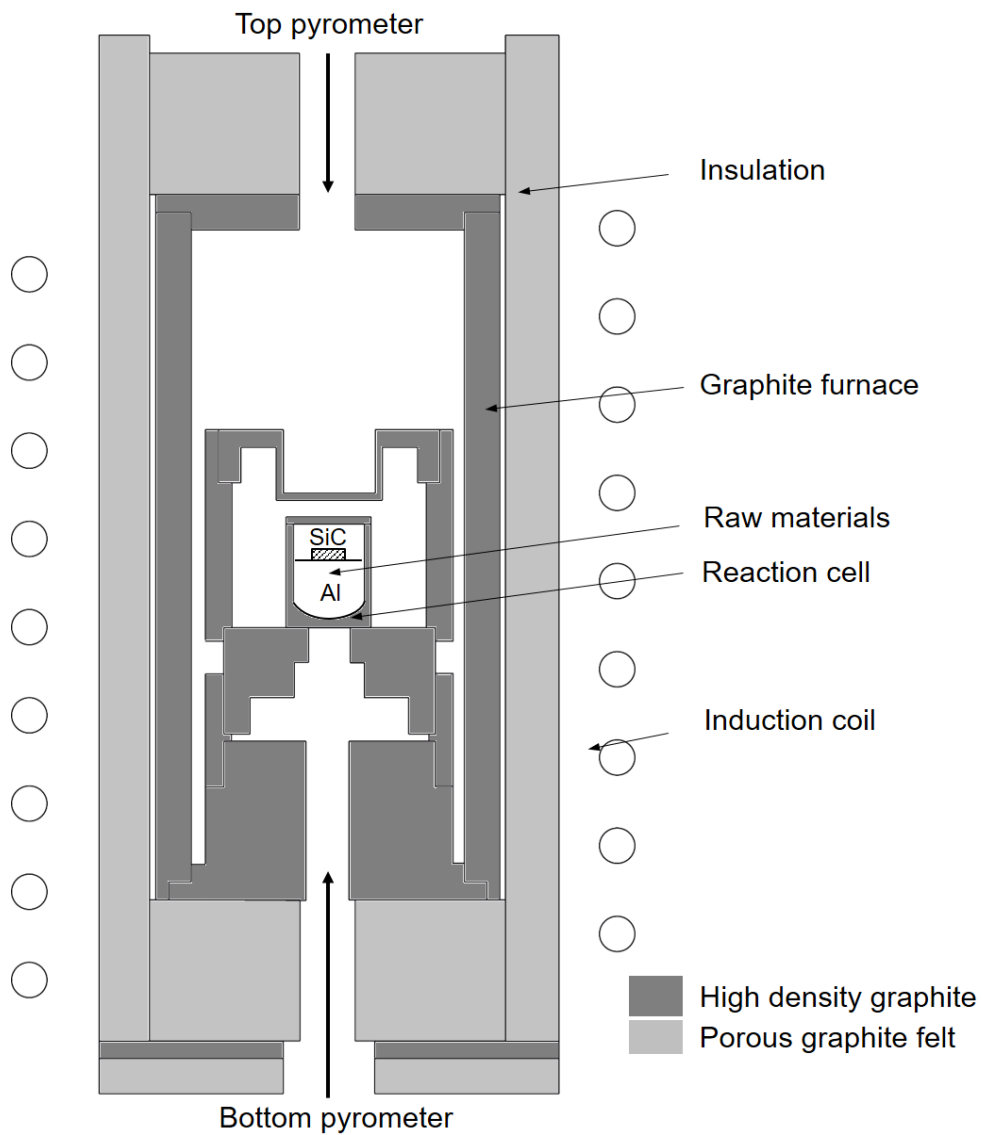


Figure 5.3: Experimental set-up used for the synthesis of Al_4C_3 crystals.

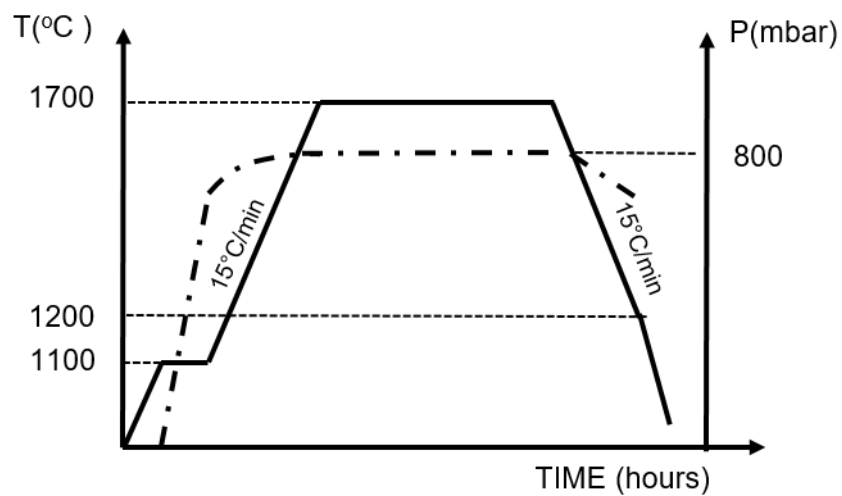


Figure 5.4: Receipt used for the synthesis of Al_4C_3 .

5.2.2. Experimental results

After the experiment, SiC was completely dissolved in liquid Al. Al_4C_3 single crystals with bright yellow color have been observed at the surface as shown in the Figure 5.5. Most of Al_4C_3 single crystals were embedded in the solidified melt. Although no selective etchant for extracting the crystals has not been found yet, a few Al_4C_3 single crystals in the millimeter scale were naturally dewetted at the end of the growth. We could thus characterize them by a variety of techniques including Raman, UV-Vis-NIR spectroscopy and X-ray diffraction.

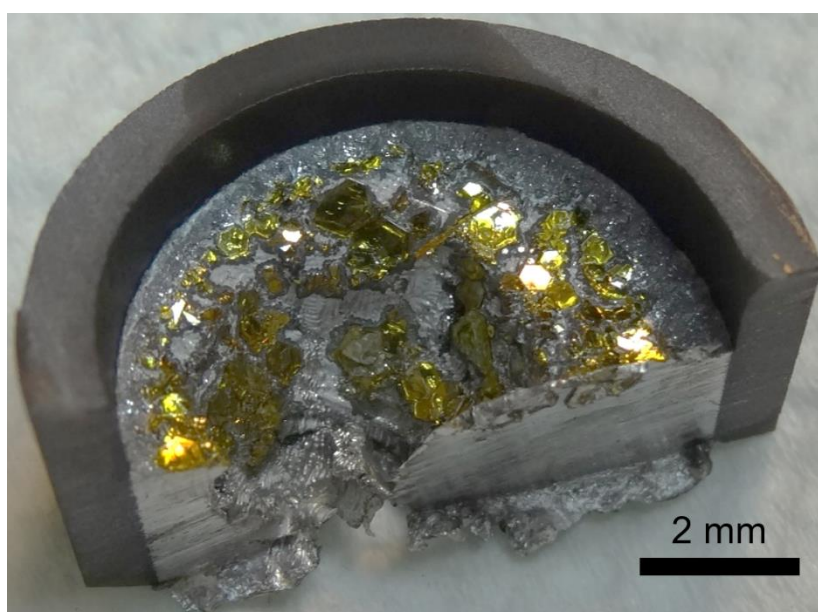


Figure 5.5: Camera picture of a crucible after experiment.

5.2.3. Characterizations of the Al_4C_3 single crystals

Raman spectroscopy. The Raman spectrum collected from the single crystals of Al_4C_3 is presented in the Figure 5.6. It is in agreement with the Raman spectrum reported in the literature¹⁴. Six Raman active modes including 3 modes E_g (252 cm^{-1} , 290 cm^{-1} , 717 cm^{-1}) and 3 modes A_{1g} (341 cm^{-1} , 492 cm^{-1} , 864 cm^{-1}) have been observed.

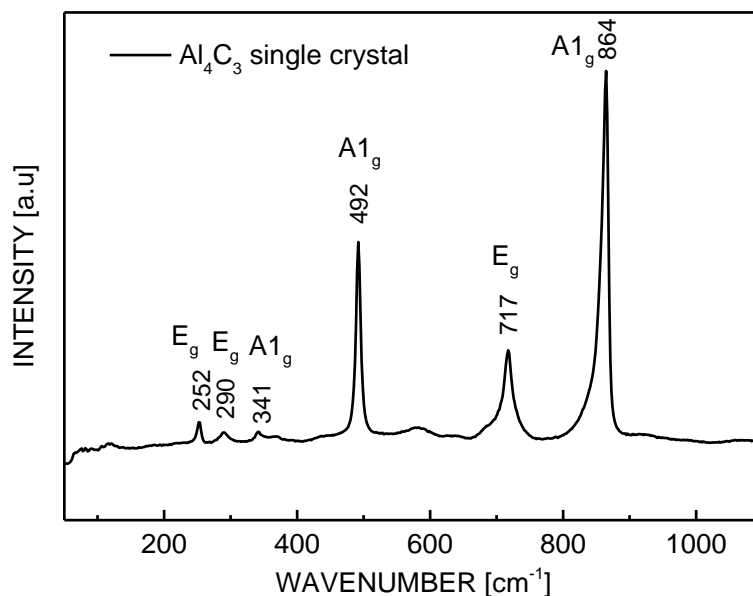


Figure 5.6: Raman spectrum collected from the single crystal of Al_4C_3 .

Optical properties. Similarly to Al_4SiC_4 , the electronic bandgap structure of Al_4C_3 was theoretically investigated by using density functional theory¹⁵ in 2008. An indirect bandgap of 1.02 eV has been reported for Al_4C_3 . However, this calculated value is not compatible with the yellowish color of the Al_4C_3 platelets observed experimentally.

Figure 5.7 shows the comparison between the absorption coefficients calculated from the absorption spectra of Al_4C_3 , Al_4SiC_4 and SiC-6H (n-doped) single crystals, which have been collected in the 250-2500 nm wavelength range at room temperature. For Al_4C_3 single crystals, the absorption edge is located around 2.3 eV which is slightly higher than the one of Al_4SiC_4 (2.1 eV). This measured optical bandgap is much higher than the calculated one reported in the literature. Thus, the reconsideration of the band structure calculation is necessary, however, it is beyond the scope of the present thesis.

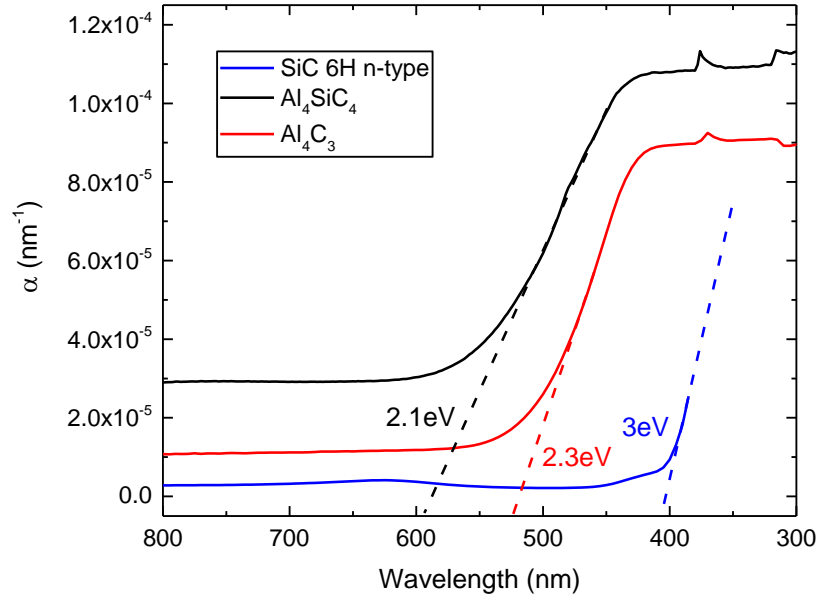


Figure 5.7: Absorption coefficients plotted as a function of incident wavelength of Al_4SiC_4 , Al_4C_3 , and SiC-6H n-type. The absorption edges are located at 2.1eV, 2.3eV and 3eV for Al_4SiC_4 , Al_4C_3 , and SiC-6H, respectively. The measurements have been conducted at room temperature 25°C.

X-ray diffraction: Diffraction analysis of the Al_4C_3 single crystals has been conducted in a θ - 2θ configuration. A sample holder with dome has been used to avoid the hydrolysis of the sample during the characterization. In fact, even using a desiccator for the storage, Al_4C_3 single crystals still degraded with time. The big crystals used for optical absorption characterization degraded into small pieces before the diffraction analysis, which exhibit a diffractogram similar to the poly-crystal as shown in the Figure 5.8. However, the preferred orientation [0001] of Al_4C_3 crystals can still be observed.

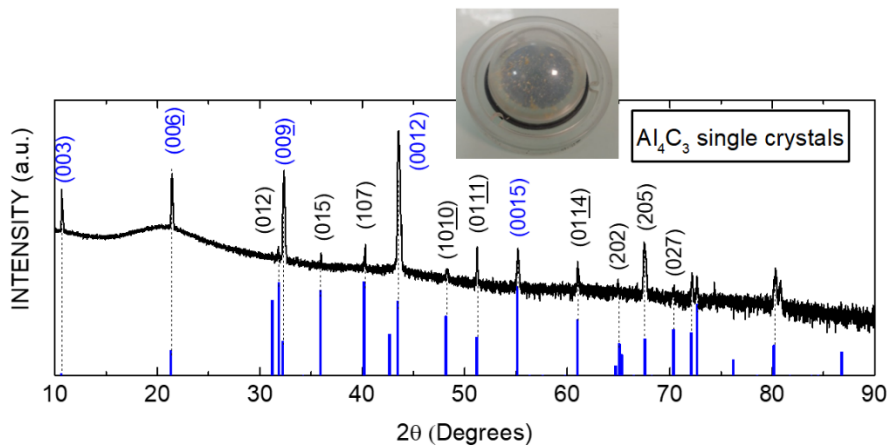
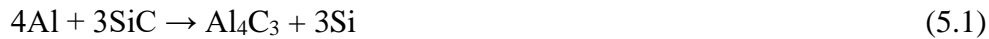


Figure 5.8: Diffractogram of the obtained Al_4C_3 single crystals. A sample holder with dome has been used to limit the hydrolysis of the crystals. The preferred orientation has been marked as blue color.

5.3. Al₄C₃/SiC hetero epitaxy

By analogy with the reactive CVD technique for the heteroepitaxial growth of 3C-SiC on Si substrate, we explored the possibility of forming Al₄C₃ epilayers on SiC by direct reaction between Al and SiC. This has also the advantage of protecting the formed Al₄C₃ upon air. Indeed, the Al₄C₃ layer is formed at the interface between the Al layer and SiC substrate. Therefore, the formed Al₄C₃ layer is protected by an Al cover.

The chemical interaction at the Al/ α -SiC interface has been investigated by Viala *et al.*^{11, 13} for the development of the α -SiC-reinforced aluminum composite materials. In this work, a full description of the reaction has been proposed, for a range of temperature varying from the melting point of aluminum (~650°C) to 1347°C. The system is characterized by a metastable equilibrium between α -SiC, Al₄C₃, and aluminum rich ternary liquid phase, which corresponds to the chemical reaction:



The mechanism and the kinetics of this reaction have been found strongly dependent on the polarity of the substrate. Indeed, the dissolution of SiC in liquid aluminum starts much more rapidly on the Si face than on the C face to form an Al₄C₃ layer at the interface¹³. For that reason, [0001] oriented Si-face SiC wafers have been chosen as substrates for the synthesis of the heterostructure with Al₄C₃.

Three different aspects will be discussed in the following. In the first part, the wetting behavior between liquid Al and SiC substrates will be discussed through morphological characterizations. In the second part, the mechanism and kinetics of the formation of Al₄C₃ will be considered by using HRTEM. Finally, electron diffraction and strain field analysis will be conducted in order to investigate the epitaxial relationship of the heterostructure, and the strain state of the Al₄C₃ layer.

5.3.1. Experimental process

An experimental process has been setup in order to fabricate the heterostructure Al₄C₃/SiC. In the first step, [0001] Si oriented hexagonal 6H-SiC substrates were covered by a polycrystalline Al layer. This Al layer, with a thickness of 650 nm was deposited on the Si face of SiC substrate by sputtering which had been done by using the CIME clean room facilities, and after deoxidization of the SiC surface by wet HF treatment (30 min in HF 50%).

The second step of the process is the annealing step. The annealing temperature varies from 700 to 900°C, and the duration of annealing varied from 5 min to 8 hours. All the parameters are gathered in the Table 5.2.

The annealing was performed in a quartz tube, resistive-furnace. The sample was contained in an alumina boat (Figure 5.9a). At the beginning, the furnace was pump out completely and then fill up with 1 atm of high purity Ar. After that, the reactor was heated up with a constant heating rate of 20°C/min until the annealing temperature. At the end of the annealing, the furnace was cooled down to ambient temperature with a constant rate of 20°C/min (Figure 5.21b).

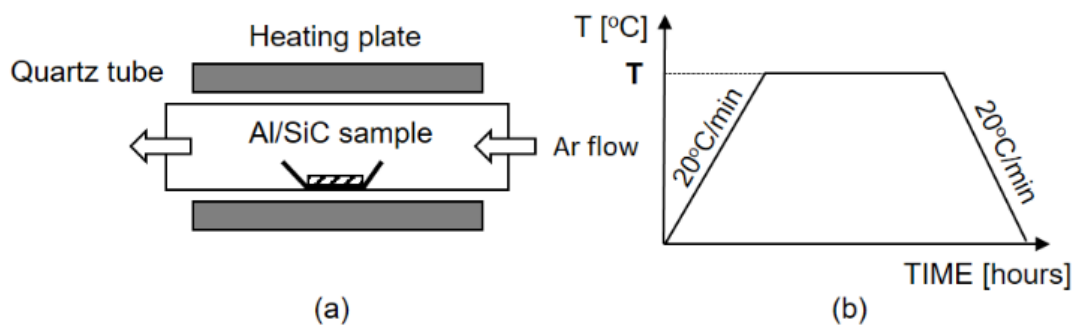


Figure 5.9: (a) Schematic drawing of the furnace. (b) Temperature profile of the heat treatment. T indicates the annealing temperature.

Table 5.2: Parameters of the annealing processes.

Substrate	Orientation	Temperature	Duration of annealing
6H-SiC	[0001]-Si face	800°C	5 min
6H-SiC	[0001]-Si face	800°C	2 hours
6H-SiC	[0001]-Si face	800°C	4 hours
6H-SiC	[0001]-Si face	800°C	6 hours
6H-SiC	[0001]-Si face	800°C	8 hours
6H-SiC	[0001]-Si face	700°C	8 hours
6H-SiC	[0001]-Si face	900°C	8 hours

The SEM coupled with EDS have been used to characterize the morphology and the chemical composition of the samples after annealing. For the secondary electron (SE) and backscattered electron (BSE) images, an electron beam with an energy of 15 keV has been used. For the EDS analysis, electron beams with lower energy of 10keV and 5keV have been used to reduce the interaction thickness of BSE, and thus to limit the contribution which could

come from the substrate. Moreover, by comparing the analysis results from different depths of interaction, the thickness of the probed layer could be estimated.

In fact, the maximum range of the interaction field in material is estimated by the simulation of the electron's trajectory. In this work, the simulation has been performed using the software Casino v.2.4 which is based on the Monte-Carlo method. The density of Al and SiC were used as input parameters which values of 2.7 and 3.21 g/cm³, respectively. For an incident electron beam of 5keV and 10keV, the maximum depth of interaction (d_{int}) in aluminum is estimated at ~300 nm and ~800 nm, respectively. As compared to the initial thickness of the Al layer, for incident electron beam of 5keV, the analyzed area is located inside the layer whereas for incident electron beam of 10keV, the interaction also propagates into the SiC substrate.

Phase analysis has been conducted by X-Ray Diffraction (XRD) using a Bruker D8 Advance diffractometer with the CuK α 1 radiation in the Bragg-Brentano configuration. After that, the interface of the heterostructure was characterized by HRTEM. The lamellas were prepared by using standard polishing procedures as described in chapter II.

5.3.2. Wetting behavior of Al/[0001] 6H-SiC system

Surface morphology and chemical composition

The Figure 5.10 presents the SE and BSE pictures of the top surface after annealing at 800°C during different time. For the reference sample and the sample annealed for 5 min, the surface morphology did not change and a homogenous contrast has been observed in the BSE pictures. After 2 hours, a surface roughness has appeared. Two different contrasts (dark and bright) have been observed in the BSE image as illustrated in Figure 5.10(f), which exhibits the coexistence of several phases. After longer annealing time such as 6 hours and 8 hours, the surface roughness increases whereas the bright contrast areas are slightly expanded. EDS analysis has been conducted on areas with different contrasts in order to analyze the chemical composition of the layer. The results of the EDS analysis are gathered in Table 5.3. The standard deviations of the measurements (at least two different positions for each measurement) are also given in the table.

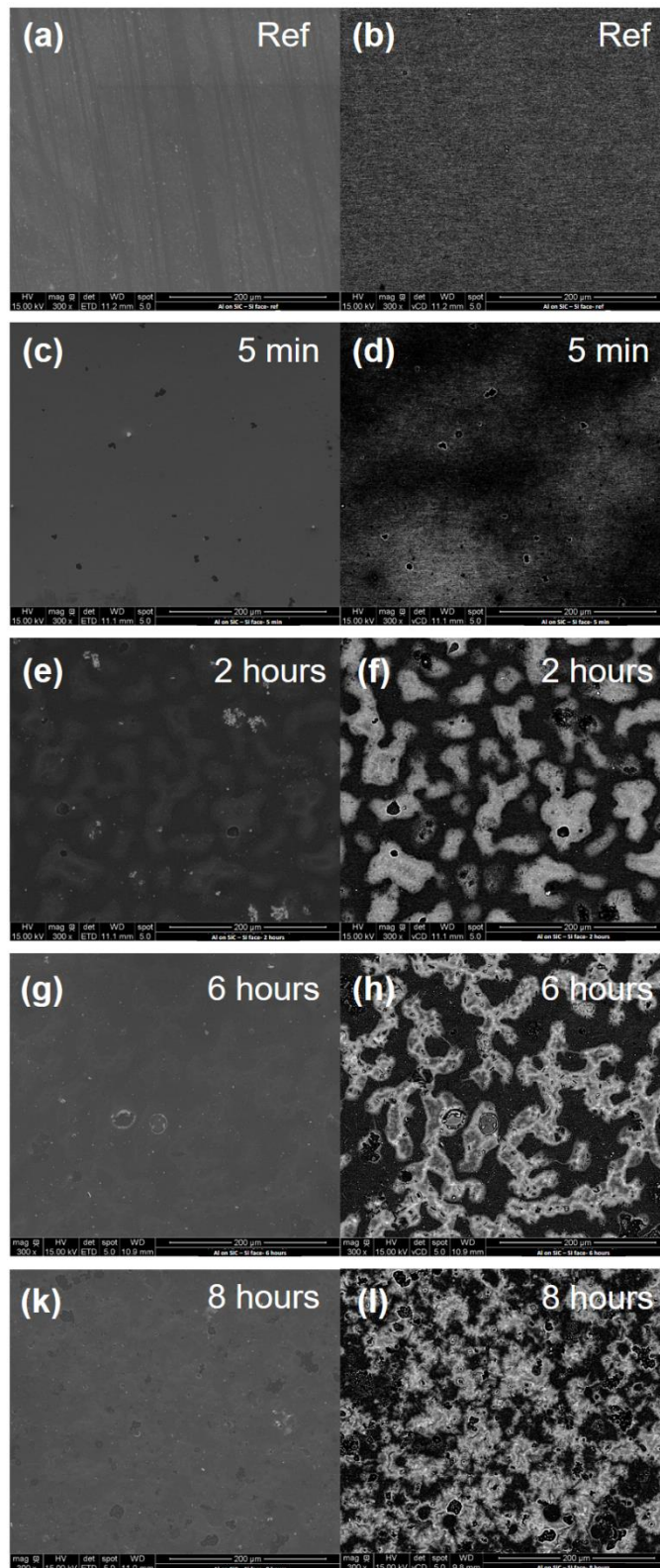


Figure 5.10: SEM photographs showing the evolution of morphology of samples at 800°C as a function of time: (a), (b) reference sample (before annealing); (c), (d) after 5 min; (e), (f) after 2 hours; (g), (h) after 6 hours; (k), (l) after 8 hours. (a), (c), (e), (g), (k) are SE images with corresponding BSE images ((b), (d), (f), (h), (l)).

Table 5.3: EDS quantitative analysis results collected from the Al/SiC samples after annealing at 800°C for different time. Beam energy of 5 keV and 10 keV have been used. The standard deviations (Std.) of the measures are also given.

		EDS analysis (% atomic)									
		5keV					10keV				
		Al	Si	C	O	Std.	Al	Si	C	O	Std.
Reference (before annealing)		94	1	5	1	0.1	73	18	9	0	0.1
After 5 min		86	2	3	9	0.1	75	19	4	2	0.1
After 2 hours	Dark zone	14	30	44	11	2.6	3	45	46	6	1.4
	Bright zone	59	5	19	18	3.7	65	6	19	10	2.1
After 6 hours	Dark zone	54	2	6	38	0.4	22	41	14	23	1.3
	Bright zone	56	1	7	36	1.9	78	2	5	15	1.2
After 8 hours	Dark zone	57	3	4	36	0.7	27	40	12	21	1.4
	Bright zone	63	1	3	32	0.9	77	1	6	16	1.2

However, due to the significant uncertainties of the carbon element quantification, the phase identification could not be done by this method. For that reason, the XRD analysis has been conducted to identify the phase composition of the layer.

Phase identification

The Figure 5.11 presents the X-ray diffraction data of the sample after annealing at 800°C during different time. After 2 hours, the (111) peak of Si and the (00012) peak of Al₄C₃ slightly emerged in the diffractogram. After 6 hours, Al₄C₃ phase formed with the preferred orientation [0001] which is parallel to the one of the SiC substrate. After 8 hours, beside the {0001} family peaks, some other orientations of Al₄C₃ phase developed along with the increase of the roughness of the deposited layer.

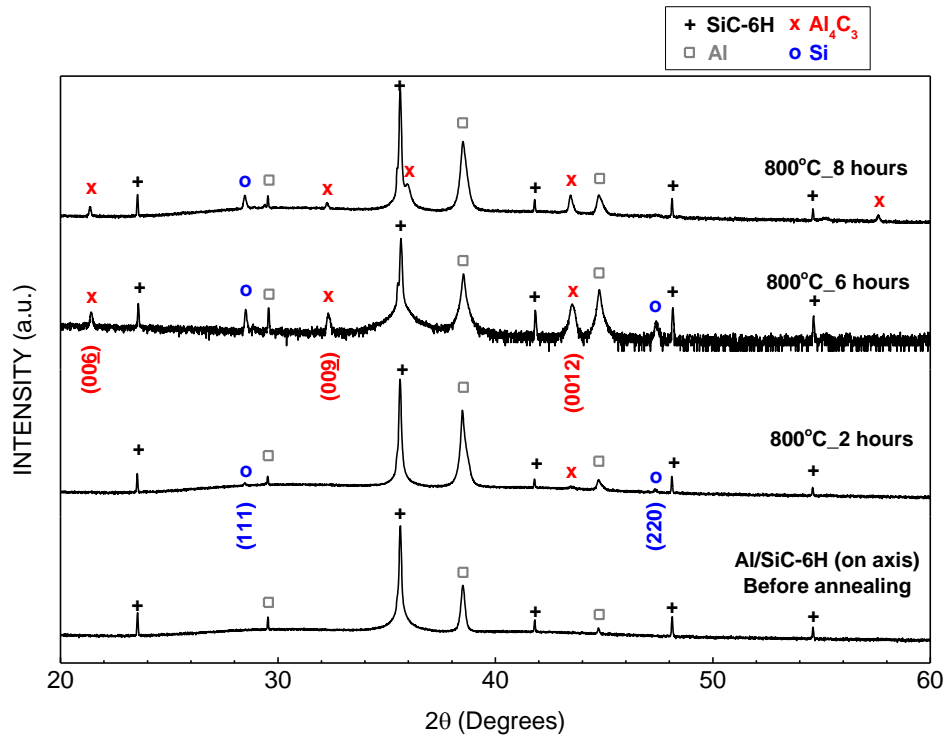


Figure 5.11: X-ray diffractograms collected from Al/SiC samples after annealing at 800°C during different time. The SiC substrate is of the 6H polytype and oriented toward [0001]. Al, Si, Al_4C_3 and SiC phases are tracked in the diffractograms and the preferred orientation of Al_4C_3 are also indicated.

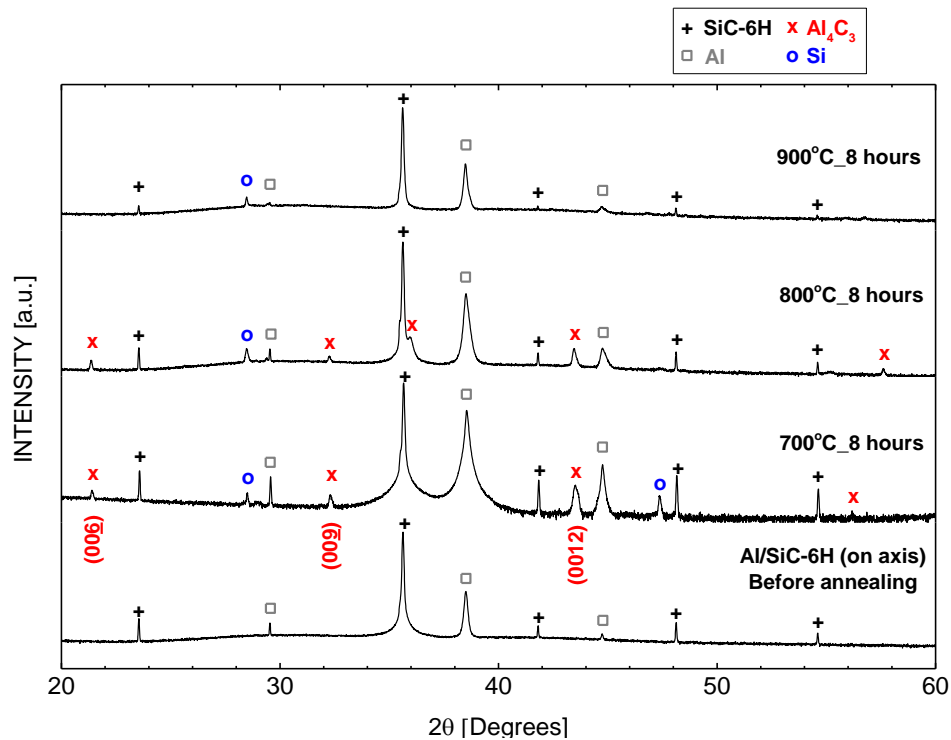


Figure 5.12: X-ray diffractograms collected from Al/SiC samples after annealing for 8 hours at different temperatures. The SiC substrate is of the 6H polytype, and oriented toward [0001].

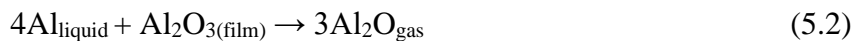
Al, Si, Al₄C₃ and SiC phases are tracked in the diffractograms and the preferred orientation of Al₄C₃ are also indicated.

Considering the effect of temperature, Figure 5.12 present the X-ray diffraction analysis of the sample after annealing for 8 hours at temperature varying from 700 to 900°C. At 700°C and 800°C, Al₄C₃ is found with a preferred [0001] orientation. However, at 900°C, Al₄C₃ peaks are not found.

Discussion

The wetting behavior between liquid Al and SiC substrate has been reconsidered by a series of experiments. After very short annealing time (5 min), no change has been observed. After 2 hours of annealing, beside different chemical composition indicated by different contrast in the BSE image (Figure 5.10f), the picture suggests the retraction of liquid Al on SiC under the effect of surface tensions. Indeed, with different beam energy of 5keV and 10keV, the composition of the dark contrast area does not change much, which is mainly associated to the composition of the SiC substrate. In the bright contrast area, even with a beam energy of 10keV, the composition is still in excess of Al and not perturbed by the SiC substrate. It demonstrates the increase of the layer thickness due to the retraction of liquid Al.

Actually, due to the dissolution-precipitation mechanism, which is the origin of the formation of Al₄C₃ at the interface, the wetting kinetic between liquid Al and SiC belongs the “reactive wetting” category. Such phenomenon has been investigated in the literature by performing sessile drop experiments in vacuum furnaces¹⁶⁻¹⁸. By considering the evolution of the contact angle (θ) and the radius of drop base as a function of time, three kinetic area could be distinguished as shown in the Figure 5.13(a). In the first area, since the temperature was increased from 660 to 800°C in about 15 min, θ sharply decreased from 160° to 110°, which has been explained by the elimination of the Al₂O₃ oxide film covering Al. Al liquid reacts with the oxide to produce Al₂O by the reaction below:



In the second wetting kinetic, by annealing at 800°C, the contact angle decreases slowly from 110° to 65°. It is attributed to the in-situ cleaning of the SiC surface. In fact, the silica film on SiC substrate slows down the de-oxidation kinetic of Al, which acts as an oxygen source for Al according the following reaction:



The resulting alumina layer on SiC continues to react with Al to produce the Al₂O by the reaction 5.2.

The third wetting kinetic corresponds to the nearly steady contact angle $\sim 55^\circ$. A very low decrease of θ has been observed due to the progressive replacement of the Al/SiC interface by an Al-Si/Al₄C₃ interface.

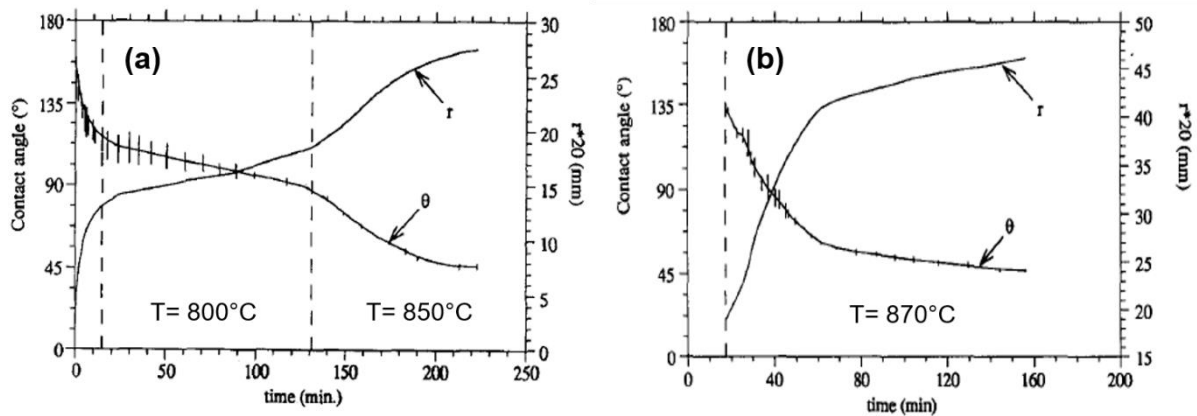


Figure 5.13: Contact angle and radius of drop base as function of time (a) showing the effect of temperature on the kinetics of wetting of Al on SiC, (b) at constant temperature.¹⁸

In the Figure 5.13(b), the evolution of the contact angle and radius of drop base at constant temperature has been presented. With higher temperature (870°C), the first and the second kinetic have been accelerated and not been easily observed. In this case, only 40 min was needed to reach the steady state instead of more than 3 hours at 800°C.

In our case, since SiC substrates had been cleaned by HF before the experiment and the Al polycrystalline layers had been deposited by sputtering in vacuum, we can avoid the oxide at the interface. Thus, the first and second stages could be neglected and the wetting behavior is only governed by the third kinetic which depends on the nucleation of Al₄C₃ at the interface. Unfortunately, we cannot measure directly the contact angle at the liquid/solid interface. However, it is possible to get an indirect estimation through the coverage ratio of Al on SiC surface. Indeed, the coverage ratio is calculated by image processing of the SEM pictures, using the ImageJ software. For the calculation, the contrast of the SEM image has first been adjusted, and then converted to a binary file as shown in the Figure 5.14.

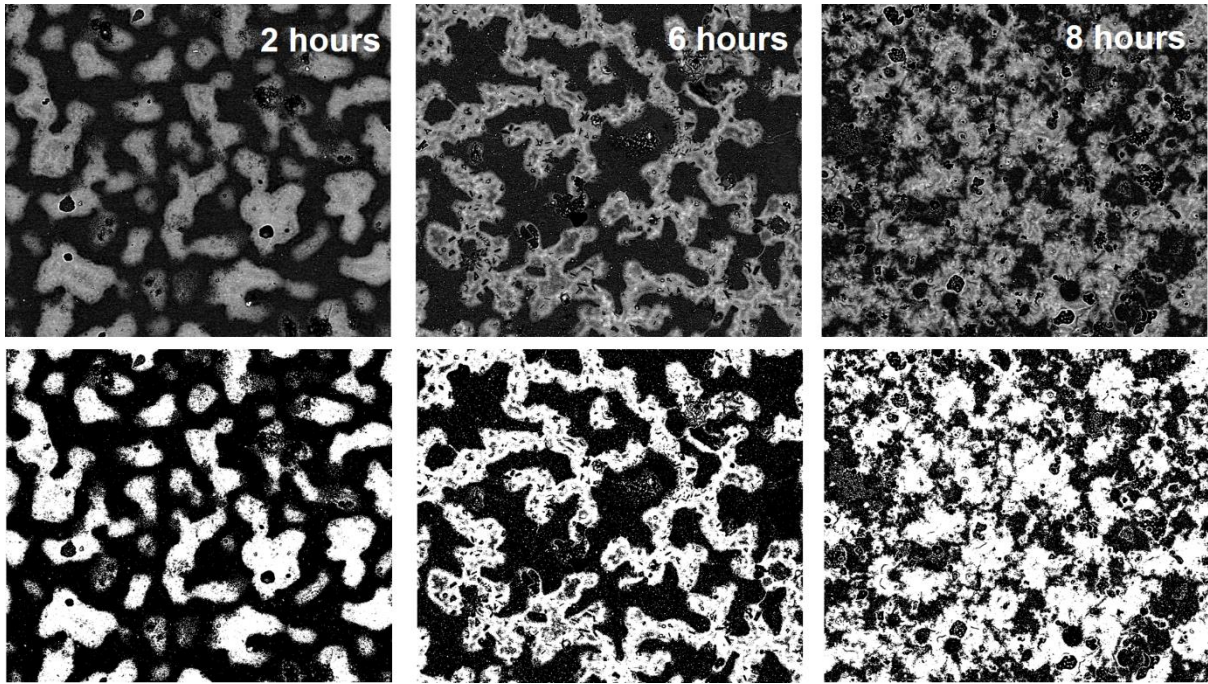


Figure 5.14: SEM images with the corresponding adjusted contrast images used for the coverage ratio calculation.

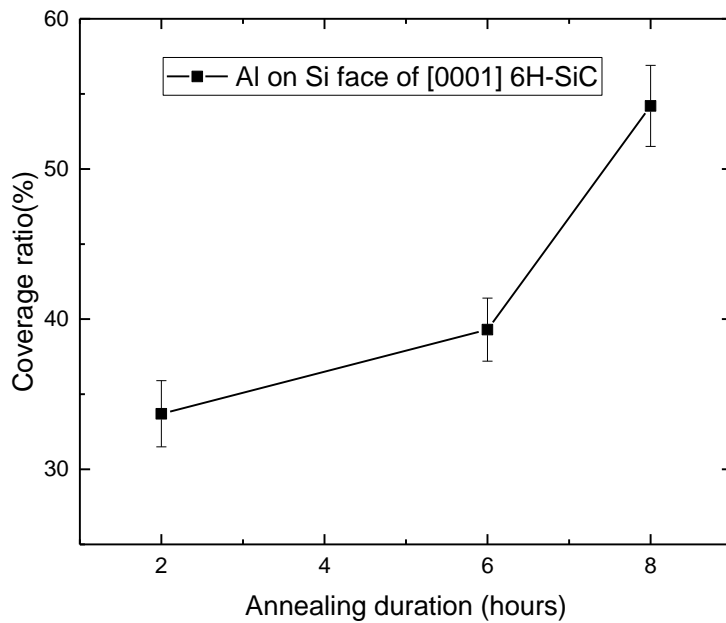


Figure 5.15: Coverage ratio of Al on Si face of [0001] 6H-SiC substrate as function of annealing time at 800°C.

As shown in Figure 5.15, the calculated coverage ratio of Al on Si face of [0001] 6H-SiC substrate increases with annealing time. It is associated to the decrease of the contact angle between liquid Al and SiC due to the development of Al_4C_3 layer at the interface. The formation of Al_4C_3 layer after 2 hours of annealing has been confirmed by the XRD analysis as shown in

Figure 5.11. Therefore, assuming that there is no loss of Al due to vaporization, a higher coverage ratio is expected for longer annealing time until it reaches a saturation value, which should correspond to the equilibrium wetting angle.

Concerning the effect of temperature, the increase of the reaction temperature (i.e. 900°C) leads to a higher dissolution rate¹³. Indeed, the Al₄C₃ layer formed at the interface in the early stage could not totally protect the SiC substrate from the dissolution. Thus, the liquid aluminum continued to dissolve SiC at a reduced rate while the Al₄C₃ layer was released from the interface. In this case, the Al₄C₃ layer may be tilted off the basal plane of the substrate, and does not meet the Bragg's law condition for the θ -2 θ scan. For that reason, Al₄C₃ peaks have not been found in the diffractogram shown in Figure 5.12.

Note that no oxide has been revealed in the diffractogram, the amount of oxygen measured by EDS came from the oxidation of the surface during storage. Therefore, the concentration of oxygen measured with beam energy of 10keV is always smaller than with beam energy of 5keV.

5.3.3. Dissolution-precipitation mechanism of Al/[0001] Si face 6H-SiC system

In this section, in order to investigate the dissolution-precipitation mechanism of Al/[0001] Si face 6H-SiC system at 800°C, the interface will be analyzed using HRTEM. The electron diffraction analysis will also be conducted on HRTEM images to identify the phases and the epitaxial relationship of the heterostructure Al₄C₃/SiC.

At first, the interface after annealing for 2 hours has been observed. A low magnification TEM image of the interface is presented in Figure 5.16. As observed, the surface morphology of the SiC substrate is characterized by island with a pyramidal shape. The top surface of the pyramid is covered by a very thin interfacial layer with thickness of 4.6 nm, whereas its sides are exposed to aluminum.

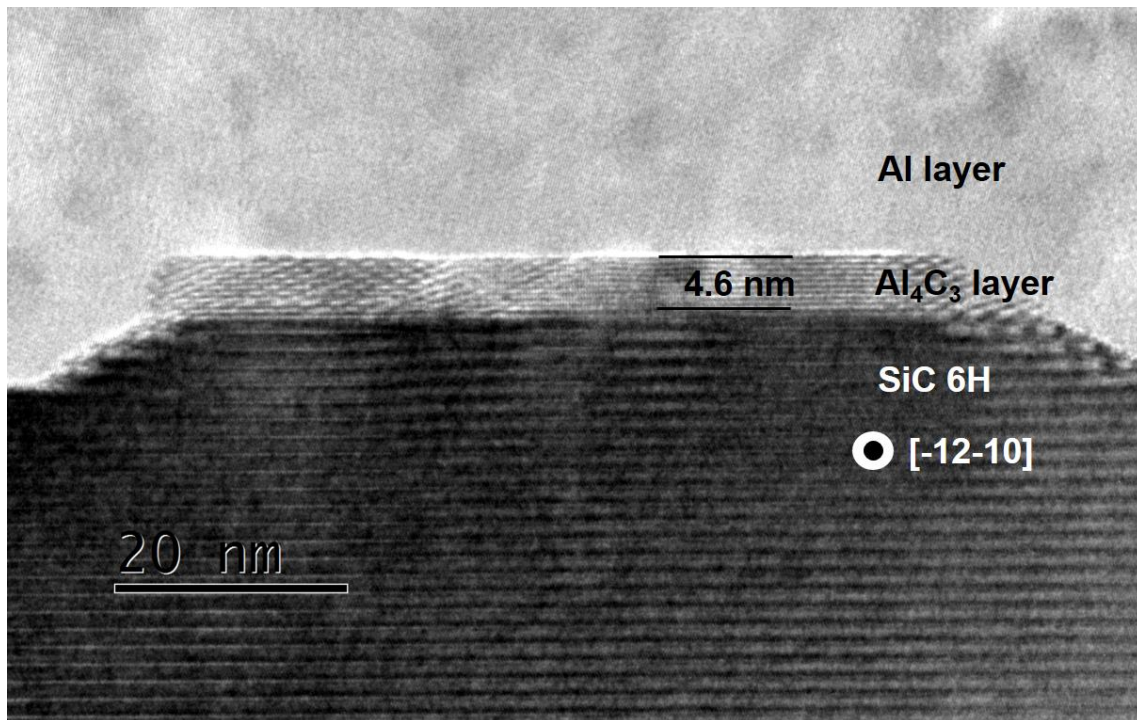


Figure 5.16: Low magnification TEM image of the interface between Al and SiC substrate after annealing at 800°C for 2 hours.

In order to identify the nature of the different layers, HRTEM images at the interface have been taken and a typical is presented in Figure 5.17. The indexing of the spatial frequencies on the fast Fourier transform (FFT) of each layer has been performed. Four different areas have been examined.

- In the area 1, the diffraction pattern of Al is identified, the $\{111\}$ planes are found as the strongest diffracted planes.
- The area 2 is taken on the interfacial layer between the SiC substrate and the Al layer. By indexing the FFT, this layer corresponds to the Al_4C_3 phase. The $\{0006\}$ planes of Al_4C_3 are perpendicular to the growth direction.
- In the area 3, the rectangle ROI (region of interest) is located on the perturbed structure of the interfacial layer. Beside of the Al_4C_3 FFT, some Al frequencies are found. It is probably due to the co-existence of Al and Al_4C_3 .
- In the area 4, the FFT of 6H-SiC substrate is revealed with the $\{0006\}$ planes being perpendicular to the growth direction. The SiC zone axis is $[-12-10]$.

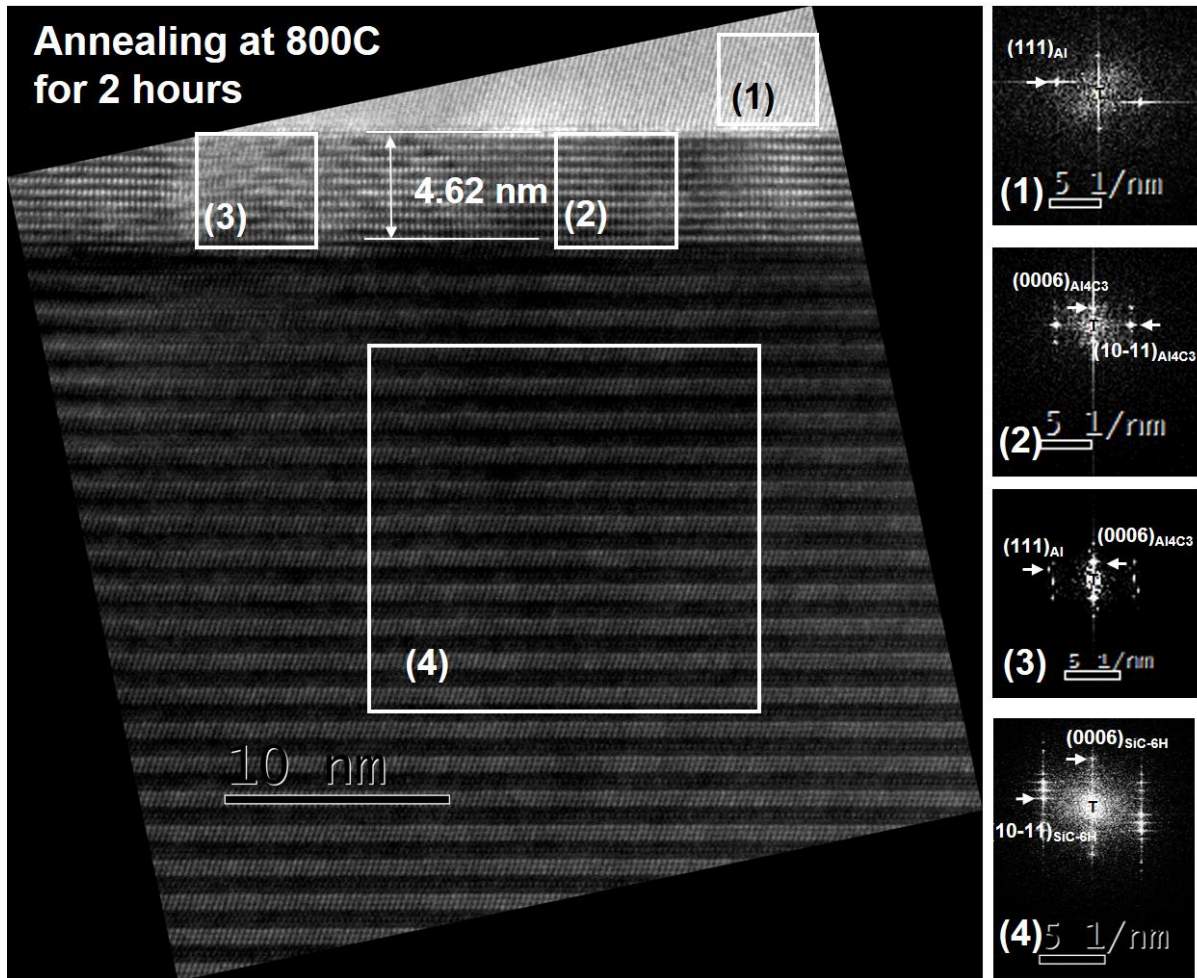


Figure 5.17: HRTEM image of the interface after annealing at 800°C for 2 hours and corresponding FFT of different areas such as: (1) Al layer; (2) and (3) intermediate layer; (4) 6H-SiC substrate.

As the reaction proceeds further, the sample after annealing for 4 hours is considered. Figure 5.18 presents a low magnification TEM image of the heterostructure of Al/Al₄C₃/SiC allowing the measure of the full thickness of the Al₄C₃ layer which was found equal to 309±1nm. It should be noted that the thickness of the initial polycrystalline Al layer was 650nm. Two indexed diffraction patterns are given in the inset (1) and (2) corresponding to the Al₄C₃ layer and SiC substrate, respectively. With the [-12-10] zone axis, {0003}, {10-11} planes of Al₄C₃ and {0006}, {10-11} planes of 6H-SiC are indexed.

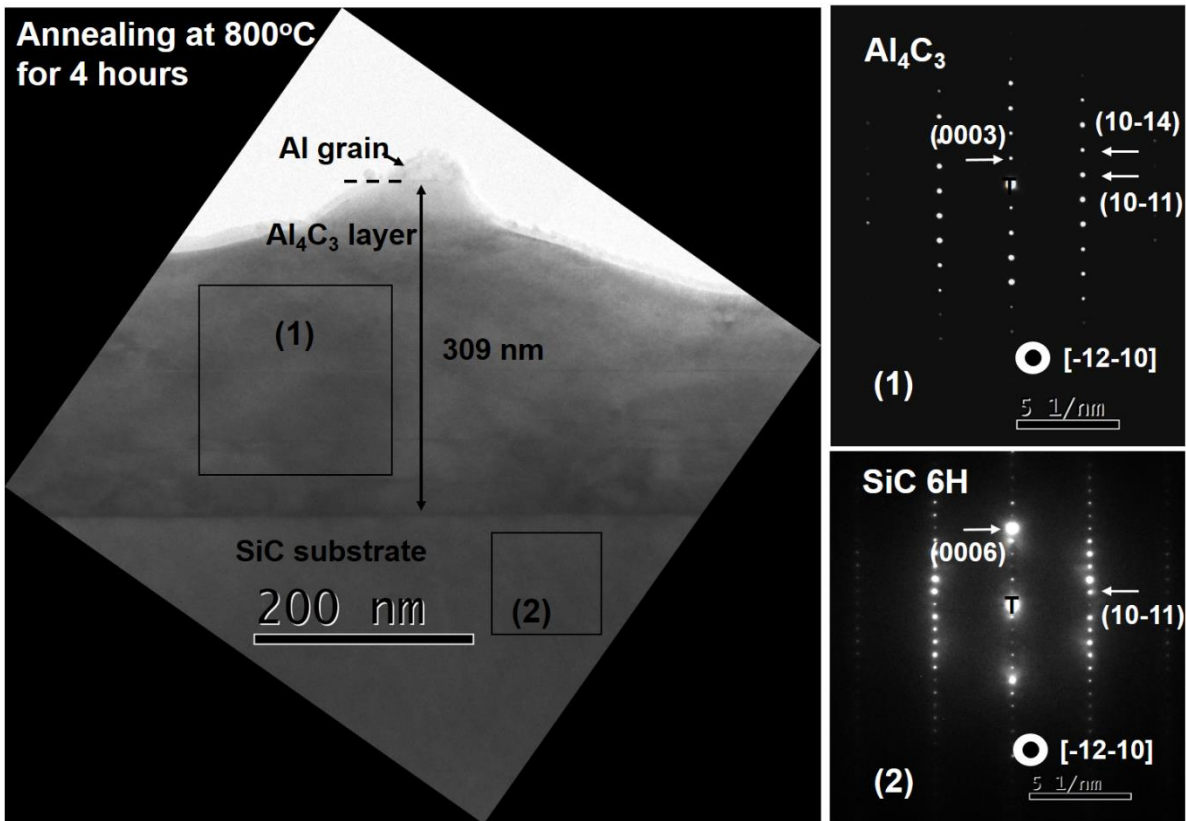


Figure 5.18: Low magnification TEM image of heterostructure after annealing at 800°C for 4 hours. The diffraction patterns of the inset pictures are also presented which were identified as (1) Al_4C_3 and (2) 6H-SiC.

A HRTEM image of the interface between Al_4C_3 and Al is given in the Figure 5.19. The FFT of two different areas are also gathered for the analysis.

- In the area 1, a grain of Al is identified in the corresponding FFT through the indexation of the 111, 200 and 1-1-1 spatial frequencies along the [01-1] zone axis.
- In the area 2, an Al_4C_3 layer is identified in the corresponding FFT along the [-12-10] zone axis, and [0006] is the growth direction.

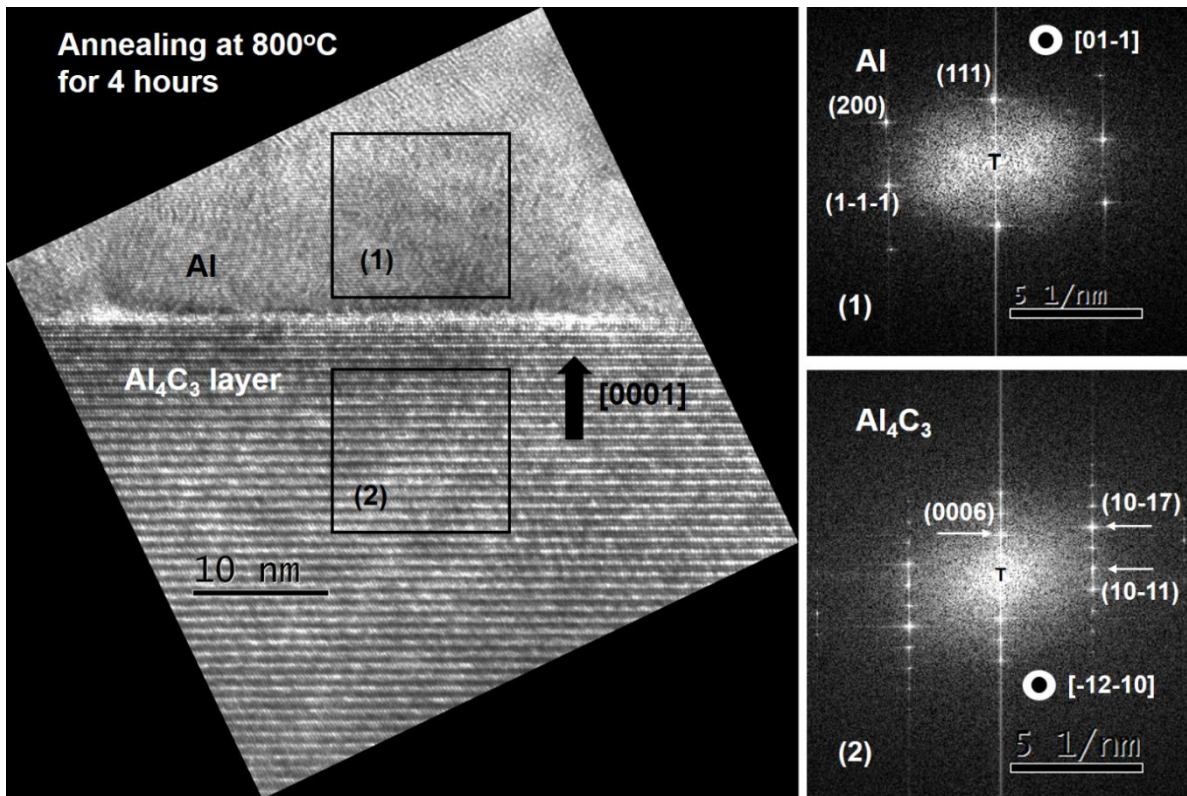


Figure 5.19: HRTEM image of the interface between Al and Al₄C₃ layer with corresponding FFT of different areas: (1) Al and (2) Al₄C₃. The sample was annealed at 800°C for 4 hours.

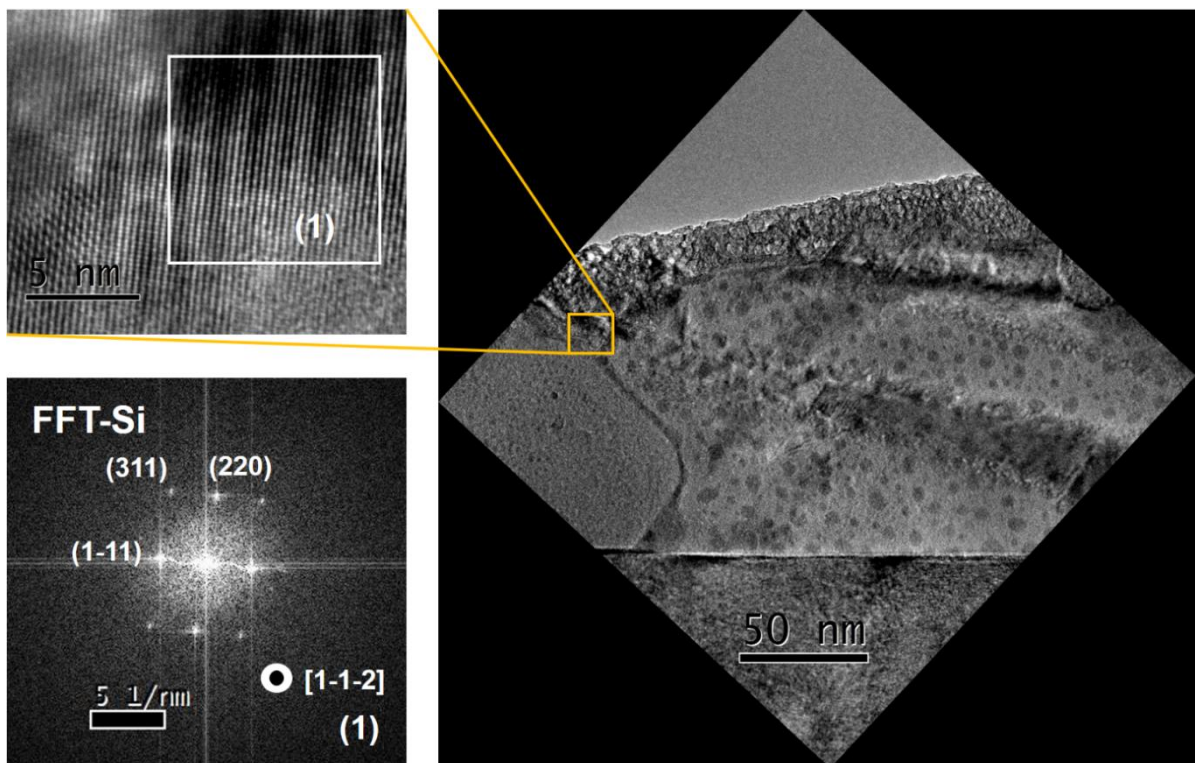


Figure 5.20: Low magnification TEM image of the heterostructure Al₄C₃/SiC. HRTEM image of the Si grain is given in the inset with the corresponding FFT. The sample was annealed at 800°C for 4 hours.

The Si phase, being a product of the reaction, was also observed. The Figure 5.20 presents the low magnification TEM image of the heterostructure. A grain of Si has been identified through the corresponding FFT given in the figure. It was found near to the surface of the cover layer and enclosed by aluminum. The spatial frequencies of 1-11, 220 and 311 have been indexed along the [1-1-2] zone axis.

Discussion

Through the observation of interface after 2 hours of annealing, the dissolution-precipitation mechanism of Al/[0001] Si face 6H-SiC system is investigated, which has good agreement with the mechanism reported by Viala et al. in 1994¹³.

This mechanism could be described by the schematic presented in Figure 5.21. At the beginning, the dissolution starts rapidly leading to the increase of the concentration of carbon and silicon in the liquid solution. The initial concentration of carbon in the liquid lies on the metastable prolongation of the liquid + SiC equilibrium curve (Figure 5.21a). Since the supersaturation condition for the nucleation is reached, Al₄C₃ phase crystallizes at the Al/ α -SiC interface. The concentration of C in liquid then decreases to reach the point A which corresponds to Al₄C₃ + L equilibrium. In this case, the gradient of C concentration acts as the driving force for the growth of Al₄C₃. The Al₄C₃ crystallites nucleate at the interface between Al and SiC, then extend laterally along the basal plane, and protect this surface against the dissolution Figure 5.21(b). Meanwhile, the erosion by dissolution continues in non-protected places leading to a typical surface morphology of the surface with many islands which have pyramidal shapes (Figure 5.21c) as observed in the Figure 5.16.

The thickness of Al₄C₃ epilayer increased with annealing duration. After 4 hours of annealing, an Al₄C₃ layer with thickness of 309 ± 1 nm has been observed. The Si released from the dissolution was rejected near the surface of the layer.

According to literature¹³, the dissolution-precipitation mechanism on the C face of SiC is rather different. The C face is quite stable against the dissolution into the liquid aluminum. The dissolution steps were just observed at the surface after a very long reaction time i.e. 1500 hours. For that reason, C face has not been chosen for developing the heterostructure by this mechanism.

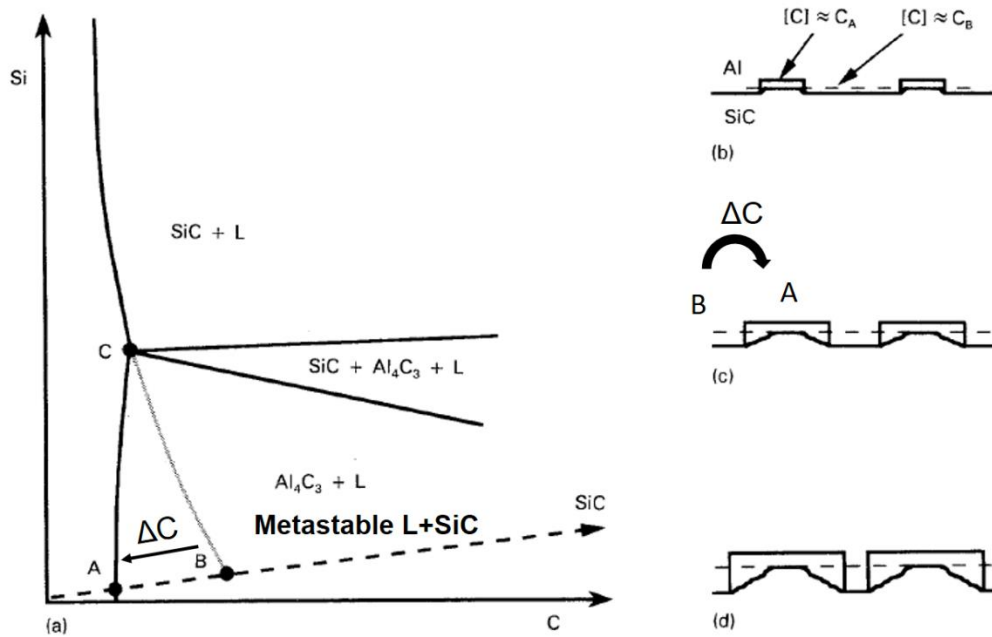


Figure 5.21: Schematic description of the dissolution-precipitation mechanism occurring at the Si face of α -hexagonal SiC substrate to liquid aluminum. (a) The aluminum rich partial Al-Si-C section at 800°C; (b), (c), (d) The nucleation and growth of Al_4C_3 ¹³.

Moreover, through the electron diffraction analysis, the epitaxial relationship between Al_4C_3 layer and [0001] oriented 6H-SiC substrate has been verified. The {0003} planes of Al_4C_3 are parallel to the {0006} planes of 6H-SiC which is also the growth direction. Moreover, the {10-11} planes of Al_4C_3 and the {10-11} planes of SiC make an angle of 3.5°, which has good agreement with the theoretical calculation. It could be compared with the literature, where thin foil specimens were prepared from samples consisting of an adhered aluminum drop on the SiC substrate which has been annealed at 800°C for 60 to 100 min under vacuum conditions⁷. As results, [0001] of Al_4C_3 is parallel to [0001] of SiC and [21-30] of Al_4C_3 is parallel to [21-30] of SiC.

In conclusion, the synthesis process based on the dissolution-precipitation mechanism is unlikely to produce a full Al_4C_3 layer coverage on SiC substrate due to the shortage of C source which is provided from the dissolution of SiC. However, the procedure is simple and still constitute a good basic for the synthesis of this heterostructure.

5.3.4. Strain field analysis

In this section, the strain field analysis using the Geometric phase analysis (GPA) method¹⁹,²⁰ will be conducted on the HRTEM images of the interface to study the strain state of the Al_4C_3 epilayer, and its evolution with annealing time.

Heterostructure of Al₄C₃/SiC after annealing at 800°C for 2 hours

At first, the nanoscale layer of Al₄C₃ formed on the top of pyramidal shape island is considered which has been observed at the interface after annealing at 800°C for 2 hours. The HRTEM image of Al/Al₄C₃/6H-SiC interface used for the GPA analysis is presented in the Figure 5.22(a) which gives the power spectrum shown in Figure 5.22(b). The strain analysis is conducted on various diffraction spots.

For the GPA strain analysis along the [0001] direction, a Gaussian mask with size of 0.5g has been used to select the frequency g as illustrated in the Figure 5.22(b). The GPA mask is placed on the position of the diffraction spot of (0006) planes of Al₄C₃ and (0004) planes of 6H-SiC substrate which has a bulk inter-planar spacing of 4.16 Å, and 3.77 Å, respectively. The power spectrum of the filtered Fourier transform is shown in Figure 5.22(c). The amplitude image and the phase image of the inverse filtered Fourier transform are given in Figure 5.22(d) and (e), respectively. The reference region has been chosen inside the 6H-SiC substrate supposing that the strain is zero in the substrate. As results, the strain field along the c axis is calculated as presented Figure 5.22(f).

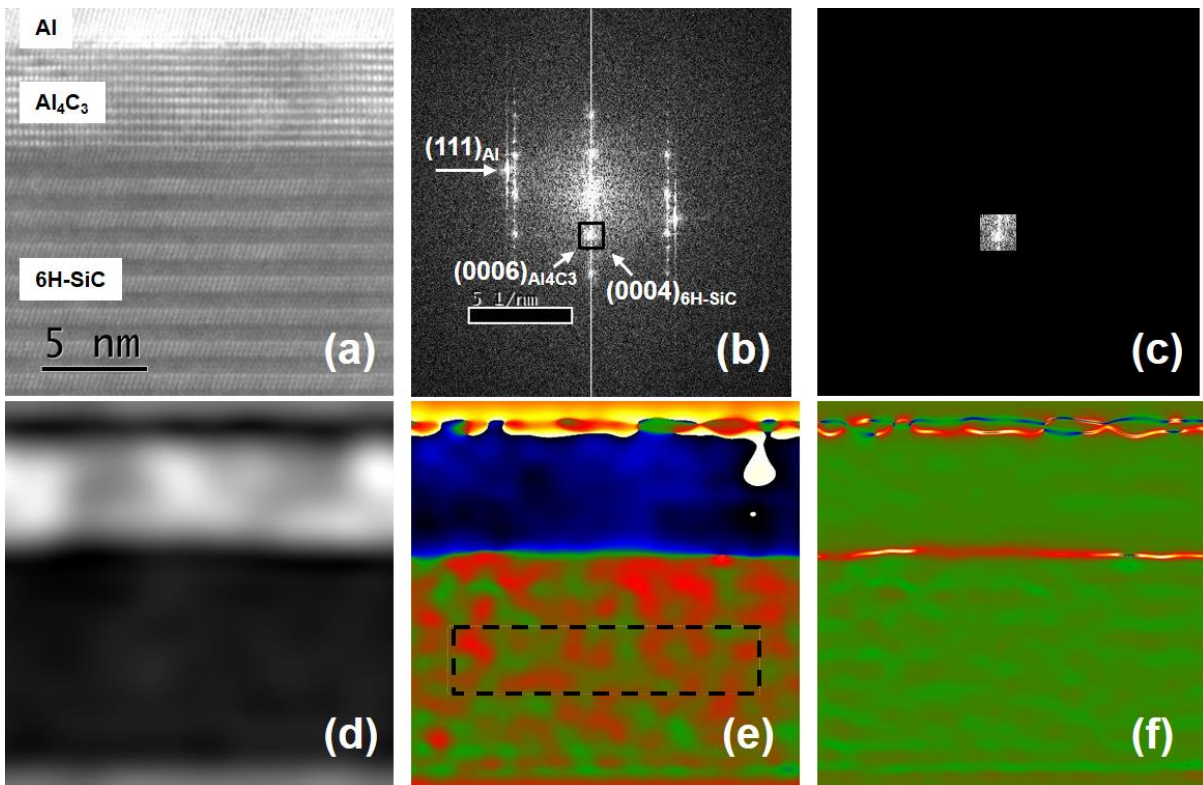


Figure 5.22: GPA strain analysis along the [0001] direction. (a) The high resolution TEM image of the interface. (b) Power spectrum of the image (a) allowing to select a frequency g by

a Gaussian mask, its position corresponds to the position of the diffraction spots of the plane $(0006)_{Al_4C_3}$ and $(0004)_{SiC}$. (c) The power spectrum of the filtered Fourier transform. (d) The amplitude image of the inverse filtered Fourier transform. (e) The phase image with the chosen reference region inside the SiC substrate. (f) The strain field along the c axis.

Noted that, for the selected diffraction spots, choosing SiC substrate as the reference, the lattice mismatch (Δd) between bulk Al_4C_3 and bulk 6H-SiC is:

$$\Delta d_{bulk} = \frac{d_{(0006)Al_4C_3} - d_{(0004)SiC}}{d_{(0004)SiC}} = 10.3\% \quad (5.4)$$

However, if we look the profile of the calculated strain field along the growth direction (Figure 5.23), the strain in Al_4C_3 layer and SiC substrate are almost zero along the c direction while a discontinuity is observed at the interfacial area. Or said differently, the Δd_{bulk} of 10.3% has been absorbed by the lattice structure of Al_4C_3 which is compressed in the c direction leading to a common diffraction spot of the (0006) plane of Al_4C_3 and the (0004) plane of SiC substrate.

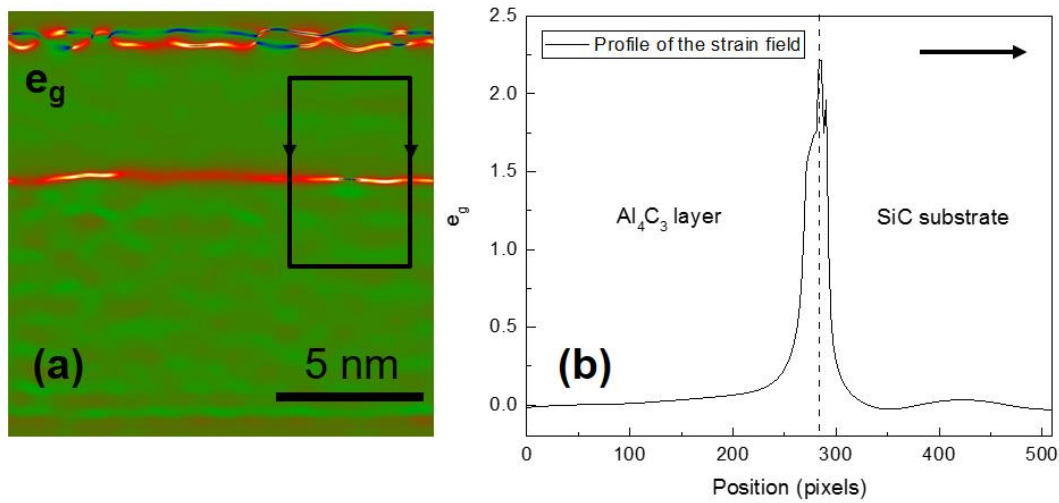


Figure 5.23: (a) GPA strain map along the $[0001]$ direction. (b) Strain profile corresponding to the outline presented in (a).

Next, the analysis has been conducted for another direction. The $(10-17)$ plane of Al_4C_3 and $(10-13)$ plane of SiC are considered which have a relaxed inter-planar spacing of 2.24 \AA and 2.35 \AA , respectively. For these planes, Δd between bulk Al_4C_3 and bulk 6H-SiC is:

$$\Delta d_{bulk} = \frac{d_{(10-17)Al_4C_3} - d_{(10-13)SiC}}{d_{(10-13)SiC}} = -4.6\% . \quad (5.5)$$

In the FFT of the Figure 5.24(a), a filter mask has been used to select the area which corresponds to the position of the (10-17) plane of Al_4C_3 and the (10-13) plane of SiC, as illustrated in the Figure 5.24(b).

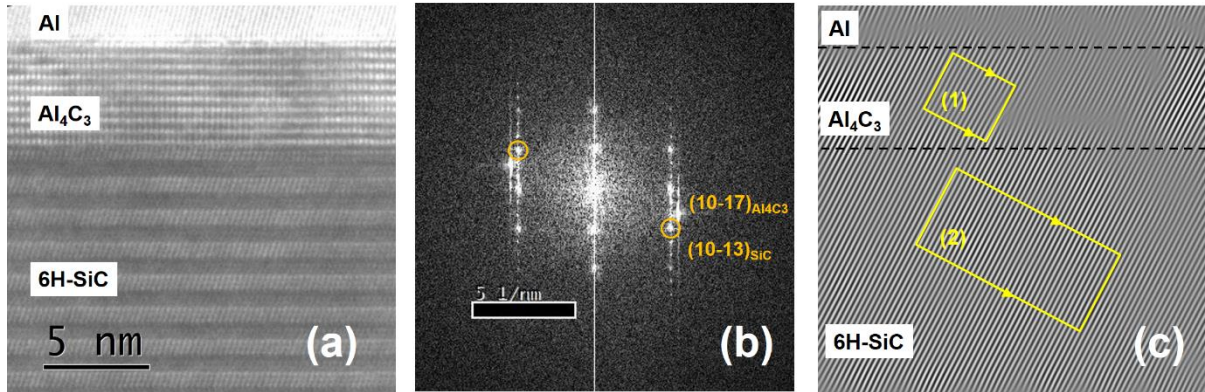


Figure 5.24: (a) HRTEM image of the Al/ Al_4C_3 /6H-SiC interface. (b) Power spectrum of the image (a), the common diffraction spot of the plane $(10-17)_{\text{Al}_4\text{C}_3}$ and $(10-13)_{\text{SiC}}$ has been selected by a mask. (c) The Bragg image of the masked area.

From the Bragg image of the masked area presented in Figure 5.24(c), we compare the interplanar spacing between the Al_4C_3 epilayer and the 6H-SiC substrate. The profiles of the interplanar spacing corresponding to Al_4C_3 and SiC areas are presented in Figure 5.25. As results, a common interplanar spacing of $2.34 \pm 0.01 \text{ \AA}$ has been found in both areas, which corresponds to the bulk $d_{(10-13)}$ of the 6H-SiC. It means that the (10-17) plane of Al_4C_3 and the (10-13) plane of SiC have a common diffraction peak which demonstrates the expansion of lattice structure of Al_4C_3 along the a direction.

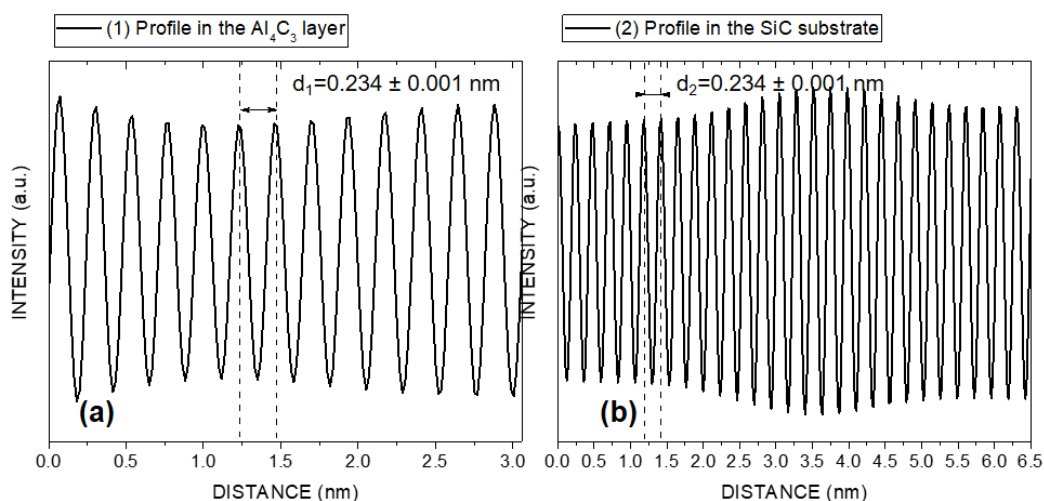


Figure 5.25: Intensity profiles corresponding to different outlines presented in the figure 5.16(c): (a) the outline (1) located in the Al_4C_3 layer, (b) the outline (2) located in the 6H-SiC substrate.

Heterostructure of $\text{Al}_4\text{C}_3/\text{SiC}$ after annealing at 800°C for 4 hours

For a longer annealing duration, the lattice structure of Al_4C_3 epilayer after 4 hours of annealing is analyzed. Unfortunately, in our TEM lamella, the interface of $\text{Al}_4\text{C}_3/\text{SiC}$ is not transparent under the electron beam. Instead, the interface between the Al and Al_4C_3 is analyzed which is presented in the Figure 5.26(a).

First, a Gaussian mask with size of 0.5g has been used to select the area in the power spectrum as illustrated in Figure 5.26(b), which corresponds to the position of the diffraction spots of the $(-111)_{\text{Al}}$ and $(10-14)_{\text{Al}_4\text{C}_3}$ planes. The bulk interplanar spacing of $(-111)_{\text{Al}}$ and $(10-14)_{\text{Al}_4\text{C}_3}$ plane are 2.338 and 2.617 Å, respectively. The amplitude image and phase image of the inverse filtered Fourier transform with the reference region selected in aluminum are shown in Figure 5.26(d) and (e).

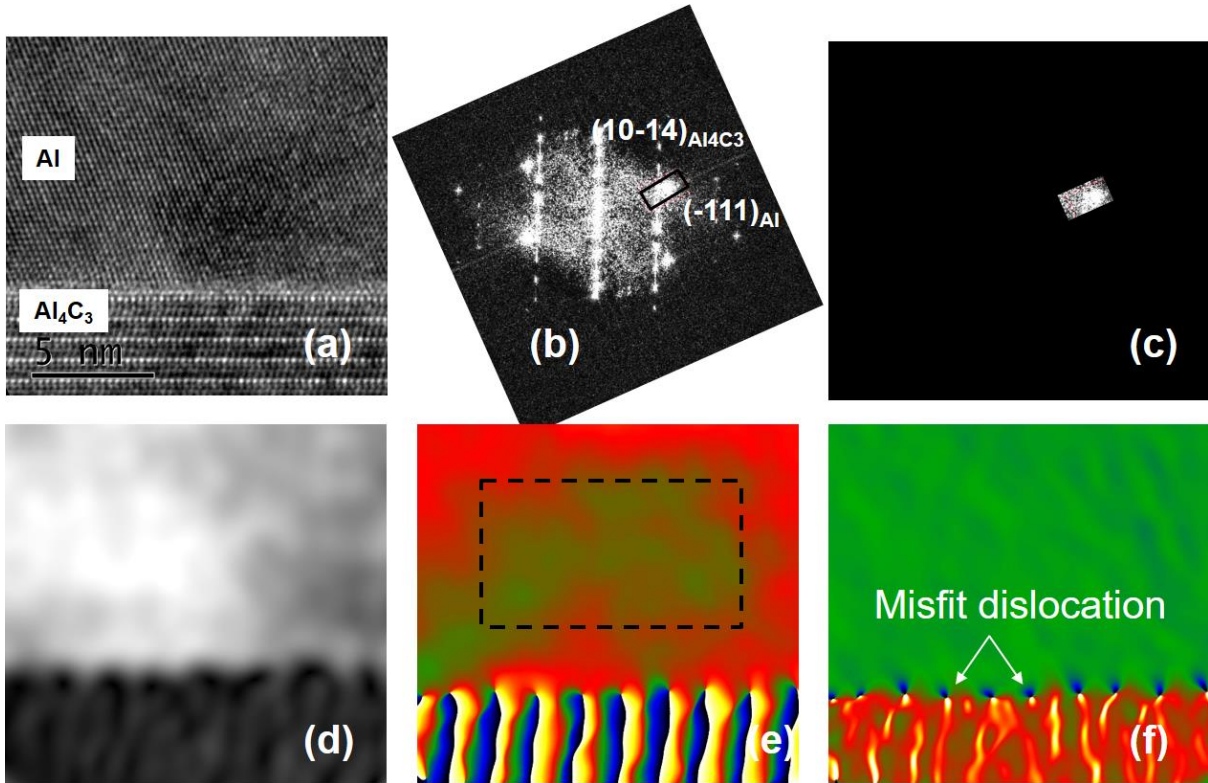


Figure 5.26: GPA analysis at $\text{Al}_4\text{C}_3/\text{Al}$ interface. (a) The high resolution TEM image of the interface. (b) Power spectrum of the image (a) allowing to select a frequency \mathbf{g} indicated by a Gaussian mask, which corresponds to the position of the diffraction spots of the plane $(-111)_{\text{Al}}$ and $(10-14)_{\text{Al}_4\text{C}_3}$. (c) The power spectrum of the filtered Fourier transform. (d) The amplitude image of the inverse filtered Fourier transform. (e) The phase image with the chosen reference region inside the aluminum. (f) The calculated strain field.

The calculated strain field is presented in the Figure 5.26(f) and the strain profile at the interface is considered in the Figure 5.27. Since Al is chosen as the reference area, the strain in Al is zero, whereas the calculated strain in the Al_4C_3 area has an average value of $13.4 \pm 0.35\%$ which corresponds to the equation:

$$e_{\text{Al}_4\text{C}_3} = \frac{d_{(10-14)\text{Al}_4\text{C}_3} - d_{(-111)\text{Al}}}{d_{(-111)\text{Al}}} \quad (5.6)$$

From the FFT, the diffraction spot of (-111) plane of Al is identified, the inter-planar spacing $d_{(-111)}$ of Al is 2.338 \AA . By using the equation (5.6), the calculated inter-planar spacing $d_{(10-14)}$ of the Al_4C_3 epilayer is $2.65 \pm 0.01 \text{ \AA}$.

Moreover, an array of misfit dislocations is observed at the interface which exhibits a discontinuity in the strain profile.

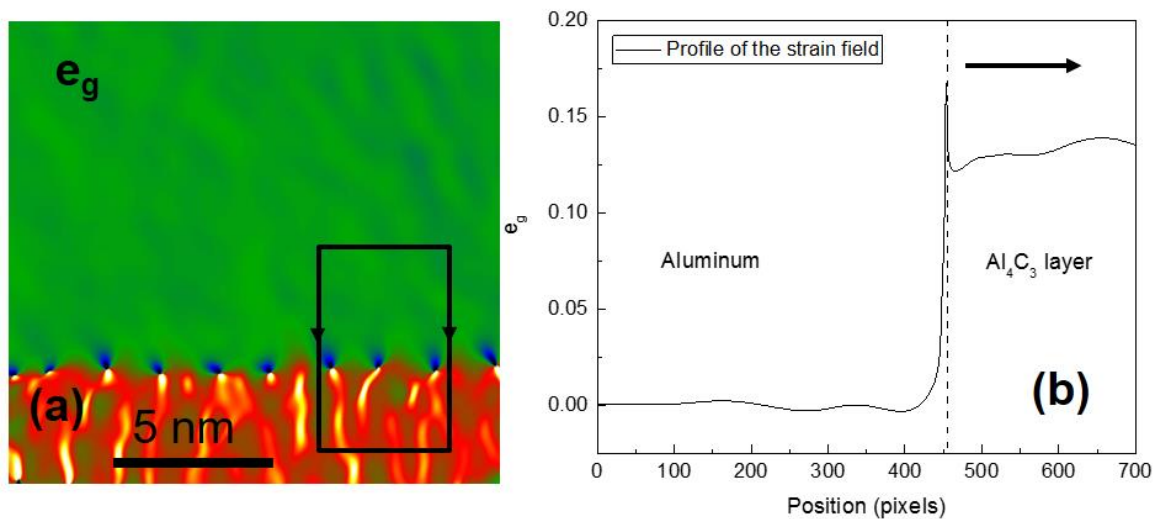


Figure 5.27: (a) The result GPA strain map. (b) Strain profile corresponding to the outline presented in (a).

Next, the analysis is conducted along the c axis. In the FFT image presented in the Figure 5.28(b), a mask has been used to select the area which corresponds to the position of the diffraction spot of $(00012)_{\text{Al}_4\text{C}_3}$ planes. The Bragg image of the masked area is presented in the Figure 5.28(c) which exhibits well-periodic fringes in the Al_4C_3 area. The intensity profile corresponding to the outline marked in the Al_4C_3 epilayer is given in Figure 5.29. Based on that, the interplanar spacing $d_{(00012)}$ of the Al_4C_3 epilayer is measured which has value of $2.10 \pm 0.01 \text{ \AA}$.

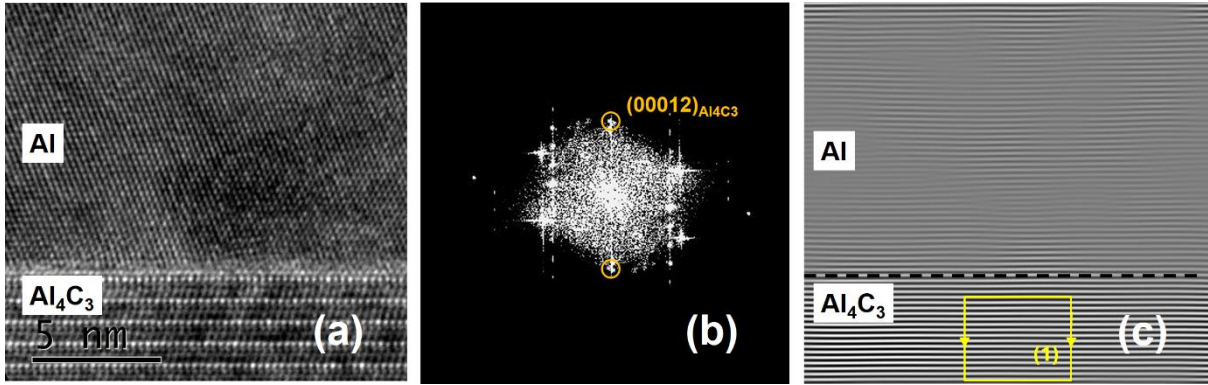


Figure 5.28: (a) HRTEM image of the interface Al/Al₄C₃. (b) The fast Fourier transform of (a), a mask has been used to select the area corresponding to the diffraction spot of the (00012)_{Al₄C₃} plane. (c) The Bragg image of the masked area, an outline of profile is taken in the Al₄C₃ epilayer.

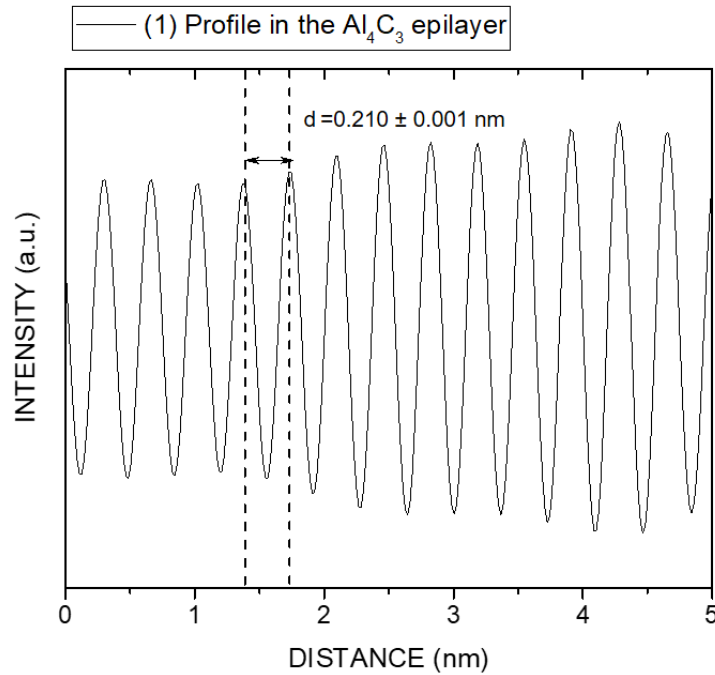


Figure 5.29: Intensity profiles corresponding to the outline presented in the Figure 5.28(c).

Discussion

In summary, after 2 hours of annealing, a biaxial strain has been investigated in the lattice structure of Al₄C₃ epilayer by the GPA strain analysis.

In the [0001] direction, the same interplanar spacing value has been found for both (0006) plane of Al₄C₃ and the (0004) plane of SiC substrate. It demonstrates the compression of the lattice structure of Al₄C₃ in the [0001] direction. The calculated lattice constant c of the Al₄C₃

epilayer is $22.62 \pm 0.01 \text{ \AA}$ which is smaller than the relaxed lattice constant of Al_4C_3 ($c_{\text{bulk}} = 24.98 \text{ \AA}$).

In order to maintain the cell volume, an expansion in the basal plane has been conducted. Indeed, the interplanar spacing of the (10-17) plane of Al_4C_3 epilayer has extended to the one of the (10-13) plane of SiC which has value of $2.34 \pm 0.01 \text{ \AA}$.

In this case, the lattice constant a of the Al_4C_3 epilayer could be calculated by the relation between interplanar spacing d and (hkl) planes in the hexagonal structure²¹:

$$\frac{1}{d^2} = \frac{4}{3} \left(\frac{h^2 + hk + k^2}{a^2} \right) + \frac{l^2}{c^2} \quad (5.7)$$

For the (10-17) plane of Al_4C_3 epilayer, we have:

$$\frac{1}{d_{(107)}^2} = \frac{4}{3} \left(\frac{1}{a_{\text{epi}}^2} \right) + \frac{7^2}{c_{\text{epi}}^2} \quad (5.8)$$

Thus, a_{epi} is $3.92 \pm 0.03 \text{ nm}$ which is higher than the bulk lattice constant of Al_4C_3 ($a_{\text{bulk}} = 3.329 \text{ \AA}$). As compared to the lattice constant of SiC ($a = 3.0815 \text{ \AA}$), we have a high lattice mismatch Δa of 27%. With such a high mismatch, a possible relaxation mechanism could be through the introduction of basal misfit dislocations at the interface, which are expected to be with $a_{\text{Al}_4\text{C}_3} / a_{\text{SiC}} = 13/10$ as shown in the simple lattice model given in Figure 5.30. Unfortunately, our HRTEM images cannot elucidate this hypothesis.

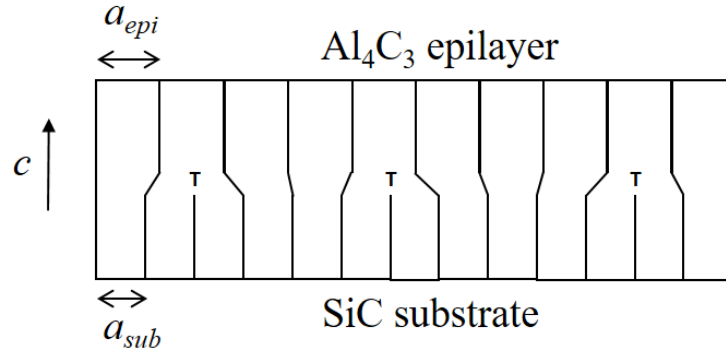


Figure 5.30: A schematic diagram showing the epitaxial relationship of the heterostructure after 2 hours of annealing.

Based on the linear elasticity theory for the case of a hexagonal crystal (appendix), the relationship between the elastic constants and the strained lattice constants of the Al_4C_3 epilayer is given by the function:

$$\frac{c_{\text{epi}}}{c_{\text{bulk}}} = 1 - 2 \frac{C_{13}}{C_{33}} \frac{a_{\text{epi}} - a_{\text{bulk}}}{a_{\text{bulk}}} \quad (5.9)$$

The calculated value reported in the literature²² for the C_{13}/C_{33} ratio is:

$$\left(\frac{C_{13}}{C_{33}} \right)_{cal} = \frac{52}{391} = 0.133 \quad (5.10)$$

Taking into account the equation 5.9 and the measured a_{epi} value of Al_4C_3 , an c_{epi} value of 23.80 Å is calculated giving a $d_{(0006)}$ of 3.97Å. When comparing with the $d_{(0004)}$ of 6H-SiC (3.773Å), a difference of 5% is calculated. It means that the Al_4C_3 is also strained along c and that the dominant relaxation mechanism of the Al_4C_3 layer is through a biaxial strain. Although no dislocation has been observed at the interface under the [-12-10] zone axis, there presence should be considered. It should be noticed that the introduction of dislocation is not a consequence of the plastic relaxation mechanism but as a part of the biaxial strain mechanism.

Since the nucleation of Al_4C_3 at the interface experiences a constraint in the growth direction by the liquid Al, an estimation of critical thickness of the Al_4C_3 epilayer could not be done using the energy balance theory²³. Further, due to the high lattice mismatch between Al_4C_3 and SiC substrate ($f = 8\%$), this theory is not applicable.

After 4 hours of annealing, the lattice constant c_{epi} and a_{epi} are also calculated from the measured interplanar spacing of (00012) planes and (10-14) planes by using the relation 5.7.

$$\begin{cases} \frac{1}{d_{(0012)}^2} = \frac{12^2}{c_{epi}^2} \\ \frac{1}{d_{(104)}^2} = \frac{4}{3} \left(\frac{1}{a_{epi}^2} \right) + \frac{4^2}{c_{epi}^2} \end{cases} \quad (5.11)$$

$$\Rightarrow \begin{cases} c_{epi} = 12 \cdot d_{(0012)} \\ a_{epi} = \sqrt{\frac{4}{3 \left(\frac{1}{d_{(104)}^2} - \frac{4^2}{c_{epi}^2} \right)}} \end{cases} \quad (5.12)$$

$$\Rightarrow \begin{cases} c_{epi} = 25.2 \pm 0.12 \text{ \AA} \\ a_{epi} = 3.37 \pm 0.01 \text{ \AA} \end{cases} \quad (5.13)$$

For the comparison, the lattice constants of the Al_4C_3 epilayer for different experimental conditions and the Al_4C_3 bulk are gathered in the

Table 5.4. In order to evaluate the strain state of the epilayer lattice structure, we define the strain of the epilayer as compared to the bulk: $\Delta a/a$ and $\Delta c/c$ by the following equations:

$$\frac{\Delta a}{a} = \frac{a_{Al_4C_3-epi} - a_{Al_4C_3-bulk}}{a_{Al_4C_3-bulk}} \quad (5.14)$$

$$\frac{\Delta c}{c} = \frac{c_{Al_4C_3-epi} - c_{Al_4C_3-bulk}}{c_{Al_4C_3-bulk}} \quad (5.15)$$

Table 5.4: Lattice constant of Al_4C_3 epilayer for different experimental conditions compared with Al_4C_3 bulk (diffraction pattern: 03-065-9731).

Samples	Lattice constant (Å)		Strain of lattice constants in epilayer as compared to bulk (%)	
	a	c	$\Delta a/a$	$\Delta c/c$
Al_4C_3 bulk	3.329	24.98		
Al_4C_3 epilayer-800°C-2 hours	3.92 ±0.03	22.6 ±0.01	17.7	-9,5
Al_4C_3 epilayer-800°C-4 hours	3.37 ±0.01	25.2 ±0.12	1.3	0.8

As results, from 2 hours to 4 hours of annealing, with the increase of thickness, the in-plane component strain reduce from 17.7% to 1.3% whereas the out-of-plane component reduce from -9.5% to 0.8%. According to these small residual strains after 4 hours of annealing, the Al_4C_3 epilayer is nearly relaxed. The biaxial strain observed after 2 hours of annealing was probably elastically relaxed.

5.4. Al_4SiC_4/SiC hetero epitaxy

As mentioned in the previous chapter, a heterostructure of Al_4SiC_4 on [0001] oriented hexagonal SiC substrate has been obtained by the sublimation process. From the X-ray diffraction analysis, the growth direction of the Al_4SiC_4 layer has been investigated and found parallel to the orientation of the SiC substrate. In this section, using the HRTEM, the epitaxial relationship and strain field at interface of Al_4SiC_4/SiC heterostructure are analyzed for different type of hexagonal SiC substrates.

5.4.1. Experiments

The epilayer of Al_4SiC_4 with thickness of 50 μm are grown by sublimation growth process on different [0001] oriented C face hexagonal SiC substrates: on-axis 6H polytype and 4° off-axis 4H polytype. Source materials were composed of a mixture of high purity powders of Al_4C_3 (Alfa Aesar, 99+% purity) and SiC (Sika tech E301) with a molar ratio $X_{Al_4C_3}=0.2$. A

same experimental process as presented in chapter IV has been used. The growth temperature was 1800°C and the pressure was 300 mbar. The deposition duration was 2 hours with a temperature difference of 29°C between source and seed in order to avoid the condensation of parasitic phases. The receipt of the experimental process is illustrated in Figure 5.31.

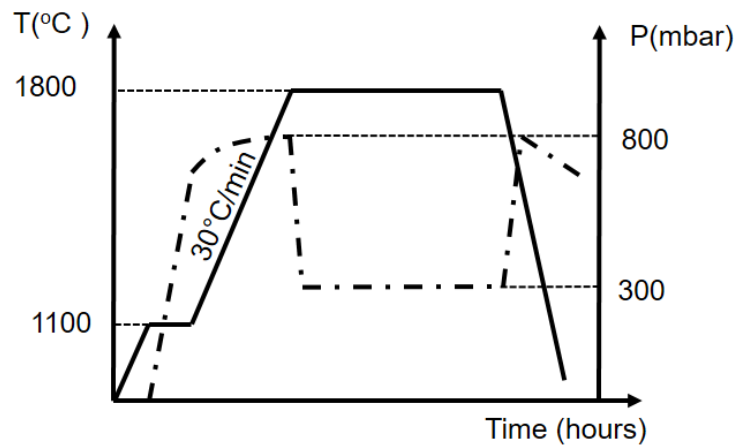


Figure 5.31: Receipt of the sublimation process.

For the TEM observation, the lamellas were prepared using standard polishing procedures as described in chapter II. The diffraction and strain field analysis are conducted on the HRTEM images in order to identify the phases and investigate the crystallographic relationship between the Al_4SiC_4 deposit and the SiC substrate.

5.4.2. Residual oxygen in the system

As mentioned in chapter IV, the oxygen that exists in the raw materials such as Al_4C_3 and SiC powder could cause the formation of parasitic phases near the interface at the early stages of the growth. Indeed, by the TEM observation, a parasitic layer with thickness of 50 nm has been found at the interface between Al_4SiC_4 and 4° off axis [0001] oriented 4H-SiC substrate as shown in the Figure 5.32. A composition with almost 20 atomic% of oxygen has been revealed by the EDS analysis.

Based on the composition given by EDS results and the diffraction pattern shown in Figure 5.33, the parasitic phase of Al_2OC is identified which belongs to the $\text{P6}_3\text{mc}$ space group (diffraction pattern: 01-072-3584) with the measured lattice parameters: $a=3.145\text{\AA}$ and $c=5.043\text{\AA}$. The inclusion of Al_2OC due to the residual oxygen is a common phenomenon in the Al-rich environment sublimation growth process, the sublimation growth of AlN on SiC substrate²⁴ for example. From the diffraction analysis, we found that Al_2OC has the same growth orientation with SiC substrate. However, in [0001] direction, the highest intensity

diffraction peak (0002) of Al_2O_3 ($2\theta = 35.605^\circ$) is very close to the (0004) of 4H-SiC ($2\theta = 35.66^\circ$) and the (0006) of 6H-SiC ($2\theta = 35.69^\circ$). Thus, the existence of Al_2O_3 has not been easily observed in the diffractograms collected from the samples (Figure 5.34).

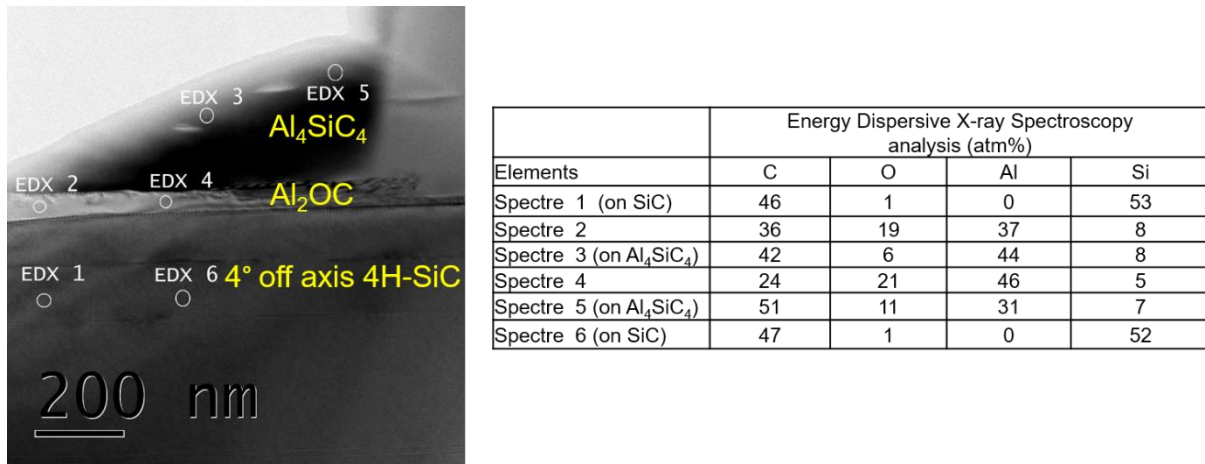


Figure 5.32: TEM image of the Al_4SiC_4 /4H-SiC interface with Al_2O_3 inclusion. The EDS analysis with corresponding analyzed position in different layer are given.

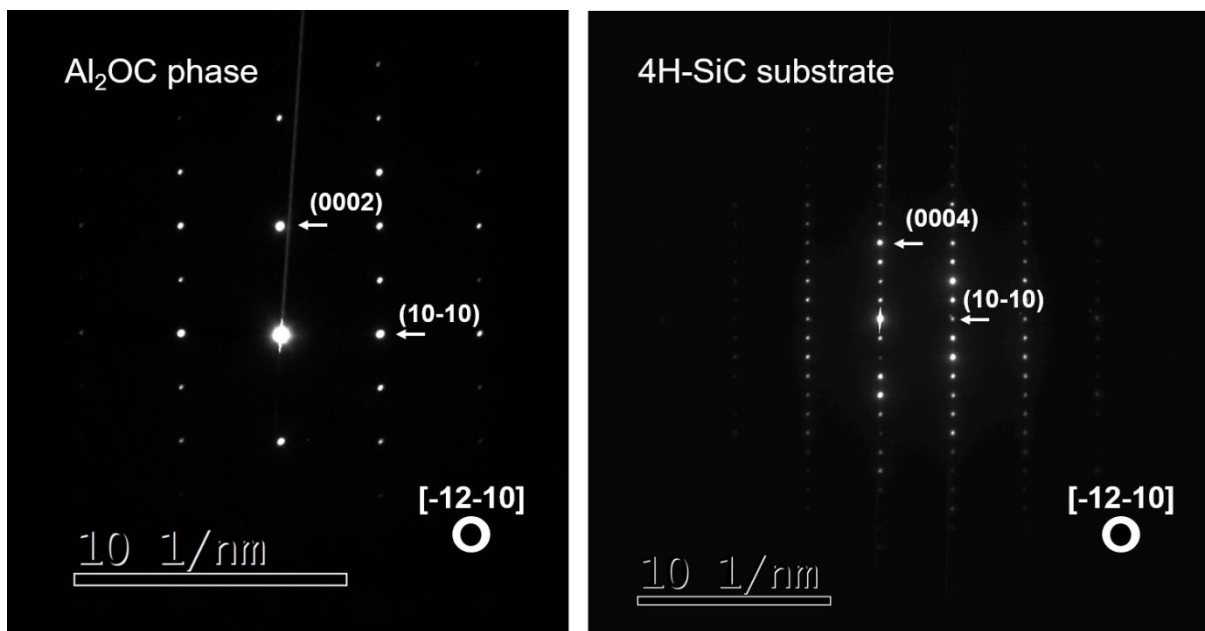


Figure 5.33: Diffraction pattern of Al_2O_3

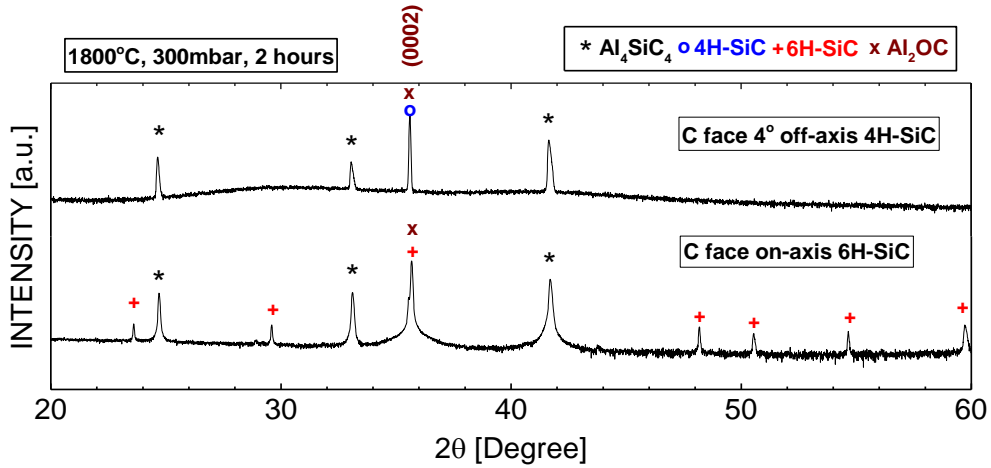


Figure 5.34: X-ray diffractograms collected from the deposited layer after 2 hours of growth at 1800°C, 300mbar, on different types of [0001] oriented C-face hexagonal SiC substrates: on-axis 6H polytype and 4° off-axis 4H polytype.

5.4.3. Al₄SiC₄/SiC epitaxial relationship

Hetero-structure of Al₄SiC₄ on C face [0001] oriented on axis SiC-6H

The Figure 5.35 presents the HRTEM image of the deposited Al₄SiC₄ layer. As illustrated, a perfect crystalline layer of the Al₄SiC₄ has been observed free of defects. From the diffraction image of Al₄SiC₄, with the [-1100] zone axis, the {0002} planes and {11-20} planes are indexed as presented in the inset (i). From the diffraction pattern, the measured interplanar spacing $d_{(0002)}$ and $d_{(11-20)}$ are found equal to $10.9 \pm 0.05 \text{ \AA}$ and $1.64 \pm 0.01 \text{ \AA}$, respectively, which are also presented in the direct space through the high magnification image given in the inset (ii).

Concerning the interface, the Figure 5.36 presents the diffraction pattern of the interface of the heterostructure. The {0002} planes of Al₄SiC₄ and the {0006} planes of the 6H-SiC are indexed along the growth direction. The {11-20} planes of Al₄SiC₄ and the {11-20} planes of SiC are indexed in the basal direction. As results, the {0002}_{Al₄SiC₄} planes are parallel to the {0006}_{6H-SiC} planes and the {11-20}_{Al₄SiC₄} planes are parallel to the {11-20}_{6H-SiC} planes which demonstrates the epitaxial relationship between the Al₄SiC₄ deposited layer and the 6H-SiC substrate.

From the electron diffraction analysis and by using the equation (5.7), the lattice constants (a_{epi} and c_{epi}) of Al₄SiC₄ deposited on 6H-SiC are calculated as below:

$$\begin{cases} \frac{1}{d_{(0002)}^2} = \frac{4}{c_{epi}^2} \\ \frac{1}{d_{(11-20)}^2} = \frac{4}{3} \left(\frac{1^2 + 1 + 1^2}{a_{epi}^2} \right) \end{cases} \quad (5.16)$$

$$\begin{cases} c_{epi} = 21.8 \pm 0.1 \text{ \AA} \\ a_{epi} = 3.27 \pm 0.02 \text{ \AA} \end{cases} \quad (5.17)$$

These calculated lattice constants are in good agreement with the bulk lattice parameters of Al_4SiC_4 (diffraction pattern: 04-009-0133).

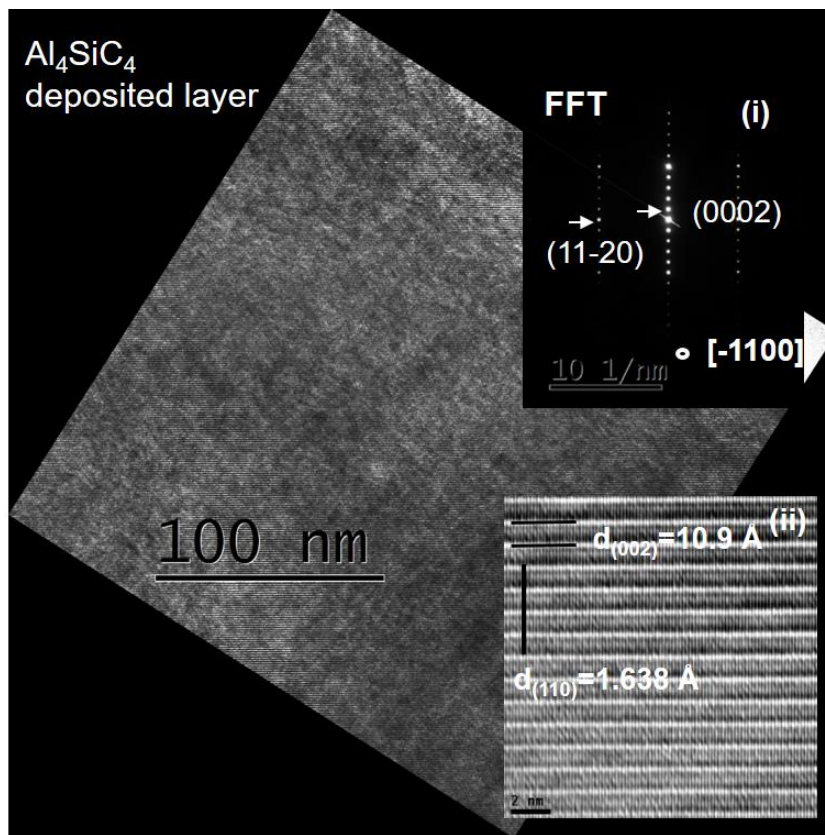


Figure 5.35: TEM picture of the Al_4SiC_4 deposited layer observed along the $[-1100]$ zone axis; (i) diffraction pattern of the Al_4SiC_4 crystal; (ii) high resolution image of the Al_4SiC_4 crystal structure.

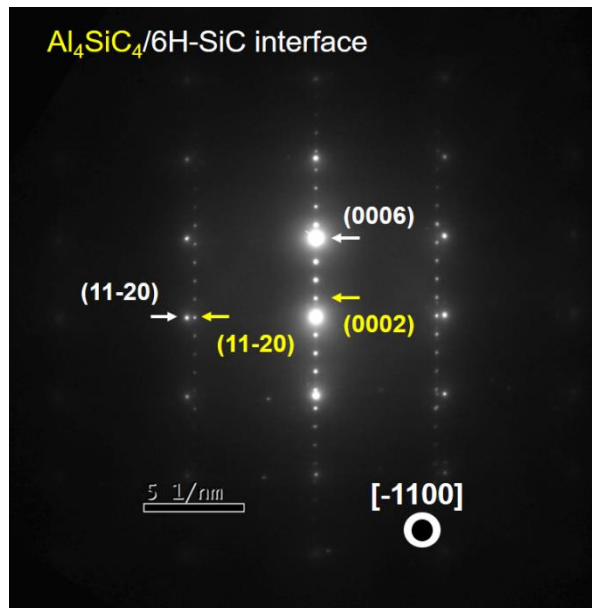


Figure 5.36: Diffraction pattern of the interface between Al_4SiC_4 and 6H-SiC.

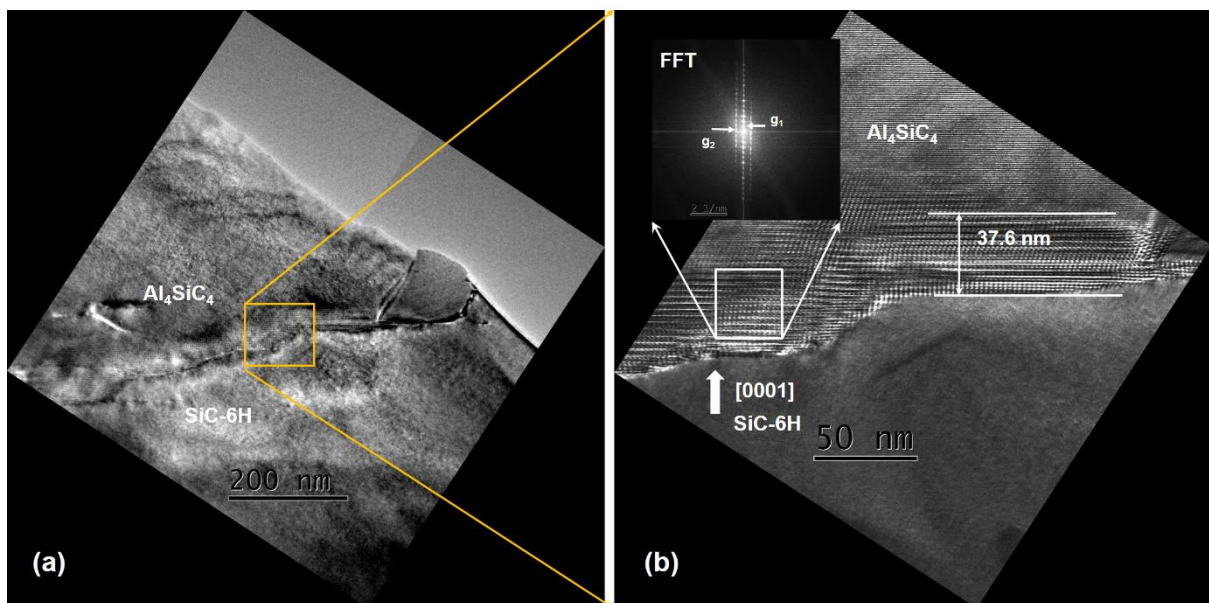


Figure 5.37: (a) Low magnification TEM image of the interface $\text{Al}_4\text{SiC}_4/6\text{H-SiC}$, (b) HRTEM image of the interface $\text{Al}_4\text{SiC}_4/6\text{H-SiC}$. A superstructure layer has been found along the observed interface. The FFT of the interfacial layer is shown in the inset.

Taking a closer look to the interface, through the low magnification TEM image presented in Figure 5.37(a), a rough morphology was observed at the surface of 6H-SiC substrate. It is an evidence of the dissolution of SiC at the early stage of the condensation phenomena while contacting with the vapor dominated by Al-containing species. Moreover, a superstructure

layer has been found between the deposited Al_4SiC_4 layer and 6H-SiC substrate. In the HRTEM presented in the Figure 5.37(b), the measured thickness of this layer is about 37.6 ± 10 nm. Through the FFT of the interfacial layer given in the inset, along the growth direction, the closest diffraction spot g_1 exhibits an interplanar spacing of $31.28 \pm 0.01 \text{ \AA}$. Along the basal direction, the diffraction spot g_2 exhibits an interplanar spacing of $23.58 \pm 0.01 \text{ \AA}$. These values do not correspond to any known phase.

Hetero-structure of Al_4SiC_4 on C face 4° off axis (toward [11-20]) [0001] oriented 4H-SiC.

The electron diffraction analysis is also conducted at the proper interface between Al_4SiC_4 and 4° off axis [0001] oriented 4H-SiC substrate (without the inclusion of parasitic phase). The Figure 5.38 presents the high resolution TEM image of the interface with the corresponding FFT image. However, in contrast with the 6H-SiC case, the interfacial superstructure layer was not found in the observed interface. In the FFT image, under the [-12-10] zone axis, the {00010} planes of Al_4SiC_4 and the {0004} planes of the 4H-SiC are indexed along the growth direction. The {10-10} planes of Al_4SiC_4 and the {10-10} planes of 4H-SiC are indexed along the basal direction. As results, the {00010} $_{\text{Al}_4\text{SiC}_4}$ planes are parallel to the {0004} $_{\text{4H-SiC}}$ planes and the {11-20} $_{\text{Al}_4\text{SiC}_4}$ planes are parallel to the {11-20} $_{\text{6H-SiC}}$ planes which demonstrates the epitaxial relationship between Al_4SiC_4 deposit and the 4H-SiC substrate.

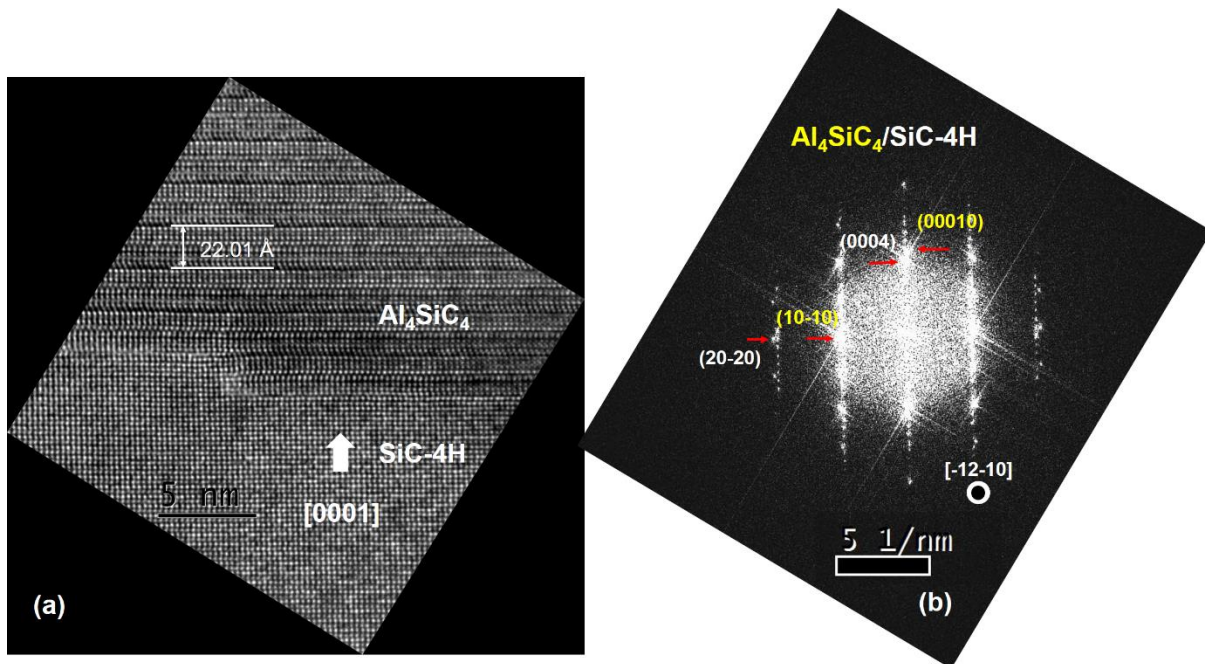


Figure 5.38: (a) HRTEM image of the interface between Al_4SiC_4 and [0001] oriented SiC-4H. (b) Indexed FFT of (a).

Discussion

The epitaxial relationship has been investigated in the heterostructure of Al_4SiC_4 and on axis and 4° off axis [0001] oriented SiC substrate for both case of polytype 4H and 6H.

In case of $\text{Al}_4\text{SiC}_4/6\text{H-SiC}$ heterostructure, an interfacial superstructure layer with the thickness of 37.4 nm has been found. Through the diffraction analysis, high interplanar spacing of 31.28 Å and 23.58 Å have been revealed along the growth direction and basal direction, respectively. It could present an intermediate phase between 6H-SiC and Al_4SiC_4 which was formed from the Al rich vapor at the early stage of the growth process. Moreover, by the diffraction analysis, the lattice constants of the Al_4SiC_4 deposit have been determined which are in good agreement with the reported bulk values. The lattice mismatch of about 6.5% is accommodated by the interfacial superstructure.

In the case of $\text{Al}_4\text{SiC}_4/4\text{H-SiC}$ heterostructure, the Nagai tilt angle of 0.2° observed in the chapter IV has not been easily observed in this case due to the resolution of the image. Moreover, the interfacial superstructure layer has not been found at the observed interface. For that reason, the HRTEM image of the interface (Figure 5.38(a)) allows for the strain field analysis which will be presented in the next section.

5.4.4. Strain field analysis of $\text{Al}_4\text{SiC}_4/\text{C}$ face 4° off axis [0001] 4H-SiC

The GPA analysis has been conducted on the HRTEM image of the interface between Al_4SiC_4 deposit and the 4° off axis 4H-SiC substrate which presents in the Figure 5.39(a).

At first, the analysis is conducted along the [10-10] direction. On the power spectrum of the interface presented in Figure 5.39(b), a Gaussian mask of $0.5\text{g} (\text{nm}^{-1})$ is used to select the frequencies corresponding to the (10-10) plane of Al_4SiC_4 and 4H-SiC which have relaxed interplanar spacing of 2.84Å and 2.67Å, respectively. The Bragg image of the masked area is given in Figure 5.39(c). The amplitude image and the phase image of the inverse filtered Fourier transform are given in Figure 5.39(d) and (e). Taking the SiC substrate as the reference, the strain field along the [10-10] direction is mapped in Figure 5.39(f).

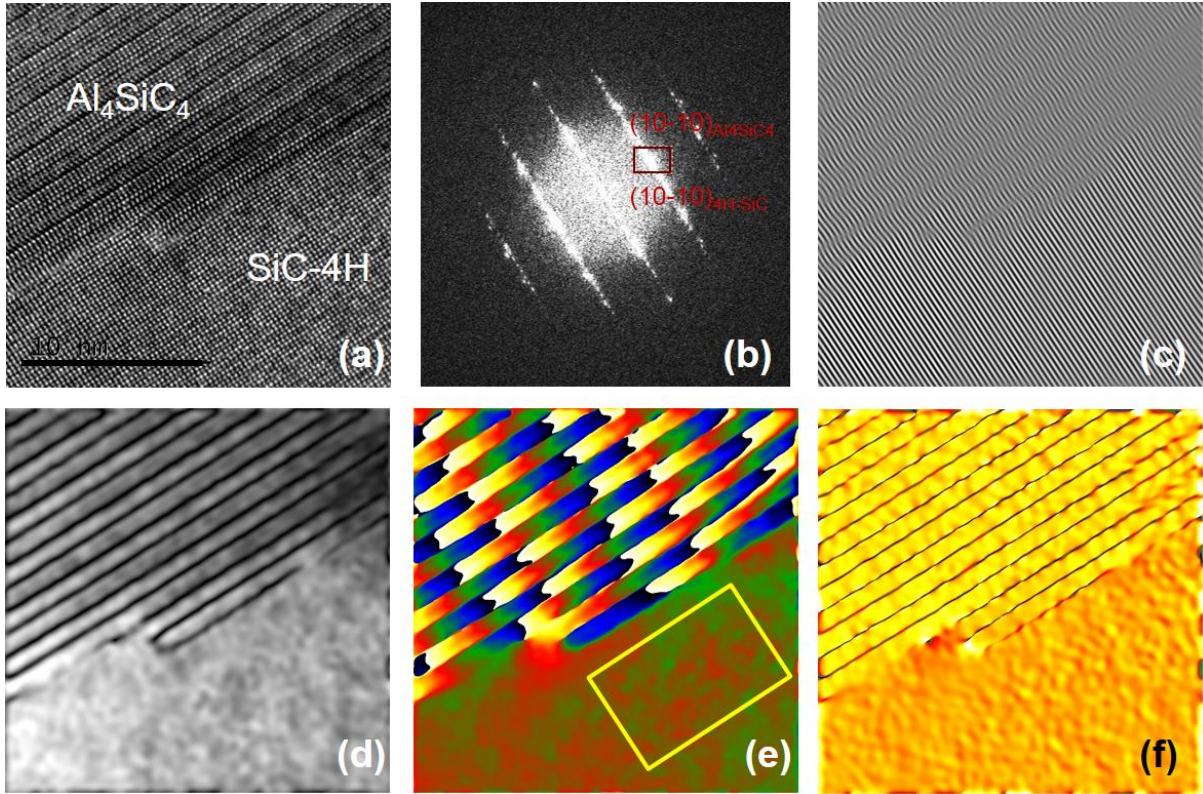


Figure 5.39: GPA strain analysis along the [10-10] direction. (a) The high magnification TEM image of the interface. (b) Power spectrum of the image (a) allowing to select a frequency g by a Gaussian mask, which corresponds to the position of the diffraction spots of the plane $(10-10)_{Al_4SiC_4}$ and $(10-10)_{SiC}$. (c) The Bragg image of the filtered Fourier transform. (d) The amplitude image of the inverse filtered Fourier transform. (e) The phase image with the chosen reference region inside the SiC substrate. (f) The strain field along the [10-10] direction.

The strain profile at the interface along the [10-10] direction is presented in Figure 5.40. As results, with supposing that the strain is zero in the SiC substrate, the strain in Al_4SiC_4 layer is $3 \pm 0.6 \%$ which corresponds to the following equation:

$$e_{epi} = \frac{d_{(10-10)Al_4SiC_4} - d_{(10-10)SiC}}{d_{(10-10)SiC}} \quad (5.18)$$

Thus, if the relaxed $d_{(10-10)}$ of SiC is 2.67 \AA , the calculated $d_{(10-10)}$ of the Al_4SiC_4 deposit has value of $2.75 \pm 0.015 \text{ \AA}$. By using the equation (5.7), the lattice constant a of the Al_4SiC_4 deposit is determined: $a_{epi} = 3.175 \pm 0.017 \text{ \AA}$.

Moreover, the discontinuities in the strain profile are also observed which correspond to the black lines in the HRTEM image. It is probably due to the experimental observation conditions (thickness and defocus) of the image.

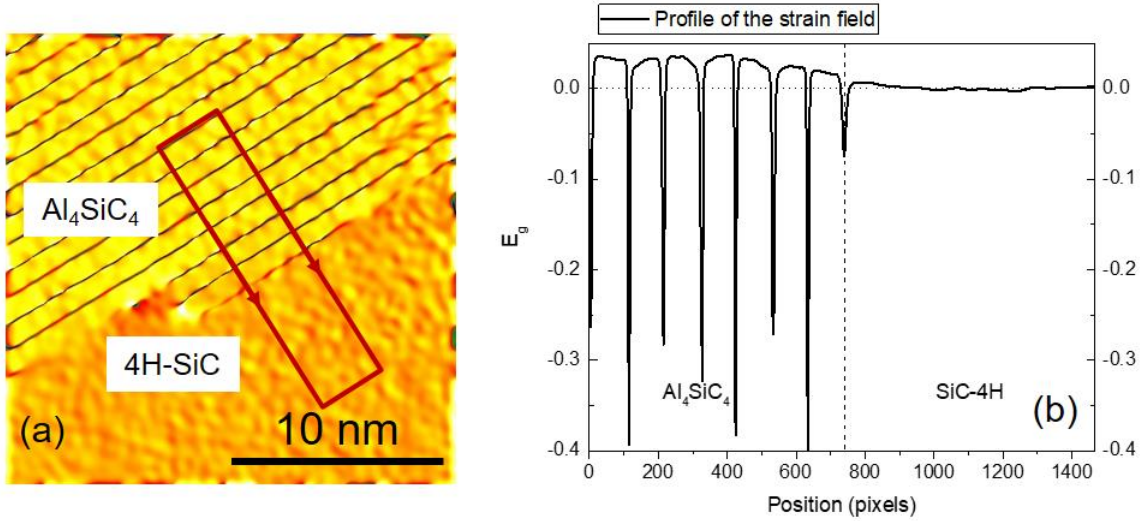


Figure 5.40: (a) The result GPA strain map along the $[10-10]$ direction. (b) Strain profile corresponding to the outline presented in (a).

Next, the strain field at interface along the $[0001]$ direction is analyzed. On the power spectrum of the interface presented in Figure 5.41(b), a Gaussian mask of $0.5\text{g} (\text{nm}^{-1})$ is used to select the frequencies corresponding to the (0008) plane of Al_4SiC_4 and the (0004) plane of SiC which have relaxed interplanar spacing of 2.715 \AA and 2.515 \AA , respectively. The Bragg image of the masked area is given in Figure 5.41(c). The amplitude image and the phase image of the inverse filtered Fourier transform are given in Figure 5.41(d) and (e). Taking the SiC substrate as the reference, the strain field along the $[0001]$ direction is given in Figure 5.41(f). Noted that, with the selected planes, the lattice mismatch Δd between Al_4SiC_4 deposit and 4H-SiC substrate is:

$$\Delta d_{\text{bulk}} = \frac{d_{(0008)\text{Al}_4\text{SiC}_4} - d_{(0004)\text{4H-SiC}}}{d_{(0004)\text{4H-SiC}}} = 7.9\% . \quad (5.19)$$

The strain profile at the interface along the $[0001]$ direction is given in Figure 5.42. As results, the strain in the Al_4SiC_4 could not be identified due to the experimental observation conditions of the HRTEM image. However, on average, the calculated strain is still higher than the relaxed strain marked by the blue line. Thus, the lattice constant c of the Al_4SiC_4 deposit is higher than the c of the relaxed structure. In another words, it demonstrates an extension of Al_4SiC_4 lattice structure along the $[0001]$ direction.

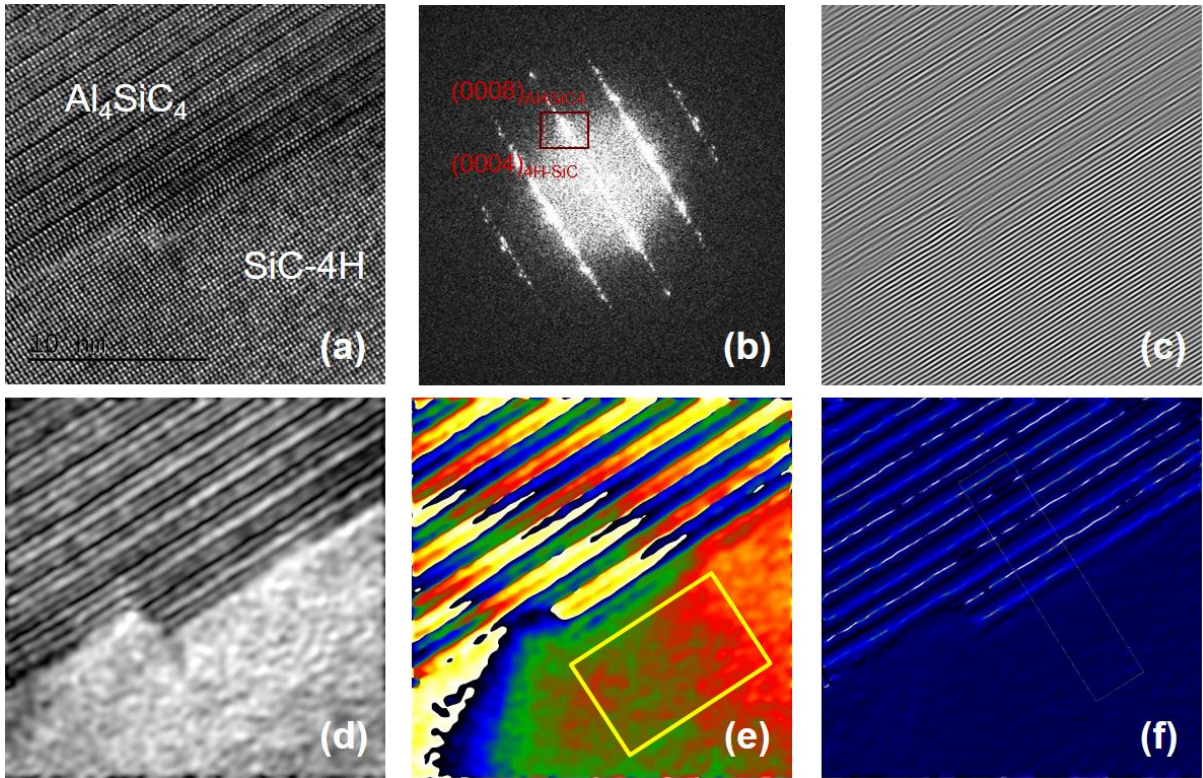


Figure 5.41: GPA strain analysis along the $[0001]$ direction. (a) The high magnification TEM image of the interface. (b) Power spectrum of the image (a) allowing to select a frequency \mathbf{g} by a Gaussian mask, which corresponds to the position of the diffraction spots of the plane $(0008)_{\text{Al}_4\text{SiC}_4}$ and $(0004)_{\text{SiC}}$. (c) The Bragg image of the filtered Fourier transform. (d) The amplitude image of the inverse filtered Fourier transform. (e) The phase image with the chosen reference region inside the SiC substrate. (f) The strain field along the $[0001]$ direction.

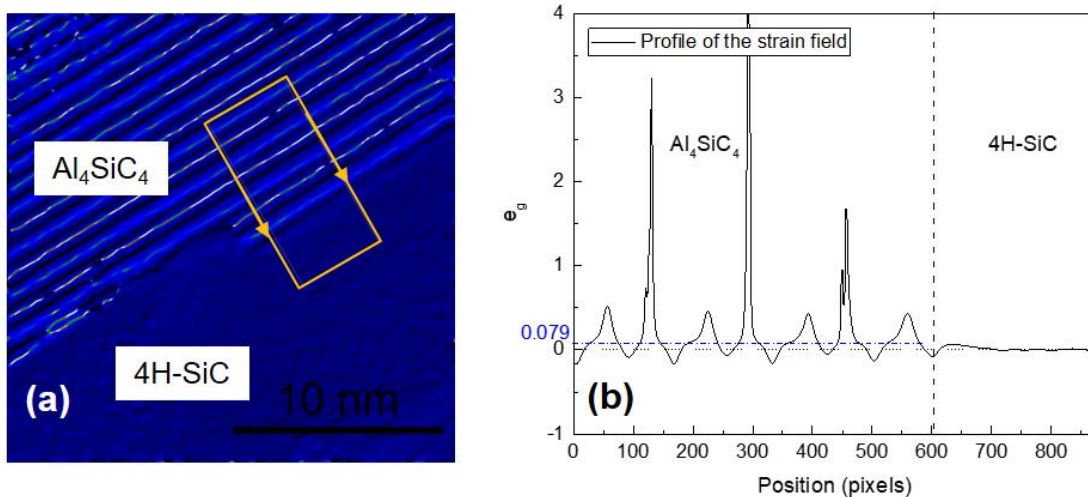


Figure 5.42: (a) The result GPA strain map along the $[0001]$ direction. (b) Strain profile corresponding to the outline presented in (a). The relaxed strain of Al_4SiC_4 is given by the blue dot line.

Discussion

The strain field at the interface between the Al_4SiC_4 deposit and the 4° off axis C-face 4H-SiC substrate has been analyzed by the GPA method. A biaxial strain has been investigated along the [10-10] and [0001] direction. Through the analysis along the [10-10] direction, the lattice constant a of the deposit is determined: $a_{\text{epi}}=3.175 \pm 0.017 \text{ \AA}$ which is smaller than the relaxed $a=3.28 \text{ \AA}$. It demonstrates a compression of the lattice structure of Al_4SiC_4 in the basal plane. For the analysis along the [0001] direction, an expansion of the lattice structure of Al_4SiC_4 along the c has been investigated through the increasing of lattice constant c .

Table 5.5: Lattice constant of Al_4SiC_4 epilayer deposited on 4° off axis 4H-SiC substrate compared with Al_4SiC_4 bulk (diffraction pattern: 04-009-0133).

Samples	Lattice constant (\AA)		Strain of epilayer as compared to the bulk (%)	
	a	c	$\Delta a/a$	$\Delta c/c$
Al_4SiC_4 bulk	3.28	21.72		
Al_4SiC_4 /on axis 6H-SiC	3.27 ± 0.02	21.8 ± 0.1	inside the error bar	inside the error bar
$\text{Al}_4\text{SiC}_4/4^\circ$ off axis 4H-SiC	3.175 ± 0.017	> 21.8	-3.35	> 0.37

For the comparison, the lattice constants of Al_4SiC_4 epilayer deposited on different SiC substrates (on-axis C-face 6H and 4° off-axis C face 4H) are gathered in the Table 5.5, with the relaxed lattice constant of Al_4SiC_4 as reference. The strains of the epilayer as compared to the bulk are also calculated and given in the table.

The biaxial strain found at the interface of Al_4SiC_4 epilayer and 4° off axis 4H-SiC substrate is probably related with the misorientation of the substrate and the absence of an interfacial superstructure layer. This strain of the lattice structure has been expected in chapter 4 causing a tilt angle of 0.2° between the basal plane of the epilayer and the 4° off axis SiC substrate. In case of vicinal substrates, since the growth is governed by the step flow growth mechanism, strains and defects (i.e. dislocations) are introduced at the interfacial steps to accommodate the change in stacking sequence and the lattice mismatch in the growth direction²⁵.

An atomic model has been built to simulate the interface structure of $\text{Al}_4\text{SiC}_4/4\text{H-SiC}$ shown in the HRTEM image (Figure 5.43). The Al_4SiC_4 epilayer has been grown on the $2c$ step of 4H-SiC substrate and the interface has been indicated by the black lines. The atomic model is just an arrangement of the relaxed lattice structures, thus it is rather different to the structure observed in the HRTEM images, where the Al_4SiC_4 epilayer is not relaxed. However, some

similarities could be observed. Indeed, the shift of the atomic plane indicated by the red line, are observed in both images, which are caused by the different stacking sequence and lattice mismatch between $2c$ of 4H-SiC and c of Al_4SiC_4 ($\Delta c = 1.6 \text{ \AA}$). Beside of that, an interfacial dislocation is also observed (**T**) in order to accommodate the in-plane lattice mismatch Δa between Al_4SiC_4 and 4H-SiC.

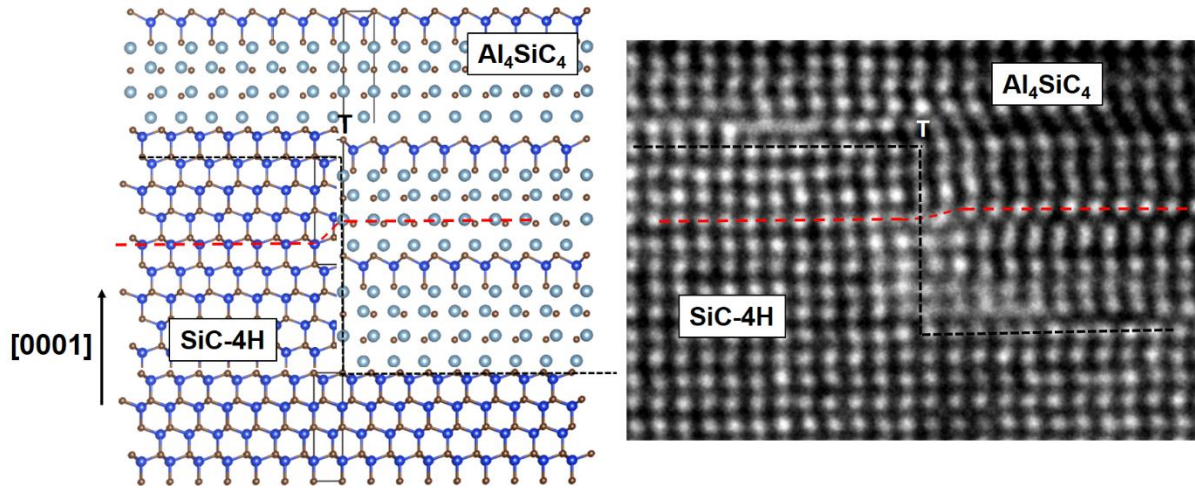


Figure 5.43: High resolution TEM image of the interface of $\text{Al}_4\text{SiC}_4/4\text{H-SiC}$ and corresponding atomic model. The zone axis of the TEM image is $[-12-10]$. The Al_4SiC_4 has been grown on $2c$ step of 4H-SiC substrate and the interface has been indicated by the black lines.

Critical thickness calculation

Although the critical thickness of Al_4SiC_4 epilayer is not experimentally determined, its theoretical value could be calculated by the energy balance theory which has been reported by People *et al.*²³ with the assumption that a pseudomorphic layer is initially formed with the same in-plane lattice constants as the SiC substrate. Thus, the growing film is initially free of misfit dislocations. The interfacial misfit dislocations will be generated when the strain energy density exceeds the self-energy of an isolated edge dislocation. The homogeneous strain energy (ε_H) and the areal energy (ε_D) associated with an edge dislocation are given as below, respectively²³:

$$\varepsilon_H = 2G \left(\frac{1+\nu}{1-\nu} \right) h_c f^2 \quad (5.20)$$

$$\varepsilon_D = \left(\frac{Gb^2}{8\pi\sqrt{2}a(1-\nu)} \right) \ln \left(\frac{h_c}{b} \right) \quad (5.21)$$

Where ν is the Poisson ratio of Al_4SiC_4 which is theoretical estimated at 0.206²⁶, a is the bulk lattice constant of Al_4SiC_4 , h_c is the critical thickness of the epilayer, b is the Burger's vector, G is the shear modulus, $f=6.5\%$ is the in-plane lattice mismatch of the heterostructure.

The Burger's vector in Al_4SiC_4 deposited on SiC is not yet investigated in literature. Thus, we use a Burger's vector equal to $b=1/3[2-1-10]=a$ for the calculation, which has been reported in another wurtzite structure (InN/GaN heterostructure²⁷). The critical thickness h_c is determined by the equation below:

$$h_c = \left(\frac{b^2}{16\pi a f^2 (1+\nu) \sqrt{2}} \right) \ln \left(\frac{h_c}{b} \right) \quad (5.22)$$

As results, we have a critical thickness of 10.8Å. This value nearly corresponds to $c/2$ atomic layers of Al_4SiC_4 which composes of one Al_4C_3 cell unit and one SiC cell unit.

CONCLUSIONS OF THE CHAPTER

In this chapter, different heteroepitaxial structures of Al-Si-C system on hexagonal SiC substrate have been investigated such as Al₄C₃/SiC and Al₄SiC₄/SiC. The characteristics of these structures like growth mechanism and crystallographic relationship have been mainly analyzed at a nanoscopic scale by using HRTEM.

As motivation of the study, due to the lack of experimental results on the semiconducting properties of Al₄C₃, the synthesis of Al₄C₃ single crystals has been conducted. Some characterizations such as Raman, XRD, and optical absorption have been carried out on the obtained Al₄C₃ single crystals. The experimental optical bandgap of Al₄C₃ has been firstly measured around 2.3 eV which inspired the study of the heterostructure after.

An indirect process has been proposed to fabricate the Al₄C₃/SiC heterostructure based on the chemical interaction between Al deposit and the Si face of [0001] oriented 6H-SiC substrate. As product of the reaction, Al₄C₃ layer is formed at the interface of Al and SiC. By using different characterization methods (i.e. SEM, XRD, TEM), the wetting behavior of the system, as well as the dissolution-precipitation of Al₄C₃ layer at the interface has been verified. Moreover, the crystallographic relationship of the heterostructure has been analyzed by HRTEM. Through the electron diffraction analysis, epitaxial relationship between Al₄C₃ layer and [0001] oriented 6H-SiC substrate has been investigated along the growth direction: the {0006} planes of Al₄C₃ // {0006} planes of SiC, and along the basal plane: the {1000} planes of Al₄C₃// the {1000} planes of SiC. Furthermore, the strain field analysis at interface of the heterostructure has been conducted on the HRTEM images using GPA method in order to investigate the evolution of the crystalline structure of Al₄C₃ as function of annealing duration. At early stage of the growth (i.e. 2 hours), in the Al₄C₃ epilayer having thickness of 4.6 nm, a biaxial strain has been found. Indeed, the lattice structure of Al₄C₃ is compressed along the growth direction and extended along the basal direction. A strained crystalline structure has been initially formed due to the growth conditions. As the reaction proceeds further (i.e. 4 hours), with the increasing of the thickness, the lattice structure of Al₄C₃ epilayer is nearly relaxed when reaching the interface with Al layer. The biaxial strain observed at early stage is almost elastically relaxed.

For Al₄SiC₄/SiC heterostructure, the sublimation growth process described in the chapter 4 has been used. In this work, the Al₄SiC₄/SiC heterostructures are fabricated with two different types of substrates: [0001] on-axis C-face 6H-SiC and [0001] 4° off-axis C-face 4H-SiC. The

analysis have been conducted on HRTEM images of the interface in order to study the crystallographic relationship between the Al_4SiC_4 deposit and different types of SiC substrates.

Through the electron diffraction analysis, epitaxial relationships have been investigated. For the Al_4SiC_4 /on-axis 6H-SiC structure, along the growth direction: the {0002} planes of Al_4SiC_4 // the {0006} planes of 6H-SiC, and along the basal direction: the {11-20} planes of Al_4SiC_4 // the {11-20} planes of 6H-SiC. For the $\text{Al}_4\text{SiC}_4/4^\circ$ off-axis 4H-SiC structure, along the growth direction: the {00010} planes of Al_4SiC_4 // the {00010} planes of 4H-SiC, and along the basal direction the {10-10} planes of Al_4SiC_4 // the {10-10} planes of 4H-SiC. The Nagai tilt angle of 0.2° observed in the chapter IV has not been easily observed in this case due to the resolution of the image. However, according to the strain field analysis, a difference in elastic strains has been observed for different type of substrates. In the case of the growth on on-axis C-face 6H-SiC substrate, the relaxation of the Al_4SiC_4 epilayer has been demonstrated through the negligible difference between the lattice constant of the epilayer and the bulk material. The lattice mismatch of about 6.5% is accommodated by the interfacial superstructural layer. However, in case of the growth on off-axis C face 4H-SiC substrate, without the presence of an interfacial superstructural layer, a significant biaxial strain and misfit dislocations have been found at the interface, which are introduced to accommodate both the lattice mismatches in the basal plane and along the growth direction. Furthermore, based on the energy balance theory, a critical thickness of 10.8\AA has been estimated.

REFERENCE

1. F. Capasso and A. Y. Cho, *Bandgap engineering of semiconductor heterostructures by molecular beam epitaxy: physics and applications*, Surface Science **299-300**, 878-891 (1994).
2. H. Morkoç, S. Strite, G. B. Gao, M. E. Lin, B. Sverdlov and M. Burns, *Large-band-gap SiC, III-V nitride, and II-VI ZnSe-based semiconductor device technologies*, Journal of Applied Physics **76** (3), 1363-1398 (1994).
3. C. F. Zhe, *Silicon Carbide: Materials, Processing & Devices*. (CRC Press, 2003).
4. M. Bhatnagar and B. J. Baliga, *Comparison of 6H-SiC, 3C-SiC, and Si for power devices*, IEEE Transactions on Electron Devices **40** (3), 645-655 (1993).

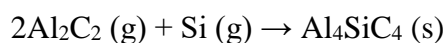
5. M. E. Levinshtein, S. L. Rumyantsev and M. S. Shur, *Properties of Advanced Semiconductor Materials: GaN, AlN, InN, BN, SiC, SiGe*. (John Wiley & Sons, 2001).
6. M. Soueidan and G. Ferro, *A Vapor–Liquid–Solid Mechanism for Growing 3C-SiC Single-Domain Layers on 6H-SiC(0001)*, *Advanced Functional Materials* **16** (7), 975-979 (2006).
7. S. D. Peteves, P. Tambuyser, P. Helbach, M. Audier, V. Laurent and D. Chatain, *Microstructure and microchemistry of the Al/SiC interface*, *Journal of Materials Science* **25** (8), 3765-3772 (1990).
8. S. Tengeler, *Cubic Silicon Carbide For Direct Photoelectrochemical Water Splitting*, Thesis dissertation, 2017.
9. G. Beaucarne, A. Brown, M. Keevers, R. Corkish and M. Green, *The impurity photovoltaic (IPV) effect in wide-bandgap semiconductors: an opportunity for very-high-efficiency solar cells?*, *Progress in Photovoltaics: Research and Applications* **10** (5), 345-353 (2002).
10. C. Persson and U. Lindefelt, *Detailed band structure for 3C-, 2H-, 4H-, 6H -SiC, and Si around the fundamental band gap*, *Physical Review B* **54** (15), 10257-10260 (1996).
11. J. Viala, P. Fortier and J. Bouix, *Stable and metastable phase equilibria in the chemical interaction between aluminium and silicon carbide*, *Journal of Materials Science* **25** (3), 1842-1850 (1990).
12. G. Charlot, *Qualitative inorganic analysis: a new physio-chemical approach*. (Methuen, 1954).
13. J. Viala, F. Bosselet, V. Laurent and Y. Lepetitcorps, *Mechanism and kinetics of the chemical interaction between liquid aluminium and silicon-carbide single crystals*, *Journal of materials science* **28** (19), 5301-5312 (1993).
14. Y. Sun, H. Cui, L. Gong, J. Chen, J. She, Y. Ma, P. Shen and C. Wang, *Carbon-in-Al₄C₃ Nanowire Superstructures for Field Emitters*, *ACS Nano* **5** (2), 932-941 (2011).
15. D. V. Suetin, I. R. Shein and A. L. Ivanovskii, *Structural, elastic and electronic properties and formation energies for hexagonal (W_{0.5}Al_{0.5})C in comparison with binary carbides WC and Al₄C₃ from first-principles calculations*, *Physica B: Condensed Matter* **403** (17), 2654-2661 (2008).
16. A. C. Ferro and B. Derby, *Wetting behaviour in the Al-Si/SiC system: interface reactions and solubility effects*, *Acta Metallurgica et Materialia* **43** (8), 3061-3073 (1995).

17. V. Laurent, D. Chatain, C. Chatillon and N. Eustathopoulos, *Wettability of monocrystalline alumina by aluminium between its melting point and 1273 K*, *Acta Metallurgica* **36** (7), 1797-1803 (1988).
18. V. Laurent, C. Rado and N. Eustathopoulos, *Wetting kinetics and bonding of Al and Al alloys on α -SiC*, *Materials Science and Engineering: A* **205** (1), 1-8 (1996).
19. J. L. Rouvière and E. Sarigiannidou, *Theoretical discussions on the geometrical phase analysis*, *Ultramicroscopy* **106** (1), 1-17 (2005).
20. M. J. Hÿtch, E. Snoeck and R. Kilaas, *Quantitative measurement of displacement and strain fields from HREM micrographs*, *Ultramicroscopy* **74** (3), 131-146 (1998).
21. D. Brandon and W. D. Kaplan, *Microstructural characterization of materials*. (John Wiley & Sons, 2013).
22. T. Liao, J. Wang and Y. Zhou, *Atomistic deformation modes and intrinsic brittleness of Al₄SiC₄: A first-principles investigation*, *Physical Review B* **74** (17) (2006).
23. R. People and J. Bean, *Calculation of critical layer thickness versus lattice mismatch for Ge x Si_{1-x}/Si strained-layer heterostructures*, *Applied Physics Letters* **47** (3), 322-324 (1985).
24. C. Hartmann, M. Albrecht, J. Wollweber, J. Schuppang, U. Juda, C. Guguschev, S. Golka, A. Dittmar and R. Fornari, *SiC seed polarity-dependent bulk AlN growth under the influence of residual oxygen*, *Journal of Crystal Growth* **344** (1), 19-26 (2012).
25. J. E. Ayers, T. Kujofsa, P. Rago and J. Raphael, *Heteroepitaxy of semiconductors: theory, growth, and characterization*. (CRC press, 2016).
26. L. Sun, Y. Gao, Y. Li, K. Yoshida, T. Yano and D. Yi, *Structural, bonding, anisotropic mechanical and thermal properties of Al₄SiC₄ and Al₄Si₂C₅ by first-principles investigations*, *Journal of Asian Ceramic Societies* **4** (3), 289-298 (2016).
27. J. Kioseoglou, E. Kalesaki, G. Dimitrakopoulos, T. Kehagias, P. Komninou and T. Karakostas, *Atomistic modeling and HRTEM analysis of misfit dislocations in InN/GaN heterostructures*, *Applied Surface Science* **260**, 23-28 (2012).

GENERAL CONCLUSIONS AND PERSPECTIVES

The main objective of this work was the development of a seeded sublimation process for the growth of Al_4SiC_4 single crystals, starting from the Al_4C_3 and SiC powders. Different aspects of the process have been investigated.

As a preamble of the experimental study, a conventional thermodynamic analysis has been performed to describe the vaporization and condensation phenomena in the Al_4C_3 - SiC pseudo-binary system (chapter III). It clearly appeared that the vaporization of an Al_4C_3 - SiC mixture always exhibits a strong excess of Al in the gas phase. Despite such a strong non-congruency, we identified the favorable conditions for condensing different aluminum-silicon ternary carbides such as Al_4SiC_4 and Al_8SiC_7 , as a function of both source and seed temperatures, and for different initial compositions of the source materials ($X_{\text{Al}_4\text{C}_3}$). The condensation of Al_4SiC_4 single phase requires: i) a SiC -rich initial composition ($X_{\text{Al}_4\text{C}_3} < 0.5$) and ii) a temperature difference between the vaporization and condensation zones smaller than 40°C . The formation of Al_4SiC_4 is governed by Al_2C_2 (g) and Si (g) gaseous species, suggesting the following reaction as the “thermodynamically limiting” reaction:



On an experimental footing, two high temperature approaches for the synthesis of Al_4SiC_4 have been investigated, both starting from a mixture of Al_4C_3 and SiC powders (chapter IV). All the trends were found in overall agreement with the known phase diagrams and the thermodynamic calculations presented in chapter III.

First, a natural reactive sintering process (pressure-less) has been investigated, with the main objective to synthesis Al_4SiC_4 single phase. Unfortunately, whatever the initial composition of Al_4C_3 and SiC , the goal could not be achieved because the global composition of the source systematically deviates from the initial binary section. Indeed, the behavior of the Al_4C_3 - SiC mixture at high temperature could be described by considering two phenomena: i) the solid state reaction between the two carbides, which shows a low reaction yield, and ii) the relative vaporization rates of different elements which can lead to significant changes of the overall composition. A hot isostatic pressing approach could significantly help to improve the two steps.

Second, a sublimation growth process for the synthesis of Al_4SiC_4 single crystalline samples has been explored. This could be achieved with the following constraints: i) SiC -rich initial composition ($X_{\text{Al}_4\text{C}_3} < 0.5$) of the source materials, ii) a small temperature gradient between the source and the seed to avoid the condensation of parasitic phases, iii) moderated mass transport to avoid strong evolutions of the system and again, the condensation of parasitic phases. The source material has shown a complex evolution, giving rise to the formation of the strata. This could be explained by the interplay between thermodynamics and mass transport phenomena, i.e. the relative vaporization rate of the different species. We have successfully applied this sublimation growth process to the epitaxial growth of high quality, thick single phase Al_4SiC_4 layers, on hexagonal- SiC commercial wafers. From this first experience, it occurred really problematic to keep stationary conditions for the growth of bulk Al_4SiC_4 single crystals.

Basic characterizations were conducted in order to get a first picture of the morphology of the growth surface and the structural quality of the obtained Al_4SiC_4 crystalline layers (chapter IV). For example, we have shown that the nature of the substrate (C-face vs. Si-face, off-axis vs. on-axis) had a significant effect on the mosaicity of the layer and also on the crystal lattice matching between the layer and the substrates. Indeed, the Al_4SiC_4 deposits grown on on-axis SiC substrates have a better crystalline quality than the ones grown on off-axis SiC substrates. A relative tilt angle (Nagai tilt) of 0.2° between the basal plane of the Al_4SiC_4 epilayer and the 4° off-axis SiC substrate was found. An assumption related to the presence of biaxial strain in the epilayer grown on off-axis substrate was proposed as an explanation. Concerning the effect of polarity, a higher mosaicity was obtained on C-face on-axis SiC substrates, which has been explained by the different reactivity of both polarities. For thin layers, the best quality has been obtained on Si-face on-axis SiC substrates. Also, the

quality drastically improved with the thickness and a FWHM of 0.303° has been measured for the (00010) reflection of a $185\ \mu\text{m}$ thick Al_4SiC_4 layer, which is an excellent “preliminary” value, considering the high lattice mismatch between the epilayer and the substrate.

A deeper investigation of the interfacial structure has been performed using HRTEM (chapter V), with a special focus on the strain state. Indeed, the relaxation of the Al_4SiC_4 epilayer grown on the C-face on-axis 6H-SiC substrate was observed with the presence of an interfacial superstructure, whose nature is still unclear. We think that it is an intermediate phase which has been formed from the Al-rich vapor at the early stage of the sublimation growth process. Additionally, there is evidence that the lattice mismatch about 6.5% is accommodated through this interfacial superstructure. In case of growth on C-face 4° off-axis 4H-SiC substrate, a significant elastic strain was found at the interface without the presence of the superstructure. This elastic strain was introduced to accommodate the lattice mismatches along both the basal and the growth directions. These results confirm the preliminary investigations presented in chapter IV.

Concerning the optical properties of Al_4SiC_4 , UV-Vis spectroscopy revealed an absorption edge demonstrating an indirect bandgap of about 2.10 eV for the sublimation grown crystals (chapter IV). This value is slightly higher than one observed for the solution grown crystals (1.93 eV). By analogy with SiC, a bandgap shrinkage could be expected in case of high doping level, which is usually the case in solution growth, as compared to sublimation growth. However, other characterizations are required for both qualitative and quantitative description of the properties. For example, Hall Effect measurements would be necessary to determine the doping type, carrier concentration and carrier mobility of the material. The advantage of sample size ($1 \times 1\ \text{cm}^2$) when the Al_4SiC_4 layers are heteroepitaxially grown on SiC substrates, is partially hidden by the presence of many cracks in the layer, making the measurement very difficult.

As a strategy to control the $\text{Al}_4\text{SiC}_4/\text{SiC}$ interface, we investigated a two-steps indirect process. It consists of first, the formation of an Al_4C_3 layer at low temperature, from the chemical interaction between Al deposit and the Si face of [0001] oriented 6H-SiC substrates, and the second, the solid state reaction, at higher temperature, between Al_4C_3 and SiC to form the $\text{Al}_4\text{SiC}_4/\text{SiC}$ interface. Even the final goal (second stage of the process) has not been reached yet, it appeared that Al_4C_3 and the $\text{Al}_4\text{C}_3/\text{SiC}$ interface were themselves worth being

studied. The indirect optical bandgap around 2.3eV was experimentally measured for the first time, which does not match with the calculated value reported in the literature (chapter V). By using different characterization methods, the wetting behavior of the system, and the dissolution-precipitation of Al_4C_3 layer at the interface have been reconsidered. Since the C source for the precipitation of Al_4C_3 was provided from the dissolution of SiC, a full Al_4C_3 coverage of the SiC substrate could not be obtained. For a future development of this approach, this could be rather easily overcome by an additional C source (C_3H_8 , C_2H_4 – from vapor phase) to control the C supersaturation from the beginning. As an important characteristic of the heterostructure, the evolution of strain state at the $\text{Al}_4\text{C}_3/\text{SiC}$ interface was analyzed from the HRTEM images. Indeed, during the early stages of the growth (i.e. 2 hours), the lattice structure of the Al_4C_3 epilayer initially endures a biaxial strain. As the reaction proceeds further, with increasing of the thickness, the biaxial strain is elastically relaxed. After 4 hours of annealing, the lattice structure of Al_4C_3 epilayer is nearly relaxed when reaching the top interface, in contact with Al.

As the first PhD thesis on the exploration of the Al-Si-C based semiconductors, all is not complete, of course. But it brings many building blocks, and contributes many information for the further development of the topic. It clearly appeared that the sublimation growth process is too non-stationary to consider the growth of large size, bulk single crystals. A more realistic view would consist in optimizing the seeded sublimation growth for thin to thick layers. Another approach, not explored here, is the solution growth, which usually allows to reach very good crystal quality. A key point for a further improvement of the layer quality is the control of the early stages of growth and the initial interface properties between the layer and the SiC substrates. Difficult to implement in the sublimation growth process, because of the high temperatures used, an interface engineering approach through the use of buffer layers would allow to accommodate more the layer and the substrates. A buffer layer with an appropriated thickness could be introduced to release the stress and to reduce the cracks in the deposit caused by lattice mismatch and the difference of CTE. The nature of the buffer layer could be the Al_4SiC_4 formed by chemical conversion of the $\text{Al}_4\text{C}_3/\text{SiC}$ heterostructure which was partly investigated in this work. To prepare the buffer layer, a full Al_4C_3 layer coverage on SiC substrate must be firstly achieved. Later, a buffer layer of Al_4SiC_4 is expected to be formed from the reaction between Al_4C_3 and SiC during annealing step at higher temperature. More realistic, from a control point of view, is to form the buffer layer on SiC by chemical vapor deposition (CVD) or by reactive CVD. This technique usually allow a

good control of the interfaces. To our knowledge, CVD has never been explored for the deposition of such carbides, but is perfectly adapted for carbides in general, as can be shown by the developments which have been done on SiC coatings and semiconductor grade epilayers.

At this stage, we have no idea on the doping level, dopant nature, and dopant type of our carbide samples. By analogy with SiC, it is probable that N was a donor in Al_4SiC_4 and in high concentration, as we used the sublimation growth process. To check this point, the growth under N_2 containing atmosphere will be implemented. On a more general footing, the use of these new carbides in semiconductor applications will require an extensive investigation of possible dopants and their incorporation.

The highest potential of this work, in terms of perspectives, lies in the realization of carbides heterostructures. Though not optimized yet, we have successfully demonstrated the possibility to heteroepitaxially grow Al_4SiC_4 and Al_4C_3 on α -SiC commercial wafers. Also, although the properties of Al_8SiC_7 have not been investigated yet, the heterostructure $\text{Al}_8\text{SiC}_7/\text{SiC}$ heterostructure is also interesting. By developing further the crystal growth processes and by a deeper knowledge of the crystallographic relationships between these carbides, heterojunctions between various Al-Si-C compounds (Al_4SiC_4 , Al_4C_3 and Al_8SiC_7) and SiC could give rise to the totally disruptive, carbide-based bandgap engineering field.

ANNEX: Linear elasticity

Elastic constants definition

According to the Hooke's law, the stress σ_{ij} of a material is directly proportional to the strain ϵ_{ij} .

$$\sigma_{ij} = \sum_{kl} C_{ijkl} \cdot \epsilon_{kl}$$

Where C_{ijkl} is the tensor of the elastic module.

In order to simplify notation pairs of indices $\{xx, yy, zz, yz, zx, xy\}$ are replaced by indices $\{1, 2, 3, 4, 5, 6\}$. So strain and stress matrices become column vectors:

$$\epsilon_{ij} \rightarrow \epsilon = \begin{cases} \epsilon_1 = \epsilon_{11} \\ \epsilon_2 = \epsilon_{22} \\ \epsilon_3 = \epsilon_{33} \\ \epsilon_4 = 2\epsilon_{23} = 2\epsilon_{32} \\ \epsilon_5 = 2\epsilon_{13} = 2\epsilon_{31} \\ \epsilon_6 = 2\epsilon_{12} = 2\epsilon_{21} \end{cases} \quad \sigma_{ij} \rightarrow \sigma = \begin{cases} \sigma_1 = \sigma_{11} \\ \sigma_2 = \sigma_{22} \\ \sigma_3 = \sigma_{33} \\ \sigma_4 = \sigma_{23} = \sigma_{32} \\ \sigma_5 = \sigma_{13} = \sigma_{31} \\ \sigma_6 = \sigma_{12} = \sigma_{21} \end{cases}$$

And the elastic module C_{ijkl} can be presented by a matrix (second-rank tensor). For the case of a hexagonal crystal this matrix takes the following form:

$$C = \begin{pmatrix} C_{11} & C_{12} & C_{13} & & & \\ C_{12} & C_{11} & C_{13} & & & \\ C_{13} & C_{13} & C_{33} & & & \\ & & & C_{44} & & \\ & & & & C_{44} & \\ & & & & & C_{66} \end{pmatrix}$$

It contains six elastic modules, five of which are independent and $C_{66} = (C_{11} - C_{12})/2$.

When a thin film is coherently deposited on a substrate with a misfit f_0 , it is strained in order to adapt its lattice parameter to that of the substrate. The in-plane lattice misfit between the film and the substrate is defined by the following equation:

$$f_0 = \frac{a_e - a_s}{a_s}$$

Based on the matrix of elastic module, we can calculate the deformation of the film due to biaxial strain. For the hexagonal crystals and when the growth is carried out on a [0001] direction, the strain components ϵ_1 and ϵ_2 are equal to the lattice misfit f_0 .

$$\epsilon_1 = \epsilon_2 = f_0$$

Since along the growth direction, the surface is free of stress, $\sigma_3 = 0$, considering in plane isotropy, the Hooke's law can be written as:

$$\begin{pmatrix} \sigma_1 \\ \sigma_1 \\ 0 \end{pmatrix} = \begin{pmatrix} C_{11} & C_{12} & C_{13} \\ C_{12} & C_{11} & C_{13} \\ C_{13} & C_{13} & C_{33} \end{pmatrix} \begin{pmatrix} \epsilon_1 \\ \epsilon_1 \\ \epsilon_3 \end{pmatrix}$$

As a consequence, the biaxial strain induces a strain ϵ_3 perpendicular to the surface and of opposite sign along the [0001] axis, which is equal to:

$$\epsilon_3 = -2 \frac{C_{13}}{C_{33}} \epsilon$$

This equation can be written in terms of lattice parameter as following:

$$\frac{c_{epi}}{c_s} = 1 - 2 \frac{C_{13}}{C_{33}} \frac{(a_e - a_s)}{a_s}$$

Al₄SiC₄

Aluminum Silicon Carbide

Lattice : Hexagonal
S.G. : P63mc (186)
a = 3.28000
c = 21.72000
Z = 2

Mol. weight = 184.06
Volume [CD] = 202.37
Dx = 3.021
l/|cor = 0.94

ANX: NO3P5. LPF Collection Code: 462546. Sample Preparation: STARTING MATERIAL:Al,Si,C.Compound Formation:heated at 1973-2073 K. Minor Warning: Magnitude of e.s.d. on cell dimension is >1000 ppm. Unit Cell Data Source: Powder Diffraction. Data collection flag: Ambient.

Calculated from LPF using POWD-12++
Schoennahl J., Willer B., Daire M., J. Solid State Chem., volume 52, page 163 (1984)

Radiation : CuKα1
Lambda : 1.54060
SS/FOM : F30=1000(0.0007,31)

Filter :
d-sp : Calculated spacings

<i>d</i> (Å)	<i>i</i>	<i>h</i>	<i>k</i>	<i>l</i>	<i>d</i> (Å)	<i>i</i>	<i>h</i>	<i>k</i>	<i>l</i>
10.86000	59	0	0	2	*0.86243	35	2	1	15
5.43000	57	0	0	4	0.84583	4	1	1	
3.62000	105	0	0	6	0.84210	18	2	1	
2.84056	135	1	0	0	0.83899	2	3	0	12
2.81658	999	1	0	1	0.83609	5	2	0	
2.74811	289	1	0	2	0.83539	5	0	0	
2.71500	74	0	0	8	0.83081	10	1	0	
2.64432	170	1	0	3	0.82196	11	2	1	
2.51697	313	1	0	4	0.82000	60	2	2	0
2.37740	655	1	0	5	0.81066	27	2	0	
2.23470	707	1	0	6	*0.81066	27	2	2	4
2.17200	522	0	0	10	0.80822	2	3	0	14
2.09518	62	1	0	7	0.80210	5	2	1	
1.96268	54	1	0	8	0.80145	10	1	0	
1.83918	363	1	0	9	0.79974	3	2	2	6
1.81000	5	0	0	12					
1.72540	16	1	0	10					
1.64000	860	1	1	0					
1.62132	30	1	1	2					
*1.62132	30	1	0	11					
1.56996	7	1	1	4					
1.55143	5	0	0	14					
1.52645	246	1	0	12					
1.49385	27	1	1	6					
1.44013	27	1	0	13					
1.42028	12	2	0	0					
1.41725	72	2	0	1					
1.40829	27	2	0	2					
1.40377	22	1	1	8					
1.39372	13	2	0	3					
1.37406	49	2	0	4					
1.36158	64	1	0	14					
1.35750	9	0	0						
1.34996	87	2	0	5					
1.32216	96	2	0	6					
1.30881	417	1	1	10					
1.29006	69	1	0	15					
1.25848	8	2	0	8					
1.22404	78	2	0	9					
*1.22404	78	1	0						
1.21532	6	1	1	12					
1.20667	2	0	0						
1.18870	3	2	0	10					
1.16521	17	1	0						
1.15299	6	2	0	11					
1.12704	7	1	1	14					
1.11735	61	2	0	12					
1.11061	6	1	0						
1.08600	19	0	0						
1.08213	8	2	0	13					
1.07232	42	2	1	1					
1.06842	16	2	1	2					
1.06202	9	2	1	3					
1.06050	27	1	0						
1.05324	31	2	1	4					
1.04759	21	2	0	14					
1.04573	14	1	1						
1.04227	56	2	1	5					
1.02932	63	2	1	6					
1.01395	32	2	0	15					
*1.01395	32	1	0						
0.99840	6	2	1	8					
0.98727	1	0	0						
0.98094	57	2	1	9					
*0.98094	57	2	0						
0.97187	12	1	1						
*0.97187	12	1	0						
0.96247	3	2	1	10					
0.94987	8	2	0						
0.94685	83	3	0	0					
0.94322	6	3	0	2					
*0.94322	6	2	1	11					
0.93255	38	1	0						
*0.93255	38	3	0	4					
0.92340	60	2	1	12					
0.91959	3	2	0						
0.91604	4	3	0	6					
0.90547	61	0	0						
*0.90547	61	1	1						
0.90322	9	2	1	13					
0.89612	4	1	0						
0.89404	4	3	0	8					
0.89053	15	2	0						
0.88285	22	2	1	14					
0.86796	85	3	0	10					
0.86243	35	1	0						

Al₈SiC₇

Aluminum Silicon Carbide

Lattice : Hexagonal

S.G. : P3 (143)

a = 3.31270

c = 19.24200

Z = 1

Mol. weight = 328.01

Volume [CD] = 182.87

Dx = 2.978

Sample Preparation: Made by reaction at 2000 C in a sealed tantalum tube.
Data collection flag: Ambient.

Kidwell, B. et al., J. Appl. Crystallogr., volume 17, page 481 (1974)

Radiation : CuKα1

Lambda : 1.54050

SS/FOM : F30= 35(0.0177,49)

Filter :

d-sp : Diffractometer

d (Å)	i	h	k	l
9.63000	4	0	0	2
6.42000	1	0	0	3
4.81000	2	0	0	4
3.84700	14	0	0	5
2.86900	1	1	0	0
2.83700	4	1	0	1
2.74700	23	0	0	7
2.62000	1	1	0	3
2.46300	4	1	0	4
2.40300	1	0	0	8
2.30000	6	1	0	5
2.13700	100	0	0	9
1.98400	1	1	0	7
1.92400	2	0	0	10
1.84300	4	1	0	8
1.74800	1	0	0	11
1.71400	1	1	0	9
1.65600	6	1	1	0
1.59800	1	1	0	10
1.52200	1	1	1	5
1.49400	2	1	0	11
1.43000	1	2	0	1
1.41900	1	1	1	7
1.40000	1	1	0	12
1.37400	2	0	0	14
1.34400	1	2	0	5
1.31500	2	1	0	13
1.30900	4	1	1	9
1.28200	1	0	0	15
1.23900	1	1	0	14
1.23200	1	2	0	8
1.20200	1	0	0	
1.19100	1	2	0	9
1.17100	1	1	0	15
1.15000	1	2	0	10
1.13200	1	0	0	
1.10900	1	2	0	11
1.08200	1	2	1	1
1.06900	2	0	0	
1.05800	1	2	1	4
1.05300	1	1	0	
1.04400	1	2	1	5
1.03000	1	2	0	13
1.02700	1	2	1	6
1.01300	1	0	0	
1.00200	1	1	0	
0.99300	1	2	0	14
0.98900	1	2	1	8
0.95600	1	3	0	0
0.95500	1	3	0	1
0.94500	1	2	1	10
0.93400	1	1	1	
0.92200	1	2	1	11
0.91600	1	3	0	6
0.91200	1	1	0	
0.89800	1	2	1	12
0.88900	1	3	0	8
0.87500	1	2	1	13
0.87300	1	1	0	
0.85700	1	2	0	
0.85100	1	2	1	14
0.83700	1	1	0	
0.82800	1	2	2	1
*0.82800	1	2	2	0

Al₄C₃

Aluminum Carbide

Lattice : Rhombohedral
S.G. : R-3m (166)
a = 3.32900
c = 24.98000

Z = 3

Mol. weight = 143.96
Volume [CD] = 239.75
Dx = 2.991
l/lcor = 1.03

NIST M&A collection code: L 51359 ST1735 1. Calculated Pattern Original
Remarks: Authors gave structure in rhombohedral setting. Temperature
Factor: TF TF was not given, B set to 1.000 for calc. Minor Warning:
Magnitude of e.s.d. on cell dimension is >1000 ppm. No Rfactor
reported/abstracted. Unit Cell Data Source: Single Crystal.
Data collection flag: Ambient.

Calculated from NIST using POWD-12++
Stackelberg, M. v., Schnorrenberg, E., Z. Phys. Chem. (B), volume 27B, page
37 (1934)

Radiation : CuKα1
Lambda : 1.54060
SS/FOM : F30=513(0.0015,34)

Filter :
d-sp : Calculated spacings

d (Å)	i	h	k	l
8.32667	22	0	0	3
4.16333	57	0	0	6
2.86399	465	1	0	1
2.80913	970	0	1	2
2.77556	83	0	0	9
2.61754	3	1	0	4
2.49706	692	0	1	5
2.24259	999	1	0	7
2.11820	113	0	1	8
2.08167	448	0	0	12
1.88791	241	1	0	10
1.78394	100	0	1	11
1.66450	822	1	1	0
*1.66450	822	0	0	15
1.63221	2	1	1	3
1.59893	2	1	0	13
1.54556	10	1	1	6
1.51722	209	0	1	14
1.43911	30	0	2	1
1.43199	75	2	0	2
1.42749	48	1	1	9
1.40457	3	0	2	4
1.38500	93	2	0	5
1.37287	12	1	0	0
1.33657	136	0	2	7
1.30917	120	2	0	8
*1.30917	120	0	1	0
1.30001	396	1	1	12
1.24853	39	0	2	10
1.21702	19	2	0	11
1.19622	71	1	0	0
1.17727	3	1	1	15
1.15310	1	0	2	13
1.14607	2	0	1	0
1.12130	53	2	0	14
1.08864	17	2	1	1
1.08555	48	1	2	2
1.07345	2	2	1	4
1.06464	57	1	2	5
1.05910	5	0	2	0
1.05647	5	1	0	0
1.04217	92	2	1	7
1.04083	36	0	0	0
1.02902	45	2	0	0
*1.02902	45	1	2	8
1.01636	27	0	1	0
0.99878	30	2	1	10
0.98242	15	1	2	11
0.97139	29	0	2	0
0.96100	76	3	0	0
0.94787	1	2	1	13
0.94395	2	2	0	0
*0.94395	2	1	0	0
0.93638	1	0	3	6
0.92997	52	1	2	14
0.91149	17	0	1	0
0.90811	3	0	3	9
0.89355	4	2	1	0
0.89197	2	0	2	0
0.88250	89	1	1	0
0.87527	44	1	2	0
0.87251	86	3	0	12
0.86743	17	2	0	0
0.85227	1	1	0	0
0.83897	36	2	1	0
0.83225	54	0	3	15
*0.83225	54	2	2	0
0.82533	12	0	1	0
0.82110	2	0	2	0
*0.82110	2	1	2	0
0.81610	1	2	2	6
0.80866	1	1	1	0
0.79947	16	1	3	1
*0.79947	16	2	0	0
0.79797	19	3	1	2

SiC

Silicon Carbide
Moissanite-6H, syn

Lattice : Hexagonal
S.G. : P63mc (186)
a = 3.08150
c = 15.09210

Z = 6

Mol. weight = 40.10
Volume [CD] = 124.11
Dx = 3.219
l/lcor = 1.33

ANX: NO. LPF Collection Code: 1411641. Sample Preparation: STARTING MATERIALS: SiC Compound Formation: hot-pressing at 2073 K. Minor Warning: No R factors reported/abstracted. No e.s.d reported/abstracted on the cell dimension. Unit Cell Data Source: Powder Diffraction. Data collection flag: Ambient.

Calculated from LPF using POWD-12++
Bind, J., Mater. Res. Bull., volume 13, page 91-96 (1978)

Radiation : CuK α 1
Lambda : 1.54060
SS/FOM : F30= 96(0.0051,60)

Filter :
d-sp : Calculated spacings

d (Å)	i	h	k	l
7.54605	1	0	0	2
3.77303	1	0	0	4
2.62789	342	1	0	1
2.51596	999	0	0	6
*2.51596	999	1	0	2
2.35749	358	1	0	3
2.17875	143	1	0	4
1.99930	52	1	0	5
1.88651	1	0	0	8
1.83042	1	1	0	6
1.67708	63	1	0	7
1.54075	439	1	0	8
*1.54075	439	1	1	0
1.41985	125	1	0	9
1.32914	24	2	0	1
1.31386	294	1	0	10
*1.31386	294	1	1	6
1.28973	40	2	0	3
1.25798	33	0	0	12
*1.25798	33	2	0	4
1.22040	15	2	0	5
*1.22040	15	1	0	11
1.13461	12	2	0	7
1.08938	33	2	0	8
1.06456	4	1	0	13
1.04412	34	2	0	9
1.00641	15	2	1	1
0.99977	61	1	0	14
*0.99977	61	2	1	2
0.98897	27	2	1	3
0.97430	44	2	1	4
*0.97430	44	1	1	12
0.95666	9	2	0	11
*0.95666	9	2	1	5
0.94145	24	1	0	15
0.91362	11	2	1	7
0.88950	82	1	0	
*0.88950	82	2	1	8
0.87584	2	3	0	3
*0.87584	2	2	0	13
0.86434	39	2	1	9
0.85327	1	3	0	5
0.84238	5	1	0	
0.83865	74	3	0	6
*0.83865	74	0	0	
0.81267	4	2	1	11
0.80335	17	2	0	15

SiC

Silicon Carbide
Moissanite-4H, syn

Lattice : Hexagonal
S.G. : P63mc (186)
a = 3.08150
c = 10.06140

Z = 4

Mol. weight = 40.10
Volume [CD] = 82.74
Dx = 3.219
l/|cor = 1.35

ANX: NO. LPF Collection Code: 1411640. Sample Preparation: STARTING MATERIALS: SiC Compound Formation: hot-pressing at 2173 K. Minor Warning: No R factors reported/abstracted. No e.s.d reported/abstracted on the cell dimension. Unit Cell Data Source: Powder Diffraction. Data collection flag: Ambient.

Calculated from LPF using POWD-12++
Bind, J., Mater. Res. Bull., volume 13, page 91-96 (1978)

Radiation : CuK α 1
Lambda : 1.54060
SS/FOM : F30=1000(0.0000,32)

Filter :
d-sp : Calculated spacings

d (Å)	i	h	k	l
5.03070	1	0	0	2
2.66866	245	1	0	0
2.57947	999	1	0	1
2.51535	647	0	0	4
2.35749	978	1	0	2
2.08823	169	1	0	3
1.83042	77	1	0	4
1.67690	1	0	0	6
1.60670	208	1	0	5
1.54075	480	1	1	0
1.47320	1	1	1	2
1.41985	342	1	0	6
1.33433	17	2	0	0
1.32275	75	2	0	1
1.31386	321	1	1	4
1.28973	108	2	0	2
1.26546	42	1	0	7
1.25768	23	0	0	8
1.23981	25	2	0	3
1.17875	13	2	0	4
1.13767	5	1	0	8
1.11206	42	2	0	5
1.04412	92	2	0	6
1.03111	18	1	0	9
1.00866	10	2	1	0
1.00363	47	2	1	1
0.98897	74	2	1	2
0.97790	15	2	0	7
0.97430	48	1	1	8
0.96592	19	2	1	3
0.94145	65	1	0	10
0.93619	11	2	1	4
0.91521	2	2	0	8
0.90172	42	2	1	5
0.88955	56	3	0	0
0.86526	27	1	0	11
0.86434	107	2	1	6
0.85692	10	2	0	9
0.83865	72	0	0	12
*0.83865	72	3	0	4
0.82565	19	2	1	7
0.80335	47	2	0	10
0.79990	4	1	0	12

Al
 Aluminum
 Aluminum, syn

<i>d</i> (Å)	<i>i</i>	<i>h</i>	<i>k</i>	<i>l</i>
2.33800	100	1	1	1
2.02400	47	2	0	0
1.43100	22	2	2	0
1.22100	24	3	1	1
1.16900	7	2	2	2
1.01240	2	4	0	0
0.92890	8	3	3	1
0.90550	8	4	2	0
0.82660	8	4	2	2

Lattice : Face-centered cubic		Mol. weight = 26.98
S.G. : Fm-3m (225)		Volume [CD] = 66.40
a = 4.04940	Z = 4	Dx = 2.699
		l/lor = 3.62

Additional Patterns: See PDF 01-085-1327. ANX: N. Analysis: The chemical analysis (%): Si 0.011, Cu 0.006, Fe 0.007, Ti 0.0001, Zr 0.003, Ga 0.004, Mo 0.00002, S 0.0001, Al 99.9+ (by difference). Color: Light gray metallic. General Comments: Mineral species of doubtful validity, Am. Mineral., 65 205 (1980). Sample Preparation: The material used for the NBS sample was a melting point standard sample of aluminum prepared at NBS, Gaithersburg, Maryland, USA. Temperature of Data Collection: Pattern taken at 298 K. Unit Cell Data Source: Powder Diffraction. Data collection flag: Ambient.

Swanson, Tatge., Natl. Bur. Stand. (U.S.), Circ. 539, volume I, page 11 (1953)
 CAS Number: 7429-90-5

Radiation : CuKα1	Filter : Beta
Lambda : 1.54056	d-sp : Not given
SS/FOM : F9= 92(0.0100,9)	

Si

Silicon
Silicon, syn

<i>d</i> (Å)	<i>i</i>	<i>h</i>	<i>k</i>	<i>l</i>
3.13550	100	1	1	1
1.92010	55	2	2	0
1.63750	30	3	1	1
1.35770	6	4	0	0
1.24590	11	3	3	1
1.10860	12	4	2	2
1.04520	6	5	1	1
0.96000	3	4	4	0
0.91800	7	5	3	1
0.85870	8	6	2	0
0.82820	3	5	3	3

Lattice : Face-centered cubic

Mol. weight = 28.09

S.G. : Fd-3m (227)

Volume [CD] = 160.18

a = 5.43088

Dx = 2.329

Z = 8

l/lor = 4.70

Additional Patterns: To replace 00-005-0565 and 00-026-1481. Color: Gray.
General Comments: Reflections calculated from precision measurement of a0. a0 uncorrected for refraction. Sample Source or Locality: This sample is NBS Standard Reference Material No. 640. Temperature of Data Collection: Pattern taken at 298(1) K. Unit Cell Data Source: Powder Diffraction. Data collection flag: Ambient.

Natl. Bur. Stand. (U.S.) Monogr. 25, volume 13, page 35 (1976)

CAS Number: 7440-21-3

Radiation : CuKα1

Filter : Monochromator crystal

Lambda : 1.54060

d-sp : Diffractometer

SS/FOM : F11=443(0.0018,13)

Al₂O₃

Aluminum Oxide Carbide

Also called: α'-Al₂O₃C, dialuminum oxide carbide

Lattice : Hexagonal

S.G. : P63mc (186)

a = 3.10000

c = 5.00000

Z = 1

Mol. weight = 81.97

Volume [CD] = 41.61

Dx = 3.271

l/cor = 1.40

d (Å)	i	h	k	l
2.68468	999	1	0	0
2.50000	643	0	0	2
2.36529	898	1	0	1
1.82957	312	1	0	2
1.55000	493	1	1	0
1.41599	403	1	0	3
1.34234	64	2	0	0
1.31735	306	1	1	2
1.29643	102	2	0	1
1.25000	14	0	0	4
1.18264	47	2	0	2
1.13319	14	1	0	4
1.04543	101	2	0	3
1.01471	36	2	1	0
0.99444	66	2	1	1
0.97302	30	1	1	4
0.94022	37	2	1	2
0.93710	78	1	0	5
0.91479	6	2	0	4
0.89489	48	3	0	0
0.86672	109	2	1	3
0.84254	54	3	0	2
0.83333	6	0	0	6
0.80193	54	2	0	5

ANX: AX. Analysis: C1 Al2 O1. Formula from original source: Al2 O C. ICSD Collection Code: 250129. Minor Warning: No e.s.d reported/abstracted on the cell dimension. Wyckoff Sequence: b2(P63MC). Unit Cell Data Source: Powder Diffraction. Data collection flag: Ambient.

Calculated from ICSD using POWD-12++
Sitnikov, P.A., Goldin, B.A., Ryabkov, Yu.I., Grass, V.E., Zh. Strukt. Khim., volume 45, page 103 (2004)

Radiation : CuKα1

Lambda : 1.54060

SS/FOM : F24=1000(0.0000,25)

Filter :

d-sp : Calculated spacings

Al₂O₃

Aluminum Oxide Carbide

Also called: α'-Al₂O₃ C, dialuminum oxide carbide

Lattice : Hexagonal

S.G. : P63mc (186)

a = 3.10000

c = 5.00000

Z = 1

Mol. weight = 81.97

Volume [CD] = 41.61

Dx = 3.271

l/cor = 1.40

2th	i	h	k	l
33.348	999	1	0	0
35.892	643	0	0	2
38.012	898	1	0	1
49.799	312	1	0	2
59.599	493	1	1	0
65.913	403	1	0	3
70.038	64	2	0	0
71.568	306	1	1	2
72.907	102	2	0	1
76.084	14	0	0	4
81.285	47	2	0	2
85.650	14	1	0	4
94.923	101	2	0	3
98.776	36	2	1	0
101.538	66	2	1	1
104.682	30	1	1	4
110.025	37	2	1	2
110.571	78	1	0	5
114.715	6	2	0	4
118.807	48	3	0	0
125.435	109	2	1	3
132.201	54	3	0	2
135.144	6	0	0	6
147.707	54	2	0	5

ANX: AX. Analysis: C1 Al2 O1. Formula from original source: Al2 O C. ICSD Collection Code: 250129. Minor Warning: No e.s.d reported/abstracted on the cell dimension. Wyckoff Sequence: b2(P63MC). Unit Cell Data Source: Powder Diffraction. Data collection flag: Ambient.

Calculated from ICSD using POWD-12++
Sitnikov, P.A., Goldin, B.A., Ryabkov, Yu.I., Grass, V.E., Zh. Strukt. Khim., volume 45, page 103 (2004)

Radiation : CuKα1

Lambda : 1.54060

SS/FOM : F24=1000(0.0000,25)

Filter :

d-sp : Calculated spacings

Resumé de la thèse en français

I. Introduction

1.1. Histoire d' Al_4SiC_4

Al_4SiC_4 a été mentionné pour la première fois par Barczak dans une lettre publiée en 1961¹, dans laquelle il a été signalé pour la première fois les données de diffraction des rayons X pour ce composé. Selon l'auteur, deux polymorphes différents d' Al_4SiC_4 pourraient être synthétisés à haute température : (i) phase α - Al_4SiC_4 avec une structure hexagonale formée par la fusion du mélange molaire 4 : 1 d'aluminium et de silicium avec un excès de carbone dans un creusé fermé de carbone à 1620°C et (ii) phase β - Al_4SiC_4 avec une structure inconnue formée par recuit d'un mélange 1 : 1 molaire de Al_4C_3 : SiC à 1870°C.

Vingt ans plus tard, les données cristallographiques des rayons X de Al_4SiC_4 ont été affinées par Schoennahl et al.² (1984). Il a trouvé une dimension de cellule unitaire différente de celle de Barczak et a présenté une description complète de la phase α - Al_4SiC_4 . Cependant, le β - Al_4SiC_4 -le second polymorphe proposé par Barczak n'a pas été observé. Le processus de synthèse de la poudre Al_4SiC_4 a été détaillé dans le rapport. L'auteur a également évoqué la possibilité de synthétiser de petits monocristaux d' Al_4SiC_4 par recuit à haute température, soit un corps fritté en Al_4SiC_4 , soit un mélange de matières premières Al_4C_3 et SiC. Ils ont également souligné la fenêtre de température extrêmement étroite, d'environ 30°C entre 1950°C et 1980°C, conditions dans lesquelles de petites plaquettes jaunes et transparentes ont été obtenues.

En 1987, les équilibres de phase dans le système ternaire Al-Si-C ont été étudiés expérimentalement par Oden et McCune³ afin de faciliter les recherches et le développement d'une réduction carbo-thermique pour l'aluminium. Dix ans plus tard, en 1996, les paramètres thermodynamiques du système ternaire Al-Si-C ont été évalués par Grobner et al.⁴ grâce à la capacité thermique donnée par Beyer et al.⁵ en 1984.

Dans les années 1990, l'interaction chimique de l'interface Al/SiC a été étudiée pour le développement de matériaux composites d'aluminium renforcés par SiC⁶⁻¹². On a trouvé Al_4SiC_4 sous forme de plaquettes en faisant réagir SiC en excès d'aluminium pendant 30 min à 1497°C. De plus, en raison de la formation de Al_4C_3 au début de la réaction, l'auteur a également prédit la croissance de Al_4SiC_4 par diffusion à l'état solide⁶.

En 2002, une excellente résistance à l'oxydation d' Al_4SiC_4 à une température inférieure à 850°C a été trouvée¹³. Cinq ans plus tard, les propriétés mécaniques et thermiques d' Al_4SiC_4 synthétisé par réaction à l'état solide ont été étudiées^{14,15}.

En 2008, la structure électronique de Al_4SiC_4 a été étudiée théoriquement par des calculs ab initio par Hussain et al.¹⁶. Une bandgap indirecte de 1.05eV a été prédite, faisant d' Al_4SiC_4 comme composé avec des propriétés semi-conductrices.

Cependant, cette valeur de bandgap n'est pas compatible avec la transparence des plaquettes rapportée par Schoennahl et al., où le cristal Al_4SiC_4 était reconnu avec une couleur jaune². Cet écart était le point de départ de notre étude sur Al_4SiC_4 . Les petites plaquettes monocristallines de haute qualité ont été synthétisées par notre groupe afin de mesurer le spectre d'absorption UV-Vis de Al_4SiC_4 . Une bandgap d'optique d'environ 2.5eV¹⁷ s'est révélée être en bon accord

avec celle calculée plus récemment par Pedesseau et al¹⁸. Selon la structure de la bandgap calculée, Al₄SiC₄ présente des bandgap d'énergie directes et indirectes de 2.5eV et 3.2eV, respectivement. Légèrement supérieur à la bande interdite de 3C-SiC (polytype cubique de SiC), Al₄SiC₄ pourrait être un matériau potentiel pour des applications telles que l'électronique à haute température, le fractionnement de l'eau photovoltaïque ou photoélectrochimique.

1.2. Structure cristalline

Du point de vue cristallographique, Al₄SiC₄ appartient à une famille de carbures ternaires aluminium-silicium à structure hexagonale dont la formule générale est (Al₄C₃)_x(SiC)_y (x, y=1 ou 2). Selon la structure cristalline illustrée sur la Figure 1, Al₄SiC₄ est constitué de deux types de couches qui sont alternativement empilées selon la direction [0001]. Une couche est la plaque Al-C suivant la structure de type Al₄C₃ et l'autre couche est constituée d'une plaque de Si-C suivant la structure 2H-SiC. La structure cristalline de Al₄SiC₄ a été confirmée expérimentalement par microscopie électronique à transmission (TEM) et diffraction des rayons X pour appartenir au groupe spatial P6₃mc avec des paramètres de réseau a = 3,2812 (± 0,0045) Å et c = 21,7042 (± 0,0554) Å en bon état accord avec les données cristallographiques rapportées².

Tableau 1: Données cristallographiques des différentes phases identifiées dans le système Al-Si-C.

Formula	Space group	Lattice constant (Å)		c/a
		a	c	
SiC-4H	P6 ₃ mc	3.08	10.06	3.27
SiC-6H	P6 ₃ mc	3.08	15.09	4.90
Al ₄ C ₃	R-3m	3.33	24.98	7.50
Al ₄ SiC ₄ (Al ₄ C ₃ .SiC)	P6 ₃ mc	3.28	21.72	6.62
Al ₈ SiC ₇ (2Al ₄ C ₃ .SiC)	P3	3.31	19.24	5.81
Al ₄ Si ₂ C ₅ (Al ₄ C ₃ .2SiC)	R-3m	3.25	40.10	12.34

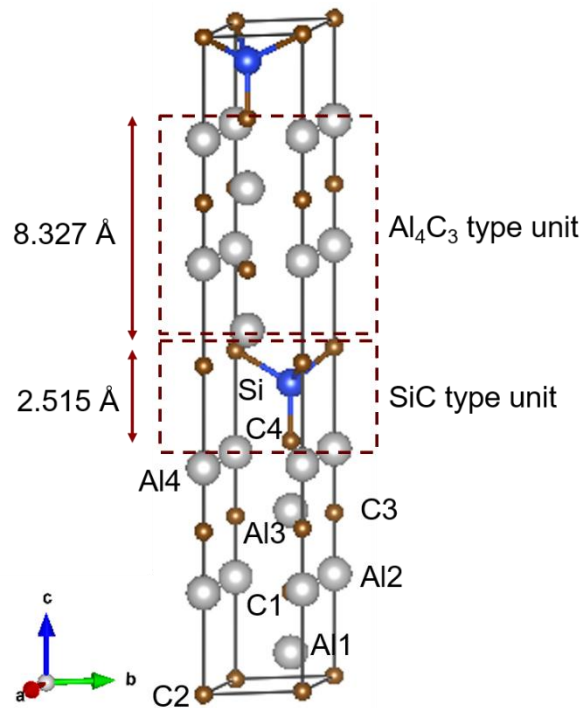


Figure 1: Structure cristalline de Al_4SiC_4 . Les boules grises, bleues et brunes représentent respectivement les atomes d'Al, Si et C. Les atomes d'Al et de C dans Al_4SiC_4 sont indexés avec des nombres selon le fichier d'informations cristallographiques (CIF) donné par Schoennahl et al. Les cellules Al_4C_3 et les cellules SiC dans Al_4SiC_4 sont aussi indiquées avec la hauteur dans la direction normale de 8.327 et 2.515 Å, respectivement.

Deux autres carbures ternaires Al-Si-C tels que $Al_4Si_2C_5$ et Al_8SiC_7 ont été découverts par Inoue¹⁹ en 1980 et Kidwell²⁰ en 1984, respectivement. Selon la stoechiométrie, $Al_4Si_2C_5$ est constitué d'une unité structurale de type Al_4C_3 et de deux unités structurales de type SiC, tandis que Al_8SiC_7 comprend deux unités structurales de type Al_4C_3 et une unité structurale de type SiC.

Les cellules unitaires relatives de différents composés de carbures ternaires aluminium-silicium sont comparées dans le tableau 1.

1.3. Al_4SiC_4 comme matériel électronique

Jusqu'à présent, la plupart des travaux rapportés sur Al_4SiC_4 concernent des applications de matériaux structuraux à haute température, avec d'excellentes propriétés céramiques et une résistance à l'oxydation et à la corrosion. Compte tenu de ces propriétés, combinées avec ses propriétés semi-conductrices, il est raisonnable d'envisager, par rapport à Si, de nombreux avantages pour les appareils électroniques qui sont capables de fonctionner à haute température et plus généralement dans des environnements difficiles, tels que les capteurs de gaz, les capteurs de rayonnement, les photo-électrodes pour le fractionnement de l'eau, etc.

Cependant, étant donné que le processus de synthèse des monocristaux d' Al_4SiC_4 n'a pas encore été étudié, les caractérisations expérimentales sur les propriétés monocristallines d' Al_4SiC_4 sont toujours inaccessibles. Par conséquent, presque toutes les propriétés

électroniques importantes de Al_4SiC_4 n'ont pas encore été explorées dans la littérature, telles que la mobilité des porteurs (électron et trou), la possibilité de dopage, etc. Avec une bandgap autour de 2.5eV, Al_4SiC_4 ne sera évidemment pas en concurrence avec les semi-conducteurs à large bande interdite (GaN, AlN, α -SiC) dans les domaines de l'électronique à haute puissance et / ou de l'optoélectronique à courte longueur d'onde (LED UV-Vis et lasers).

Cependant, par analogie avec le 3C-SiC, il pourrait présenter certains avantages pour les dispositifs basés sur l'absorption naturelle de la lumière, tels que les applications de fractionnement de l'eau photovoltaïques et photoélectrochimiques. En outre, l'un des intérêts les plus importants est sa compatibilité avec la technologie de 4H ou 6H-SiC. Il a un réseau cristallin similaire et une compatibilité chimique. Avec une bandgap plus petite que SiC, nous spéculons donc sur la possibilité de développer des hétérostructures et des hétérojonctions originales.

Certaines propriétés importantes d' Al_4SiC_4 sont comparées aux matériaux semi-conducteurs bien connus (GaN, AlN, SiC) dans le tableau 2. Notez que la conductivité thermique rapportée de Al_4SiC_4 est relativement faible, cependant, cette valeur a été mesurée pour les Al_4SiC_4 frittés ; une valeur plus élevée est attendue pour le monocristal d' Al_4SiC_4 .

Tableau 2 : Propriétés des matériaux semi-conducteurs.

Propriétés	Si	GaN	AlN	4H-SiC	3C-SiC	Al_4SiC_4	
Bandgap (eV)	1.12	3.39	6.2	3.2	2.36	2.5	
Densité (g/cm ³)	2.329	6.15	3.23	3.21	3.21	2.97*	
Point de fusion à 1atm (°C)	1412	2500	3000	-	-	2080	
Conductivité thermique (W.cm ⁻¹ .C ⁻¹)	1.3	1.3	2.85	3.7	3.6	0.8*	
Dilatation thermique (C ⁻¹)	a	2.60E-06	5.59E-06	4.15E-06	3.21E-06	2.77E-06	9.96E-06
	c		3.17E-06	5.27E-06	3.09E-06		

Une simple considération peut être discutée en ce qui concerne les candidats dopants potentiels pour Al_4SiC_4 , car la structure se compose des blocs de SiC et Al_4C_3 . En effet, pour le dopage de type p, les atomes d'Al (Z = 13, à configuration électronique de la couche externe: 3s² 3p¹) de l' Al_4SiC_4 pourraient être remplacés par des atomes de Mg ayant un électron de moins dans la couche externe (Z = 12, 3s²), il est également connu comme source de dopant pour AlN de type p. Les atomes de Si (Z = 14, 3s² 3p²) dans Al_4SiC_4 pourraient être substitués par des atomes de B (Z = 5, 2s² 2p¹). Pour le dopage de type n, P (Z = 15, 3s² 3p³) et N (Z=7, 2s² 2p³) pourraient respectivement occuper le site de Si et le site de C. De plus, Al et Si pourraient être substitués l'un à l'autre pour générer le niveau de donneur et d'accepteur dans le matériau car ils occupent les positions consécutives dans le tableau périodique. Ce comportement d'auto-dopage pourrait entraîner à une concentration élevée de porteurs d' Al_4SiC_4 . Cependant, il est plus difficile de contrôler le niveau de dopage du matériau.

1.4. Contribution de la thèse

Le présent travail se concentre sur la synthèse de la couche monocristalline ou épitaxiale de Al_4SiC_4 par le processus de sublimation sur germe de SiC. Trois sujets principaux seront discutés.

Le premier concerne les études thermodynamiques du système pseudo-binaire Al_4C_3 -SiC. Grâce aux calculs thermodynamiques, les phénomènes de vaporisation et de condensation seront discutés afin de proposer un processus en phase vapeur pour la synthèse de Al_4SiC_4 .

Le second est la démonstration expérimentale de la croissance d' Al_4SiC_4 basée sur les conditions obtenues par les calculs thermodynamiques. À partir d'une approche expérimentale approfondie, un processus de sublimation pour la croissance de monocristaux d' Al_4SiC_4 sera ainsi étudié. Ensuite, la caractérisation de la texture sera effectuée sur les monocristaux obtenus afin d'évaluer la dépendance de l'orientation de la croissance et de la qualité du dépôt sur différents types de substrats SiC. De plus, la caractérisation de l'absorption UV sera effectuée pour étudier les propriétés optiques du matériau.

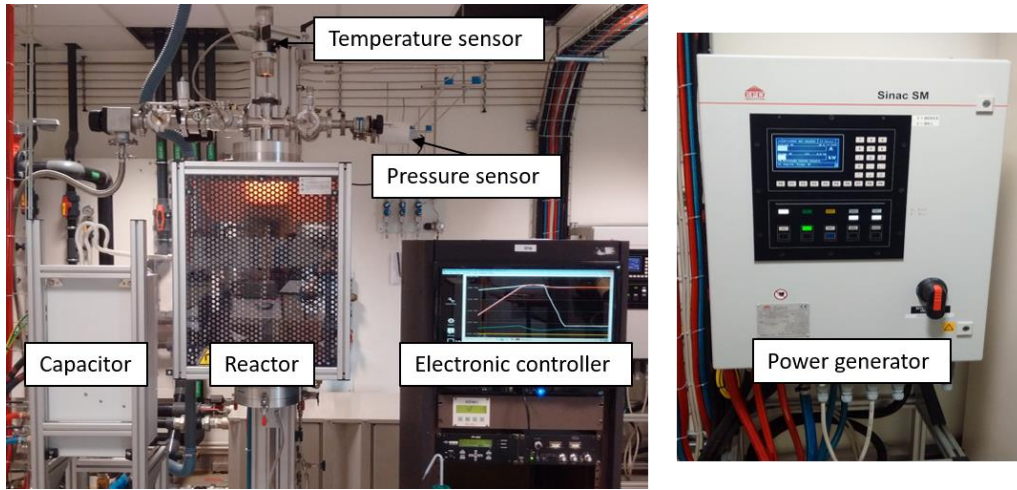
Comme troisième sujet, l'étude de l'hétérostructure de Al_4C_3 et Al_4SiC_4 sur des substrats hexagonaux SiC pourrait être intéressante pour de nombreuses applications. En utilisant la microscopie électronique à transmission, l'interface des hétérostructures sera caractérisée afin d'étudier leurs propriétés cristallographiques et de donner un retour sur le mécanisme de croissance.

II. Dispositif expérimental

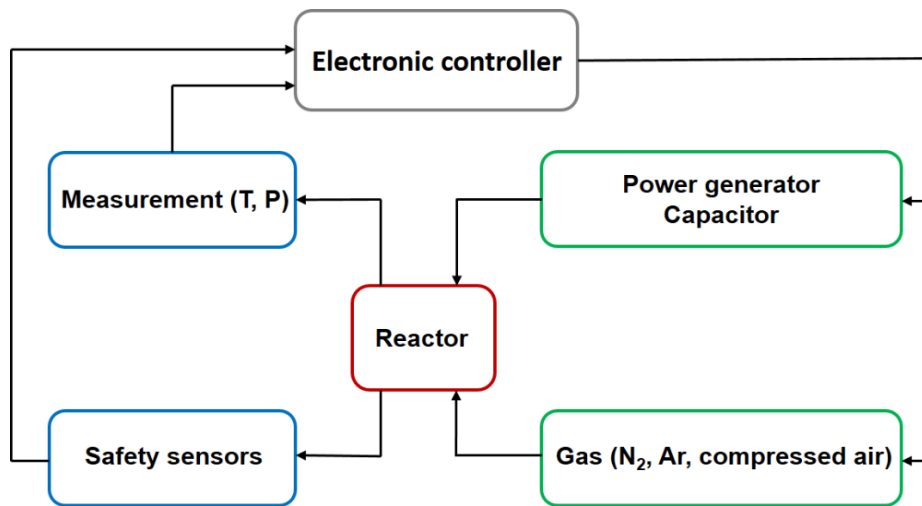
Avec une température de fonctionnement supérieure à 1800°C , un réacteur de recuit par induction a été développé pour le procédé de transport physique en phase vapeur (PVT). Dans cette section, différentes unités du réacteur PVT et du creuset utilisé pour les expériences sont décrites.

2.1. Configuration du réacteur de transport physique des vapeurs

L'appareil expérimental utilisé pour la croissance de Al_4SiC_4 comprend les unités suivantes : le générateur, le boîtier de condensateur, le contrôleur électronique, le dispositif de mesure (pression et température), la chambre du réacteur et le générateur de puissance, comme indiqué dans la Figure 2.



(a)



(b)

Figure 2: (a) Photo de l'appareil expérimental utilisé pour la croissance de PVT. (b) Schéma de la configuration du réacteur PVT.

Un circuit de courant alternatif a été conçu pour un réacteur de chauffage par induction comprenant : un générateur, un condensateur et un inducteur. Le circuit parallèle RLC équivalent avec résistance en série avec inducteur est représenté à la . Deux types de pertes de puissance sont considérés dans le circuit RLC : les pertes actives dues aux composants résistifs et les pertes réactives dues à l'inductance. La puissance complexe S (Volt-Ampere) définie comme la puissance réelle requise par notre système est la somme vectorielle des puissances actives P (Watts) et réactives Q (Volt-Ampères Reactive) et est un produit de carré-racine de circuit de tension et de courant donné par l'expression ci-dessous :

$$S = V_{rms} I_{rms} = \sqrt{P^2 + Q^2}$$

Parmi eux, la puissance active est la puissance « réelle » consommée par une résistance qui ne provoquera pas de déphasage entre tension et courant, tandis que la puissance réactive compense les effets de la puissance « réelle » due au déphasage de 90° entre tension et courant. Ainsi, afin de réduire la puissance réactive générée du système, la capacité est intégrée pour

générer suffisamment de puissance réactive consommée par l'inducteur en provoquant le déphasage "opposé" (-90°) entre tension et courant.

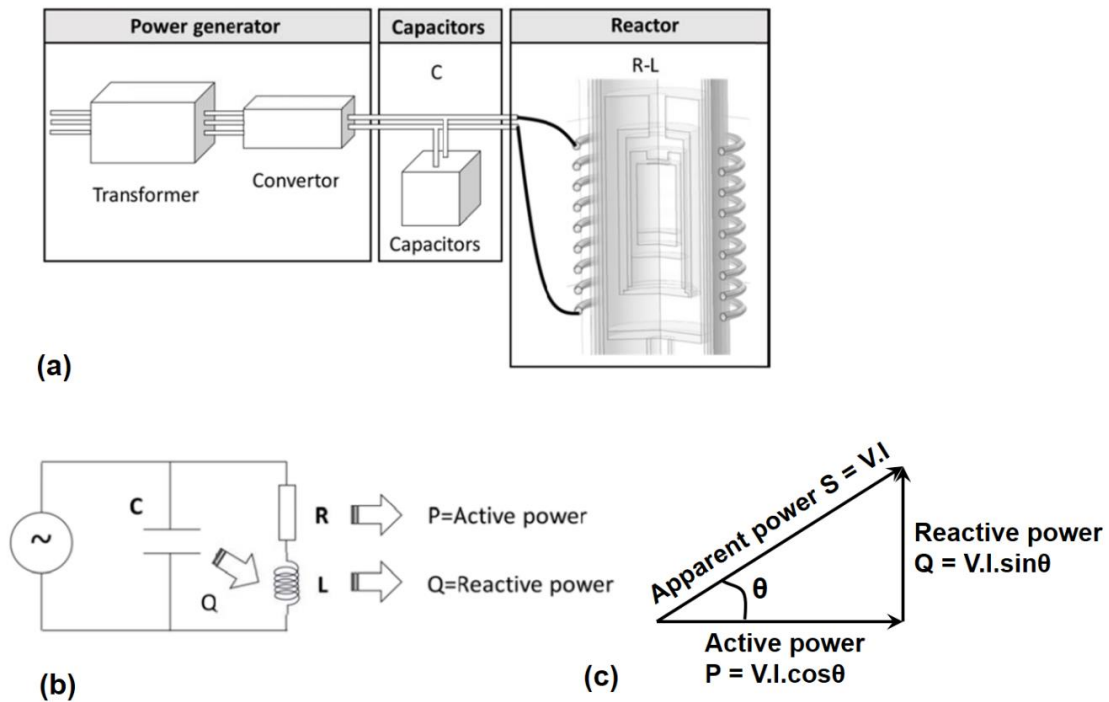


Figure 3: a) Représentation schématique du raccordement topologique du générateur, des condensateurs, du réacteur; (b) le circuit parallèle RLC équivalent; (c) triangle de puissance du circuit RLC représentant la relation entre la puissance apparente, la puissance réactive et la puissance active.

La conception de la bobine a également été optimisée en modifiant les paramètres géométriques tels que : le nombre de tours, le diamètre et la hauteur de la bobine pour atteindre la condition de résonance au moyen d'une adaptation de l'impédance, dans laquelle l'impédance du circuit RLC équivalent est proche de l'impédance du générateur de puissance. De plus, la topologie du circuit de notre système étant un circuit parallèle, la résonance parallèle est considérée pour une conception optimale, ce qui a l'avantage que le courant est amplifié par la bobine de travail, le générateur n'a donc besoin que de transporter une partie du courant de charge qui fait réellement le travail réel.

Le contrôleur électrique se compose d'une unité électronique maison (automatisation) qui contrôle tous les systèmes électroniques périphériques tels que : un système de gaz (régulateurs de pression, régulateurs de débit massique et vannes pneumatiques) et un système de chauffage (régulateurs de température).

La chambre du réacteur est composée d'une enveloppe en quartz refroidie à l'eau, montée sur des brides en aluminium spécialement conçues en haut et en bas. Le creuset est fixé sur l'axe vertical à l'intérieur du tube de quartz. En dehors du tube, une bobine d'induction est placée, qui est faite de cuivre et refroidie par l'eau. La bobine peut se déplacer dans la direction verticale afin de régler la position relative entre le creuset et la bobine. La température à l'intérieur du réacteur est mesurée à partir du haut par un pyromètre dichromatique, à travers

une fenêtre en quartz située dans le couvercle supérieur en aluminium, comme illustré sur la Figure 4 . La chambre du réacteur est parfaitement étanche et aucune fuite ne peut être détectée à l'aide d'un testeur He sous vide secondaire. Deux capteurs de pression ont été utilisés pour mesurer la pression en dessus du réacteur. Le premier est utilisé pour la basse pression (<1 mbar) et le second est utilisé pour la haute pression (> 1 mbar).

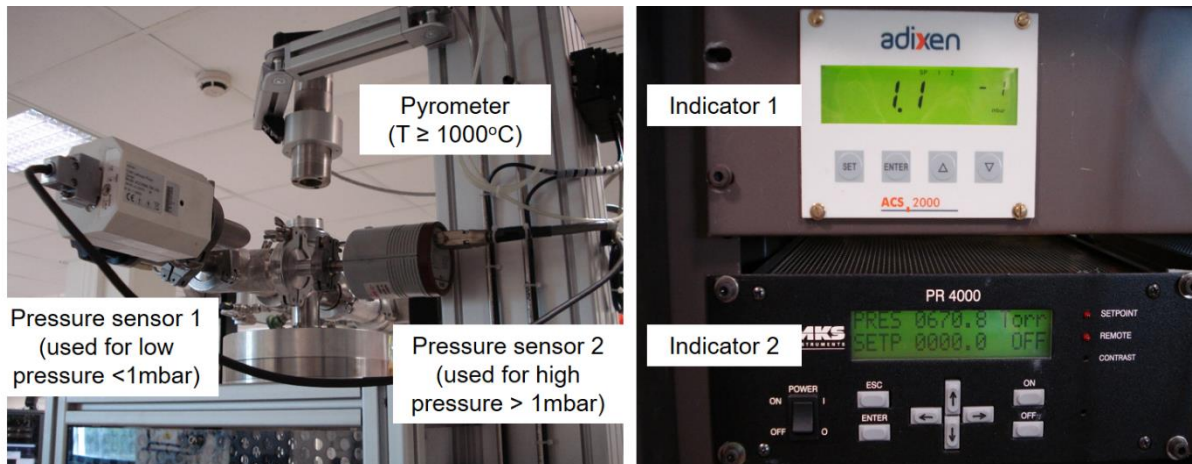


Figure 4: Photo du pyromètre dichromatique et des capteurs de pression en dessus du réacteur.

Le réacteur est raccordé à un panneau de gaz, qui a été conçu pour des expériences et constitué d'argon et d'azote. Pour ces gaz, un ensemble de régulateurs de débit massique, de vannes pneumatiques et de microvannes assure une grande flexibilité des injections de gaz sous pression totale contrôlée. L'entrée des gaz se situe dans la partie inférieure du réacteur. Dans cette étude, seul l'argon a été utilisé. En haut, une soupape de sécurité et une vanne papillon sont équipées. Une pompe rotative capable de créer un vide de 10^{-3} mbar est utilisée pour le contrôle de la pression.

2.2. Creuset

Connu comme un matériau réfractaire couramment utilisé dans la synthèse des carbures, le graphite peut résister au traitement à haute température (1700-2100°C) et a une stabilité chimique avec le système $\text{Al}_4\text{C}_3\text{-SiC}$. Par conséquent, le graphite a été utilisé pour la fabrication du creuset dans nos expériences. La Figure 5 présente le schéma de la géométrie de la pièce externe. Selon les exigences des processus expérimentaux, la partie interne (appelée chambre de réaction) sera modifiée pour adapter les conditions expérimentales. Les détails de chaque géométrie expérimentale, à savoir la chambre de réaction, seront décrits en même temps que le processus expérimental correspondant dans les chapitres suivants. En général, deux types différents de matériaux de graphite sont combinés, la pièce à haute densité est utilisée pour fabriquer un creuset et le feutre de graphite poreux avec une structure de type "fibre" est utilisé comme isolant. Toutes les parties du creuset en graphite externe utilisé pour les expériences sont présentées à la Figure 6.

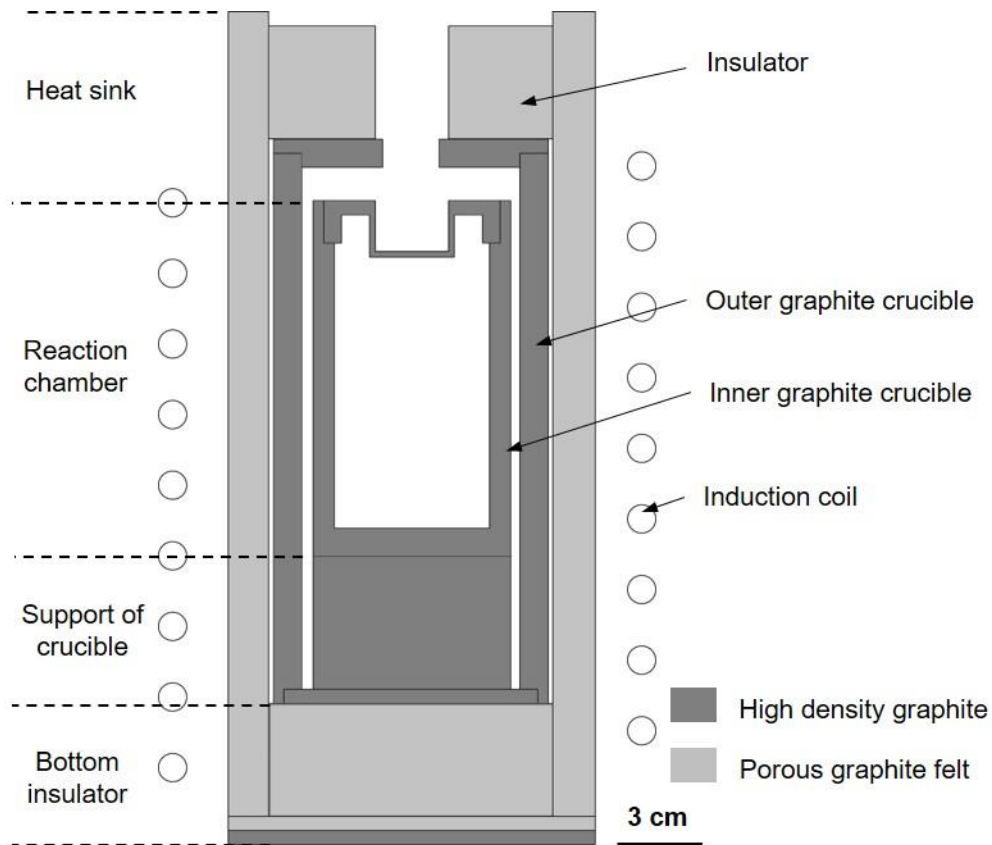


Figure 5: Schéma de la géométrie de la pièce externe.



Figure 6: Parties principales du creuset en graphite externe utilisé pour les expériences.

III. Thermochimie du système $\text{Al}_4\text{C}_3\text{-SiC}$

Selon la littérature, Al_4SiC_4 pourrait être synthétisé à partir de deux processus différents tels que (i) la croissance en solution et (ii) le frittage. La croissance de la solution peut être réalisée en faisant fondre de l'aluminium (Al) et du silicium (Si) dans un environnement de carbone (C) avec une stœchiométrie molaire à 1800°C sous la pression atmosphérique¹⁷. Cependant, cette approche est difficile à reproduire. En fait, à cause de réaction de l'aluminium liquide avec le graphite, le creuset en graphite est souvent endommagé (cassé), entraînant une perte de liquide. En revanche, selon le diagramme de phase, la phase Al_4SiC_4 pourrait être synthétisée en frittant une composition équimolaire de Al_4C_3 et de SiC à une température inférieure à 2085°C . Cette approche était couramment utilisée pour synthétiser les céramiques ou poudres en vrac d' Al_4SiC_4 dans la littérature². Cependant, la réaction à l'état solide montre généralement un faible rendement conduisant à un mélange de phases (résidus n'ayant pas réagi) et ne sont pas intrinsèquement adaptés à la croissance de monocristaux.

Afin de proposer un procédé en phase vapeur pour la croissance d' Al_4SiC_4 , l'étude thermodynamique du système est essentielle. Dans ce chapitre, la thermochimie du système pseudo-binaire Al_4C_3 -SiC sera étudiée par calcul thermodynamique.

3.1. Calcul thermodynamique

Les calculs thermodynamiques du Al-Si-C ternaire ont été effectués avec le logiciel Factage 7.1, à l'aide d'une base de données cohérentes provenant du groupe scientifique Thermodata Europe (SGTE), SGPS (Groupe scientifique Thermodata Europe Pur Substances) qui est compilé à partir du raffinement proposé par Gröbner et al.⁴ Toutes les espèces considérées dans ce travail sont rassemblées dans le tableau 3.

Tableau 3: Détails des espèces chimiques considérées dans le travail, avec les bases de données correspondantes.

	Espèces chimiques	Database
Phase vapeur	Al, Al ₂ , AlC, Al ₂ C, AlC ₂ , Al ₂ C ₂ , Si, Si ₂ , Si ₃ , SiC, Si ₂ C, SiC ₂ , Si ₂ C ₂ , Si ₃ C, Si ₃ C ₂ , Si ₄ C, C ₂ , C ₃ , C ₄ , C ₅ , Ar	SGPS
Phase liquide	Al, Si, C	SGTE
Solutions	Alloys liquide, Al-carbide avec solubility pour Si, Phase compacte hexagonale avec interstitiel C	SGTE
Phase solide	Al_4SiC_4 , Al_8SiC_7 , SiC, Al_4C_3 , C (graphite)	SGTE

Avant de discuter de la composition de la phase gazeuse, la validité de la base de données compilée a été évaluée. Les calculs ont été trouvés en parfait accord avec les travaux expérimentaux d'Oden et al.³.

Les calculs ont été effectués en minimisant l'énergie libre totale du système dans la range de température de 1500 à 2100°C avec l'hypothèse du volume constant. La phase vapeur est supposée se comporter comme un gaz parfait. Comme conditions initiales, nous avons placé un mélange de SiC et Al_4C_3 avec diverses compositions, une atmosphère d'argon et un excès de carbone solide. Ces conditions ont été sélectionnées car elles sont proches de celles expérimentales présentées dans le chapitre suivant. Pour simuler le processus de croissance par

sublimation, à savoir une cavité de croissance soumise à un gradient de température, nous avons utilisé la procédure suivante : premièrement, la composition de la phase vapeur d'équilibre est calculée à une température donnée (T_{POWDER}). Ensuite, toutes les espèces gazeuses sont sélectionnées et utilisées en tant que conditions initiales pour un deuxième calcul, à une température inférieure (T_{SEED}). Avec une telle approche, il est possible de décrire sur une base purement thermodynamique, la nature et la composition des phases solide condensées. Le schéma du processus de calcul est présenté à la Figure 7.

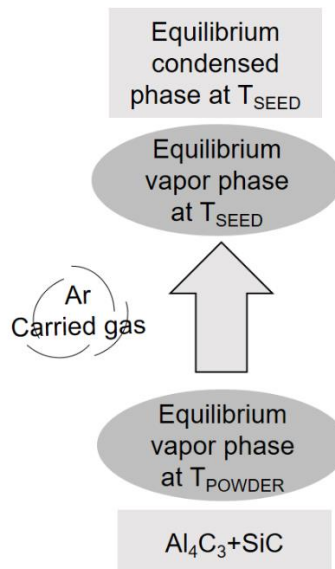


Figure 7: Schéma du processus de calcul thermodynamique.

3.2. Thermochimie du système gaz-solide

Afin d'étudier la thermochimie du système gaz-solide, deux phénomènes différents ont été considérés séparément, tels que la vaporisation des poudres et la condensation au germe.

3.2.1. La vaporisation des poudres

Pour la première étape, la phase vapeur à l'équilibre vaporisée à partir du système $\text{Al}_4\text{C}_3\text{-SiC}$ a été considérée. Le tableau 4 donne les pressions partielles d'équilibre calculées des différentes espèces gazeuses à 2000°C pour la composition initiale de $X_{\text{Al}_4\text{C}_3} = 0,5$. On peut voir que les pressions partielles se sont étendues sur une large gamme de valeurs, réparties sur dix ordres de grandeurs. Pour cette raison, certaines espèces à faible pression partielle peuvent être négligées. Le système peut être décrit avec précision en considérant seulement 6 espèces parmi lesquelles $\text{Al}(\text{g})$, $\text{Al}_2(\text{g})$, $\text{Al}_2\text{C}_2(\text{g})$, $\text{Si}(\text{g})$, $\text{SiC}_2(\text{g})$, $\text{Si}_2\text{C}(\text{g})$. L'évolution de la pression partielle de ces espèces en fonction de la température est représentée sur la Figure 8. À côté de cela, les activités correspondantes des éléments Al, Si et C dans la composition de la phase vapeur sont reportées sur la Figure 8(b).

Tableau 4: Pressions partielles d'équilibre des différentes espèces gazeuses calculées à partir d'un mélange initial de $X_{\text{Al}_4\text{C}_3} = 0,5$ à 2000°C .

Espèces	$\text{C}_2(\text{g})$	$\text{C}_3(\text{g})$	$\text{C}_4(\text{g})$	$\text{C}_5(\text{g})$	$\text{Al}(\text{g})$	$\text{Al}_2(\text{g})$	$\text{AlC}(\text{g})$
---------	------------------------	------------------------	------------------------	------------------------	-----------------------	-------------------------	------------------------

p_i [bar]	8.82E-10	1.01E-8	2.30E-12	1.01E-11	0.07	2.22E-4	1.35E-7
-------------	----------	---------	----------	----------	------	---------	---------

Espèces	AlC ₂ (g)	Al ₂ C ₂ (g)	Si(g)	Si ₂ (g)	Si ₃ (g)	CSi(g)	C ₂ Si(g)
p_i [bar]	2.88E-6	4.19E-4	1.08E-4	7.95E-7	3.90E-8	1.07E-8	1.36E-5

Espèces	CSi ₂ (g)	C ₂ Si ₂ (g)	CSi ₃ (g)	C ₂ Si ₃ (g)	CSi ₄ (g)
p_i [bar]	2.54E-5	4.36E-7	2.27E-7	1.22E-7	1.00E-10

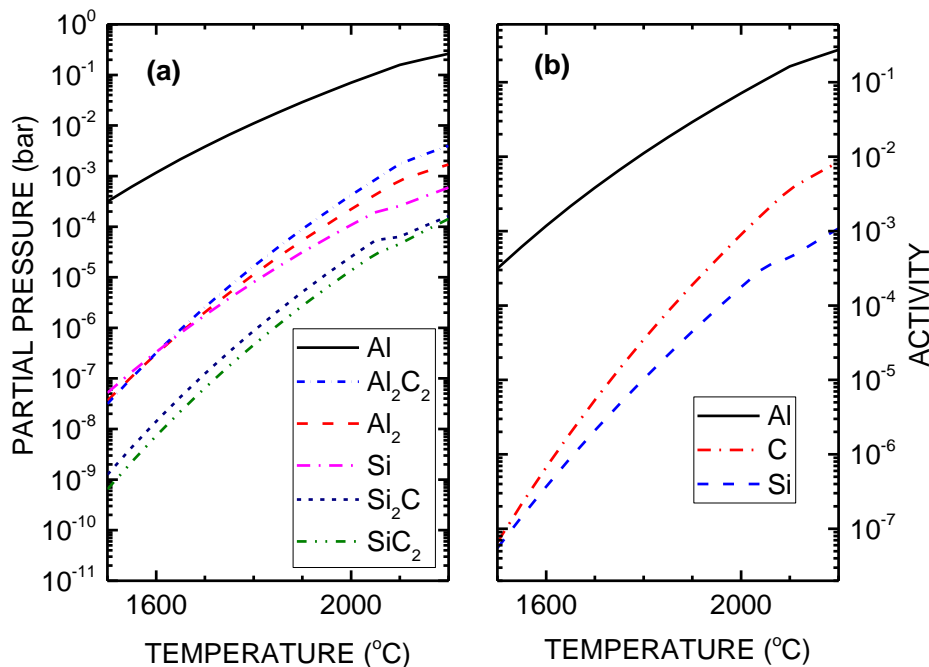


Figure 8: (a) Des pressions partielles d'équilibre de la principale espèce de vapeur en fonction de la température pour une composition initiale $X_{Al_4C_3}=0.5$ des matériaux sources. (b) Activités des éléments Al, Si et C en phase vapeur en fonction de la température.

Comme prévu, la vaporisation du mélange Al₄C₃-SiC augmente fortement avec la température. La composition de la phase vapeur est caractérisée par la grande prédominance de Al(g) qui représente plus de 95% de la pression totale. L'espèce contenant le carbone la plus abondante est Al₂C₂(g), quelle que soit la température. De manière similaire à l'aluminium, l'espèce de silicium dominante est le Si(g). La pression partielle de Si₂C(g) et SiC₂(g), qui sont les espèces de vaporisation connues du SiC, est environ un ordre de grandeur inférieur aux espèces principales contenant C et Si. Concernant les activités des éléments, comme illustré sur la Figure 8(b), l'activité des éléments Al en phase vapeur est la plus élevée avec un ordre de grandeur supérieur à celui de Si et C pour l'intervalle de température 1500-2200°C. L'activité de C et l'activité de Si sont assez similaires à une température de 1500°C, cependant, la différence augmente avec la température. À 2200°C, l'activité de C est environ un ordre de grandeur supérieure à l'activité de Si. Notez qu'une petite discontinuité autour de 2080°C correspond à la décomposition péritectique : Al₄SiC₄ → L + C.

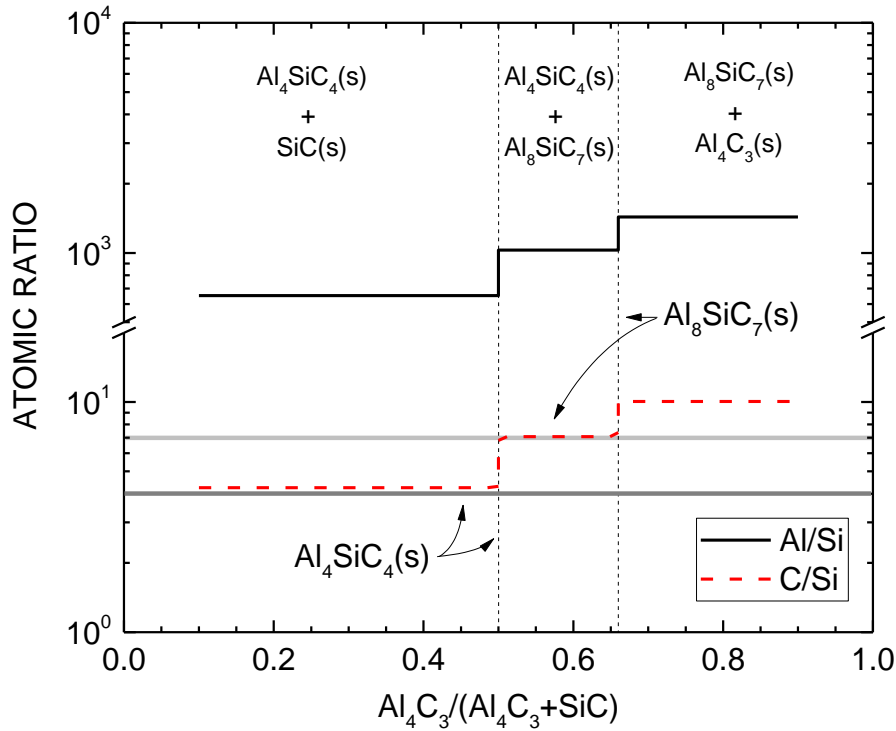


Figure 9: Rapports atomiques Al/Si et C/Si en phase gazeuse en fonction de $X_{Al_4C_3}$ dans les produits de départ. La température de recuit a été fixée à 1900°C. L'état d'équilibre du mélange correspondant au diagramme de phase est également indiqué.

Le comportement de la composition du phase vapeur en fonction de la composition initiale des matériaux sources est également intéressant. La description de la composition de la phase gazeuse en fonction du rapport molaire $X_{Al_4C_3}$ est donnée à la Figure 9, pour une température fixée à 1900°C. Évidemment, l'activité apparente de Si dans la phase gazeuse diminue de celle en équilibre avec SiC(s) pur à zéro, tout en déplaçant la composition de SiC pur vers Al₄C₃(s) pur au long de la section pseudo-binaire. Inversement, l'activité de Al augmente de zéro (pour un SiC pur) à l'équilibre d'un Al₄C₃(s) pur.

- Pour $X_{Al_4C_3} < 0.5$, l'état d'équilibre appartient à l'équilibre biphasique Al₄SiC₄-SiC. Pour une pression totale fixe, la variance du système est $F = 4 - P = 1$. Donc, la fixation de la température détermine totalement la composition de la phase gazeuse et est indépendante de la composition source.
- Pour la fraction équimolaire $X_{Al_4C_3} = 0.5$, seule la phase Al₄SiC₄ est en équilibre avec la vapeur. Lorsque le système ayant une phase de moins, la variance augmente d'un ($F = 2$). Ainsi, la stœchiométrie de la phase gazeuse est variable.

En effet, les rapports Al/Si et C/Si augmentent avec la fraction molaire de Al₄C₃. À n'importe quelle composition de source dans la section pseudo-binaire, la phase vapeur est caractérisée par un fort excès de Al. Cependant, le C/Si en phase gazeuse correspond presque à celui de Al₄SiC₄ pour une fraction molaire initiale < 0.5 et celle de Al₈SiC₇ pour une fraction molaire initiale comprise entre 0.5 et 0.66. Pour cette raison, nous spéculons que ces deux compositions initiales pourraient convenir à la condensation de Al₄SiC₄ et Al₈SiC₇, respectivement.

L'effet de la pression totale sur la vaporisation du mélange est également considéré. Le calcul de l'équilibre a été effectué avec différentes quantités d'argon de départ. En tant que gaz inerte, l'argon ne contribue pas à la réaction, donc la pression d'équilibre de l'espèce de vapeur et les résultats du calcul d'équilibre sont inchangés thermodynamiquement avec la quantité variable d'argon. Cependant, la pression totale a un impact significatif sur le transport de masse de la source vers la zone de cristallisation et peut fortement affecter le taux de croissance. Ceci sera discuté dans la section expérimentale.

3.2.2. La condensation au germe

Fraction molaire $X_{Al_4C_3} < 0.5$. À partir de ces résultats, la composition de mélange initiale riche en SiC ($X_{Al_4C_3} < 0.5$) a été choisie pour la synthèse de Al_4SiC_4 en raison de l'adéquation entre la composition en phase vapeur et la stœchiométrie du matériau. Afin de simuler la nature de la condensation en phase solide au niveau de la zone de cristallisation (point froid), les espèces gazeuses vaporisées à partir de la poudre ont été utilisées comme le condition initiale pour le calcul d'équilibre. Evidemment, la cinétique de réaction et le transport de masse n'étant pas pris en compte, les résultats présentés ici ne sont que de nature qualitative.

À partir de la composition en phase gazeuse à l'équilibre calculée à $2000^\circ C$ pour la fraction molaire initiale $X_{Al_4C_3} = 0.4$, nous avons calculé les quantités nettes de composés solides formés (figure (a)) en fonction de ΔT défini par $T_{SOURCE} - T_{SEED}$. La composition en phase gazeuse correspondante (Al/Si et C/Si) dans la zone de cristallisation est représentée sur la figure. En partant de la même température de la source, ou autrement dit, du même flux d'espèces vaporisé à partir de la source, on peut identifier différents composés se condensant au niveau de la zone de cristallisation, en fonction de la différence de température. En effet, Al_4SiC_4 se condense pour de petites différences de température (ΔT) inférieures à $40^\circ C$. Entre 40 et $80^\circ C$, Al_8SiC_7 domine. Notons qu'à $40 \pm 10^\circ C$, les conditions de cristallisation sont caractérisées par la coexistence des deux carbures ternaires. Ensuite, pour $\Delta T > 80^\circ C$, Al_4C_3 seul se condense.

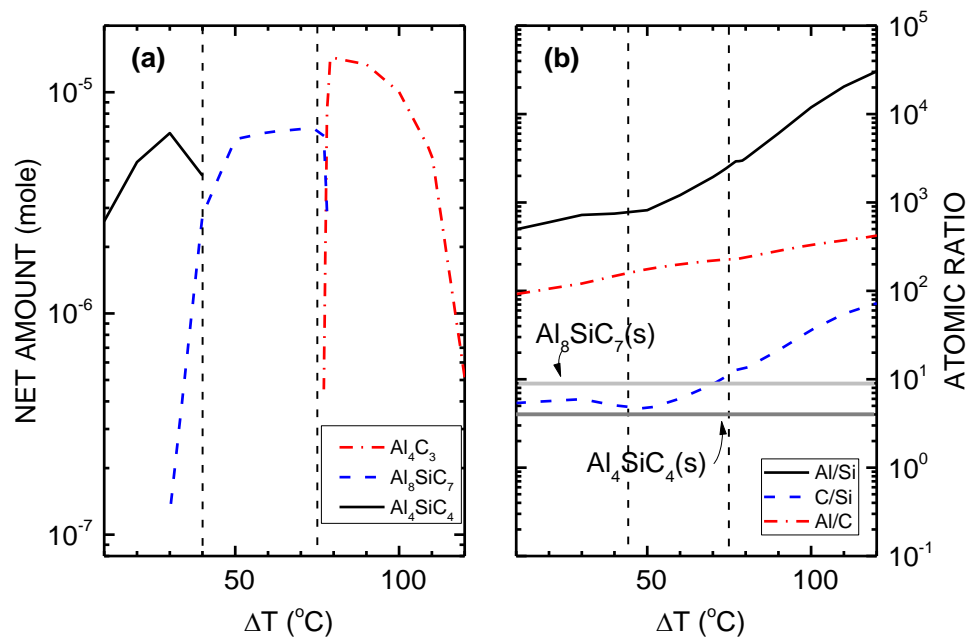


Figure 10: Les quantités nettes de composés solides formées en fonction de ΔT . b) Composition de la phase gazeuse correspondante dans la zone de cristallisation (graine). La composition de la phase gazeuse à la zone de vaporisation (source) a été calculée à 2000 ° C pour une composition source initiale $X_{Al_4C_3} = 0.4$. ΔT est défini par $T_{SOURCE} - T_{SEED}$. Des lignes pointillées verticales ont été ajoutées comme guide pour séparer les différentes conditions de dépôt.

Une comparaison entre les calculs effectués en phase homogène (sans aucun solide autorisé à se former) et en phase hétérogène donne une bonne estimation des principales espèces gazeuses qui contribuent au dépôt. La contribution nette représentée à la Figure 11(a) est définie comme la différence entre la pression partielle des différentes espèces calculée en phase homogène et celles en phase hétérogène. Afin de pondérer la contribution de chaque composant gazeux, nous avons tracé sur la Figure 11(b) la contribution relative, définie comme le rapport de la contribution nette et de la pression partielle provenant du calcul de phase hétérogène. À faible ΔT , condition dans laquelle la cristallisation de Al_4SiC_4 se produit, Al_2C_2 (g) apporte la plus grande contribution de Al et C. Par contre, le Si (g) atomique est l'espèce la plus importante contribution de Si. De toute évidence, la contribution de ces espèces augmente avec le gradient de température. Une réaction très simple peut donc être réalisée pour la condensation de Al_4SiC_4 à partir de la phase vapeur :

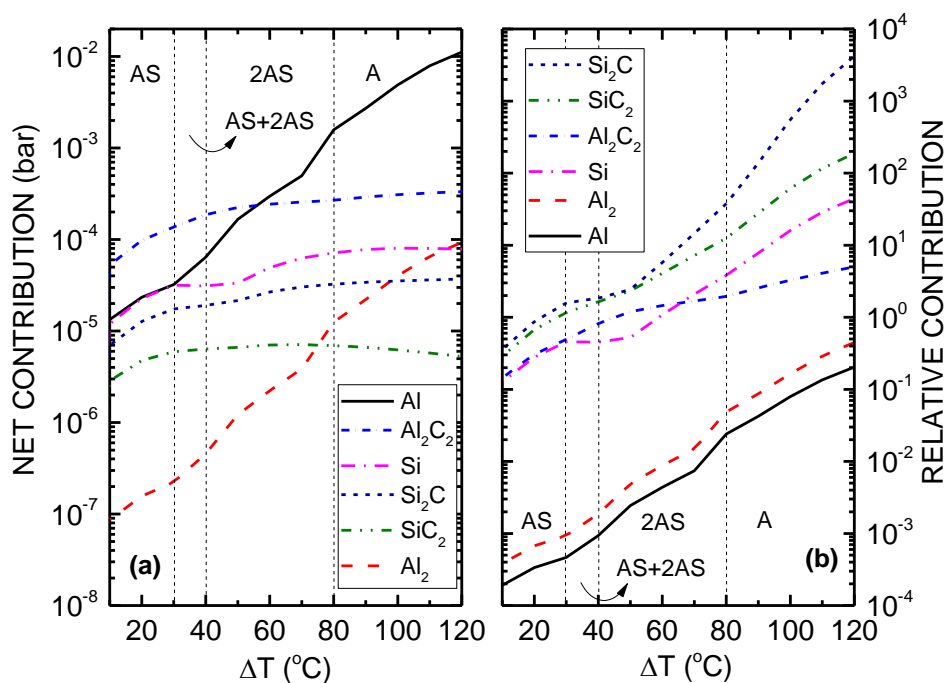
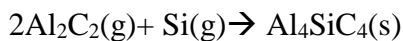


Figure 11: (a) Contribution nette de la principale espèce vapeur (vaporisée à 2000°C avec une pression proche de 300mbar) au dépôt en fonction du gradient de température. (b) Contribution relative de la même espèce, définie par le rapport entre la contribution nette et la pression partielle d'équilibre de l'espèce, calculée dans le cas hétérogène. Trois zones en phase condensée sont identifiées consécutivement, telles que Al_4SiC_4 (AS), Al_8SiC_7 (2AS) et Al_4C_3 (A) en augmentant le gradient de température.

Pour un ΔT supérieur à 40°C , la contribution nette de Al_2C_2 (g) et Si (g) est assez stable. Cependant, la contribution des molécules d'aluminium monoatomiques et polyatomiques telles que Al (g) et Al_2 (g) augmente fortement avec le gradient de température, conduisant à un enrichissement en Al de la phase solide. En ce qui concerne la contribution relative, Al_2C_2 (g) et Si (g) sont les espèces les plus contributives, environ quelques ordres de grandeur supérieures à Al(g) et Al_2 (g). Cela signifie également que Al_2C_2 (g) et Si (g) sont l'espèce "thermodynamiquement limitante" pour la condensation de Al_4SiC_4 dans toutes les conditions étudiées.

IV. Synthèse d' Al_4SiC_4 et croissance par sublimation

Inspiré par le processus industriel standard de croissance de cristaux du SiC, nous étudions dans cette section un processus de croissance par sublimation pour Al_4SiC_4 utilisant un mélange de Al_4C_3 et de SiC comme matières sources. Dans ce cas, en raison de la vitesse de vaporisation élevée de Al_4C_3 , des expériences ont été menées dans des conditions riches en SiC ($X_{\text{Al}_4\text{C}_3} < 0.5$). En tant qu'approche générale, les phénomènes de vaporisation et de condensation dans le système Al_4C_3 -SiC seront étudiés afin de déterminer les conditions de croissance de la phase Al_4SiC_4 seul.

4.1. Processus expérimental

Les matériaux sources étaient composés d'un mélange de poudres de haute pureté d' Al_4C_3 (Alfa Aesar, pureté 99 +%) et de SiC (Sika tech E301) avec une composition définie par le rapport molaire d' Al_4C_3 ($X_{\text{Al}_4\text{C}_3}$). Cependant, le mélange, chargé dans un creuset en graphite, n'a pas été pressé avant l'expérience. La pression et la température ont été contrôlées pendant le processus. Un pyromètre optique bi-chromatique a été utilisé pour mesurer la température de l'arrière de la zone de cristallisation. La température de croissance variait de 1900 à 2000°C et la pression de croissance était fixée à 150 ou 300 mbar en utilisant une atmosphère d'argon. Les substrats de SiC ont été utilisés comme germes et collés en haut de la zone de cristallisation à l'aide d'une colle de graphite. Différents types de substrats SiC tels que le 6H-SiC on-axis et 4H-SiC 4° off-axis (vers [11-20]) avec différentes polarités (face Si et face C) ont été utilisés pour évaluer l'épitaxie. La surface initiale des substrats de SiC a été polie par un polissage chimique mécanique dans tous les cas.

La procédure expérimentale est représentée à la Figure 12. Au début, le réacteur a été pompé pour atteindre un vide de 10^{-3} mbar. Plus tard, le réacteur est chauffé manuellement avec une puissance constante jusqu'à une température supérieure à 1000°C . Ensuite, la vitesse de chauffage a été fixée à $30^\circ\text{C}/\text{min}$ jusqu'à la température de croissance. Une pression de ≈ 800 mbar est fixée pendant le chauffage afin de limiter la sublimation des matières sources. Lorsque la température de croissance atteinte, la pression a été réduite à la pression de croissance. Pendant la croissance, tous les paramètres sont restés stables. À la fin du processus de recuit, la pression a été augmentée à 800 mbar pour éviter la re-sublimation, et le réacteur a été refroidi en coupant le courant.

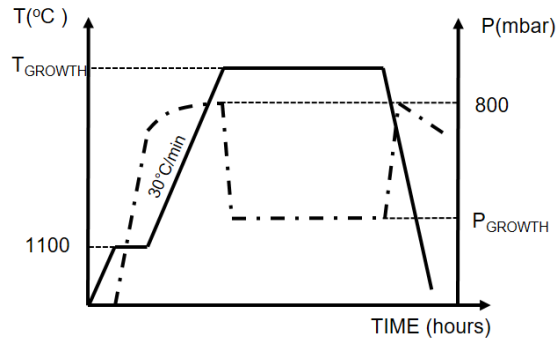


Figure 12: Représentation de la recette utilisée dans toutes les expériences de croissance par sublimation. La variation de la température (trait plein) et de la pression (ligne pointillée) à différentes étapes est indiquée.

4.2. Résultats expérimentaux

Pour décrire les phénomènes de vaporisation-condensation dans le système $\text{Al}_4\text{C}_3\text{-SiC}$, il est nécessaire de combiner la thermochimie du système et le transport de masse se produisant dans le creuset. Pour cela, nous devons différencier l'évolution de la poudre, c'est-à-dire la formation des différentes strates, à ce que se passe dans la cavité au-dessus de la poudre. Dans la première partie, l'évolution de la poudre en fonction du temps sera étudiée. Dans la deuxième partie, le dépôt sur le substrat SiC sera considéré.

Evolution de la poudre. Une série d'expériences a été réalisée à température de 2000°C et à pression de 300 mbar avec un temps de recuit variant de 20 minutes à 2 heures. La deuxième série d'expériences a été menée à 1900°C , 150 mbar avec la même composition initiale mais pour un temps plus long. Selon les résultats des calculs thermodynamiques, une composition initiale $X_{\text{Al}_4\text{C}_3} < 0.5$ a été utilisée comme la condition la plus appropriée pour la cristallisation de Al_4SiC_4 . La Figure 13(a) est une image de caméra de la section du matériau source après recuit d'un mélange $\text{Al}_4\text{C}_3\text{-SiC}$, ayant une composition molaire initiale $X_{\text{Al}_4\text{C}_3} = 0.2$, pendant 2 heures à 2000°C . Trois couches différentes peuvent être identifiées à la section : couche en bas (3), au milieu (2) et en haut (1). Le niveau initial du mélange de poudres est indiqué par la ligne pointillée noire entre les couches (1) et (2). Une image d'électrons rétrodiffusés (BSE) de chaque couche a été ajoutée à la Figure 13. Pour chaque strate, un échantillon de poudre a été extrait et broyé par broyage à billes pour les analyses qualitatives (identification de phase) et quantitative (rapport atomique de chaque phase) à l'aide de mesures XRD.

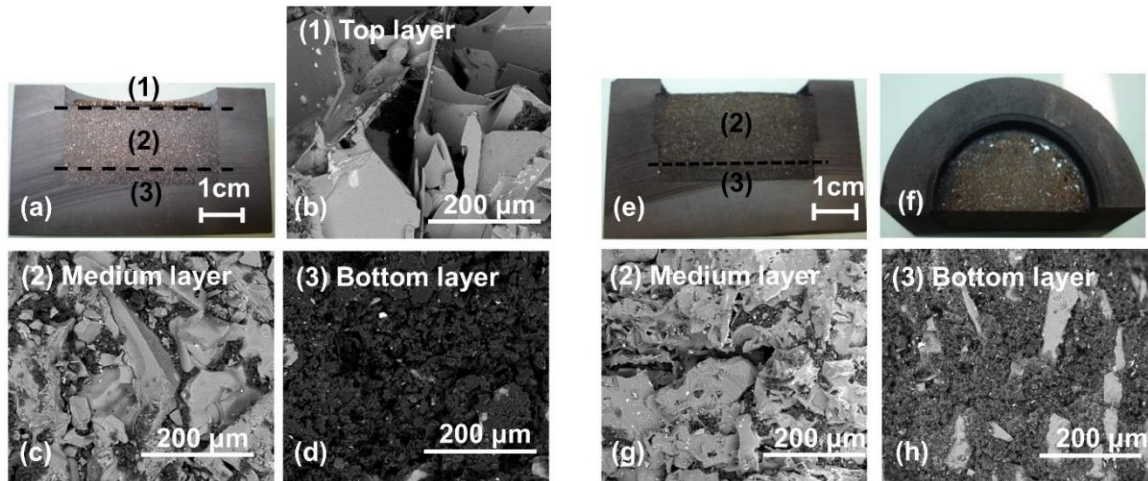


Figure 13: a) Coupe transversale de la charge de poudre après expérience ; la composition de la source est $X_{Al4C3} = 0.2$ et les conditions de recuit sont $T=2000^{\circ}C$, $P=300mbar$ et temps=2heures. Trois couches différentes, notées (1) en haut, (2) en milieu et (3) en bas, peuvent être identifiées. Les images d'électrons rétrodiffusés (BSE) correspondantes sont présentées sur les images b, c et d, respectivement. Les images e et f sont des vues en coupe et en dessus de la poudre qui a été recuit pendant 4 heures à $1900^{\circ}C$ et $150mbar$ avec la même composition de source. Dans ce cas, seules deux couches différentes peuvent être identifiées, notées couches intermédiaire et inférieure. Les images BSE correspondantes sont présentées sur les images g et h.

Les diffractogrammes de rayons X collectés dans chaque strate après recuit à $2000^{\circ}C$, $300 mbar$ en 2 heures, sont donnés à la Figure 14.

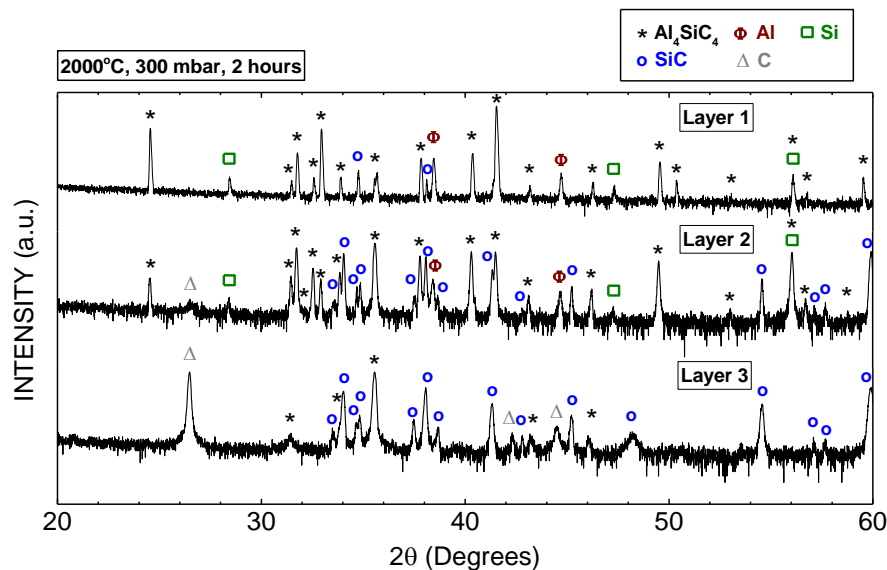


Figure 14: Les diffractogrammes de rayons X collectés dans chaque strate de poudre après expérience. La composition de source $X_{Al4C3}=0.2$ et les conditions de recuit sont $T=2000^{\circ}C$, $P=300mbar$ et le temps=2heures.

- La couche en haut (couche 1) est principalement composée d'un enchevêtrement de plaquettes très fines et orange. Cette couche était formée au-dessus du niveau initial de la poudre et n'était donc due qu'à la réaction de vaporisation-condensation dans la cavité ouverte. L'analyse DRX a révélé une majorité de Al_4SiC_4 et très petites quantités de SiC, Al et Si. Les petites particules contenant Al et Si sont visibles à la surface des plaquettes dans les images MEB qui ressemblent à des gouttelettes solidifiées. Ces phases minoritaires pourraient se former lors du refroidissement ou pourraient être résidus provenant d'une contamination croisée lors de la séparation des couches (1) et (2).
- La couche intermédiaire (couche 2) présente une densité de solide plus élevée avec au moins deux contrastes de niveaux de gris, suggérant la coexistence de plusieurs phases. Aucune plaquette réelle n'a pu être observée et le solide présente une texture granuleuse. Les phases identifiées par DRX sont Al_4SiC_4 , SiC, C, Al et Si avec la composition correspondante indiquée dans le tableau 5.
- La couche en bas (couche 3), de couleur noire dominante, consiste en une densité élevée de petits grains ayant un contraste proche de celui du creuset en graphite. En effet, cette strate est majoritairement composée de SiC (80% molaire) et de graphite (19% molaire) avec une très faible quantité d' Al_4SiC_4 (1% molaire). Le front de graphitisation se propageant du bord des grains au centre, il n'est pas surprenant d'observer une couleur noire (attribuée au graphite avec l'ESB) bien que la DRX ait révélé une teneur de SiC beaucoup plus élevée, probablement confinée au cœur des grains et non directement observable en utilisant l'ESB.

De 20 min à 2 heures, les diffractogrammes de rayons X collectés de la couche intermédiaire (couche 2) sont présentés à la Figure 15. La composition de Al_4SiC_4 , SiC, C, Al et Si a été relevées dans le tableau 5.

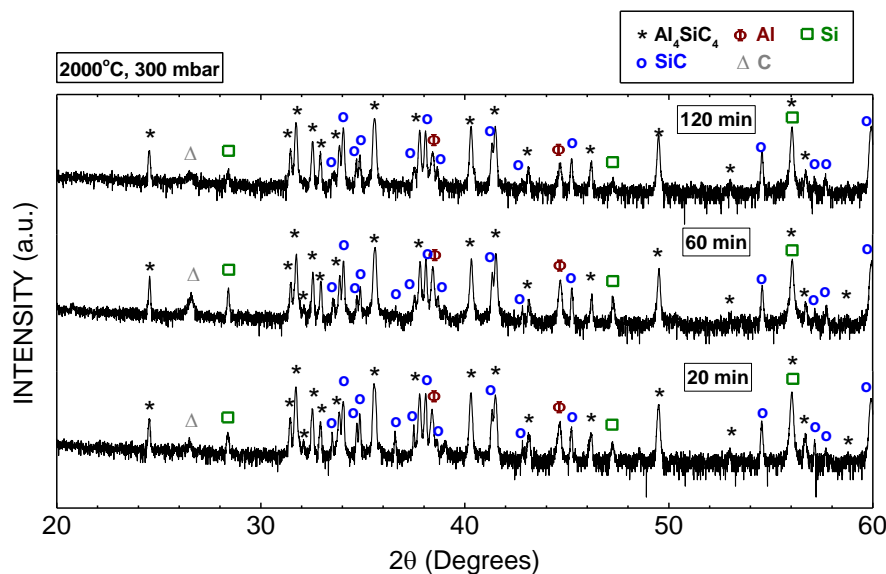


Figure 15: Diffractogrammes de rayons X collectés de la couche intermédiaire après recuit pendant des temps différents. La composition de source est $X_{\text{Al}_4\text{C}_3}=0.2$ et les conditions de recuit sont $T = 2000^\circ\text{C}$, $P = 300\text{mbar}$.

À température 1900°C, il n'y a aucune preuve de la formation de la couche (1), la section transversale de la poudre recuite pendant 4 heures ne montre que les couches (2) et (3) (Figure 13(e)). Dans ce cas, seuls Al_4SiC_4 , SiC et C sont observés dans les diffractogrammes de rayons X de la couche de milieu de 2 à 6 heures, comme illustrés dans la Figure 16. La composition a aussi relevée dans le tableau 5.

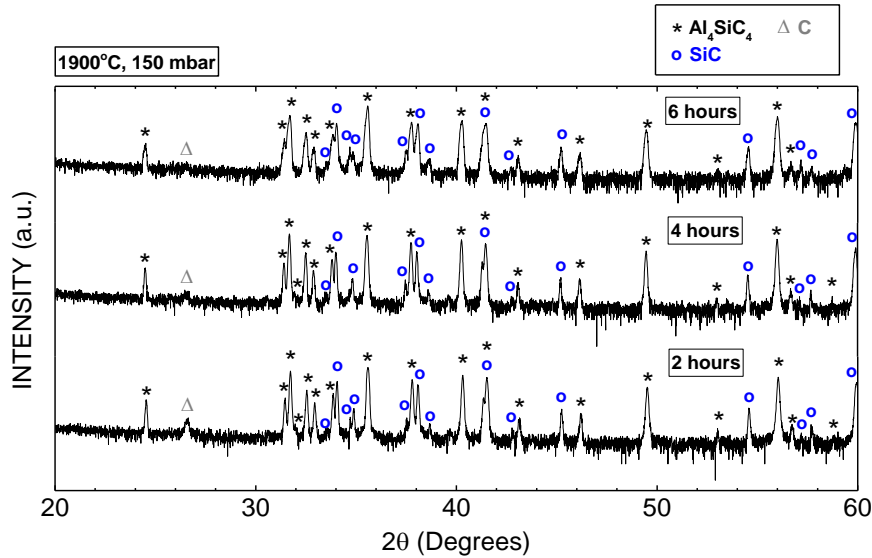


Figure 16: Diffractogrammes de rayons X collectés dans chaque strate après recuit pendant des temps différents. La composition de source est $X_{\text{Al}_4\text{C}_3} = 0.2$ et les conditions de recuit sont $T = 1900^\circ\text{C}$, $P = 150\text{mbar}$.

Tableau 5 : Fraction molaire de chaque composant, obtenue par analyse DRX Rietveld d'échantillons de poudre extraits de la couche intermédiaire (située au milieu du creuset et près de la surface de la poudre) pour différentes conditions expérimentales.

Experimental conditions	Mole fraction				
	Al_4SiC_4	SiC	C	Si	Al
2000°C, 300 mbar, 20 min	0.13	0.43	0.06	0.04	0.34
2000°C, 300 mbar, 60 min	0.10	0.34	0.14	0.03	0.39
2000°C, 300 mbar, 120 min	0.13	0.53	0.11	0.02	0.21
1900°C, 150 mbar, 120min	0.20	0.59	0.21		
1900°C, 150 mbar, 240 min	0.29	0.60	0.11		
1900°C, 150 mbar, 360 min	0.19	0.74	0.07		

Afin d'obtenir une estimation des flux de masse provenant de deux carbures, nous avons d'abord mesuré la perte de poids de SiC pure (définie en poids initial – poids finale, en pourcentage) en fonction du temps. Des expériences ont été réalisées à deux températures différentes 1900°C et 2000°C sous une pression de 300 mbar avec la géométrie utilisée pour la croissance par sublimation. Le même volume de poudre et les mêmes conditions de recuit ont

été appliqués afin de maintenir une constante distance entre la source et le germe, et une distribution de température équivalente. Comme indiqué sur la Figure 17, la perte de poids de SiC est presque linéaire en fonction du temps pour les deux températures. En raison de la pression "élevée", le taux de vaporisation du SiC est très lent. Après avoir atteint la température de recuit, le taux de vaporisation est d'environ 10 et 7mg/heure pour 2000°C et 1900°C, respectivement. C'est important de noter que le poids initial du SiC est d'environ 22 g.

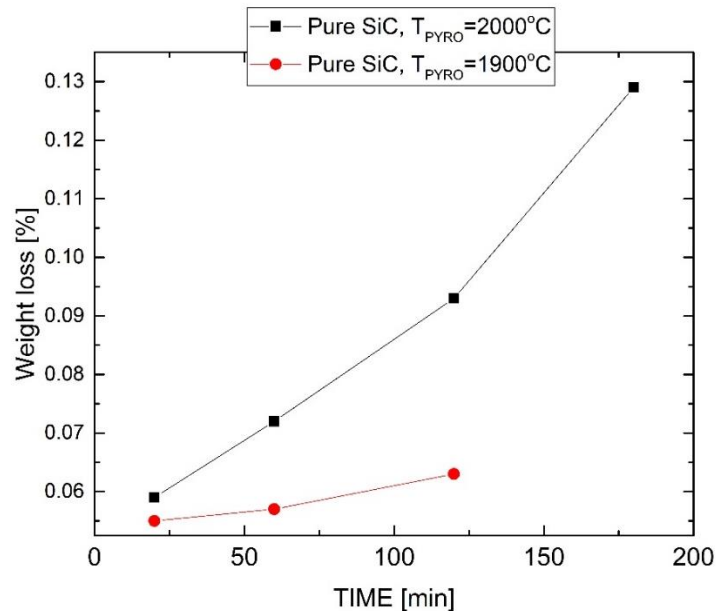


Figure 17: Evolution de la perte de poids (%) de SiC pure en fonction du temps pour deux températures différentes : 1900°C et 2000°C. Les expériences ont été effectuées sous une pression de 300 mbar.

Pour comparer les flux de masse sublimés du mélange ($X_{Al_4C_3}=0.2$) dans les deux conditions, la perte de poids du mélange en fonction du temps est représentée sur la figure 4.22 à côté de celle du SiC pur. Le taux de vaporisation du mélange à 2000°C et à 300 mbar est deux fois plus élevé que celui du SiC pur avec la même condition. Une augmentation spectaculaire du taux de vaporisation démontre le rôle dominant d' Al_4C_3 dans la sublimation du mélange. De plus, le taux de vaporisation dépend fortement de la température. En effet, à basse température (1900°C et 150mbar), 6 heures de recuit sont nécessaires pour obtenir presque la même perte de poids qu'après 2 heures à 2000°C et 300 mbar.

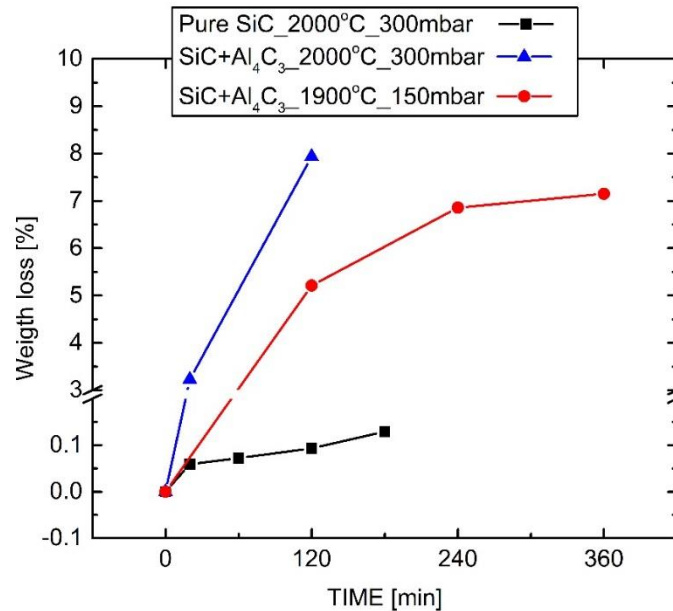


Figure 18: Evolution de la perte de poids (%) de la poudre en fonction du temps pour deux compositions initiales : SiC pur (courbe noire) pour une condition de recuit de $T=2000^{\circ}\text{C}$, $P=300$ mbar et mélange Al_4C_3 -SiC de composition $X_{\text{Al}_4\text{C}_3}=0.2$. Le mélange a été recuit dans deux conditions différentes : $T=2000^{\circ}\text{C}$, $P=300$ mbar (courbe bleue); et $T=1900^{\circ}\text{C}$, $P=150$ mbar (courbe rouge).

Dépôt sur le substrat 4H-SiC à face C (4° hors axe). Au début, l'effet de la pression et de la température ont été pris en compte. En fixant la température à 1900°C , la vitesse de dépôt est de $30 \mu\text{m/h}$ pour une pression de 300 mbar. Lorsque la pression diminue jusqu'à 150 mbar, le taux de dépôt augmente légèrement jusqu'à $37 \mu\text{m/h}$. Sinon, en augmentant la température de croissance à 2000°C et en fixant la pression à 300 mbar, la vitesse de dépôt augmente de façon spectaculaire de 30 à $75 \mu\text{m/h}$. Cette comparaison démontre que dans de telles conditions, la vitesse de dépôt dépend beaucoup plus de la température que la pression dépendante. Ainsi, l'effet de la pression sera négligé dans la discussion.

La Figure 19 montre l'évolution de l'épaisseur du dépôt en fonction du temps pour deux conditions de sublimation différentes. Car la vitesse de dépôt plus faible, les expériences à 1900°C et à 150 mbar ont été effectuées plus longtemps. Les barres d'erreur ajoutées aux tracés représentent l'écart type des valeurs d'épaisseur. Ils ont été calculés à partir d'un nombre de mesures statistiquement pertinent au long du diamètre du dépôt. C'est donc une sorte de traceur de l'évolution de la rugosité du dépôt à l'échelle macroscopique. Evidemment, une telle rugosité augmente d'abord avec l'épaisseur du film, et aussi avec la vitesse de dépôt.

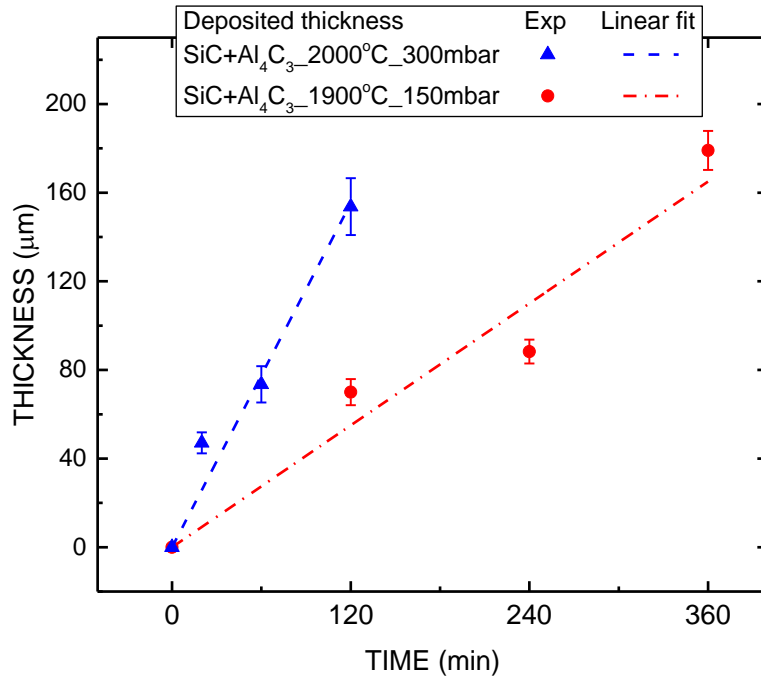


Figure 19: Épaisseur de la couche déposée en fonction du temps de recuit pour deux conditions expérimentales différentes avec le mélange Al_4C_3 -SiC.

La nature des couches déposées est identifiée par analyse DRX. Les diffractogrammes de rayons X collectés à partir des couches déposées sont illustrés à la Figure 20, correspondant aux différents points rassemblés à la Figure 19. À 2000°C, 300 mbar et après 20 minutes, le dépôt consiste en Al_4SiC_4 avec une orientation préférée [0001]. Après une heure, les pics d' Al_4C_3 commencent à apparaître dans le dépôt avec la même orientation [0001]. Après 2 heures, Al_4SiC_4 et Al_4C_3 sont présents dans le dépôt et le diffractogramme est similaire à celui d'un polycristallin, c'est-à-dire sans aucune orientation spécifique. Pour les expériences à 20 minutes et une heure, quelques très petits pics d'Al et Si apparaissent. En observant la surface de ces dépôts avec le MEB, on a trouvé des gouttelettes solidifiées microscopiques et des faisceaux de nanofibres développés à partir des gouttelettes, comme illustrés dans la Figure 21. Une analyse de spectroscopie de rayons X à dispersion d'énergie (EDS) a été effectuée afin d'identifier leurs compositions rassemblées dans le tableau 6. Le premier situé sur la couche de dépôt montre la composition stœchiométrique de Al_4SiC_4 . La seconde a été réalisée sur le faisceau de nanofibres et la troisième sur les gouttelettes solidifiées. La quantité d'oxygène présente dans l'analyse EDS provient probablement de l'oxydation au cours du stockage. En raison de leur emplacement (uniquement à la surface du dépôt) et de leur composition (très faible quantité de Si), celles-ci étaient supposées se former à partir de la phase vapeur pendant le refroidissement, ce que sera discuté plus loin.

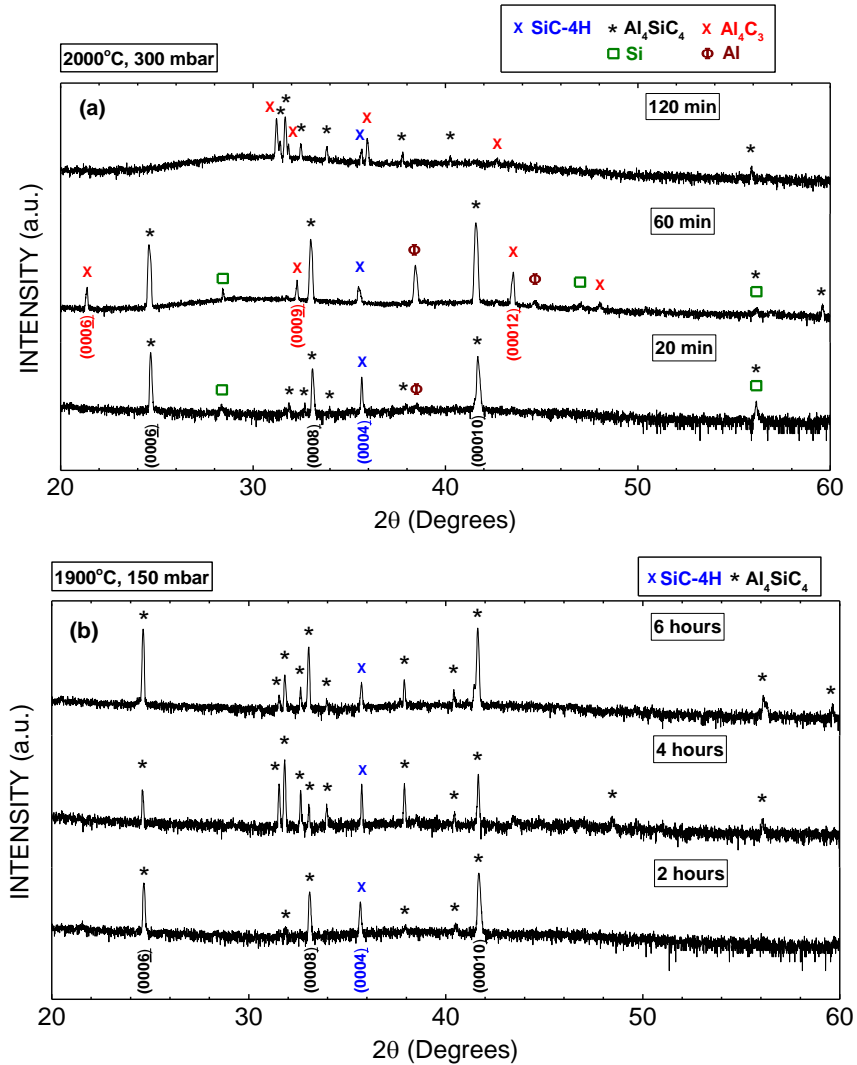


Figure 20: Diffractogrammes de rayons X collectées à partir des couches déposées sur des substrats 4H-SiC (face C) 4° hors axe, après sublimation à (a) 2000°C, 300mbar et (b) 1900°C, 150mbar pendant les temps différents. Le mélange Al₄C₃-SiC avec une composition de X_{Al₄C₃}=0.2 a été utilisé comme la source. L'orientation préférée trouvée dans les couches est aussi indiquée.

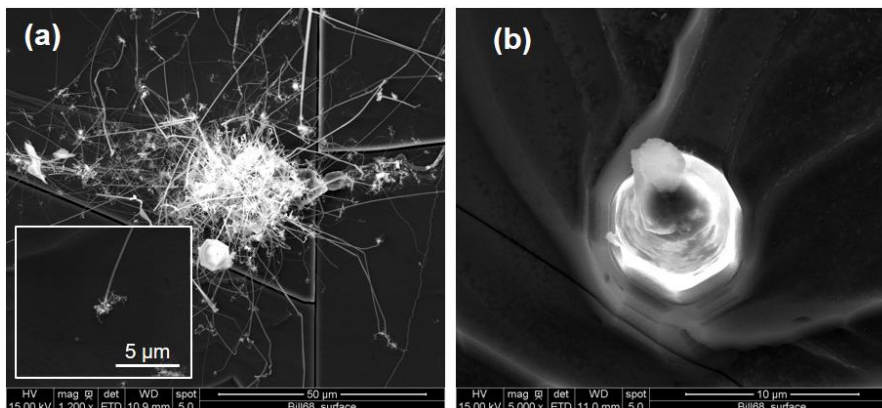


Figure 21: Image MEB observant la surface du dépôt après croissance à 2000 ° C, 300 mbar en 20 minutes. (a) Gouttelettes avec des nanofibres, l'insert de la figure est la pointe de la fibre; b) gouttelettes solidifiées.

Tableau 6 : L'analyse de l'EDS se produit à trois endroits différents correspondant à l'image donnée à la Figure 21. L'énergie du faisceau de 5 kV a été utilisée.

Elements	Energy Dispersive X-ray Spectroscopy analysis (atomic%)			
	Al	Si	C	O
Al ₄ SiC ₄ surface	48.7	13.6	37.3	0.4
Droplet (a)	55.1	1.4	17.6	25.9
Droplet (b)	26.7	3.4	61.4	8.5

À 1900°C, de 2 à 6 heures, le dépôt se compose uniquement d'Al₄SiC₄. Après 2 heures, la couche d'Al₄SiC₄ montre clairement une orientation préférée qui est celle du substrat SiC. Pour plus de temps, même si les pics de la famille {0001} conservent les intensités les plus fortes, d'autres orientations se développent provoquant l'augmentation de la rugosité de la couche déposée.

4.3. Discussion

Afin de comparer avec la composition brute, la fraction molaire des trois éléments (Al, Si, C) a été extraite des analyses de Rietveld des poudres, uniquement pour la couche intermédiaire. Les résultats obtenus pour différents temps et les deux conditions de recuit étudiées dans cette section sont rassemblés dans le tableau 7. À 1900°C, la composition élémentaire de la source était à peu près constante, même pour un temps de recuit long, i.e. 6 heures, en accord avec les résultats de la section 4.2. À 2000°C, la couche de milieu présentait un enrichissement en Al d'environ 10% pendant la première heure. Puis, pendant plus longtemps, la composition est progressivement revenue à la composition initiale.

Tableau 7 : Fraction molaire des trois éléments, extraite de l'analyse XRD Rietveld de la poudre dans la couche de milieu, pour différentes conditions expérimentales.

Experimental conditions	Mole fraction		
	Al	Si	C
Initial composition, X _{Al4C3} =0.2	0.27	0.27	0.46
2000°C, 300 mbar, 20 min (1)	0.33	0.24	0.43
2000°C, 300 mbar, 60 min (2)	0.37	0.22	0.42
2000°C, 300 mbar, 120 min (3)	0.29	0.26	0.45
1900°C, 150 mbar, 120min (4)	0.25	0.25	0.5
1900°C, 150 mbar, 240 min (5)	0.29	0.23	0.48
1900°C, 150 mbar, 360 min (6)	0.24	0.28	0.48

Comme mentionné précédemment, à une température donnée, le taux de vaporisation du SiC pur est constant pendant le temps étudié. Même si le mécanisme est une vaporisation non congruente, il indique que le flux de Si est constant. C'est assez différent pour Al_4C_3 . Le taux de vaporisation du mélange Al_4C_3 -SiC est extrêmement fort au début et atteint progressivement une saturation (Figure 18). En effet, il ne reste plus d' Al_4C_3 après le temps de recuit étudié. Ainsi, lors d'expériences de courte durée (20 min à 60 min) à 2000°C , la composition de la vapeur à la surface de la graine était dominée par des espèces de vapeurs contenant de l'aluminium au cours de la croissance. Tandis que la pression était augmentée afin d'empêcher la sublimation pendant le refroidissement, la vaporisation des espèces contenant du Si était bloquée, ce qui interrompait la formation d' Al_4SiC_4 . Au lieu de cela, des gouttelettes solidifiées se sont formées en raison de la phase vapeur sursaturée avec Al (g). Notez que la pression de vapeur à l'équilibre de Al à 2000°C est d'environ 61mbar²¹, ce qui est inférieur à la pression partielle de Al (g) calculée dans la condition expérimentale (95mbar). Après cela, des nanofibres d'Al se sont développées à partir des gouttelettes grâce à un mécanisme vapeur-liquide-solide²². L'évidence de la gouttelette est restée sur le bout de la fibre, comme le montre l'encart de la Figure 21(a).

Selon le diagramme de phase, avec un mélange ayant une composition initiale $X_{\text{Al}_4\text{C}_3}=0.2$, l'état d'équilibre devrait appartenir à l'équilibre biphasique Al_4SiC_4 -SiC. Comme la vitesse de réaction à l'état solide entre Al_4C_3 et SiC est plutôt lente, on peut supposer qu'une partie de celle-ci s'est directement vaporisée, produisant le taux de vaporisation élevé initial. De plus, étant un composé de fusion non-congruant, Al_4C_3 produit du graphite lors de la vaporisation. C'est ce que nous avons expérimentalement observé. Une fois que tout Al_4C_3 est consommé, le taux de vaporisation diminue et est ensuite régi par l'équilibre Al_4SiC_4 -SiC.

À 1900°C , même si la partie en bas de la poudre commence à graphiter (Figure 13 (h)), la composition élémentaire en Al, Si, C de la couche moyenne (Figure 13(g)) est presque constante jusqu'à 6 heures de recuit. Aucune couche d' Al_4SiC_4 ne se forme à la surface de la poudre. Autrement dit, le matériau source faisant face au germe conserve la même composition atomique, qui appartient à la section pseudo-binaire initiale. En conséquence, des conditions stables pour la condensation d' Al_4SiC_4 sur le substrat SiC sont remplies, sur toute la durée du dépôt.

À 2000°C , l'évolution est assez différente. L'énorme flux d'espèces provenant de la couche en bas (couche 3) entraîne un fort enrichissement de la couche intermédiaire en Al. Progressivement, une croûte de plaquettes d' Al_4SiC_4 (couche 1) se développe sur la surface de la poudre. Avant la formation de cette croûte, la vaporisation est fixée par l'équilibre biphasique Al_4SiC_4 -SiC. De manière similaire à ce qu'on a été observé à 1900°C , un tel cas fournit des conditions appropriées pour la condensation d' Al_4SiC_4 sur le substrat SiC. Cependant, lorsque la croûte d' Al_4SiC_4 est formée, la surface "émettant" le flux d'espèces à la graine est une surface pure d' Al_4SiC_4 . D'un point de vue thermodynamique, cela est associé à une augmentation de l'activité d'Al et à une diminution de l'activité de Si dans la phase gazeuse. Autrement dit, la composition en phase gazeuse subit une augmentation des rapports Al/Si et C/Si. Le substrat SiC voyant des flux élevés d'Al et de C par rapport à celui de Si, il n'est pas surprenant de condenser Al_4C_3 une fois cette situation atteinte. En effet, comme observé dans la section

transversale de la couche déposée de la Figure 22(a), qui a été développée en 2 heures, trois couches différentes ont été identifiées par l'analyse EDS. Le profil en pourcentage atomique de Al, Si et C donné à la Figure 22(b) correspond respectivement à SiC, Al₄SiC₄ et Al₄C₃. Il démontre la formation tardive de Al₄C₃.

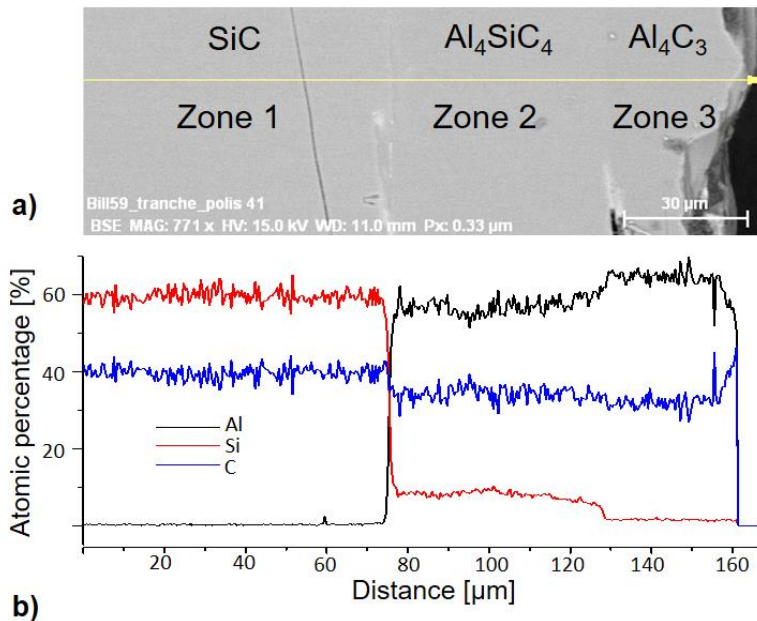


Figure 22: Coupe transversale de la couche déposée à 2000 ° C, 300 mbar pendant 2 heures, avec l'analyse EDS correspondante.

Comme mentionné dans le chapitre précédent, la condensation de l'Al₄SiC₄ monphasé à la surface de la graine nécessite une faible différence de température entre la source et la germe, généralement inférieure à 40°C. Conçu à l'aide de la simulation numérique, la répartition de la température dans notre creuset correspond parfaitement à cette condition pour la plage de température de 1800 à 2000°C. Ainsi, les conditions pour la condensation d'Al₄SiC₄ monphasée estimée par calcul thermodynamique ont été vérifiées expérimentalement, au moins au stade initial pour des expériences à 2000°C.

4.4. Orientation de la croissance et texture des couches d'Al₄SiC₄

La dépendance de l'orientation de la croissance et de la texture de Al₄SiC₄ sur différents types de substrats SiC a été étudiée par des expériences durées courtes ($X_{Al_4C_3}=0.2$, $T=1900^\circ C$, $P=300\text{mbar}$, durée = 10min). Une analyse détaillée de la courbe de DRX a été réalisée pour la couche d'Al₄SiC₄ déposée sur différents types de substrats, i.e. 4H-SiC (4° hors axe) C-face et Si-face, 6H-SiC (sur l'axe) C-face et Si-face. Les résultats des analyses, y compris la position (Omega), FWHM, Phi et Chi des courbes de bascule sont relevées dans le tableau 8 pour différentes réflexions: (0004) de 4H-SiC, (00012) de 6H-SiC, (00010) et (10-16) de Al₄SiC₄. L'épaisseur des couches d'Al₄SiC₄ est d'environ $7 \pm 1 \mu\text{m}$.

Tableau 8 : Analyse de la courbe de bascule des couches d'Al₄SiC₄ déposées sur différents substrats SiC. Plan symétrique (00010) et plan asymétrique (10-16) sont considérés pour la comparaison.

Hetero-structure	Material	Plan	Omega (°)	FWHM RC (°)	Phi (°)	Chi (°)
Al ₄ SiC ₄ /4H-SiC 4° off-axis C face	4H-SiC	(0004)	17.836	0.253	4.1	4.2
	Al ₄ SiC ₄	(00010)	20.761	1.780	4.2	4.4
		(10-16)	20.215	1.130	24.3	56.3
Al ₄ SiC ₄ /4H-SiC 4° off-axis Si face	4H-SiC	(0004)	13.701	0.363	90	0
	Al ₄ SiC ₄	(00010)	16.578	1.213	90	0
		(10-16)	16.055	0.834	91	51.9
Al ₄ SiC ₄ /6H-SiC on-axis C face	6H-SiC	(00012)	36.697	0.295	88.8	-0.9
	Al ₄ SiC ₄	(00010)	19.798	1.405	89.3	-0.8
		(10-16)	20.174	1.174	87.5	51
Al ₄ SiC ₄ /6H-SiC on-axis Si face	6H-SiC	(00012)	37.498	0.304	90	-0.3
	Al ₄ SiC ₄	(00010)	20.664	0.832	90	-0.2
		(10-16)	20.182	0.655	87.4	51.6

L'orientation de la croissance d'Al₄SiC₄ a été déterminée et comparée systématiquement à l'orientation des substrats SiC correspondants. Pour les substrats 4H-SiC hors axe, l'angle d'inclinaison des substrats pourrait contribuer au décalage dans les mesures de Chi ou d'Omega (les échantillons ont été inclinés le long des axes Chi et Omega, qui sont parallèles à la surface de l'échantillon).

Considérons d'abord la couche qui a été déposée sur la face C de substrat 4H-SiC hors axe. Les valeurs Theta sont égales aux valeurs théoriques. La réflexion symétrique (0004) du 4H-SiC a une valeur de Chi de 4.2° qui correspond à l'angle d'inclinaison du substrat. La réflexion (00010) de Al₄SiC₄ a une valeur de Chi de 4.4°, ce qui démontre un angle d'inclinaison relatif de 0.2° entre les plans de base du dépôt et du substrat. La réflexion asymétrique (10-16) de Al₄SiC₄ a un décalage de 4.4° en Chi qui, comparé à la valeur théorique (51.9°), présente également un angle d'inclinaison relatif de 0.2°. Ces décalages en Chi sont illustrés dans les figures de pôles de la Figure 23.

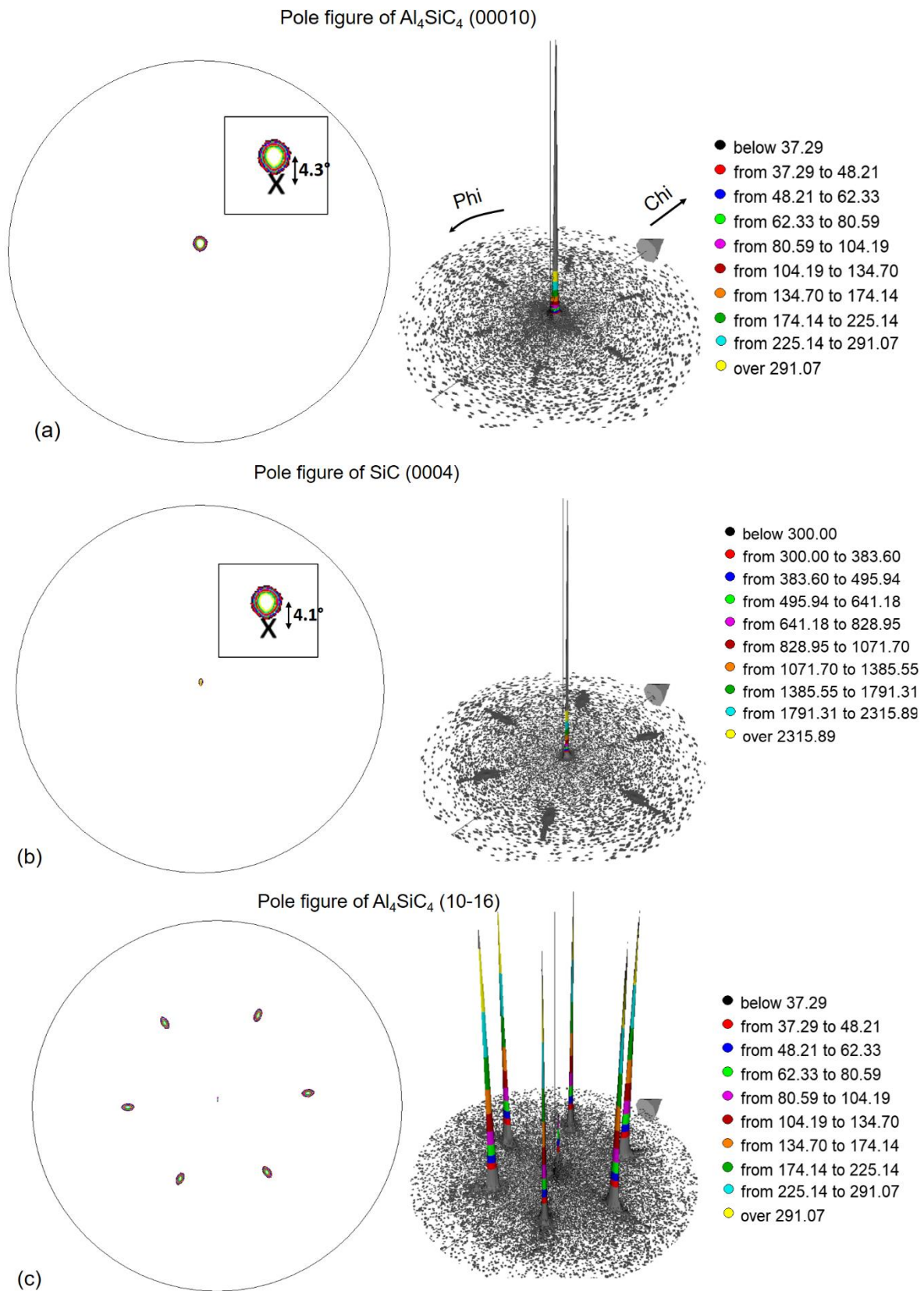


Figure 23: Figures de pôle (2D et 3D) de réflexion (a) (00010) d' Al_4SiC_4 , (b) (0004) de SiC, (c) (10-16) d' Al_4SiC_4 . Encart images est le zoom au centre de la figure polaire 2D.

Dans le cas du substrat 4H-SiC (face Si) hors axe, les angles d'inclinaison du substrat et de la couche déposée contribuent au décalage dans Omega. En effet, Omega de la réflexion (0004) SiC (13.7°) présente un décalage de 4.1° par rapport à la valeur théorique (17.8°). De même, Omega des réflexions (00010) et (10-16) d' Al_4SiC_4 présente aussi un décalage de 4.3° par rapport à la valeur théorique. Par conséquent, un angle d'inclinaison relatif de 0.2° entre le plan de base du dépôt et le substrat a été observé.

Concernant l'utilisation des substrats Si face et C face 6H-SiC, des valeurs théoriques d'Omega et de Chi ont été trouvées, ce qui indique l'alignement parfait du réseau Al_4SiC_4 sur celui du substrat SiC.

Une estimation de la qualité du cristal Al_4SiC_4 a été réalisée par la mesure de la courbe de basculement. Pour cela, la largeur totale à mi-hauteur (FWHM) des réflexions (00010) et (10-16) d' Al_4SiC_4 ont été comparées et rassemblées à la Figure 24. Les tendances sont claires : premièrement, le FWHM augmente avec l'angle d'inclinaison relatif entre le substrat Al_4SiC_4 et SiC. Il est donc plus élevé sur le substrat SiC hors axe. Deuxièmement, le FWHM est systématiquement plus bas sur la face Si-que sur la face C. Le gain de qualité lors de l'utilisation de substrats SiC à face Si est significatif car le FWHM est généralement réduit d'un facteur deux.

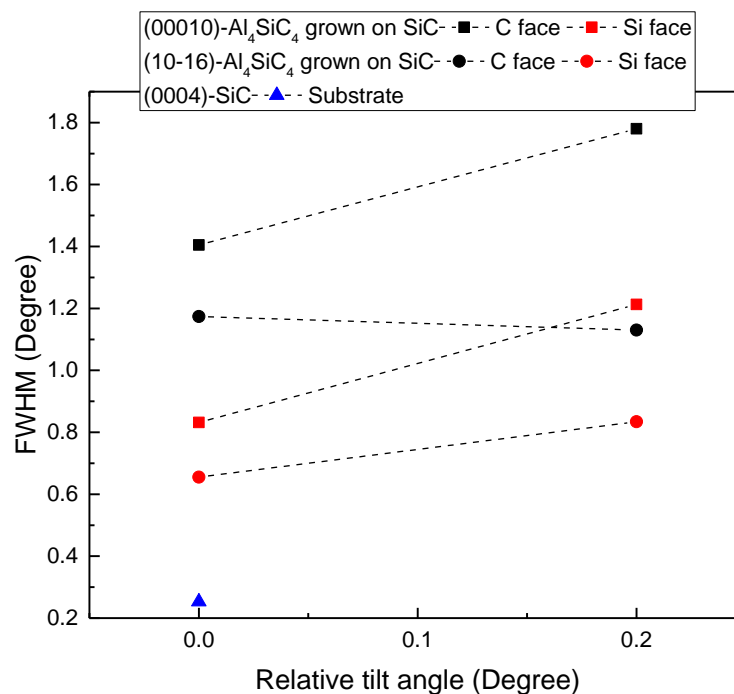


Figure 24: Dépendance de la qualité de la structure Al_4SiC_4 sur l'angle d'inclinaison relatif (entre le dépôt Al_4SiC_4 et le substrat SiC) et la polarité des substrats SiC (face Si et face C). FWHM de réflexions symétriques (00010) et asymétriques (10-16) ont été considérées. FWHM de (0004) réflexion du substrat 4H-SiC est également indiqué comme valeur de référence.

Selon les mesures DRX, les couches d' Al_4SiC_4 développées sur des substrats SiC hors axe sont légèrement inclinées de 0.2° par rapport au substrat. Ce type d'inclinaison, généralement appelé inclinaison Nagai, a été largement étudié dans la croissance hétéro-épitaxiale de différents matériaux sur des substrats hors axe^{23,24}. En fait, en raison de la présence de défauts

d'adaptation et de déformations du réseau dans la direction normale (Δc), il peut y avoir une déviation de la direction de croissance de la couche déposée par rapport à celle du substrat. Pour cette raison, un FWHM plus élevé a été trouvé dans la couche épilaire sur des substrats hors axe par rapport au substrat dans l'axe. Autrement dit, la couche doit s'adapter à la fois dans le plan basal et le long de la direction c lorsque le substrat hors axe est utilisé. L'angle d'inclinaison relative est illustré par $\Delta\alpha$ dans le modèle de l'interface entre Al_4SiC_4 et le substrat SiC hors axe représenté sur la Figure 25. Cette déformation du réseau à l'interface de l'hétérostructure sera étudiée plus en détail par la microscopie électronique à transmission à haute résolution au chapitre suivant.

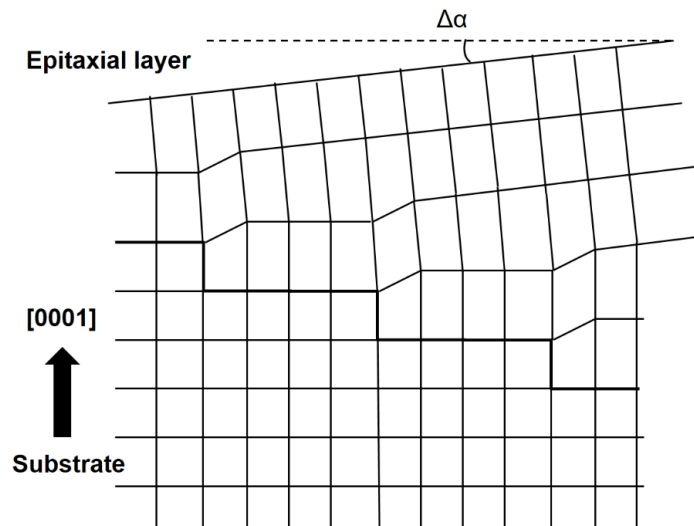


Figure 25: Modèle de l'interface entre Al_4SiC_4 et le substrat SiC hors axe. Pour simplifier le dessin, la non-concordance du réseau dans le plan horizontal (basal) est négligée dans la figure.

V. Hétéro-épitaxie d' Al_4SiC_4 sur SiC

Comme mentionné dans le chapitre précédent, une hétérostructure de Al_4SiC_4 sur un substrat SiC hexagonal orienté [0001] a été obtenue par le procédé de sublimation. À partir de l'analyse par diffraction des rayons X, la direction de croissance de la couche Al_4SiC_4 a été étudiée et trouvée parallèlement à l'orientation du substrat SiC. Dans cette section, en utilisant le HRTEM, la relation épitaxiale et la déformation à l'interface de l'hétérostructure Al_4SiC_4 /SiC sont analysés pour différents types de substrats hexagonaux SiC.

5.1. Expériences

Les couches d' Al_4SiC_4 d'une épaisseur de 50 μm synthétisé par procédé de sublimation sur différents substrats hexagonaux SiC (face C) orientés : polytype 6H sur l'axe et polytype 4H hors axe 4° . Les matériaux sources étaient composés d'un mélange de poudres de haute pureté d' Al_4C_3 (Alfa Aesar, pureté 99%) et de SiC (Sika tech E301) avec un rapport molaire $X_{\text{Al}_4\text{C}_3}=0.2$. Le processus expérimental présenté au chapitre IV a été utilisé. La température de croissance était 1800°C et la pression était 300 mbar. La durée de dépôt était 2 heures avec une

différence de température de 29°C entre la source et le germe afin d'éviter la condensation des phases parasites. Le processus expérimental est illustré dans la Figure 26.

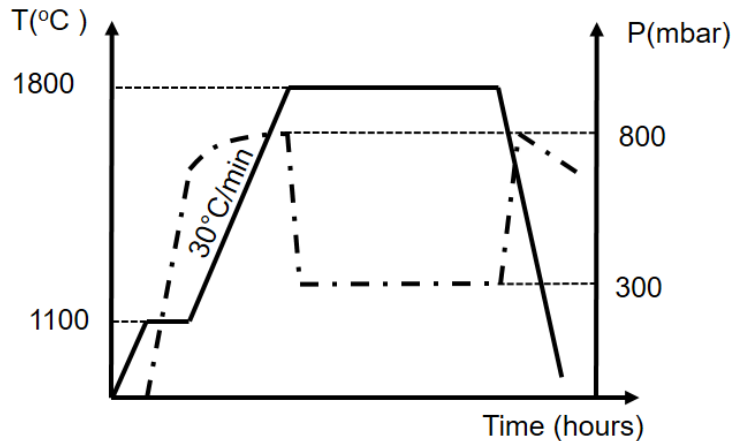


Figure 26: Représentation de la recette utilisée pour le processus de sublimation.

Pour l'observation TEM, les lamelles ont été préparées en utilisant les procédures de polissage standard. L'analyse de la diffraction et de la déformation est effectuée sur les images HRTEM afin d'identifier les phases et d'étudier la relation cristallographique entre le dépôt Al_4SiC_4 et le substrat SiC.

5.2. Relation épitaxiale d' Al_4SiC_4 /SiC

Hétéro-structure d' Al_4SiC_4 sur la face C de SiC-6H [0001] orientée sur l'axe.

La Figure 27 présente l'image HRTEM de la couche Al_4SiC_4 déposée. Comme illustré, une couche cristalline parfaite du Al_4SiC_4 a été observée exempte de défauts. A partir de l'image de diffraction de Al_4SiC_4 , avec l'axe de zone [-1100], les plans {0002} et les plans {11-20} sont indexés comme présenté dans l'encart (i). D'après le diagramme de diffraction, l'espacement interplanaire mesuré $d_{(0002)}$ et $d_{(11-20)}$ est respectivement égal à $10.9 \pm 0.05 \text{ \AA}$ et $1.64 \pm 0.01 \text{ \AA}$, qui sont également présentés dans l'espace direct à travers l'image à fort grossissement donnée dans l'encart (ii).

Concernant l'interface, la Figure 28 présente le diagramme de diffraction de l'interface de l'hétérostructure. Les {0002} plans de Al_4SiC_4 et les {0006} plans du 6H-SiC sont indexés dans le sens de la croissance. Les {11-20} plans de Al_4SiC_4 et les {11-20} plans de SiC sont indexés dans la direction basale. Comme résultats, les plans {0002} d' Al_4SiC_4 sont parallèles aux plans {0006} de 6H-SiC et les plans {11-20} d' Al_4SiC_4 sont parallèles aux plans {11-20} de 6H-SiC, ce qui démontre la relation épitaxiale entre les couches d' Al_4SiC_4 et le substrat de 6H-SiC.

A partir de l'analyse par diffraction électronique, les constantes de maille d' Al_4SiC_4 (a_{epi} et c_{epi}) déposées sur 6H-SiC sont calculées comme suivant:

$$\begin{cases} \frac{1}{d_{(0002)}^2} = \frac{4}{c_{epi}^2} \\ \frac{1}{d_{(11-20)}^2} = \frac{4}{3} \left(\frac{1^2 + 1 + 1^2}{a_{epi}^2} \right) \end{cases}$$

$$\begin{cases} c_{epi} = 21.8 \pm 0.1 \text{ \AA} \\ a_{epi} = 3.27 \pm 0.02 \text{ \AA} \end{cases}$$

Ces constantes de maille calculées sont en bon accord avec les paramètres de maille d' Al_4SiC_4 (diagramme de diffraction : 04-009-0133).

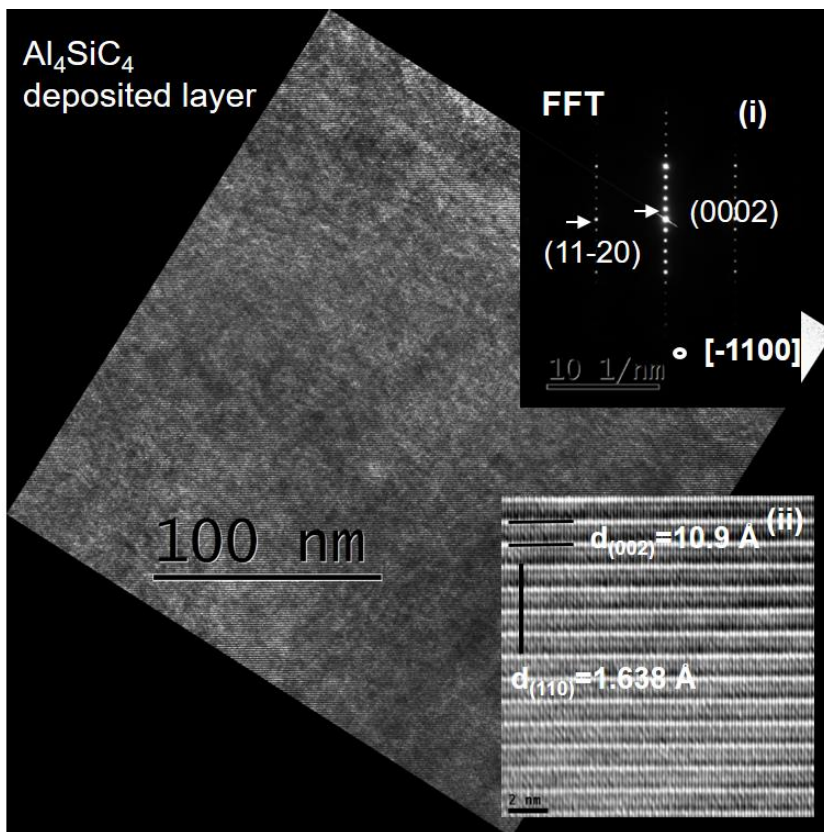


Figure 27: Image TEM de la couche d' Al_4SiC_4 observée le long de l'axe de la zone $[-1100]$; (i) diagramme de diffraction du cristal Al_4SiC_4 ; (ii) image haute résolution de la structure cristalline Al_4SiC_4 .

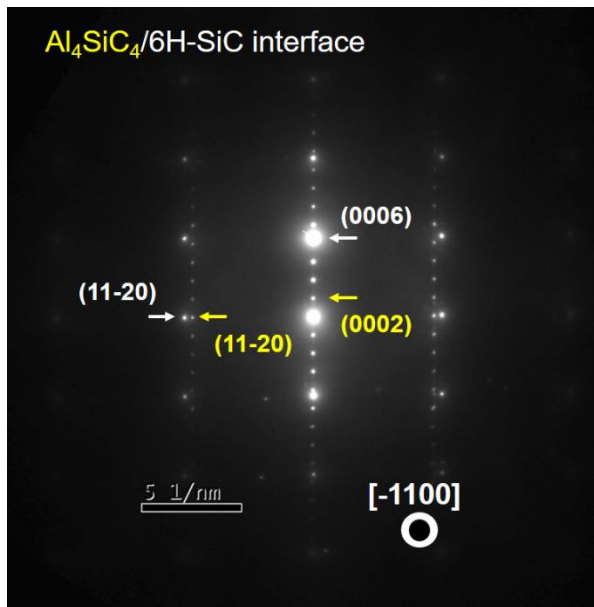


Figure 28: Diagramme de diffraction de l'interface entre Al_4SiC_4 et 6H-SiC.

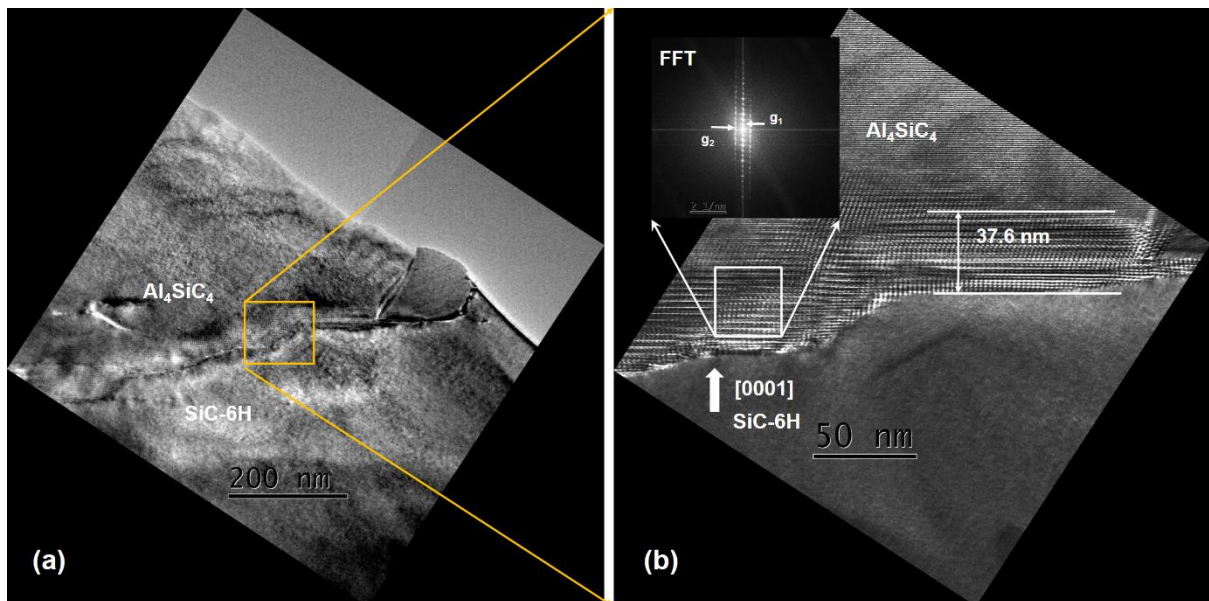


Figure 29: (a) Image TEM à faible résolution de l'interface $Al_4SiC_4/6H-SiC$, (b) Image HRTEM de l'interface $Al_4SiC_4/6H-SiC$. Une couche de superstructure a été trouvée le long de l'interface observée. La FFT de la couche interfaciale est indiquée dans l'encart.

En regardant de plus près l'interface, à travers l'image TEM à faible résolution présentée à la Figure 29(a), une morphologie a été observée à la surface du substrat 6H-SiC. C'est une preuve de la dissolution du SiC au début des phénomènes de condensation en contact avec la vapeur dominée par les espèces contenant de l'Al. De plus, une couche de superstructure a été trouvée entre la couche Al_4SiC_4 et le substrat 6H-SiC. Dans le HRTEM présenté dans la Figure 29(b), l'épaisseur mesurée de cette couche est d'environ 37.6 ± 10 nm. Grâce à la FFT de la couche interfaciale donnée dans l'encart, le long de la direction de croissance, le point de diffraction le plus proche g_1 présente un espacement interplanaire de 31.28 ± 0.01 Å. Le long

de la direction basale, la tache de diffraction g_2 présente un espacement interplanaire de $23.58 \pm 0.01 \text{ \AA}$. Ces valeurs ne correspondent à aucune phase connue.

Hétéro-structure d' Al_4SiC_4 sur C face de 4H-Si orienté hors axe 4° (vers [11-20])

L'analyse de diffraction d'électrons est réalisée à l'interface entre le substrat 4H-SiC hors axe 4° et Al_4SiC_4 (sans inclusion de phase parasite). La Figure 30 présente l'image TEM haute résolution de l'interface avec l'image FFT correspondante. Cependant, contrairement au cas du SiH 6H, la couche de superstructure interfaciale n'a pas été trouvée à l'interface observée. Dans l'image FFT, sous l'axe des zones $[-12-10]$, les plans $\{00010\}$ d' Al_4SiC_4 et $\{0004\}$ de 4H-SiC sont indexés dans le sens de la croissance. Les $\{10-10\}$ plans d' Al_4SiC_4 et les $\{10-10\}$ plans de 4H-SiC sont indexés dans le sens basal. Comme résultats, les plans $\{00010\}$ d' Al_4SiC_4 sont parallèles aux plans $\{0004\}$ de 4H-SiC et les plans $\{11-20\}$ d' Al_4SiC_4 sont parallèles aux plans $\{11-20\}$ de 6H-SiC, ce qui démontre la relation épitaxiale entre le dépôt d' Al_4SiC_4 et le substrat de 4H-SiC.

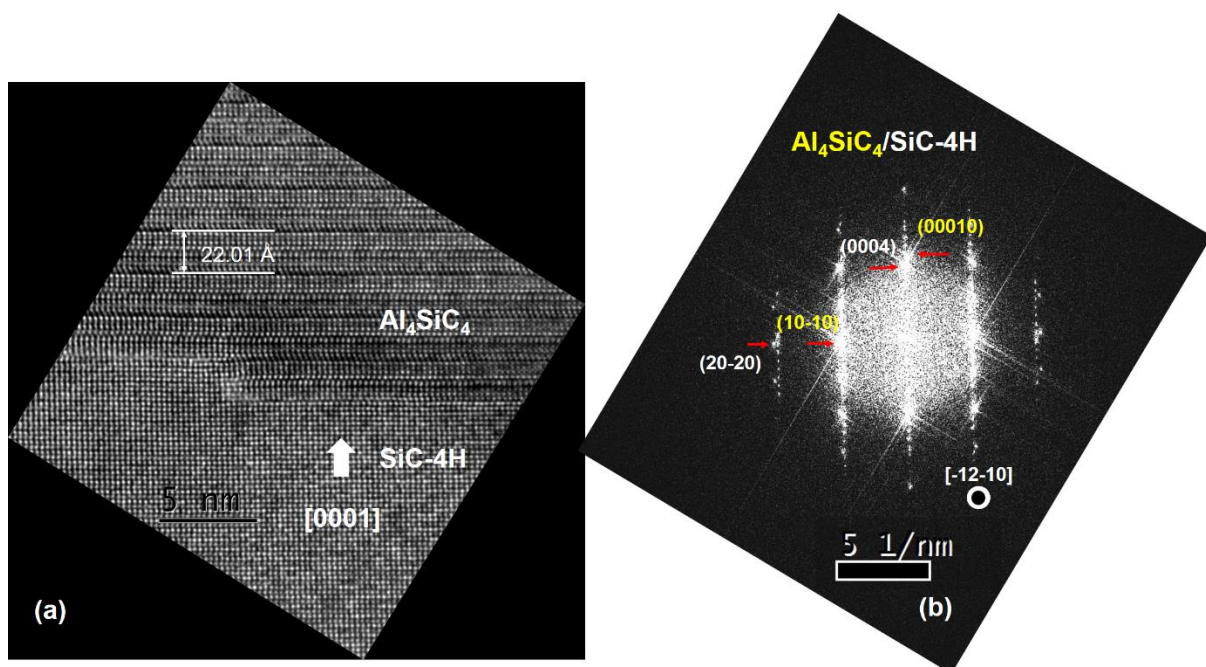


Figure 30: a) Image HRTEM de l'interface entre Al_4SiC_4 et SiC-4H orienté. (b) FFT indexée de (a).

Discussion

La relation épitaxiale a été étudiée dans l'hétérostructure d' Al_4SiC_4 sur le substrat SiC orienté sur l'axe et hors l'axe 4° pour les deux cas de polytype 4H et 6H.

Dans le cas d'une hétérostructure $\text{Al}_4\text{SiC}_4/6\text{H-SiC}$ sur l'axe, une couche de superstructure interfaciale ayant une épaisseur de 37.4 nm a été trouvée. Grâce à l'analyse par diffraction, un espacement interplanaire élevé de 31.28 Å et 23.58 Å a été révélé respectivement dans la direction de croissance et dans la direction basale. Il pourrait présenter une phase intermédiaire entre 6H-SiC et Al_4SiC_4 qui se serait formée à partir de la vapeur riche en Al au début du processus. De plus, par l'analyse de diffraction, les paramètres de maille du dépôt Al_4SiC_4 ont

été déterminées et correspondent bien aux valeurs de masse rapportées. Le mismatch du système d'environ 6,5% est compensé par la superstructure interfaciale.

Dans le cas de l'hétérostructure $\text{Al}_4\text{SiC}_4/4\text{H-SiC}$, l'angle d'inclinaison de 0.2° observé dans le chapitre IV n'a pas été facilement observé à cause de la résolution de l'image. De plus, la couche de superstructure interfaciale n'a pas été trouvée à l'interface observée. Pour cette raison, l'image HRTEM de l'interface (Figure 30(a)) permet l'analyse du champ de contrainte qui sera présentée dans la section suivante.

5.3. Analyse de la déformation à l'interface d' Al_4SiC_4 / C face- $[0001]$ 4H-SiC hors axe 4°

L'analyse GPA a été réalisée sur l'image HRTEM de l'interface entre le dépôt d' Al_4SiC_4 et le substrat 4H-SiC hors axe 4° qui figure dans la Figure 31(a).

Dans un premier temps, l'analyse se fait selon la direction $[10-10]$. Sur le spectre de puissance de l'interface présentée à la Figure 31(b), un masque gaussien de $0.5 \text{ g} (\text{nm}^{-1})$ est utilisé pour sélectionner les fréquences correspondant au plan $(10-10)$ d' Al_4SiC_4 et 4H-SiC qui ont espacements interplanaires relâchées de 2.84 \AA et de 2.67 \AA , respectivement. L'image de Bragg de la zone masquée est donnée à la Figure 31(c). L'image d'amplitude et l'image de phase de la transformée de Fourier filtrée en inverse sont données à la Figure 31(d) et (e). En prenant le substrat SiC comme référence, le champ de contrainte suivant la direction $[10-10]$ est représenté sur la Figure 31(f).

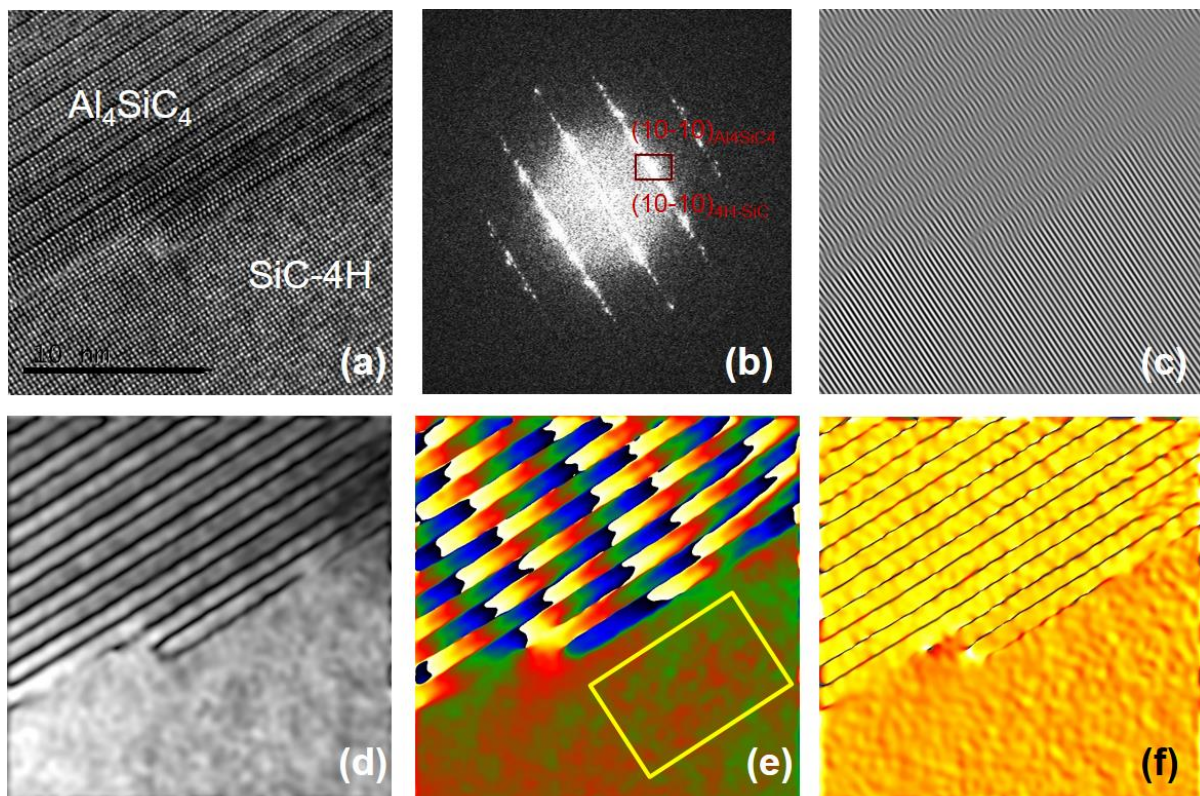


Figure 31: Analyse de déformation (GPA) selon la direction $[10-10]$. (a) L'image TEM à haute résolution de l'interface. (b) Spectre de puissance de l'image (a) permettant de sélectionner

une fréquence g par un masque gaussien, qui correspond à la position des points de diffraction du plan (10-10) Al_4SiC_4 et (10-10) SiC. (c) L'image de Bragg de la transformée de Fourier filtrée. (d) L'image d'amplitude de la transformée de Fourier filtrée en inverse. (e) L'image de phase avec la région de référence choisie à l'intérieur du substrat SiC. (f) Le champ de contrainte suivant la direction [10-10].

Le profil de la tension à l'interface suivant la direction [10-10] est présenté à la Figure 32. Comme résultat, en supposant que la déformation est nulle dans le substrat SiC, la déformation dans la couche Al_4SiC_4 est de $3 \pm 0.6\%$, ce qui correspond à l'équation suivante:

$$e_{\text{epi}} = \frac{d_{(10-10)\text{Al}_4\text{SiC}_4} - d_{(10-10)\text{SiC}}}{d_{(10-10)\text{SiC}}}$$

Ainsi, si le $d_{(10-10)}$ détendu du SiC est égal à 2.67\AA , le $d_{(10-10)}$ calculé du dépôt Al_4SiC_4 a une valeur de $2.75 \pm 0.015 \text{\AA}$. Le paramètre de maille d' Al_4SiC_4 est déterminé : $a_{\text{epi}} = 3.175 \pm 0.017 \text{\AA}$.

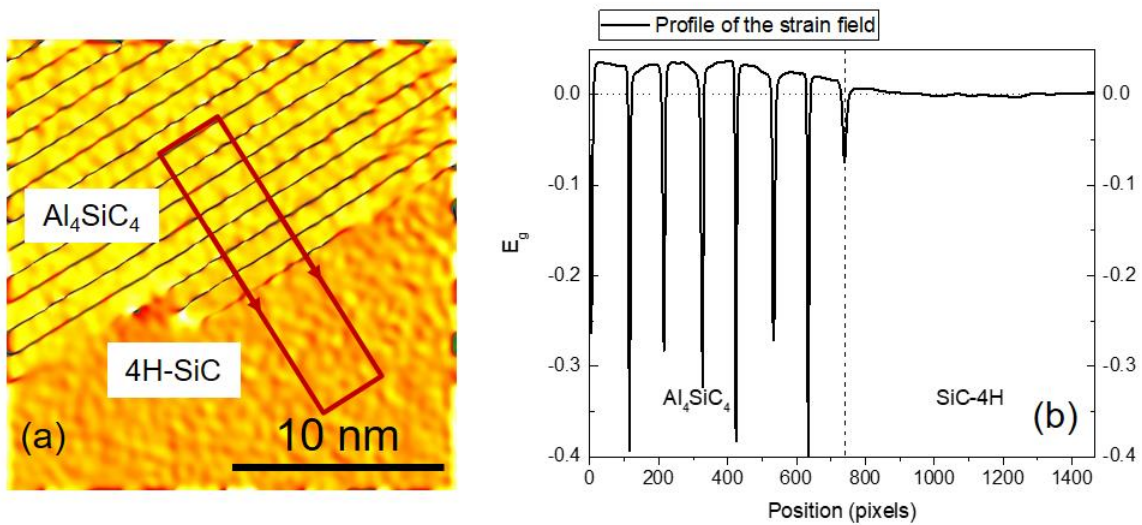


Figure 32: (a) La déformation à l'interface dans la direction [10-10]. (b) Profil de la tension correspondant au contour présenté en (a).

De plus, les discontinuités du profil de déformation sont également observées et correspondent aux lignes noires de l'image HRTEM. C'est probablement dû aux conditions d'observation expérimentales (épaisseur et défocalisation) de l'image.

Ensuite, le champ de contrainte à l'interface selon la direction [0001] est analysé. Sur le spectre de puissance de l'interface présentée à la Figure 33(b), un masque gaussien de $0.5g$ (nm^{-1}) est utilisé pour sélectionner les fréquences correspondant au plan (0008) d' Al_4SiC_4 et au plan (0004) de SiC qui ont un espacement interplanaire relâché de 2.715\AA et 2.515\AA respectivement. L'image de Bragg de la zone masquée est donnée à la Figure 33(c). L'image d'amplitude et l'image de phase de la transformée de Fourier filtrée en inverse sont données à la Figure 33(d) et (e). En prenant le substrat en SiC comme référence, le champ de contrainte selon la direction [0001] est donné sur la Figure 33(f). On note que, avec les plans sélectionnés, le désaccord de réseau Δd entre le dépôt Al_4SiC_4 et le substrat 4H-SiC est:

$$\Delta d_{bulk} = \frac{d_{(0008)Al_4SiC_4} - d_{(0004)4H-SiC}}{d_{(0004)4H-SiC}} = 7.9\% .$$

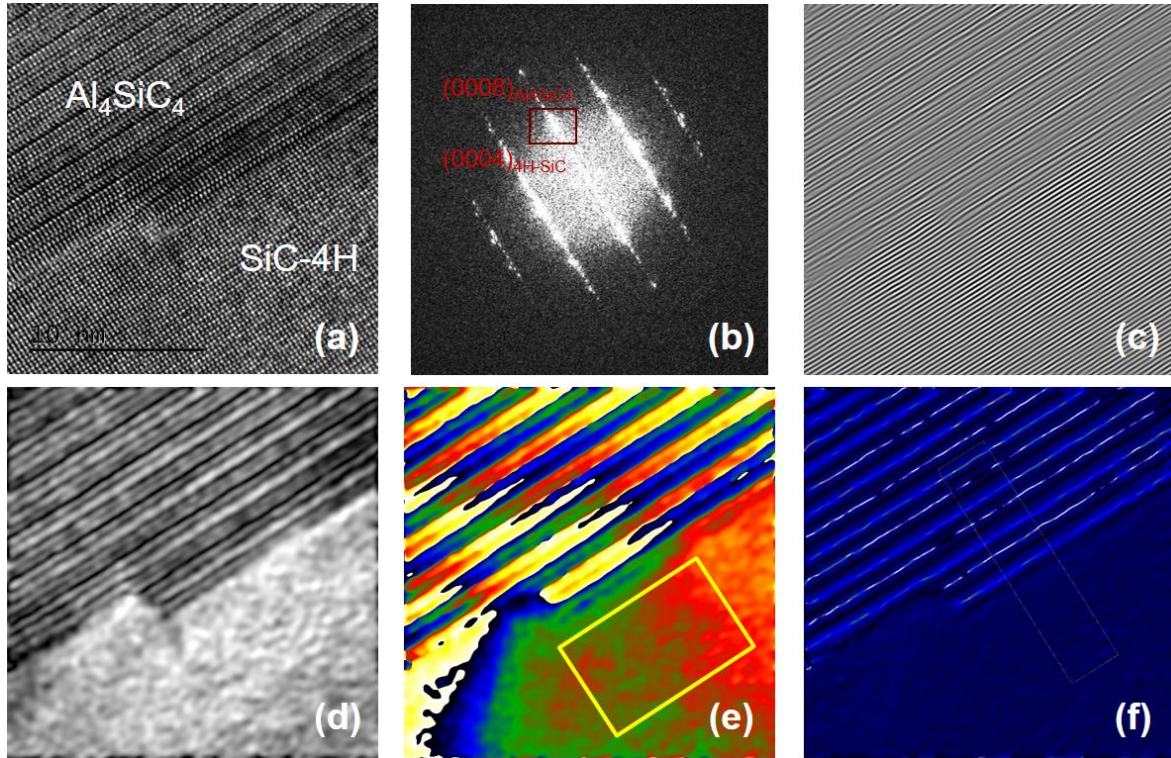


Figure 33: Analyse de déformation selon la direction [0001]. (a) L'image TEM à haute résolution de l'interface. (b) Spectre de puissance de l'image (a) permettant de sélectionner une fréquence g par un masque gaussien, qui correspond à la position des points de diffraction du plan (0008) Al_4SiC_4 et (0004) SiC . (c) L'image de Bragg de la transformée de Fourier filtrée. (d) L'image d'amplitude de la transformée de Fourier filtrée en inverse. (e) L'image de phase avec la région de référence choisie à l'intérieur du substrat SiC . (f) Le champ de déformation selon la direction [0001].

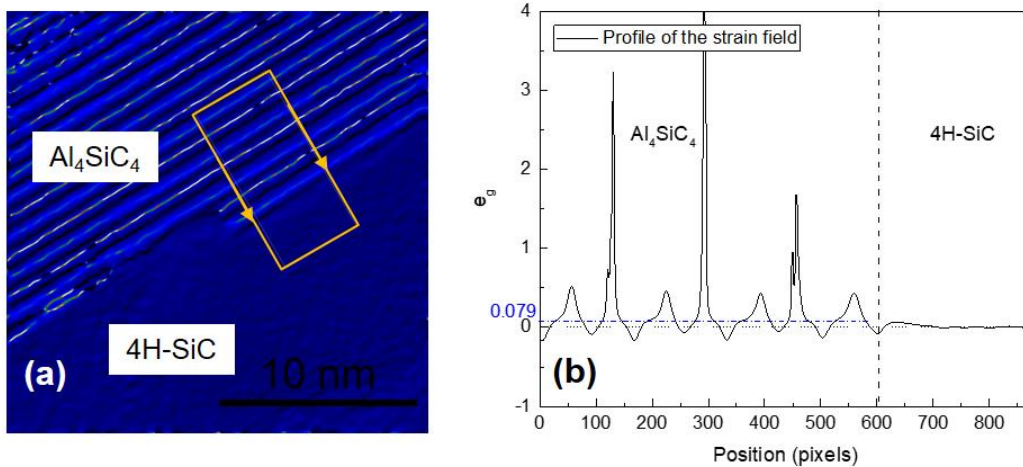


Figure 34: (a) La déformation à l'interface dans la direction [0001]. (b) Profil de la tension correspondant au contour présenté en (a).

Le profil de déformation à l'interface selon la direction [0001] est donné à la Figure 34. Comme résultat, la déformation dans Al_4SiC_4 n'a pas pu être identifiée à cause des conditions d'observation expérimentales de l'image HRTEM. Cependant, en moyenne, la déformation

calculée est toujours supérieure à la tension relâchée marquée par la ligne bleue. Ainsi, le paramètre de maille c du dépôt Al_4SiC_4 est supérieure à celle de la structure relâchée. Autrement dit, il démontre une extension de la structure d' Al_4SiC_4 selon la direction [0001].

Discussion

Le champ de contrainte à l'interface entre le dépôt Al_4SiC_4 et le substrat 4H-SiC à face C hors axe 4° a été analysé par la méthode GPA. Une tension biaxiale a été étudiée dans les directions [10-10] et [0001]. Grâce à l'analyse selon la direction [10-10], la paramètre de maille a du dépôt est déterminée : $a_{\text{epi}} = 3.175 \pm 0.017 \text{ \AA}$ plus petit que le relaxé $a = 3.28 \text{ \AA}$. Il démontre une compression de la structure d' Al_4SiC_4 dans le plan basal. Pour l'analyse selon la direction [0001], une expansion de la maille d' Al_4SiC_4 le long du c a été étudiée par l'augmentation du paramètre de maille c .

Pour la comparaison, les paramètre de maille d' Al_4SiC_4 déposée sur différents substrats SiC (face C de 6H sur l'axe et face C de 4H hors axe) sont rassemblées dans le tableau 9, avec les paramètres de maille relâchées d' Al_4SiC_4 . Les déformations de l'épilayer par rapport à la masse sont également calculées et indiquées dans le tableau.

Tableau 9 : Paramètre de maille d' Al_4SiC_4 déposée sur un substrat 4H-SiC hors axe 4° par rapport à Al_4SiC_4 bulk (diagramme de diffraction: 04-009-0133).

Samples	Lattice constant (Å)		Tension d'épilayer à comparer avec la valeur théorique (%)	
	a	c	$\Delta a/a$	$\Delta c/c$
Al_4SiC_4 bulk	3.28	21.72		
Al_4SiC_4 /on axis 6H-SiC	3.27 ± 0.02	21.8 ± 0.1	dans l'error bar	dans l'error bar
$\text{Al}_4\text{SiC}_4/4^\circ$ off axis 4H-SiC	3.175 ± 0.017	> 21.8	-3.35	> 0.37

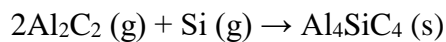
La déformation biaxiale trouvée à l'interface de la couche Al_4SiC_4 et du substrat 4H-SiC hors axe 4° est probablement liée à la désorientation du substrat et à l'absence d'une couche de superstructure interfaciale. Cette déformation de la structure en treillis était mentionnée au chapitre 4, provoquant un angle d'inclinaison de 0.2° entre le plan basal de la couche de dépôt et le substrat SiC hors axe de 4° . Dans le cas de substrats vicinaux, étant donné que la croissance est régie par le mécanisme de croissance par étapes, des contraintes et des défauts (dislocations) sont introduits aux étapes interfaciales pour s'adapter au changement de séquence d'empilement et au désaccord de réseau dans la direction de croissance²⁵.

VI. Conclusions générales

L'objectif principal de ce travail était le développement d'un procédé de sublimation pour la croissance de monocristaux d' Al_4SiC_4 , à partir des poudres d' Al_4C_3 et de SiC. Différents aspects du processus ont été étudiés.

En préambule de l'étude expérimentale, une analyse thermodynamique conventionnelle a été réalisée pour décrire les phénomènes de vaporisation et de condensation dans le système

pseudo-binaire Al_4C_3 -SiC (chapitre III). Il apparaît clairement que la vaporisation d'un mélange Al_4C_3 -SiC présente toujours un fort excès d'Al dans la phase gazeuse. Malgré une si forte non-congruence, nous avons identifié les conditions favorables à la condensation de différents carbures ternaires aluminium-silicium tels que Al_4SiC_4 et Al_8SiC_7 , en fonction des températures de source et de germe et pour différentes compositions initiales des matériaux sources ($X_{\text{Al}_4\text{C}_3}$). La condensation de l' Al_4SiC_4 monophasé nécessite : i) une composition initiale riche en SiC ($X_{\text{Al}_4\text{C}_3} < 0.5$) et ii) une différence de température entre les zones de vaporisation et de condensation inférieures à 40°C . La formation de Al_4SiC_4 est régie par les espèces gazeuses Al_2C_2 (g) et Si (g), ce qui suggère la réaction suivante comme réaction "thermodynamiquement limitante" :



Sur une base expérimentale, deux approches à haute température pour la synthèse de Al_4SiC_4 ont été étudiées, à partir d'un mélange de poudres Al_4C_3 et SiC (chapitre IV). Toutes les tendances ont été trouvées en accord avec les diagrammes de phases connus et les calculs thermodynamiques présentés au chapitre III.

Tout d'abord, un processus de frittage réactif naturel (sans pression) a été étudié, l'objectif principal étant la synthèse de l' Al_4SiC_4 monophasé. Malheureusement, quelle que soit la composition initiale de Al_4C_3 et SiC, l'objectif n'a pas pu être atteint car la composition globale de la source dévie systématiquement de la section binaire initiale. En effet, le comportement du mélange Al_4C_3 -SiC à haute température pourrait être décrit en considérant deux phénomènes : i) la réaction à l'état solide entre les deux carbures, qui montre un faible rendement de réaction, et ii) les vitesses de vaporisation relatives des différents éléments peuvent conduire à des changements importants de la composition globale. Une approche de compression isostatique à chaud pourrait considérablement améliorer les deux étapes.

Deuxièmement, un processus de croissance par sublimation pour la synthèse d'échantillons monocristallins Al_4SiC_4 a été étudié. Ceci pourrait être réalisé avec les contraintes suivantes: i) composition initiale riche en SiC ($X_{\text{Al}_4\text{C}_3} < 0,5$) des matériaux sources, ii) faible gradient de température entre la source et la graine pour éviter la condensation des phases parasites, iii) masse modérée transport pour éviter de fortes évolutions du système et encore, la condensation des phases parasites. Le matériel source a montré une évolution complexe, donnant lieu à la formation des strates. Cela pourrait s'expliquer par l'interaction entre la thermodynamique et les phénomènes de transport de masse, c'est-à-dire le taux de vaporisation relatif des différentes espèces. Nous avons appliqué avec succès ce processus de croissance par sublimation à la croissance épitaxiale de couches Al_4SiC_4 monophasées épaisses de haute qualité, sur des plaquettes commerciales hexagonales-SiC. À partir de cette première expérience, il est devenu très problématique de maintenir des conditions stationnaires pour la croissance de monocristaux Al_4SiC_4 en vrac.

Des caractérisations de base ont été effectuées afin d'obtenir une première image de la morphologie de la surface de croissance et de la qualité structurale des couches cristallines Al_4SiC_4 obtenues (chapitre IV). Par exemple, nous avons montré que la nature du substrat (face C vs face Si, hors l'axe vs sur l'axe) avait un effet significatif sur la mosaïcité de la couche et

également sur le réseau cristallin couche et les substrats. En effet, les dépôts d' Al_4SiC_4 développés sur des substrats SiC sur l'axe ont une meilleure qualité cristalline que ceux développés sur des substrats SiC hors l'axe. Un angle d'inclinaison relative (inclinaison de Nagai) de 0.2° entre le plan de base de la couche Al_4SiC_4 et le substrat SiC hors axe de 4° a été trouvé. Une hypothèse liée à la présence de déformation biaxiale dans la couche épitaxiale développée sur un substrat hors axe a été proposée à titre d'explication. Concernant l'effet de la polarité, une mosaïcité plus élevée a été obtenue sur des substrats SiC en face C, ce qui a été expliqué par la réactivité différente des deux polarités. Pour les couches minces, la meilleure qualité a été obtenue sur des substrats SiC sur l'axe. En outre, la qualité a été considérablement améliorée avec l'épaisseur et une FWHM de 0.303° a été mesurée pour la réflexion (00010) d'une couche de Al_4SiC_4 de $185\ \mu\text{m}$ d'épaisseur, ce qui est une excellente valeur "préliminaire", compte tenu de la discordance élevée entre le substrat et la couche.

Une étude plus approfondie de la structure interfaciale a été réalisée en utilisant HRTEM (chapitre V), avec un accent particulier sur l'état de contrainte. En effet, la relaxation de la couche d'épilateur Al_4SiC_4 développée sur le substrat 6H-SiC en C-face sur l'axe, a été observée avec la présence d'une superstructure interfaciale, dont son nature n'est toujours pas claire. Nous pensons que c'est une phase intermédiaire qui s'est formée à partir de la vapeur riche en Al au début du processus de croissance par sublimation. En outre, il existe des preuves que la discordance du réseau d'environ 6,5% est pris en charge par cette superstructure interfaciale. En cas de croissance sur la face C du substrat 4H-SiC hors axe de 4° , une déformation élastique significative a été trouvée à l'interface sans la présence de la superstructure. Cette déformation élastique a été introduite pour tenir compte des asymétries de réseau le long des directions de base et de croissance. Ces résultats confirment les investigations préliminaires présentées au chapitre IV.

Concernant les propriétés optiques d' Al_4SiC_4 , la spectroscopie UV-Vis a révélé un seuil d'absorption démontrant une bande interdite indirecte d'environ 2.10eV pour les cristaux obtenus par sublimation (chapitre IV). Cette valeur est légèrement supérieure à celle observée pour les cristaux obtenus en solution (1.93 eV). Par analogie avec le SiC, on peut s'attendre à un rétrécissement de la bande interdite en cas de niveau de dopage élevé, ce qui est généralement le cas dans la croissance de la solution par rapport à la croissance par sublimation. Cependant, d'autres caractérisations sont nécessaires pour la description qualitative et quantitative des propriétés. Par exemple, des mesures à effet Hall seraient nécessaires pour déterminer le type de dopage, la concentration de porteurs et la mobilité du support. L'avantage de la taille de l'échantillon ($1 \times 1\text{cm}^2$) lorsque les couches d' Al_4SiC_4 sont développées de manière hétéroépitaxiale sur des substrats SiC, est partiellement masqué par la présence de nombreuses fissures dans la couche, ce qui rend la mesure très difficile.

Comme première thèse sur l'exploration des semi-conducteurs à base d'Al-Si-C, tout n'est pas complet, bien sûr. Mais il apporte de nombreux éléments de base et apporte de nombreuses informations pour le développement ultérieur du sujet. Il apparaît clairement que le processus de croissance par sublimation est non-stationnaire pour tenir compte de la croissance de monocristaux de grande taille. Une vision plus réaliste consisterait à optimiser la croissance de la sublimation ensemencée pour les couches minces à épaisses. Une autre approche, non

explorée ici, est la croissance de la solution, qui permet généralement d'atteindre une très bonne qualité cristalline. Un point clé pour une amélioration supplémentaire de la qualité de la couche est le contrôle des premiers stades de croissance et des propriétés d'interface initiales entre la couche et les substrats SiC. Difficile à mettre en œuvre dans le processus de croissance par sublimation, en raison des températures élevées utilisées, une approche d'ingénierie d'interface par l'utilisation de couches tampons permettrait améliorer l'interface entre la couche et les substrats. Une couche tampon avec une épaisseur appropriée pourrait être introduite pour libérer la contrainte et réduire les fissures dans le dépôt dues au désaccord du réseau et à la différence de CTE. La nature de la couche tampon pourrait être la Al_4SiC_4 formée par conversion chimique de l'hétérostructure $\text{Al}_4\text{C}_3/\text{SiC}$ qui a été partiellement étudiée dans ce travail. Pour préparer la couche tampon, il faut d'abord obtenir une couverture complète de la couche Al_4C_3 sur le substrat SiC. Plus tard, une couche tampon de Al_4SiC_4 devrait être formée à partir de la réaction entre Al_4C_3 et SiC par le recuit à température plus élevée. Plus réaliste, du point de vue du contrôle, consiste à former la couche tampon sur SiC par dépôt chimique en phase vapeur (CVD) ou par CVD réactif. Cette technique permet généralement un bon contrôle des interfaces. A notre connaissance, le dépôt chimique en phase vapeur n'a jamais été étudié pour le dépôt de tels carbures, mais il est parfaitement adapté aux carbures en général, comme le montrent les développements qui ont été effectués sur les revêtements en silicium et semi-conducteurs.

À ce stade, nous n'avons aucune idée du niveau de dopage, de la nature du dopant et du type de dopant de nos échantillons de carbure. Par analogie avec SiC, il est probable que N était un donneur dans Al_4SiC_4 et en forte concentration, car nous avons utilisé le processus de croissance par sublimation. Pour vérifier ce point, la croissance sous atmosphère contenant du N_2 sera mise en œuvre. De manière plus générale, l'utilisation de ces nouveaux carbures dans les applications de semi-conducteurs nécessitera une enquête approfondie sur les dopants possibles et leur incorporation.

Le potentiel le plus élevé de ce travail, en termes de perspectives, réside dans la réalisation d'hétérostructures de carbures. Bien que n'étant pas encore optimisé, nous avons démontré avec succès la possibilité de faire croître de manière hétéroépitaxiale Al_4SiC_4 et Al_4C_3 sur des plaquettes commerciales de SiC. De plus, bien que les propriétés de Al_8SiC_7 n'aient pas encore été étudiées, l'hétérostructure hétérostructure $\text{Al}_8\text{SiC}_7/\text{SiC}$ est également intéressante. En développant davantage les processus de croissance cristalline et en approfondissant les relations cristallographiques entre ces carbures, des hétérojonctions entre divers composés Al-Si-C (Al_4SiC_4 , Al_4C_3 et Al_8SiC_7) et SiC pourrait donner lieu au domaine de l'ingénierie de la bande interdite à base de carbure.

Références

1. Barczak, V. J. Optical and X-Ray Powder Diffraction Data for Al_4SiC_4 . *J. Am. Ceram. Soc.* **44**, 299 (1961).
2. Schoennahl, J., Willer, B. & Daire, M. Le carbure mixte Al_4SiC_4 : Préparation et données structurales. *J. Solid State Chem.* **52**, 163–173 (1984).

3. Oden, L. L. and McCune, R. A. Phase equilibria in the Al-Si-C system. *Metall. Trans. A* **18**, 2005–2014 (1987).
4. Gröbner, J., Lukas, H. L. & Aldinger, F. Thermodynamic calculation of the ternary system Al-Si-C. *Calphad* **20**, 247–254 (1996).
5. Beyer, R. P. & Johnson, E. A. Heat capacity of aluminum silicon carbide (Al₄SiC₄) from 5.26 to 1047 K. *J. Chem. Thermodyn.* **16**, 1025–1029 (1984).
6. Viala, J. C., Fortier, P. & Bouix, J. Stable and metastable phase equilibria in the chemical interaction between aluminium and silicon carbide. *J. Mater. Sci.* **25**, 1842–1850 (1990).
7. Liu, H., Madaleno, U., Shinoda, T., Mishima, Y. & Suzuki, T. Interfacial reaction and strength of SiC fibres coated with aluminium alloys. *J. Mater. Sci.* **25**, 4247–4254 (1990).
8. Lloyd, D. J. The solidification microstructure of particulate reinforced aluminium/SiC composites. *Compos. Sci. Technol.* **35**, 159–179 (1989).
9. Lloyd, D. J. & Jin, I. A method of assessing the reactivity between SiC and molten Al. *Metall. Trans. A* **19**, 3107–3109 (1988).
10. Moshier, W. C., Ahearn, J. S. & Cooke, D. C. Interaction of Al-Si, Al-Ge, and Zn-Al eutectic alloys with SiC/Al discontinuously reinforced metal matrix composites. *J. Mater. Sci.* **22**, 115–122 (1987).
11. Laurent, V., Chatain, D. & Eustathopoulos, N. Wettability of SiC by aluminium and Al-Si alloys. *J. Mater. Sci.* **22**, 244–250 (1987).
12. Viala, J.-C., Fortier, P., Bonnetot, B. & Bouix, J. Interaction sous haute pression entre l'aluminium solide et le carbure de silicium: High pressure interaction between solid Al and SiC. *Mater. Res. Bull.* **21**, 387–394 (1986).
13. Yamamoto, O., Ohtani, M. & Sasamoto, T. Preparation and oxidation of Al₄SiC₄. *J. Mater. Res.* **17**, 774–778 (2002).
14. Huang, X. & Wen, G. Mechanical properties of Al₄SiC₄ bulk ceramics produced by solid state reaction. *Ceram. Int.* **33**, 453–458 (2007).
15. Huang, X. X., Wen, G. W., Cheng, X. M. & Zhang, B. Y. Oxidation behavior of Al₄SiC₄ ceramic up to 1700 C. *Corros. Sci.* **49**, 2059–2070 (2007).
16. Hussain, A., Aryal, S., Rulis, P., Choudhry, M. A. & Ching, W. Y. Density functional calculations of the electronic structure and optical properties of the ternary carbides Al₄SiC₄ and Al₄Si₂C₅. *Phys. Rev. B* **78**, 195102 (2008).
17. Zevgitis, D. *et al.* Synthesis and Characterization of Al₄SiC₄: A “New” Wide Band Gap Semiconductor Material. in *Materials Science Forum* **821**, 974–977 (Trans Tech Publ, 2015).
18. Pedesseau, L. *et al.* Al₄SiC₄ wurtzite crystal: Structural, optoelectronic, elastic, and piezoelectric properties. *APL Mater.* **3**, 121101 (2015).
19. Inoue, Z., Inomata, Y., Tanaka, H. & Kawabata, H. X-ray crystallographic data on aluminum silicon carbide, α-Al₄SiC₄ and Al₄Si₂C₅. *J. Mater. Sci.* **15**, 575–580 (1980).

20. Kidwell, B. L., Oden, L. L. & McCune, R. A. $2\text{Al}_4\text{C}_3\text{SiC}$: a new intermediate phase in the Al–Si–C system. *J. Appl. Crystallogr.* **17**, 481–482 (1984).
21. Alcock, C. B., Itkin, V. P. & Horrigan, M. K. Vapour pressure equations for the metallic elements: 298–2500K. *Can. Metall. Q.* **23**, 309–313 (1984).
22. Wagner, R. S. & Ellis, W. C. Vapor-liquid-solid mechanism of single crystal growth. *Appl. Phys. Lett.* **4**, 89–90 (1964).
23. Nagai, H. Structure of vapor-deposited $\text{Ga}_x\text{In}_{1-x}\text{As}$ crystals. *J. Appl. Phys.* **45**, 3789–3794 (1974).
24. Pesek, A., Hingerl, K., Riesz, F. & Lischka, K. Lattice misfit and relative tilt of lattice planes in semiconductor heterostructures. *Semicond. Sci. Technol.* **6**, 705 (1991).
25. Ayers, J. E., Kujofsa, T., Rago, P. & Raphael, J. *Heteroepitaxy of semiconductors: theory, growth, and characterization*. (CRC press, 2016).